University of Southampton
Faculty of Physical & Applied Sciences
Optoelectronics Research Centre

Advanced high-power optical parametric oscillators synchronously pumped by ultrafast fibre-based sources

by
Florian Kienle

A thesis submitted in partial fulfillment for the degree of
Doctor of Philosophy

January 2012

UNIVERSITY OF SOUTHAMPTON
FACULTY OF PHYSICAL & APPLIED SCIENCES
OPTOELECTRONICS RESEARCH CENTRE

Abstract

Doctor of Philosophy

Advanced high-power optical parametric oscillators synchronously pumped by ultrafast fibre-based sources

by Florian Kienle

This thesis is concerned with investigating the generation of ultrashort, tunable pulses at high average power and / or high pulse energy using synchronously pumped optical parametric oscillators (OPO) and appropriate power-scalable fibre-amplifier pump sources. Two types of pump sources with average powers up to $\approx 100\,\mathrm{W}$ are considered: (1) a picosecond, all-fiberised, high-power, variable-repetition-rate, Yb:fibre-amplified, gain-switched laser diode system and (2) a femtosecond, high-power, chirped-pulse amplification Yb:fibre laser system incorporating a pulse shaper module. Such OPO systems find applications in fields as diverse as materials processing and nonlinear microscopy / spectroscopy.

Two OPOs based on periodically poled lithium niobate (PPLN) and pumped at $1060\,\mathrm{nm}$ from the first pump source are demonstrated. With $20\,\mathrm{ps}$-long pump pulses, average powers of up to $7.3\,\mathrm{W}$ ($3.1\,\mathrm{W}$) for the signal (idler) are generated at variable repetition rates of $\approx 0.1 \ldots 1\,\mathrm{GHz}$. With longer $100\,\mathrm{ps}$ pump pulses at a repetition rate of $< 8\,\mathrm{MHz}$ and an intracavity fibre as an OPO feedback component for compactness, combined pulse energies approaching $1\,\mu\mathrm{J}$ are obtained, which are the highest reported to date. Tuning ranges from $1.4\,\mu\mathrm{m}$ to $1.7\,\mu\mathrm{m}$ (signal) and from $2.8\,\mu\mathrm{m}$ to $4.4\,\mu\mathrm{m}$ (idler) are typical for both OPOs.

Including frequency-doubling of the $1060\,\mathrm{nm}$ light, the first pump source, operating at $230\,\mathrm{MHz}$ and $20\,\mathrm{ps}$, is used for two green-pumped OPOs tunable in the near-infrared range from $650\,\mathrm{nm}$ to $1040\,\mathrm{nm}$ (plus the idler from $1.08\,\mu\mathrm{m}$ to $2.9\,\mu\mathrm{m}$). The first OPO uses MgO-doped PPLN and up to $270\,\mathrm{mW}$ of combined output power with $1\,\mathrm{W}$ of pump power is obtained. Operation at higher power is complicated due to damage effects such as photo-refraction, nonlinear or induced absorption in lithium niobate. The second OPO uses lithium triborate (LBO) and compressed $4.4\,\mathrm{ps}$ green pump pulses to generate record average powers of up to $3.7\,\mathrm{W}$ of signal and $1.8\,\mathrm{W}$ of idler.

Using the second pump source with a liquid crystal spatial light modulator pulse shaper, the demonstration of energy-scalable output pulses from $0.1\,\mu\mathrm{J}$ to $2\,\mu\mathrm{J}$ at a centre wavelength of $1045\,\mathrm{nm}$ with typical pulse durations between $300\,\mathrm{fs}$ and $600\,\mathrm{fs}$ is reported. Pump pulses with a duration of $\approx 600\,\mathrm{fs}$ at a repetition rate of $50\,\mathrm{MHz}$ from this pump source are used for a PPLN OPO producing $\approx 1.9\,\mathrm{W}$ ($\approx 1.2\,\mathrm{W}$) of signal (idler) power at $1.5\,\mu\mathrm{m}$ ($3.6\,\mu\mathrm{m}$).

Declaration of Authorship

I, **Florian Kienle**, declare that this thesis entitled **"Advanced high-power optical parametric oscillators synchronously pumped by ultrafast fibre-based sources"** and the work presented in it are my own. I confirm that

- this work was done wholly or mainly while in candidature for a research degree at this University,
- where any part of this thesis has previously been submitted for a degree or any other qualification at this University or any other institution, this has been clearly stated,
- where I have consulted the published work of others, this is always clearly attributed,
- where I have quoted from the work of others, the source is always given. With the exception of such quotations, this thesis is entirely my own work,
- I have acknowledged all main sources of help,
- where the thesis is based on work done by myself jointly with others, I have made clear exactly what was done by others and what I have contributed myself,
- parts of this work have been published as (see appendixA):
  - F. Kienle *et al.*, Opt. Express [Accepted]
  - F. Kienle *et al.*, J. Opt. Soc. Am. B **29**(1), 144–152 (2012)
  - F. Kienle *et al.*, Opt. Lett. **35**(21), 3580–3582 (2010)
  - F. Kienle *et al.*, Opt. Express **18**(8), 7602–7610 (2010)

Signature: _____

Date: _____

"Achtung! Jetzt gibt es nur zwei Möglichkeiten:
Entweder es funktioniert oder es funktioniert nicht."

("Attention! There are only two possibilities now: Either it works or it doesn't.")

Lukas, in "Jim Knopf und Lukas der Lokomotivführer"
(Luke, in "Jim Button and Luke the Engine Driver")

Acknowledgements

I would like to express my gratitude to my supervisor Dave Shepherd, who helped me enormously to reach the goals that were set out about four years ago. He guided me through the different experiments and came up with new suggestions, when something didn't work out (and there was a lot that didn't!). But most importantly his continuous patience and kindness always gave me the confidence to keep asking. Not to mention his speed of proof-reading – wow!

I found it enormously helpful to discuss things with such wise people like Dave Hanna and Dave Richardson. Thank you very much for that. Really priceless!

The sometimes tedious and dull work (especially the daily alignment routine!) in the lab has been a lot more fun with the people around me: Cheers to Nikita, Hazel and Sarah, who gave our lab this special "girly spirit", and to Kang, Dejiao and Peh in the other lab. I have to say thanks to Jerry for passing on his huge knowledge about fibre amplifiers and pulse shaping to me. He explained so many things and taught me all the optics alignment tricks that you never find in any book.

A big thank you goes to numerous people at the ORC for the occasional chat about all sorts of stuff – be it related to work or not. You know who you are!

Thank you to Shaif-ul, Christophe and Jonathan, who patiently answered my many questions about lasers, amplifiers, fibres and so forth. Thank you also to Corin and Hazel for providing the PPLN crystals and telling me about the mysteries of those little (but essential for my PhD) components.

The ORC support staff was always very helpful. It never took long until they sorted out something to keep my work going. Thanks!

Finally, I'd like to thank all my friends, from Southampton and back in Germany, and especially my whole family for providing a strong antipole to the PhD work. I find this the most valuable thing to "stay grounded" and to avoid drifting off into the world of lasers all the time.

Contents

List of Figures

List of Tables

List of Abbreviations and Symbols

AOM	**A**cousto-**o**ptic **m**odulator
AOPDF	**A**cousto-**o**ptic **p**rogrammable **d**ispersive **f**ilter
APP	**A**namorphic **p**rism **p**air
AR	**A**nti-**r**eflection
ASE	**A**mplified **s**pontaneous **e**mission
BBO	**B**eta **b**arium **b**orate
BPM	**B**irefringent **p**hase-**m**atching
CARS	**C**oherent **a**nti-**S**tokes **R**aman **s**cattering
CCD	**C**harge-**c**oupled **d**evice
CFBG	**C**hirped **f**ibre **B**ragg **g**rating
CM	**C**urved **m**irror
CPA	**C**hirped **p**ulse **a**mplification
CSA	**C**ommunication **s**ignal **a**nalyzer
CW	**C**ontinuous **w**ave
DC	**D**irect **c**urrent
DE	**D**ifferential **e**volution
DM	**D**ichroic **m**irror
EOM	**E**lectro-**o**ptic **m**odulator
FROG	**F**requency-**r**esolved **o**ptical **g**ating
FWHM	**F**ull **w**idth at **h**alf **m**aximum
GaAsP	**Ga**llium **as**enide **p**hosphide
GDD	**G**roup **d**elay **d**ispersion [s^2]
GVD	**G**roup **v**elocity **d**ispersion [s^2/m]
GVM	**G**roup **v**elocity **m**ismatch
GRIIRA	**G**r**e**en-**i**nduced **i**nfra**r**ed **a**bsorption
HWP	**H**alf-**w**ave **p**late
InGaAs	**In**dium **ga**llium **ar**senide
IR	**I**nfra**r**ed
JADE	Self-**a**daptive **d**ifferential **e**volution
KTA	**P**otassium **t**itanyl **a**rsenate
KTP	**P**otassium **t**itanyl **p**hosphate

LBO	**L**ithium tri**bo**rate
LC	**L**iquid **c**rystal
LD	**L**aser **d**iode
LMA	**L**arge-**m**ode **a**rea
MgO	**M**a**g**nesium **o**xide
MgF_2	**M**a**g**nesium **f**luoride
MIR	**M**id-**i**nfra**r**ed
MOPA	**M**aster-**o**scillator **p**ower-**a**mplifier
NA	**N**umerical **a**perture
NCPM	**N**on-**c**ritical **p**hase-**m**atching
NIR	**N**ear-**i**nfra**r**ed
OC	**O**utput **c**oupler
OI	**O**ptical **i**solator
OPA	**O**ptical **p**arametric **a**mplifier
OPO	**O**ptical **p**arametric **o**scillator
OSA	**O**ptical **s**pectrum **a**nalyser
OP-GaAs	**O**rientation-**p**atterned **ga**llium **ar**senide
PBS	**P**olarising **b**eam **s**plitter
PC	**P**olarisation **c**ontroller
PCF	**P**hotonic **c**rystal **f**ibre
PM	**P**olarisation-**m**aintaining
PPLN	**P**eriodically **p**oled **l**ithium **n**iobate
PPLT	**P**eriodically **p**oled **l**ithium **t**antalate
QPM	**Q**uasi-**p**hase-**m**atching
QWP	**Q**uarter-**w**ave **p**late
RTA	**R**ubidium **t**itanyl **a**rsenate
SHG	**S**econd-**h**armonic **g**eneration
SLM	**S**patial **l**ight **m**odulator
SMF	**S**ingle-**m**ode **f**ibre
SPM	**S**elf-**p**hase **m**odulation
SPOPO	**S**ynchronously **p**umped **o**ptical **p**arametric **o**scillator
SRS	**S**timulated **R**aman **s**cattering
STED	**St**imulated **e**mission **d**epletion
Ti:sapphire	**Ti**tanium-doped **sapphire**
TOD	**T**hird-**o**rder **d**ispersion
TPA	**T**wo-**p**hoton **a**bsorption
UV	**U**ltra-**v**iolet
WDM	**W**avelength-**d**ivision **m**ultiplexer
YAG	**Y**ttrium **a**luminium **g**arnet
YLF	**Y**ttrium **l**ithium **f**luoride

YVO	**Y**ttrium **v**anadate
YDF	**Y**tterbium-**d**oped **f**ibre
ZDW	**Z**ero-**d**ispersion **w**avelength
ZGP	**Z**inc **g**ermanium di**p**hospide

---

a	Fibre core radius [m] / spatial span of pulse spectrum on SLM mask [m]
A	Pulse amplitude
A_0	Peak pulse amplitude
A_{eff}	Fibre mode-field area [m^2]
b	Grating slant distance of compressor [m] / confocal parameter [m]
B	B-integral [rad]
c	Speed of light [$\mathrm{m/s}$]
CR	Crossover rate
d	Diameter [m] / grating period [m]
d_{eff}	Effective nonlinear coefficient [$\mathrm{m/V}$]
dn_e/dT	Thermo-optic coefficient of extraordinary refractive index [K^{-1}]
D	Angular dispersion [$1/\mathrm{m}$] / pump depletion
$e_{in}\,(t)$	Input pulse of linear filter (time)
$E_{in}\,(\omega)$	Input spectrum of linear filter (frequency)
$e_{out}\,(t)$	Output pulse of linear filter (time)
$E_{out}\,(\omega)$	Output spectrum of linear filter (frequency)
E	Electric field [$\mathrm{V/m}$]
$E_{mask}\,(x,\omega)$	Electric field directly after SLM mask [$\mathrm{V/m}$]
f	Focal length [m]
f_{th}	Thermal lens focal length [m]
f_{fit}	Fitness function (DE)
f_{rep}	Repetition rate [Hz]
F	Mutation scaling factor
g	Reduced parametric gain coefficient [$1/\mathrm{m}$]
g_R	Raman gain coefficient [$\mathrm{m/W}$]
$g\,(t)$	Gaussian envelope of time window
g_t	Temporal overlap factor [s]
G	Perpendicular grating separation of compressor [m] / generation (DE)
$G_{inc,s}$	Incremental signal gain
$G_{mult,s}$	Multiplicative signal gain
h_2	Focusing condition integral

$h(t)$	Impulse response of linear filter
$H(\omega)$	Frequency response of linear filter
i	Imaginary unit
I	Pulse intensity [$\mathrm{W/m^2}$]
k	Wave vector [$1/\mathrm{m}$]
k_G	Poling period wave vector [$1/\mathrm{m}$]
Δk	Phase-mismatch [$1/\mathrm{m}$]
l_{eff}	Effective parametric gain length [m]
L	Length [m]
L_c	Coherence length [m]
L_D	Dispersion length [m]
L_{eff}	Effective fibre length [m]
L_{NL}	Nonlinear length [m]
M^2	Beam quality parameter
$m(t)$	Inverse Fourier transform of spectral masking function
$M(\alpha\omega)$	Spectral masking function
$M(x)$	Spatial masking function
n	Refractive index
n_2	Nonlinear refractive index [$\mathrm{m^2/W}$]
n_o	Ordinary refractive index
$n_e(\theta)$	Extraordinary refractive index
n_g	Group index
N_c	Controlled pixels per LC-mask / $2N_c$ number of components in individual (DE)
N_p	Number of individuals in population (DE)
N_{pix}	Number of pixels
ΔN	Population inversion density [$\mathrm{m^{-3}}$]
$\mathbf{P}$	Polarisation density [C/m^2]
P_0	Pulse peak power [W]
P_{av}	Average power [W]
P_p	Incident pump power [W]
P_s	Signal average power [W]
P_{th}	Threshold pump power [W]
r	Radial beam position [m]
R	Reflectivity / LC-cell retardance [m]
R_C	Effective cavity reflectivity
R_{OC}	Output coupler reflectivity
t	Time [s]
T	Time window of pulse shaper [s] / transmission
T_{OC}	Output coupler transmission

$u_{j,i,G+1}$	Single component within individual after crossover (DE)
$\mathbf{U}_{i,G+1}$	Population after crossover (DE)
v_g	Group velocity [$\mathrm{m/s}$]
$v_{j,i,G+1}$	Single component within individual after mutation (DE)
V	V-number / LC-cell drive voltage [V]
$\mathbf{V}_{i,G+1}$	Population after mutation (DE)
w	Beam waist radius inside nonlinear crystal [m]
w_0	Radius of focused frequency component [m]
w_{in}	Input beam radius [m]
$x_{j,i,G}$	Single component within individual (DE)
$\mathbf{X}$	Single individual (DE)
$\mathbf{X}_{i,G}$	Initial population (DE)
z	Propagation distance [m]

α	Loss coefficient [$1/\mathrm{m}$] / spatial dispersion [$\mathrm{ms/rad}$]
β_m	Dispersion coefficients ($m = 1, 2, 3, \ldots$)
$\chi^{(1)}$	Linear susceptibility
$\chi^{(2)}$	Second-order nonlinear susceptibility [$\mathrm{m/V}$]
$\chi^{(3)}$	Third-order nonlinear susceptibility [$\mathrm{m^2/W}$]
ϵ_0	Vacuum permittivity [$\mathrm{F/m}$]
ϵ_s	Fractional signal power loss per resonator round-trip
$\phi(\omega)$	Spectral phase [rad]
$\varphi(t)$	Temporal phase [rad]
η	Complexity of pulse shaper
γ	Nonlinear parameter [$1/\mathrm{Wm}$]
$\gamma_g(\nu)$	Gain coefficient [$\mathrm{m^{-1}}$]
γ_{heat}	Fraction of absorbed pump power dissipated as heat
Γ^2	Parametric gain coefficient [$1/\mathrm{m^2}$]
λ	Wavelength [m]
λ_0	Centre wavelength [m]
$\Delta\lambda$	FWHM pulse bandwidth [m]
$\Delta\lambda_{pix}$	Wavelength span per pixel [m]
Λ	Pitch of PCF air holes [m] / poling period of QPM materials [m]
κ	Thermal conductivity [$\mathrm{W/mK}$]
ν	Light frequency [Hz]
ν_{inst}	Instantaneous frequency [Hz]
$\delta\nu$	Minimum spectral feature on SLM [Hz]
$\Delta\nu$	FWHM pulse bandwidth [Hz]
θ_d	Grating diffraction angle [$^\circ$]

θ_{in}	Grating angle of incidence [$^{\circ}$]
$\sigma_{21}\left(\nu\right)$	Emission cross-section [m^2]
τ	Temporal FWHM pulse duration [s]
τ_g	Group delay [s]
ω	Optical (angular) frequency [$\mathrm{rad/s}$]
ω_0	Pulse carrier frequency [$\mathrm{rad/s}$]
$\delta\omega$	Pulse shaper resolution [$\mathrm{rad/s}$]
$\Delta\omega_{PA}$	Pump acceptance bandwidth [$\mathrm{rad/s}$]
$\Delta\omega_{pix}$	Frequency span per pixel [$\mathrm{rad/s}$]
$\Delta\omega_{PM}$	Signal gain or phase-matching bandwidth [$\mathrm{rad/s}$]
Ω	Frequency detuning from carrier frequency [$\mathrm{rad/s}$]
$\Delta\omega$	Spectral pulse FWHM [$\mathrm{rad/s}$]
ξ	Focusing parameter

Chapter 1

Introduction

1.1 Field of research

1.1.1 Optical parametric oscillators

Optical parametric oscillation is generally acknowledged as the preferred method for the generation of coherent light tunable over a large wavelength range spanning from the UV to the MIR and even into the THz-region. Optical parametric oscillators (OPO) are capable of producing wavelengths that are inaccessible with laser sources. In an OPO, consisting of a nonlinear medium embedded in an optical resonator, one pump photon at high frequency is converted to one signal and one idler photon at lower frequencies, obeying the laws of energy and momentum conservation. The rise of nonlinear optics for frequency conversion was a direct result of the discovery of the laser, since high intensities are required for such processes. Pioneering theoretical work in this field came from the Bloembergen group at Harvard University in the early 1960s [1]. The first successful experiment of second-harmonic generation (SHG) using a ruby laser fired into a quartz crystal was demonstrated by Franken *et al.* in 1961 at the University of Michigan [2]. Four years later, Giordmaine and Miller demonstrated the first OPO by using a $LiNbO_3$ crystal as the nonlinear medium [3], which triggered intense research in this field of tunable, coherent light sources. After a string of publications of different OPO systems it was recognised that stringent material requirements (optical nonlinearity, transparency range, phase-matching, damage threshold) as well as stringent pump laser requirements (spectral and spatial coherence, sufficiently high intensity to overcome threshold) imposed a limit on further progress and thus interest somewhat declined. This changed in the 1990s when nonlinear optics experienced a renaissance due to improved laser sources, in particular ultrashort diode-pumped solid-state lasers, and to periodic poling of nonlinear crystals for quasi-phase-matching (QPM) [4–7], greatly

alleviating the phase-matching constraints of many materials. Lithium niobate is by far the most widely used periodically poled nonlinear material mainly due to its high effective nonlinear coefficient and its wide transparency range, but also lithium tantalate and materials from the potassium titanyl phosphate (KTP) and arsenate (KTA) family are readily poled. Furthermore, orientation-patterned gallium arsenide (OP-GaAs) is of great interest for QPM due to its wide transparency range and large effective nonlinear coefficient. Other materials used for OPOs now include $ZnGeP_2$ (ZGP), $AgGaSe_2$, $AgGaS_2$, CdSe, $Ba_2NaNb_5O_{15}$ or $LiIO_3$ complementing well-established materials like LiB_3O_5 (LBO) and β-BaB_2O_4 (BBO) and an overview of their transparency ranges and effective nonlinear coefficients can be found in table 1.1.

TABLE 1.1: Overview of transparency range and effective nonlinear coefficient for various nonlinear crystals (*periodically poled). Sources: [6, 8–11].

	Transparency range [μm]	**Effective nonlinear coefficient d_{eff} [pm/V]**
$LiNbO_3$*	0.33 . . . 4.5	17
$LiTaO_3$*	0.28 . . . 5.0	9
$LiIO_3$	0.28 . . . 6.0	<8
LiB_3O_5 (LBO)	0.16 . . . 3.2	1.17
$KTiOPO_4$* (KTP)	0.35 . . . 4.5	8
$KTiOAsO_4$* (KTA)	0.35 . . . 5.2	10
$RbTiOAsO_4$* (RTA)	0.35 . . . 5.3	9
OP-GaAs*	0.90 . . . 17	69
$ZnGeP_2$ (ZGP)	0.74 . . . 12	75
$AgGaSe_2$	0.71 . . . 19	33
$AgGaS_2$	0.47 . . . 13	13
CdSe	0.70 . . . 24	36
β-BaB_2O_4 (BBO)	0.19 . . . 3.5	2.3
$Ba_2NaNb_5O_{15}$	0.37 . . . 5.0	15

OPOs now exist in all temporal domains from continuous wave (CW) down to femtoseconds at repetition rates from a few Hz to many GHz. For ultrafast OPOs emitting picosecond or femtosecond pulses, the resonating pulse is much shorter than the round-trip time and therefore it is necessary to time this pulse carefully to be in step with the next pump pulse inside the nonlinear crystal. The resonating pulse, normally the signal pulse, then experiences gain and depletes the pump on every pass through the nonlinear crystal. In other words, the repetition rate of the pump laser and OPO must match to obtain a parametric interaction, and this technique is referred to as synchronous pumping. In 1972, Burneika *et al.* demonstrated the first synchronoulsy pumped OPO emitting $\approx 100\,\mathrm{ps}$-long pulses using a mode-locked laser [12]. Later in 1988, Piskarskas *et al.* used the second harmonic of a Nd:YAG laser running at $140\,\mathrm{MHz}$ to pump a $Ba_2NaNb_5O_{15}$ crystal in a doubly resonant cavity and obtaining $37\,\mathrm{ps}$ pulses

with $56\,\mathrm{mW}$ of total average power [13]. In 1989 Edelstein *et al.* reported the first femtosecond SPOPO based on a colliding-pulse mode-locked dye pump laser at $100\,\mathrm{MHz}$ and a $KTiOPO_4$ crystal in a singly resonant cavity outputting $220\,\mathrm{fs}$ pulses in the mW range for both signal and idler [14].

OPOs are particularly attractive for the mid-infrared (MIR) spectral range up to $10\,\mu\mathrm{m}$ and beyond, where few practical laser sources are available. Numerous publications in the last decade reflect the strong research activity with PPLN (solely used for the MIR OPOs described in this work and hence the discussion here emphasises PPLN). In the picosecond regime, PPLN has been used for OPOs operating up to $6.3\,\mu\mathrm{m}$ [15] and $7.3\,\mu\mathrm{m}$ [16] with significant idler absorption. In addition to the use of different poling periods and temperature tuning, birefringent-filter-tuning [17] as well as diffraction-grating-tuning [18] have been demonstrated in such picosecond SPOPOs. The latter method was applied in a tandem-pumped SPOPO using an Nd:YLF (yttrium lithium fluoride) oscillator and a diffraction-grating-tuned PPLN SPOPO to pump a CdSe SPOPO emitting idler pulses from $9.1\,\mu\mathrm{m}$ to $9.7\,\mu\mathrm{m}$ with an estimated pulse duration of $8\,\mathrm{ps}$ and an average power of $70\,\mathrm{mW}$ [19]. The first femtosecond PPLN SPOPO was reported by McGowan *et al.* [20]. Here, a self-mode-locked Ti:sapphire laser pumped a PPLN SPOPO that was almost continuously tunable from $975\,\mathrm{nm}$ to $4.55\,\mu\mathrm{m}$ yielding $90\,\mathrm{mW}$ (signal) and $70\,\mathrm{mW}$ (idler) of average power and $140\,\mathrm{fs}$ signal pulses by carefully compensating for dispersion. Further notable reports of femtosecond MIR OPOs include an Yb:fibre-laser-pumped, $330\,\mathrm{fs}$, $54\,\mathrm{MHz}$, $90\,\mathrm{mW}$, PPLN SPOPO [21], an Yb:YAG thin-disk-laser-pumped, $700-900\,\mathrm{fs}$, $35\,\mathrm{MHz}$, $2.3-2.7\,\mathrm{W}$, periodically poled $LiTaO_3$ SPOPO using an intracavity single-mode fibre (SMF) for signal feedback [22], and a Ti:sapphire-pumped, $\approx 120\,\mathrm{fs}$, $84\,\mathrm{MHz}$, $> 100\,\mathrm{mW}$ periodically poled RTA SPOPO [23]. Table 1.2 gives an overview of the tuning ranges of the discussed publications.

In many research areas, e.g. coherent anti-Stokes Raman scattering (CARS) spectroscopy [34–37], a high demand exists for compact, user-friendly, ultrashort sources tunable in the visible and near-infrared (NIR) to replace expensive and complex Ti:sapphire systems. OPOs pumped by $\approx 1\,\mu\mathrm{m}$ solid-state lasers that are frequency-doubled into the visible such as Yb:fibre, Nd:YLF or Nd:YAG are thus of great interest. PPLN has been used for this purpose, but only at moderate power levels of a few hundred milliwatts [31]. Due to the low damage threshold and photo-refractive problems of lithium niobate, nonlinear materials such as LBO, BBO or KTP are typically applied for higher power levels. A parameter overview of the notable publications discussed in the following is given in table 1.2. A $82\,\mathrm{MHz}$, Ti:sapphire-SHG-pumped, dispersion-compensated, BBO SPOPO generating a signal pulse duration of $13\,\mathrm{fs}$, a signal average power of $130\,\mathrm{mW}$ and being tunable from $500\,\mathrm{nm}$ to $710\,\mathrm{nm}$ was reported [33], but with a highly complex setup. A ring cavity SPOPO using a KTP crystal produced $< 2\,\mathrm{ps}$ pulses at tens

TABLE 1.2: Overview of MIR and NIR OPO tuning ranges in the literature as discussed in this section (*periodically poled materials only).

Reference	Tuning range [μm] (signal)	(idler)	Total output power [W]	Temporal regime	Nonlinear crystal
Mid-infrared tuning* ($\approx 1\,\mu$m pump sources)					
[15]	1.25–1.31	6.30–5.28	<0.01	ps	PPLN
[16]	1.22–1.29	7.29–5.60	<0.01	ps	PPLN
[19]	2.29–2.52	9.70–9.10	<0.1	ps	PPLN + CdSe
[20]	0.98–1.54	4.55–1.67	<0.1	fs	PPLN
[21]	1.55–1.95	3.31–2.30	<0.1	fs	PPLN
[22]	1.43–1.47	3.67–3.43	>2	fs	PP $LiTaO_3$
[23]	1.06–1.23	4.50–2.67	>0.1	fs	PP RTA
Near-infrared tuning ($\approx 0.5\,\mu$m pump sources)					
[24]	0.95–1.15	1.16–0.96	>0.01	ps	KTP
[25]	0.89–1.06	1.32–1.06	<1	ps	PP KTP
[26]	0.74–0.93	1.89–1.24	<0.5	ps	LBO
[27]	0.74–0.93	1.83–1.22	>1	ps	LBO
[28]	0.65–1.05	2.65–1.05	>0.1	ps	LBO
[29]	0.66–1.06	2.60–1.06	<0.5	ps	LBO
[30]	0.74–1.01	1.69–1.05	>0.5	ps	LBO
[31]	0.88–1.05	1.29–1.05	>0.1	ps	PPLN
[32]	0.78–0.94	1.61–1.19	>0.5	fs	LBO
[33]	0.59–0.67	1.24–0.99	>0.1	fs	BBO

of milliwatts of average power and tunable from $938\,\mathrm{nm}$ to $1184\,\mathrm{nm}$, when pumped by a mode-locked, $2\,\mathrm{ps}$, $125\,\mathrm{MHz}$ Nd:YLF laser frequency-doubled to $523\,\mathrm{nm}$ [24]. Another experiment of a visible-pumped KTP SPOPO, now periodically poled however, generated a total output power of $570\,\mathrm{mW}$, pulses with a duration of $7.5\,\mathrm{ps}$ and a tunability from $900\,\mathrm{nm}$ to $1.3\,\mu\mathrm{m}$, and was pumped by the second harmonic of a Nd:YVO laser [25]. The majority of publications in the field of visible-pumped OPOs consists of LBO-based systems mainly due to the very high damage threshold of $> 10\,\mathrm{GW/cm^2}$, the long crystal lengths (low dispersion) and the convenient phase-matching. These include demonstrations of SPOPOs delivering $6.4\,\mathrm{ps}$ pulses and $300\,\mathrm{mW}$ of signal power [26], $25\,\mathrm{ps}$ pulses and $1.6\,\mathrm{W}$ of signal power [27] (both tunable from $740\,\mathrm{nm}$ to $930\,\mathrm{nm}$ and with $30\,\mathrm{mm}$-long LBO crystals), or $1.6\,\mathrm{ps}$ pulses and $290\,\mathrm{mW}$ of combined output power, tunable from $650\,\mathrm{nm}$ to $2.65\,\mu\mathrm{m}$ with a $15\,\mathrm{mm}$-long LBO crystal [28], all based on picosecond, LBO-frequency-doubled, Nd:YLF pump sources with repetition rates between $70\,\mathrm{MHz}$ and $110\,\mathrm{MHz}$. A similar publication reported $4\,\mathrm{ps}$ pulses, $440\,\mathrm{mW}$ signal power and $0.66\ldots2.6\,\mu\mathrm{m}$ total tunability using a $6\,\mathrm{mm}$ LBO crystal, but with a Nd:YVO pump source [29]. Also, compact, robust, user-friendly, ultrashort ytterbium-doped fibre (YDF) master-oscillator power-amplifier (MOPA) systems are now used as pump sources. Kieu *et al.* reported $550\,\mathrm{mW}$ total output power, $1.5\,\mathrm{ps}$ pulses from a commercial, $20\,\mathrm{mm}$-long LBO OPO pumped by the second harmonic of a $3.5\,\mathrm{ps}$, $81\,\mathrm{MHz}$,

6 W, 1030 nm, YDF MOPA [30]. Cleff *et al.* recently demonstrated the first femtosecond, green-pumped OPO delivering 270 mW of signal power and 300 mW of idler power with pulses as short as 100 fs by using the 6 W, frequency-doubled output of a 1050 nm YDF MOPA ($\approx$ 12 W of compressed 300 fs pulses at 61 MHz) as a pump source [32].

It is not only desirable to have OPOs with a high degree of tunability in all spectral ranges but also with high repetition rates in compact, robust, practical setups for pump-probe spectroscopy or telecommunication applications. The most compact setup is a monolithic device with the resonator mirror coatings directly evaporated onto the nonlinear crystal. This was demonstrated in 1988 with an MgO:PPLN device operating in the nanosecond regime at a few Hertz [38], but clearly not with the aim to produce ultrashort pulses at very high repetition rates at the same time. Resonator designs with discrete components operating at harmonics of the pump laser repetition rate include a 344 MHz, RTA [39] and a 322 MHz, PPLN [40] SPOPO, both with semi-monolithic V-cavities (one crystal end-facet HR-coated) and pumped by femtosecond Ti:sapphire lasers at a 4$\times$ lower repetition rate, a 1.334 GHz, $KTiOAsO_4$ SPOPO pumped by a 83.4 MHz, picosecond, Nd:YVO laser [41], as well as a 988 MHz, PPLN SPOPO pumped by a 76 MHz, femtosecond, Ti:sapphire laser [42]. All of these OPOs have a (signal) repetition rate much higher than the pump laser, but with the disadvantage that only the one signal pulse that meets the next pump pulse in the crystal is amplified while the other signal pulses suffer loss on every round-trip resulting in a cascaded peak intensity of the signal pulse train. Besides this disadvantage, problems arise in very short, non-monolithic resonators for high repetition rates, inasmuch as the beam waist size inside the crystal increases with decreasing resonator length leading to a rise in threshold. Thus, OPOs have been reported that have relatively long cavity lengths corresponding to tens of megahertz, where small waist sizes leading to optimum focusing conditions with confocal parameters close to the length of the nonlinear crystal are obtainable, and that are pumped by sources with very high repetition rates, so that there is more than just one pulse circulating in the cavity. This is often referred to as higher-order synchronous pumping. Developments of highly compact, ultrafast sources have made this pumping scheme possible. A picosecond, 2.5 GHz, mode-locked, all-diode MOPA was used to pump a 1.25 GHz, ring cavity, PPLN SPOPO generating 7.8 ps-long pulses [43]. Also, a high-repetition-rate, compact, ring cavity Ti:sapphire laser at 1 GHz was used as a pump source for a 250 MHz, ring cavity, PPLN SPOPO outputting pulses with a duration of 65 fs [44]. Lecomte *et al.* have demonstrated a 10.1 GHz, 13.9 ps pulse train from a 1.12 GHz, linear cavity, PPLN SPOPO tunable over the telecommunications C-band [45]. The pump source was a passively mode-locked Nd:YVO laser at 10.1 GHz. The same group also reported PPLN-based, ring cavity SPOPOs with repetition rates of 39 GHz (2.2 ps, 2.1 W) [46] and 81 GHz (2.4 ps, 0.9 W) [47] for applications in telecommunications. The SPOPO cavities were 62$\times$ and 130$\times$ longer compared to

the pump source, so that 62 or 130 signal pulses circulated in the cavity, respectively. Due to the increased peak power required to reach oscillation threshold at such high repetition rates, the pump source consisted of a MOPA system with a quasi-monolithic, passively mode-locked, Nd:YVO seed laser and a double-clad, large-mode area (LMA), YDF amplifier delivering up to $9.8\,\mathrm{W}$ of average power. A summary of the discussed high-repetition-rate SPOPOs can be found in table 1.3.

TABLE 1.3: Compilation of literature on compact, high-repetition-rate OPOs.

Reference	Repetition rate	Temporal regime	Resonator layout
Resonator length: OPO < pump source			
[39]	344 MHz	fs	semi-monolithic, V-shape
[40]	322 MHz	fs	semi-monolithic, V-shape
[41]	1.334 GHz	ps	standing-wave, folded
[42]	988 MHz	fs	bow-tie standing-wave
Resonator length: OPO > pump source			
[43]	1.25 GHz	ps	bow-tie ring
[44]	250 MHz	fs	bow-tie ring
[45]	10.1 GHz	ps	non-monolithic, linear
[46]	39 GHz	ps	bow-tie ring
[47]	81 GHz	ps	bow-tie ring

Using periodically poled materials for MIR pulse generation, power-scaling of the signal and idler output remains challenging due to problems with idler absorption and thus thermal loading, optical damage and photo-refractive effects. This problem is approached by increasing the aperture of periodically poled crystals to a few millimetres to facilitate spot size scaling for reduced peak intensities, by doping the nonlinear crystals with magnesium oxide (MgO) and by different crystal types and structures (stoichiometric rather than congruent melt). Regarding only the raw average output power from an OPO, Q-switched solid-state lasers proved to be effective sources to pump nanosecond OPOs that do not require a synchronous pumping configuration, since the pulse duration is typically much longer than the cavity round-trip time. An OPO using a $1\,\mathrm{mm}$ wide MgO:PPLN crystal produced $11\,\mathrm{W}$ and $2.7\,\mathrm{W}$ at $1.5\,\mu\mathrm{m}$ and $3.5\,\mu\mathrm{m}$, respectively, for $21\,\mathrm{W}$ of pump power from a pulse-shaped, $100\,\mathrm{ns}$ MOPA system (diode seed with YDF amplifiers) [48]. Even higher output powers of $46\,\mathrm{W}$ at $1.47\,\mu\mathrm{m}$ and $16.7\,\mathrm{W}$ at $3.84\,\mu\mathrm{m}$ in $150\,\mathrm{ns}$, $7\,\mathrm{kHz}$ pulses were obtained from $104\,\mathrm{W}$ of pump power using a congruent MgO:PPLN crystal with a $1\,\mathrm{mm} \times 4\,\mathrm{mm}$ aperture and a $0.8\,\mathrm{mm} \times 3\,\mathrm{mm}$ elliptical pump spot size [49]. Synchronously pumped, ultrashort OPOs generating multiple Watts of output power were also successfully demonstrated in the recent past. Relying on birefringent-phase-matching (BPM), Ruffing *et al.* applied a high-damage-threshold, $15\,\mathrm{mm}$ $KTiOAsO_4$ crystal in a standing-wave cavity SPOPO pumped by a $7\,\mathrm{ps}$, $83.4\,\mathrm{MHz}$, $1.064\,\mu\mathrm{m}$, Nd:YVO pump laser with $29\,\mathrm{W}$ output power resulting in $14.6\,\mathrm{W}$ at $1.54\,\mu\mathrm{m}$ and $6.4\,\mathrm{W}$ at $3.47\,\mu\mathrm{m}$ [41]. Examples of SPOPOs with QPM materials,

where bigger apertures are more difficult to achieve, are Hoyt *et al.*, who used a $47\,\mathrm{mm}$-long PPLN in an idler-resonant, standing-wave cavity and a $80\,\mathrm{ps}$, $76\,\mathrm{MHz}$, $1.064\,\mu\mathrm{m}$, Nd:YAG laser to obtain $8\,\mathrm{W}$ at $1.85\,\mu\mathrm{m}$ and $4\,\mathrm{W}$ at $2.5\,\mu\mathrm{m}$ for $18\,\mathrm{W}$ of pump power [50], Kokabee *et al.* with a $20.8\,\mathrm{ps}$, $81.1\,\mathrm{MHz}$, $1.064\,\mu\mathrm{m}$, YDF laser providing $11.7\,\mathrm{W}$ to pump a $50\,\mathrm{mm}$-long and $1\,\mathrm{mm}$-wide MgO:PPLN-based SPOPO producing $7.4\,\mathrm{W}$ at $1.47\,\mu\mathrm{m}$ and $4.9\,\mathrm{W}$ at $3.08\,\mu\mathrm{m}$ [51], as well as Südmeyer *et al.* reporting $840\,\mathrm{fs}$ pulses with $19\,\mathrm{W}$ at $1.45\,\mu\mathrm{m}$ and $7.8\,\mathrm{W}$ at $3.57\,\mu\mathrm{m}$ from a $17.5\,\mathrm{mm}$-long and $1\,\mathrm{mm}$-wide, periodically poled, stoichiometric $LiTaO_3$ (PPsLT), intracavity fibre-feedback ring resonator pumped by a $780\,\mathrm{fs}$, $56\,\mathrm{MHz}$, $1.030\,\mu\mathrm{m}$, Yb:YAG thin-disk laser with a maximum output power of $58\,\mathrm{W}$ [52]. The most important parameters of these publications are compiled in table 1.4.

TABLE 1.4: Publications on high-power MIR SPOPOs using periodically poled materials (*Q-switched systems, not synchronously pumped).

Reference	**Output power** [W] (signal)	(idler)	**Temporal regime**	**Nonlinear crystal**
[48]*	11	2.7	ns	MgO:PPLN
[49]*	46	16.7	ns	MgO:PPLN
[50]	8	4	ps	PPLN
[51]	7.4	4.9	ps	MgO:PPLN
[52]	19	7.8	fs	MgO:PPsLT

1.1.2 Pump sources

In order to make a pulsed OPO an attractive, versatile, scientific and industrial tool, it is also important to have appropriate pump sources that offer the necessary optical parameters (wavelength, peak intensity, pulse duration, brightness, repetition rate, bandwidth) but that are also user-friendly, reliable, compact and inexpensive. Rapid progress in the development of diode-pumped solid-state lasers, especially those based on neodymium, helped to boost the interest in SPOPOs again in the 1990s. Such lasers delivered the high average powers, good beam quality and nanosecond (Q-switched) or picosecond (mode-locked) pulses needed to obtain reasonable OPO thresholds, with Nd:YLF [17–19, 24, 26, 27, 31], Nd:YVO [29, 41, 53] and Nd:YAG [13, 38, 50, 54] the most widely used types. Other laser types used for SPOPO pumping were a picosecond, all-diode MOPA system [43], a passively mode-locked, femtosecond, Yb:YAG, thin-disk laser [52, 55] and a colliding-pulse, mode-locked, femtosecond, dye laser [14]. The most appropriate and for a long time dominating candidate for ultrashort pulse pumping ($< 1\,\mathrm{ps}$) was, however, the Kerr-lens mode-locked Ti:sapphire laser [20, 23, 29, 33, 39, 40, 42, 56, 57]. With its broad emission bandwidth in the NIR, the Ti:sapphire laser allows for OPO tuning by means of pump wavelength tuning and thus adds another tuning method to the established methods (QPM, BPM). On

the other hand, Ti:sapphire systems are usually very costly investments and often require professional servicing due to free-space optics, high complexity and thus misalignment. It is only in recent years that frequency-doubled solid-state lasers (in many commercial products) are replacing the cumbersome argon-ion lasers as pump sources for the Ti:sapphire systems. Even more recently, the possibility of direct diode pumped Ti:Sapphire lasers has become a reality [58].

Ultrashort, rare-earth-doped, fibre lasers and amplifiers became an attractive alternative to bulk-crystal solid-state systems in the last decade, because of superior properties such as thermal management, compactness, beam quality and average power scaling [59–62]. The single-pass gain is considerably higher for fibre systems, because of the confined spot sizes and long interaction length of pump, signal and dopant. Furthermore, heat dissipation is facilitated by the fibre geometry itself. Ytterbium (Yb), which is currently the preferred choice for high-power operation, has a broad gain bandwidth of $> 40\,\mathrm{nm}$ in the NIR around $1060\,\mathrm{nm}$ capable of supporting femtosecond pulses [61] and devices based on Yb have excellent optical-to-optical conversion efficiencies reaching values of up to 80%. A range of pump laser diodes with high output powers is available in the distinct absorption bands of ytterbium. Most of these high-power pump laser diodes emit multi-mode, non-diffraction-limited beams, which can not be efficiently coupled into conventional SMFs. To this end, double-clad fibres have been developed [63, 64], where the laser light propagates in a doped, single-mode core and where the (multi-mode) pump light is launched into an inner cladding with large numerical aperture (NA) surrounded by an outer cladding with lower refractive index. The pump light propagates in the inner cladding as well as the core, where it can interact with the laser-active rare-earth ions. In high-power amplifiers, the interplay of dispersion, gain and nonlinearity must be carefully balanced to avoid detrimental pulse distortion. Nonlinear effects, primarily self-phase modulation (SPM), dominate pulse distortion as the pulse peak intensity increases. Fibres with a large mode area (LMA) of the core help to reduce the peak intensities of the propagating signal pulses to a great extent [65]. Another development for high-power operation are photonic crystal fibres (PCF), which have a microstructured cladding [66]. The effective refractive index of the cladding is determined by the geometry of the (periodic) microstructure, which is normally an array of air holes that runs along the fibre. The additional degree of freedom provided by the microstructure design allows for the precise control of dispersive and nonlinear characteristics. Reports of tens of Watts of average power from ultrashort YDF amplifier systems include $10\,\mathrm{ps}$-long pulses with an average power of $51.2\,\mathrm{W}$ [67], $21\,\mathrm{ps}$ pulses with up to $100\,\mathrm{W}$ [68], compressed $80\,\mathrm{fs}$ parabolic pulses with $17\,\mathrm{W}$ [69] and compressed $110\,\mathrm{fs}$ parabolic pulses with $> 25\,\mathrm{W}$ [70]. These systems all incorporated diode-pumped, LMA, double-clad fibres in MOPA configurations operating around $1.06\,\mu\mathrm{m}$ and with repetition rates from $50\,\mathrm{MHz}$ to $80\,\mathrm{MHz}$.

It was the technique of chirped pulse amplification (CPA), first reported by Strickland and Mourou in 1985 [71], that enabled access to very high average powers from ultrashort amplifier systems. They launched $150\,\mathrm{ps}$ pulses from a commercial Nd:YAG laser into $1.4\,\mathrm{km}$ of SMF to dispersively stretch them to $300\,\mathrm{ps}$. The pulses were then amplified in a regenerative Nd:glass amplifier from a pulse energy of $28\,\mathrm{nJ}$ ($2.3\,\mathrm{W}$, $82\,\mathrm{MHz}$) to $2\,\mathrm{mJ}$ followed by compression down to $2\,\mathrm{ps}$ in a grating-based pulse compressor with 50% throughput efficiency. This experiment showed that nonlinear effects and optical damage can be mitigated by stretching ultrashort pulses prior to and compressing them after the amplification. The group velocity dispersions (GVD) of the fibre stretcher and the grating compressor have opposite signs, so linear chirp induced by the stretcher can be removed by the compressor. The first all-fibre CPA system with Yb-doped fibres was demonstrated by Galvanauskas *et al.* in 2001 [72]. In a two-stage configuration with grating-based stretcher and compressor and LMA, double-clad fibres, $220\,\mathrm{fs}$ pulses with an average power of $5.5\,\mathrm{W}$ at $1\,\mathrm{MHz}$ and excellent beam quality were obtained. With a similar setup, but with a chirped fibre Bragg grating (CFBG) as stretcher, $135\,\mathrm{W}$ and $360\,\mathrm{fs}$-long pulses at a repetition rate of $10\,\mathrm{MHz}$ were produced [73]. Output powers $> 100\,\mathrm{W}$ from LMA, double-clad, YDF chirped pulse amplifiers based on PCFs have also been demonstrated (mostly with multi-stage MOPAs). In reference [74], a system with $131\,\mathrm{W}$ of average power, a high repetition rate of $73\,\mathrm{MHz}$ and a pulse duration of $220\,\mathrm{fs}$ was described that uses PCFs and a grating-based stretcher and compressor. Recently, Eidam *et al.* presented an average output power of $325\,\mathrm{W}$ from a system producing $375\,\mathrm{fs}$ pulses at $40\,\mathrm{MHz}$ [75]. Shortly after this, the same group demonstrated record-breaking $830\,\mathrm{W}$, $640\,\mathrm{fs}$ pulses at $78\,\mathrm{MHz}$ from a three-stage amplifier system with two PCF pre-amplifiers and a solid-fibre power amplifier, where highly efficient, dielectric, reflection-mode gratings were used for the pulse stretcher and compressor [76]. The $27\,\mu\mathrm{m}$ core of the power amplifier LMA fibre was relatively small considering the very high power and consisted of ytterbium- and fluorine-doped glass rods for precise refractive index control to ensure true single-mode operation. A high-pulse-energy, femtosecond system in the millijoule regime has been reported with pulse durations of $800\,\mathrm{fs}$ at repetition rates $> 100\,\mathrm{kHz}$ and energies up to $1.45\,\mathrm{mJ}$ [77]. Whereas the pre-amplifier here consists of a doped fibre with a core and inner cladding diameter of $40\,\mu\mathrm{m}$ and $170\,\mu\mathrm{m}$, respectively, the power amplifier uses a more exotic, $1.2\,\mathrm{m}$-long, rod-type fibre with a core diameter as large as $80\,\mu\mathrm{m}$ (inner cladding $200\,\mu\mathrm{m}$) to reduce the peak intensities as much as possible. At such large mode areas and operation at very high powers, the signal beam can become multi-modal and this issue has been addressed by the same group [76]. Furthermore, active water cooling of the fibres was required under the extreme conditions as reported in [76] and [77]. In all of the CPA experiments above, the pulses from the seed oscillators (hundreds of femtoseconds or a few picoseconds) are stretched by many orders of magnitude to hundreds of picoseconds or even nanoseconds before amplification and compression.

1.1.3 Ultrashort pulse shaping

Higher-order dispersion and residual nonlinear effects that can be present when high-power, ultrashort pulses propagate in optical fibres can lead to degraded, non-transform-limited pulses with a pedestal limiting the maximum peak power. Under certain circumstances, this also applies to CPA. Apart from fibre design and order-of-magnitude pulse stretching, pulse shaping is another way of addressing these detrimental effects [78].

Shaping of optical pulses is commonly performed in the spectral domain with spatial light modulators (SLM). The most widely adopted method is the masking of the spatially dispersed frequency spectrum, with the desired pulse shape being generated by phase and / or amplitude shaping. SLMs are a flexible tool for programmable shaping of the pulse profile [79], whereby an external signal modulates the spectral phase or amplitude of each frequency component. The SLM is embedded in a zero-dispersion delay line consisting of two diffraction gratings and two lenses for the time-to-frequency mapping. All components are at a mutual distance of one focal length f and this is called a 4-f-Fourier transform pulse shaper. Liquid crystal (LC) arrays are often used as modulators [80–86]. However, the pixellation of the LC-array can lead to temporal satellite pulses in certain amplifier systems. Acousto-optic modulators (AOM) in the Fourier plane allow for a continuous masking of the pulse spectrum removing the effect of pixellation on the output pulse shape [87]. Furthermore, the reprogramming time can be much faster and is on the order of microseconds, but they can not be used at megahertz repetition rates. Deformable mirrors with specialty coatings can be used in spectral regions where LC- or AOM-modulators do not transmit [88]. The precision of phase modulation of deformable mirrors can be very high, but the shaping resolution is limited by the relatively small number of actuators.

Adaptive programmable pulse shaping is a method, where a specific output parameter of the experiment serves as feedback for an optimisation algorithm. The algorithm iterates the pulse shape until the desired optimum output pulse shape, defined by a fitness function, is found. The speed of convergence and the efficient search of the entire search space are important factors to consider. On the one hand, the algorithm might get trapped in a local minimum and therefore would not lead to the global optimum. On the other hand, the search for a truly global optimum may take many iterations and far too long. Several methods with different emphasis have been developed. Simulated annealing [89], genetic algorithm [90] and differential evolution (DE) [91] are frequently used in pulse shaping. DE is applied in this work, because it outperforms other algorithms both in theory and experiment [91–93]. It is part of the evolutionary algorithms family and is derived from the laws of biological evolution such as mutation, crossover and selection. An advanced version of DE is self-adaptive DE, abbreviated as JADE,

where the control parameters are adjusted automatically from iteration to iteration for a faster convergence.

In Ti:sapphire amplifiers, adaptive pulse shaping has led to successful experiments in higher-order dispersion compensation [80], pulse compression [81], double pulse generation [82] as well as high-fidelity transform-limited pulses [83]. Adaptive pulse shaping in fibre CPA systems with LC SLMs has been reported to compensate for higher-order dispersion and SPM in phase-only pulse shaping configurations [85]. The difference between pulse peak power and pulse pedestal was used here as the feedback parameter for a simulated annealing optimisation algorithm. An increase by a factor of three of this difference demonstrated improved peak power and pulse width. The system delivered $800\,\mathrm{fs}$, $65\,\mu\mathrm{J}$ pulses at a repetition rate of $16.67\,\mathrm{kHz}$. In reference [84], amplitude-only pulse shaping was carried out to control SPM. In this case the difference between a target spectrum and the measured spectrum at the output of the system served as optimisation parameter and $410\,\mathrm{fs}$ pulses with a low energy of $20\,\mathrm{nJ}$ at a repetition rate of $75\,\mathrm{MHz}$ were obtained. Combined phase and amplitude shaping has also been reported compensating for higher-order dispersion and SPM [94]. The feedback came from a two-photon absorption signal with the aim of maximising the peak intensity. Differential evolution was used as the optimisation algorithm and pulses of $170\,\mathrm{fs}$ duration at $50\,\mathrm{MHz}$ with a pulse energy of $252\,\mathrm{nJ}$ were produced.

1.2 Project motivation and applications

The general theme and motivation for this research project was to investigate OPOs and appropriate fibre-based pump sources that can deliver picosecond or femtosecond, widely tunable (visible, NIR and MIR), high-beam-quality output pulses at high energy or high average power and over a wide repetition rate range.

There is significant interest in both commercial applications and applied science (see special feature on optical parametric devices [95]) for ultrashort optical pulses with a high degree of flexibility in terms of wavelength tunability, average output power, pulse repetition rate or pulse energy to justify extensive research in this field. OPOs were in the past the natural choice regarding tunability over hundreds of nanometres, since most laser sources were not able to cover such a broad range. However, the obtainable average output power or pulse energy was limited by the optical properties, in particular the damage threshold, of the nonlinear crystals used. Also, the repetition rate was often limited to under $100\,\mathrm{MHz}$ by the type of pump source. Fibre-based amplification systems proved to be well-suited to OPO pump sources due to their ease

of power scaling and repetition rate control. It is the subject of this thesis to investigate their full potential for OPO pumping, which goes along with the demonstration of novel OPO regimes.

In general, OPOs find applications in fields as diverse as time-resolved pump-probe spectroscopy, materials processing, telecommunications, nonlinear microscopy, light detection and ranging or in even more exotic fields like digital projection displays (OPO as RGB source), photo-dynamic therapy (e.g. for cancer treatment) and IR countermeasures (broadband high-power MIR radiation for blinding heat-seeking missiles). Furthermore, end-users have an interest in affordable, user-friendly, compact, ultrashort sources tunable in the visible and NIR as an alternative to Ti:Sapphire systems. OPOs with both controllable and high repetition rates up to the gigahertz regime are increasingly sought-after in telecommunications [45–47] and non-invasive nonlinear microscopy / spectroscopy [96, 97]. Many applications, for instance nonlinear MIR spectroscopy of biological or chemical surfaces [98] relying on nonlinear interactions between radiation and sample, need high peak powers to generate sufficient signal strength. However, optical damage of biological samples can be induced by nonlinear processes [99]. Therefore, a trade-off between good signal-to-noise ratio and prevention of optical damage is to scale the average power by increasing the repetition rate [96]. An increased repetition rate also allows for shorter pixel dwelling times and faster acquisition frame rates in imaging applications. Furthermore, microscopy applications in the MIR, where optical microscopes typically have a very low throughput efficiency, require high-power sources to overcome the loss presented by the imaging system. Ultrashort SPOPOs are the ideal sources for coherent anti-Stokes Raman scattering (CARS) spectroscopy, where two synchronous pulses at different frequency are needed in the visible and NIR wavelength range [25, 26, 30, 32, 37]. Such OPOs are also well-suited for stimulated-emission-depletion (STED) microscopy requiring pulses in the hundreds of picosecond region with average powers of a few hundreds of milliwatts and at repetition rates of tens of megahertz [100, 101]. There is, however, further scope for higher output powers much greater than $1\,\mathrm{W}$. High-pulse-energy OPOs in the $1\,\mu\mathrm{J}$ region have applications in IR materials processing, in particular as a tabletop alternative to free-electron lasers for resonant IR pulsed laser deposition and ablation of polymers [102, 103].

Pulse shaping has been used for the compensation of dispersion and / or nonlinear effects [80, 83–85, 94]. It was used in parts of this work (with the fibre-CPA pump source) in order to compensate for the accumulated third-order dispersion (TOD) from the fibre stretcher and the grating-based compressor to achieve clean, pedestal-free, high-quality output pulses. Without the pulse shaper being activated, the pulse duration at the output of the compressor stage was typically in the low picosecond range, whereas with the pulse shaper programmed with an optimised phase and amplitude profile the pulse

duration could be reduced to around $500\,\mathrm{fs}$. Apart from the application in fibre-based CPA systems, pulse shaping has been extensively used to generate arbitrary shapes of femtosecond pulses for optical communications, biomedical imaging or coherent control to name but a few. Our group has demonstrated high-fidelity transfer of adaptively shaped NIR pulses (pump) to the MIR (idler) by using an SPOPO for frequency conversion [104–106], which is interesting for chemists and spectroscopists working in the so-called fingerprint region of organic molecules.

1.3 Thesis outline

The contents of each chapter of this thesis are outlined in the following.

Chapter 2 contains the theoretical and technological background of the three key areas: (1) Fibre-based light amplification systems, (2) femtosecond pulse shaping and (3) optical parametric oscillators. The fibre-based light amplification section describes ultrashort pulse generation methods, light amplification and pulse propagation in ordinary optical fibres and photonic crystal fibres as well as the technique of chirped pulse amplification. The concept of frequency-domain femtosecond pulse shaping by means of spatial light modulators is then introduced. Algorithms for adaptive pulse shaping in a feedback arrangement are described. The final section occupies the fundamentals of OPOs including nonlinear optics, phase-matching, gain and bandwidth, oscillation threshold and a method to estimate the resonator losses. Also, the nonlinear crystals for BPM and QPM used in this work and typical resonator configurations are discussed.

Chapter 3 presents the demonstration of a synchronously pumped, picosecond OPO with high signal ($7.3\,\mathrm{W}$) and idler ($3.1\,\mathrm{W}$) output power at a widely controllable repetition rate from $\approx 100\,\mathrm{MHz}$ to $\approx 1\,\mathrm{GHz}$ and an output pulse duration of $17\,\mathrm{ps}$. The pump source is based on a gain-switched laser diode, whose output pulses are amplified in a three-stage fibre amplifier system. This work was published in Optics Express [107] and at the 2010 Conference on Lasers and Electro-Optics US [108].

Chapter 4 discusses work on a high-pulse-energy, compact OPO. By reducing the pump pulse repetition rate of the fibre-amplified, gain-switched laser diode system under $8\,\mathrm{MHz}$, $\approx 100\,\mathrm{ps}$ pulses with energies of $488\,\mathrm{nJ}$ (signal) and $191\,\mathrm{nJ}$ (idler) are obtained, which, however, leads to a very long OPO resonator. This resonator can nevertheless be kept very compact by incorporating an intracavity single-mode fibre for feedback of the signal pulses. This work was published in Optics Letters [109] and at the 2011 Advanced Solid-State Photonics Conference [110].

Chapter 5 deals with two types of picosecond OPOs, one based on MgO:PPLN and one based on LBO, pumped with green light from the frequency-doubled ($530\,\mathrm{nm}$),

230 MHz, fibre-amplified, gain-switched laser diode system and tunable in the NIR range. For the MgO:PPLN OPO and 20 ps-long pump pulses, a combined output power of $\approx 270\,\mathrm{mW}$ is generated. Damage effects in MgO:PPLN known to occur in conjunction with visible light, which limit the OPO performance, are experimentally investigated and a study of the damage thresholds and optimum operating conditions is carried out. Compressed $4.4\,\mathrm{ps}$ pulses at $530\,\mathrm{nm}$ are used to pump the LBO OPO, which produces $3.7\,\mathrm{W}$ ($1.8\,\mathrm{W}$) of signal (idler) power with a total tuning range from $650\,\mathrm{nm}$ to $2850\,\mathrm{nm}$. This work was published in the Journal of the Optical Society of America B (MgO:PPLN OPO) [111] and accepted for publication in Optics Express (LBO OPO).

Chapter 6 describes pulse shaping experiments with different fibre-based CPA configurations for energy-scalable output pulses. The repetition rate of the system is varied between $500\,\mathrm{kHz}$ and $50\,\mathrm{MHz}$ and the pulse stretching is distributed between the amplifier stages to obtain optimum performance of the adaptive pulse shaping experiments using a self-adaptive differential evolution algorithm. This work was published at the 2009 Conference on Lasers and Electro-Optics Europe [112].

Chapter 7 presents the development of a high-power, YDF-based CPA system including the pulse shaper setup. Pulses with a duration of $\approx 600\,\mathrm{fs}$ at a repetition rate of $50\,\mathrm{MHz}$, a centre wavelength of $1045\,\mathrm{nm}$ and an output power of up to $30\,\mathrm{W}$ are obtained after adaptive pulse shaping. This source pumps a femtosecond PPLN OPO, which delivers a signal and idler output power of $1.9\,\mathrm{W}$ and $1.2\,\mathrm{W}$ at $1.5\,\mu\mathrm{m}$ and $3.6\,\mu\mathrm{m}$, respectively.

The order of the experimental chapters is not chronological but chosen such that all OPOs pumped with the picosecond, fibre-amplified, gain-switched laser diode system and that resulted in journal publications are presented first (chapters 3, 4 and 5), followed by the work carried out with the femtosecond, fibre-based CPA system (chapters 6 and 7).

Chapter 8 concludes the thesis with a summary of the most significant results obtained during the course of the work and an outlook on potential future work.

The appendices contain the complete list of publications stemming from this work (appendix A) and the analytical calculation of the B-integral (appendix B).

The bulk of the experiments presented in this thesis was undertaken by the author. However, parts of the work were carried out by co-workers or in collaboration with other groups within the research centre. It is acknowledged at the beginning of each chapter, how and to what extent other persons have contributed.

References

[1] J. A. Armstrong, N. Bloembergen, J. Ducuing, and P. S. Pershan, "Interactions between Light Waves in a Nonlinear Dielectric," Physical Review **127**(6), 1918 (1962).

[2] P. A. Franken, A. E. Hill, C. W. Peters, and G. Weinreich, "Generation of Optical Harmonics," Physical Review Letters **7**(4), 118 (1961).

[3] J. A. Giordmaine and R. C. Miller, "Tunable Coherent Parametric Oscillation in $LiNbO_3$ at Optical Frequencies," Physical Review Letters **14**(24), 973 (1965).

[4] R. L. Byer, "Quasi-phasematched nonlinear interactions and devices," Journal of Nonlinear Optical Physics & Materials **6**(4), 549–592 (1997).

[5] M. M. Fejer, G. A. Magel, D. H. Jundt, and R. L. Byer, "Quasi-Phase-Matched Second Harmonic Generation: Tuning and Tolerances," IEEE Journal of Quantum Electronics **28**(11), 2631–2654 (1992).

[6] L. E. Myers and W. R. Bosenberg, "Periodically Poled Lithium Niobate and Quasi-Phase-Matched Optical Parametric Oscillators," IEEE Journal of Quantum Electronics **33**(10), 1663–1672 (1997).

[7] L. E. Myers, R. C. Eckardt, M. M. Fejer, R. L. Byer, W. R. Bosenberg, and J. W. Pierce, "Quasi-phase-matched optical parametric oscillators in bulk periodically poled $LiNbO_3$," J. Opt. Soc. Am. B **12**(11), 2102–2116 (1995).

[8] D. N. Nikogosyan, *Nonlinear optical crystals: a complete survey*, 1st ed. (Springer, Berlin / Heidelberg, 2005).

[9] R. L. Byer, "Parametric Oscillators and Nonlinear Materials," in *Nonlinear Optics*, P. G. Harper and B. S. Wherrett, eds., chap. 2, pp. 47–117 (Academic Press, New York, 1977).

[10] K. L. Vodopyanov, O. Levi, P. S. Kuo, T. J. Pinguet, J. S. Harris, M. M. Fejer, B. Gerard, L. Becouarn, and E. Lallier, "Optical parametric oscillation in quasi-phase-matched GaAs," Opt. Lett. **29**(16), 1912–1914 (2004).

[11] K. L. Vodopyanov, F. Ganikhanov, J. P. Maffetone, I. Zwieback, and W. Ruderman, "$ZnGeP_2$ optical parametric oscillator with 3.8-12.4-μm tunability," Opt. Lett. **25**(11), 841–843 (2000).

[12] K. Burneika, M. Ignatavicius, V. Kabelka, A. Piskarskas, and A. Stabinis, "Parametric light amplification and oscillation in KDP with mode-locked pump," IEEE Journal of Quantum Electronics **8**(6), 574–574 (1972).

[13] A. Piskarskas, V. Smil'gyavichyus, and A. Umbrasas, "Continuous parametric generation of picosecond light pulses," Soviet Journal of Quantum Electronics **18**(2), 155 (1988).

[14] D. C. Edelstein, E. S. Wachman, and C. L. Tang, "Broadly tunable high repetition rate femtosecond optical parametric oscillator," Applied Physics Letters **54**(18), 1728–1730 (1989).

[15] L. Lefort, K. Puech, G. W. Ross, Y. P. Svirko, and D. C. Hanna, "Optical parametric oscillation out to 6.3μm in periodically poled lithium niobate under strong idler absorption," Applied Physics Letters **73**(12), 1610–1612 (1998).

[16] M. A. Watson, M. V. O'Connor, P. S. Lloyd, D. P. Shepherd, D. C. Hanna, C. B. E. Gawith, L. Ming, P. G. R. Smith, and O. Balachninaite, "Extended operation of synchronously pumped optical parametric oscillators to longer idler wavelengths," Opt. Lett. **27**(23), 2106–2108 (2002).

[17] M. V. O'Connor, M. A. Watson, D. P. Shepherd, and D. C. Hanna, "Use of a birefringent filter for tuning a synchronously pumped optical parametric oscillator," Applied Physics B: Lasers and Optics **79**(1), 15–23 (2004).

[18] D. C. Hanna, M. V. O'Connor, M. A. Watson, and D. P. Shepherd, "Synchronously pumped optical parametric oscillator with diffraction-grating tuning," Journal of Physics D-Applied Physics **34**(16), 2440–2454 (2001).

[19] M. A. Watson, M. V. O'Connor, D. P. Shepherd, and D. C. Hanna, "Synchronously pumped CdSe optical parametric oscillator in the 9-10μm region," Opt. Lett. **28**(20), 1957–1959 (2003).

[20] C. McGowan, D. T. Reid, Z. E. Penman, M. Ebrahim-Zadeh, W. Sibbett, and D. H. Jundt, "Femtosecond optical parametric oscillator based on periodically poled lithium niobate," J. Opt. Soc. Am. B **15**(2), 694–701 (1998).

[21] M. V. O'Connor, M. A. Watson, D. P. Shepherd, D. C. Hanna, J. H. V. Price, A. Malinowski, J. Nilsson, N. G. R. Broderick, D. J. Richardson, and L. Lefort, "Synchronously pumped optical parametric oscillator driven by a femtosecond mode-locked fiber laser," Opt. Lett. **27**(12), 1052–1054 (2002).

[22] T. Südmeyer, J. Aus der Au, R. Paschotta, U. Keller, P. G. R. Smith, G. W. Ross, and D. C. Hanna, "Femtosecond fiber-feedback optical parametric oscillator," Opt. Lett. **26**(5), 304–306 (2001).

[23] D. T. Reid, Z. Penman, M. Ebrahim-Zadeh, W. Sibbett, H. Karlsson, and F. Laurell, "Broadly tunable infrared femtosecond optical parametric oscillator based on periodically poled $RbTiOAsO_4$," Opt. Lett. **22**(18), 1397–1399 (1997).

[24] M. J. McCarthy and D. C. Hanna, "All-solid-state synchronously pumped optical parametric oscillator," J. Opt. Soc. Am. B **10**(11), 2180 (1993).

[25] F. Ganikhanov, S. Carrasco, X. Sunney Xie, M. Katz, W. Seitz, and D. Kopf, "Broadly tunable dual-wavelength light source for coherent anti-Stokes Raman scattering microscopy," Opt. Lett. **31**(9), 1292–1294 (2006).

[26] M. Jurna, J. P. Korterik, H. L. Offerhaus, and C. Otto, "Noncritical phase-matched lithium triborate optical parametric oscillator for high resolution coherent anti-Stokes Raman scattering spectroscopy and microscopy," Applied Physics Letters **89**(25), 251,116–3 (2006).

[27] T. W. Tukker, C. Otto, and J. Greve, "Design, optimization, and characterization of a narrow-bandwidth optical parametric oscillator," J. Opt. Soc. Am. B **16**(1), 90–95 (1999).

[28] S. D. Butterworth, S. Girard, and D. C. Hanna, "High-power, broadly tunable all-solid-state synchronously pumped lithium triborate optical parametric oscillator," J. Opt. Soc. Am. B **12**(11), 2158–2167 (1995).

[29] J. D. Kafka, M. L. Watts, and J. W. Pieterse, "Synchronously pumped optical parametric oscillators with LiB_3O_5," J. Opt. Soc. Am. B **12**(11), 2147–2157 (1995).

[30] K. Kieu, B. G. Saar, G. R. Holtom, X. S. Xie, and F. W. Wise, "High-power picosecond fiber source for coherent Raman microscopy," Opt. Lett. **34**(13), 2051–2053 (2009).

[31] V. Pruneri, S. D. Butterworth, and D. C. Hanna, "Low-threshold picosecond optical parametric oscillation in quasi-phase-matched lithium niobate," Applied Physics Letters **69**(8), 1029–1031 (1996).

[32] C. Cleff, J. Epping, P. Gross, and C. Fallnich, "Femtosecond OPO based on LBO pumped by a frequency-doubled Yb-fiber laser-amplifier system for CARS spectroscopy," Applied Physics B: Lasers and Optics **103**(4), 795–800 (2011).

[33] G. M. Gale, M. Cavallari, T. J. Driscoll, and F. Hache, "Sub-20-fs tunable pulses in the visible from an 82-MHz optical parametric oscillator," Opt. Lett. **20**(14), 1562–1564 (1995).

[34] R. F. Begley, A. B. Harvey, and R. L. Byer, "Coherent anti-Stokes Raman spectroscopy," Applied Physics Letters **25**(7), 387–390 (1974).

[35] A. M. Zheltikov, "Coherent anti-Stokes Raman scattering: from proof-of-the-principle experiments to femtosecond CARS and higher order wave-mixing generalizations," Journal of Raman Spectroscopy **31**(8-9), 653–667 (2000).

[36] C. L. Evans, E. O. Potma, M. Puoris'haag, D. Côté, C. P. Lin, and X. S. Xie, "Chemical imaging of tissue in vivo with video-rate coherent anti-Stokes Raman scattering microscopy," Proceedings of the National Academy of Sciences of the United States of America **102**(46), 16,807–16,812 (2005).

[37] C. L. Evans and X. S. Xie, "Coherent Anti-Stokes Raman Scattering Microscopy: Chemical Imaging for Biology and Medicine," Annual Review of Analytical Chemistry **1**(1), 883–909 (2008).

[38] W. J. Kozlovsky, E. K. Gustafson, R. C. Eckardt, and R. L. Byer, "Efficient monolithic MgO:$LiNbO_3$ singly resonant optical parametric oscillator," Opt. Lett. **13**(12), 1102–1104 (1988).

[39] D. T. Reid, C. McGowan, W. Sleat, M. Ebrahim-Zadeh, and W. Sibbett, "Compact, efficient 344-MHz repetition-rate femtosecond optical parametric oscillator," Opt. Lett. **22**(8), 525–527 (1997).

[40] P. J. Phillips, S. Das, and M. Ebrahim-Zadeh, "High-repetition-rate, all-solid-state, Ti:sapphire-pumped optical parametric oscillator for the mid-infrared," Applied Physics Letters **77**(4), 469–471 (2000).

[41] B. Ruffing, A. Nebel, and R. Wallenstein, "All-solid-state cw mode-locked picosecond $KTiOAsO_4$ (KTA) optical parametric oscillator," Applied Physics B: Lasers and Optics **67**(5), 537–544 (1998).

[42] A. Esteban-Martin, O. Kokabee, K. Moutzouris, and M. Ebrahim-Zadeh, "High-harmonic-repetition-rate, 1 GHz femtosecond optical parametric oscillator pumped by a 76 MHz Ti:sapphire laser," Opt. Lett. **34**(4), 428–430 (2009).

[43] A. Robertson, M. E. Klein, M. A. Tremont, K. J. Boller, and R. Wallenstein, "2.5-GHz repetition-rate singly resonant optical parametric oscillator synchronously pumped by a mode-locked diode oscillator amplifier system," Opt. Lett. **25**(9), 657–659 (2000).

[44] X. P. Zhang, J. Hebling, A. Bartels, D. Nau, J. Kuhl, W. W. Rühle, and H. Giessen, "1-GHz-repetition-rate femtosecond optical parametric oscillator," Applied Physics Letters **80**(11), 1873–1875 (2002).

[45] S. Lecomte, R. Paschotta, M. Golling, D. Ebling, and U. Keller, "Synchronously pumped optical parametric oscillators in the 1.5-μm spectral region with a repetition rate of 10 GHz," J. Opt. Soc. Am. B **21**(4), 844–850 (2004).

[46] S. Lecomte, R. Paschotta, S. Pawlik, B. Schmidt, K. Furusawa, A. Malinowski, D. J. Richardson, and U. Keller, "Optical parametric oscillator with a pulse repetition rate of 39 GHz and 2.1-W signal average output power in the spectral region near 1.5μm," Opt. Lett. **30**(3), 290–292 (2005).

[47] S. Lecomte, R. Paschotta, S. Pawlik, B. Schmidt, K. Furusawa, A. Malinowski, D. J. Richardson, and U. Keller, "Synchronously pumped optical parametric oscillator with a repetition rate of 81.8 GHz," IEEE Photonics Technology Letters **17**(2), 483–485 (2005).

[48] Y. Shen, S.-U. Alam, K. K. Chen, D. Lin, S. Cai, B. Wu, P. Jiang, A. Malinowski, and D. J. Richardson, "PPMgLN-Based High-Power Optical Parametric Oscillator Pumped by Yb^{3+}-Doped Fiber Amplifier Incorporates Active Pulse Shaping," IEEE Journal of Selected Topics in Quantum Electronics **15**(2), 385–392 (2009).

[49] Y. Peng, W. Wang, X. Wei, and D. Li, "High-efficiency mid-infrared optical parametric oscillator based on PPMgO:CLN," Opt. Lett. **34**(19), 2897–2899 (2009).

[50] C. W. Hoyt, M. Sheik-Bahae, and M. Ebrahim-Zadeh, "High-power picosecond optical parametric oscillator based on periodically poled lithium niobate," Opt. Lett. **27**(17), 1543–1545 (2002).

[51] O. Kokabee, A. Esteban-Martin, and M. Ebrahim-Zadeh, "Efficient, high-power, ytterbium-fiber-laser-pumped picosecond optical parametric oscillator," Opt. Lett. **35**(19), 3210–3212 (2010).

[52] T. Südmeyer, E. Innerhofer, F. Brunner, R. Paschotta, T. Usami, H. Ito, S. Kurimura, K. Kitamura, D. C. Hanna, and U. Keller, "High-power femtosecond fiber-feedback optical parametric oscillator based on periodically poled stoichiometric $LiTaO_3$," Opt. Lett. **29**(10), 1111–1113 (2004).

[53] T. Graf, G. McConnell, A. I. Ferguson, E. Bente, D. Burns, and M. D. Dawson, "Synchronously pumped optical parametric oscillation in periodically poled lithium niobate with 1-W average output power," Appl. Opt. **38**(15), 3324–3328 (1999).

[54] H. Ishizuki and T. Taira, "High-energy quasi-phase-matched optical parametric oscillation in a periodically poled $MgO:LiNbO_3$ device with a 5mm x 5mm aperture," Opt. Lett. **30**(21), 2918–2920 (2005).

[55] T. Südmeyer, J. A. d. Au, R. Paschotta, U. Keller, P. G. R. Smith, G. W. Ross, and D. C. Hanna, "Novel ultrafast parametric systems: high repetition rate single-pass OPG and fibre-feedback OPO," Journal of Physics D: Applied Physics **34**(16), 2433–2439 (2001).

[56] D. E. Spence and C. L. Tang, "Characterization and Applications of High-Repetition-Rate, Broadly Tunable, Femtosecond Optical Parametric Oscillators," IEEE Journal of Selected Topics in Quantum Electronics **1**(1), 31–43 (1995).

[57] O. Kokabee, A. Esteban-Martin, and M. Ebrahim-Zadeh, "Extended-cavity, tunable, GHz-repetition-rate femtosecond optical parametric oscillator pumped at 76 MHz," Opt. Express **17**(18), 15,635–15,640 (2009).

[58] P. W. Roth, A. J. Maclean, D. Burns, and A. J. Kemp, "Direct diode-laser pumping of a mode-locked Ti:sapphire laser," Opt. Lett. **36**(2), 304–306 (2011).

[59] D. J. Richardson, J. Nilsson, and W. A. Clarkson, "High power fiber lasers: current status and future perspectives [Invited]," J. Opt. Soc. Am. B **27**(11), B63–B92 (2010).

[60] J. Limpert, F. Röser, T. Schreiber, and A. Tünnermann, "High-Power Ultrafast Fiber Laser Systems," IEEE Journal of Selected Topics in Quantum Electronics **12**(2), 233–244 (2006).

[61] R. Paschotta, J. Nilsson, A. C. Tropper, and D. C. Hanna, "Ytterbium-doped fiber amplifiers," IEEE Journal of Quantum Electronics **33**(7), 1049–1056 (1997).

[62] M. E. Fermann and I. Hartl, "Ultrafast Fiber Laser Technology," IEEE Journal of Selected Topics in Quantum Electronics **15**(1), 191–206 (2009).

[63] E. Snitzer, H. Po, F. Hakimi, R. Tumminelli, and B. C. McCollum, "Double clad, offset core Nd fiber laser," in *Optical Fiber Sensors*, vol. PD5 (New Orleans, LA, USA, 1988).

[64] L. Zenteno, "High-power double-clad fiber lasers," Journal of Lightwave Technology **11**(9), 1435–1446 (1993).

[65] N. G. R. Broderick, H. L. Offerhaus, D. J. Richardson, R. A. Sammut, J. Caplen, and L. Dong, "Large Mode Area Fibers for High Power Applications," Optical Fiber Technology **5**(2), 185–196 (1999).

[66] P. S. J. Russell, "Photonic Crystal Fibers," Science **299**(5605), 358–362 (2003).

[67] J. Limpert, A. Liem, T. Gabler, H. Zellmer, A. Tünnermann, S. Unger, S. Jetschke, and H. R. Müller, "High-average-power picosecond Yb-doped fiber amplifier," Opt. Lett. **26**(23), 1849–1851 (2001).

[68] K. K. Chen, J. H. V. Price, S.-U. Alam, J. R. Hayes, D. J. Lin, A. Malinowski, and D. J. Richardson, "Polarisation maintaining 100W Yb-fiber MOPA producing μJ pulses tunable in duration from 1 to 21 ps," Opt. Express **18**(14), 14,385–14,394 (2010).

[69] J. Limpert, T. Schreiber, T. Clausnitzer, K. Zöllner, H. Fuchs, E. Kley, H. Zellmer, and A. Tünnermann, "High-power femtosecond Yb-doped fiber amplifier," Opt. Express **10**(14), 628–638 (2002).

[70] A. Malinowski, A. Piper, J. H. V. Price, K. Furusawa, Y. Jeong, J. Nilsson, and D. J. Richardson, "Ultrashort-pulse Yb^{3+}-fiber-based laser and amplifier system producing >25-W average power," Opt. Lett. **29**(17), 2073–2075 (2004).

[71] D. Strickland and G. Mourou, "Compression of amplified chirped optical pulses," Optics Communications **56**(3), 219–221 (1985).

[72] A. Galvanauskas, G. C. Cho, A. Hariharan, M. E. Fermann, and D. Harter, "Generation of high-energy femtosecond pulses in multimode-core Yb-fiber chirped-pulse amplification systems," Opt. Lett. **26**(12), 935–937 (2001).

[73] F. He, J. H. V. Price, A. Malinowski, A. Piper, M. Ibsen, D. J. Richardson, J. W. Dawson, C. W. Siders, J. A. Britten, and C. P. J. Barty, "High Average Power, High Energy, Femto-second Fiber Chirped Pulse Amplification System," in *Conference on Lasers and Electro-Optics (CLEO) US*, vol. CMEE5 (Baltimore, MD, USA, 2007).

[74] F. Röser, J. Rothhard, B. Ortaç, A. Liem, O. Schmidt, T. Schreiber, J. Limpert, and A. Tünnermann, "131 W 220 fs fiber laser system," Opt. Lett. **30**(20), 2754–2756 (2005).

[75] T. Eidam, S. Hadrich, F. Roser, E. Seise, T. Gottschall, J. Rothhardt, T. Schreiber, J. Limpert, and A. Tunnermann, "A 325-W-Average-Power Fiber CPA System Delivering Sub-400 fs Pulses," IEEE Journal of Selected Topics in Quantum Electronics **15**(1), 187–190 (2009).

[76] T. Eidam, S. Hanf, E. Seise, T. V. Andersen, T. Gabler, C. Wirth, T. Schreiber, J. Limpert, and A. Tünnermann, "Femtosecond fiber CPA system emitting 830 W average output power," Opt. Lett. **35**(2), 94–96 (2010).

[77] F. Röser, T. Eidam, J. Rothhardt, O. Schmidt, D. N. Schimpf, J. Limpert, and A. Tünnermann, "Millijoule pulse energy high repetition rate femtosecond fiber chirped-pulse amplification system," Opt. Lett. **32**(24), 3495–3497 (2007).

[78] A. M. Weiner, "Femtosecond Optical Pulse Shaping and Processing," Progress in Quantum Electronics **19**(3), 161–237 (1995).

[79] A. M. Weiner, "Femtosecond pulse shaping using spatial light modulators," Review of Scientific Instruments **71**(5), 1929–1960 (2000).

[80] A. Efimov, M. D. Moores, N. M. Beach, J. L. Krause, and D. H. Reitze, "Adaptive control of pulse phase in a chirped-pulse amplifier," Opt. Lett. **23**(24), 1915–1917 (1998).

[81] D. Yelin, D. Meshulach, and Y. Silberberg, "Adaptive femtosecond pulse compression," Opt. Lett. **22**(23), 1793–1795 (1997).

[82] T. Tanabe, K. Ohno, T. Okamoto, M. Yamanaka, and F. Kannari, "Feedback control for accurate shaping of ultrashort optical pulses prior to chirped pulse amplification," Japanese Journal of Applied Physics Part 1-Regular Papers Short Notes & Review Papers **43**(4A), 1366–1375 (2004).

[83] T. Brixner, A. Oehrlein, M. Strehle, and G. Gerber, "Feedback-controlled femtosecond pulse shaping," Applied Physics B: Lasers and Optics **70**, 119–S124 (2000).

[84] D. N. Schimpf, J. Limpert, and A. Tünnermann, "Controlling the influence of SPM in fiber-based chirped-pulse amplification systems by using an actively shaped parabolic spectrum," Opt. Express **15**(25), 16,945–16,953 (2007).

[85] F. He, H. S. S. Hung, J. H. V. Price, N. K. Daga, N. A. Naz, J. Prawiharjo, D. C. Hanna, D. P. Shepherd, D. J. Richardson, J. W. Dawson, C. W. Siders, and C. P. Barty, "High energy femtosecond fiber chirped pulse amplification system with adaptive phase control," Opt. Express **16**(8), 5813–5821 (2008).

[86] F. G. Omenetto, A. J. Taylor, M. D. Moores, and D. H. Reitze, "Adaptive control of femtosecond pulse propagation in optical fibers," Opt. Lett. **26**(12), 938–940 (2001).

[87] M. A. Dugan, J. X. Tull, and W. S. Warren, "High-resolution acousto-optic shaping of unamplified and amplified femtosecond laser pulses," J. Opt. Soc. Am. B **14**(9), 2348–2358 (1997).

[88] G. Chériaux, O. Albert, V. Wänman, J. P. Chambaret, C. Félix, and G. Mourou, "Temporal control of amplified femtosecond pulses with a deformable mirror in a stretcher," Opt. Lett. **26**(3), 169–171 (2001).

[89] S. Kirkpatrick, J. Gelatt, C. D., and M. P. Vecchi, "Optimization by Simulated Annealing," Science **220**(4598), 671–680 (1983).

[90] D. E. Goldberg, *Genetic Algorithms in Search, Optimization and Machine Learning* (Addison-Wesley Longman Publishing Co., Inc., Boston, 1989).

[91] R. Storn and K. Price, "Differential evolution – A simple and efficient heuristic for global optimization over continuous spaces," Journal of Global Optimization **11**(4), 341–359 (1997).

[92] M. M. Ali, C. Khompatraporn, and Z. B. Zabinsky, "A numerical evaluation of several stochastic algorithms on selected continuous global optimization test problems," Journal of Global Optimization **31**(4), 635–672 (2005).

[93] H. Y. Fan and J. Lampinen, "A trigonometric mutation operation to differential evolution," Journal of Global Optimization **27**(1), 105–129 (2003).

[94] J. Prawiharjo, N. K. Daga, R. Geng, J. H. Price, D. C. Hanna, D. J. Richardson, and D. P. Shepherd, "High fidelity femtosecond pulses from an ultrafast fiber laser system via adaptive amplitude and phase pre-shaping," Opt. Express **16**(19), 15,074–15,089 (2008).

[95] W. R. Bosenberg and Eckardt, R. C., eds., "Optical Parametric Devices," J. Opt. Soc. Am. B **12**(11), 2084 (1995). Special feature issue.

[96] S.-W. Chu, T.-M. Liu, C.-K. Sun, C.-Y. Lin, and H.-J. Tsai, "Real-time second-harmonic-generation microscopy based on a 2-GHz repetition rate Ti:sapphire laser," Opt. Express **11**(8), 933–938 (2003).

[97] A. Vogel, J. Noack, G. Hüttman, and G. Paltauf, "Mechanisms of femtosecond laser nanosurgery of cells and tissues," Applied Physics B: Lasers and Optics **81**(8), 1015–1047 (2005).

[98] Y. R. Shen, "Surfaces probed by nonlinear optics," Surface Science **299-300**, 551–562 (1994).

[99] K. König, T. W. Becker, P. Fischer, I. Riemann, and K. J. Halbhuber, "Pulse-length dependence of cellular response to intense near-infrared laser pulses in multiphoton microscopes," Opt. Lett. **24**(2), 113–115 (1999).

[100] S. W. Hell and J. Wichmann, "Breaking the diffraction resolution limit by stimulated emission: stimulated-emission-depletion fluorescence microscopy," Opt. Lett. **19**(11), 780–782 (1994).

[101] S. W. Hell, "Nanoscopy with focused light," in *The Rank Prize Funds - Symposium on Ultrafast Biophotonics* (Grasmere, UK, 2010).

[102] D. M. Bubb and R. F. Haglund Jr., "Resonant Infrared Pulsed Laser Ablation and Deposition of Thin Polymer Films," in *Pulsed Laser Deposition of Thin Films*, R. W. Eason, ed., pp. 35–60 (John Wiley & Sons, Hoboken, New Jersey, 2006).

[103] V. Z. Kolev, M. W. Duering, B. Luther-Davies, and A. V. Rode, "Compact high-power optical source for resonant infrared pulsed laser ablation and deposition of polymer materials," Opt. Express **14**(25), 12,302–12,309 (2006).

[104] N. A. Naz, H. S. S. Hung, M. V. O'Connor, D. C. Hanna, and D. P. Shepherd, "Adaptively shaped mid-infrared pulses from a synchronously pumped optical parametric oscillator," Opt. Express **13**(21), 8400–8405 (2005).

[105] H. S. S. Hung, J. Prawiharjo, N. K. Daga, D. C. Hanna, and D. P. Shepherd, "Experimental investigation of parametric transfer in synchronously pumped optical parametric oscillators," J. Opt. Soc. Am. B **24**(12), 2998–3006 (2007).

[106] J. Prawiharjo, H. S. S. Hung, D. C. Hanna, and D. P. Shepherd, "Numerical investigations of parametric transfer in synchronously pumped optical parametric oscillators for indirect mid-infrared pulse shaping," J. Opt. Soc. Am. B **24**(9), 2484–2493 (2007).

[107] F. Kienle, K. K. Chen, S.-U. Alam, C. B. E. Gawith, J. I. Mackenzie, D. C. Hanna, D. J. Richardson, and D. P. Shepherd, "High-power, variable repetition rate, picosecond optical parametric oscillator pumped by an amplified gain-switched diode," Opt. Express **18**(8), 7602–7610 (2010).

[108] F. Kienle, K. K. Chen, S.-U. Alam, C. B. E. Gawith, J. I. Mackenzie, D. C. Hanna, D. J. Richardson, and D. P. Shepherd, "A Picosecond Optical Parametric Oscillator Synchronously Pumped by an Amplified Gain-Switched Laser Diode," in *Conference on Lasers and Electro-Optics (CLEO) US*, vol. CThZ7 (San Jose, California, USA, 2010).

[109] F. Kienle, P. Siong Teh, S.-U. Alam, C. B. E. Gawith, D. C. Hanna, D. J. Richardson, and D. P. Shepherd, "Compact, high-pulse-energy, picosecond optical parametric oscillator," Opt. Lett. **35**(21), 3580–3582 (2010).

[110] F. Kienle, P. S. Teh, S.-U. Alam, C. B. E. Gawith, D. C. Hanna, D. J. Richardson, and D. P. Shepherd, "High pulse energy, picosecond MgO:PPLN optical parametric oscillator using a single-mode fiber for signal feedback," in *Advanced Solid-State Photonics (ASSP)*, vol. AMB03 (Istanbul, Turkey, 2011).

[111] F. Kienle, D. Lin, S. U. Alam, H. S. S. Hung, C. B. E. Gawith, H. E. Major, D. J. Richardson, and D. P. Shepherd, "Green-pumped, picosecond MgO:PPLN optical parametric oscillator," J. Opt. Soc. Am. B **29**(1), 144–152 (2012).

[112] J. Prawiharjo, F. Kienle, N. K. Daga, D. C. Hanna, D. J. Richardson, and D. P. Shepherd, "High-Quality Energy-Scalable Femtosecond Pulses from a Fibre-Based Chirped Pulse Amplification System via Adaptive Pulse Shaping," in *Conference on Lasers and Electro-Optics (CLEO) Europe*, vol. CJ9.5 (Munich, Germany, 2009).

Chapter 2

Theory and technology

2.1 Introduction

The background theory and technological aspects of the three essential building blocks of the work in this thesis will be introduced in this chapter. The pump sources for the optical parametric oscillators (OPO) consisting of fibre amplifier systems are described in section 2.2. Various theoretical aspects are introduced including ultrashort pulse generation, light amplification and propagation in fibres as well as the chirped pulse amplification technique. Fibre nonlinearities related to short pulse durations and high pulse energies, their role in pulse quality degradation and measures to reduce them are discussed. The following section 2.3 discusses the concept of femtosecond pulse shaping with spatial light modulators. In such devices the amplitude and phase of the spectrally dispersed pulse is controlled. Furthermore, computer-based optimisation algorithms, in particular differential evolution, used in a feedback loop for adaptive pulse shaping are described. The background on OPOs including nonlinear optics theory, a review of the nonlinear crystals used and their parameters as well as a discussion of typical OPO resonator configurations concludes the chapter.

2.2 Fibre amplification systems

2.2.1 Ultrashort pulse generation

From the host of pico- and femtosecond pulse generation methods, the brief introduction here is limited to two methods that have been used for the experiments performed during the thesis work. The first method is mode-locking and the second method is laser diode gain-switching.

2.2.1.1 Mode-locked oscillators

The front end of many pulsed laser light sources in a MOPA configuration is typically an ultrashort pulse oscillator, where the output pulses are used as a seed for the amplifier stage(s). Such ultrashort pulse oscillators are mostly based on the mode-locking method [1], in which a fixed phase relation between all resonator modes is established. In general, passively mode-locked methods are preferred as opposed to active mode-locking elements, since they do not require precise synchronisation and therefore additional electronics and since they tend to give shorter pulses (the process is driven by already short pulses).

In Ti:sapphire ultrafast oscillators, it is mostly the Kerr-lensing effect that generates the pulses. The optical Kerr effect states that the refractive index n is dependent on the intensity I, which varies in time and space

$$n\left(t,r\right) = n_0 + n_2 \cdot I\left(t,r\right) \ , \tag{2.1}$$

with n_0 the linear and n_2 the nonlinear refractive index. The effect leads to a stronger focusing of high intensities, e.g. in the centre of a Gaussian beam, due to the increased refractive index. In pulsed operation, where the intensity additionally changes with time, this corresponds to a temporally varying converging lens. Therefore, the losses at an intracavity aperture are only low for the pulse peak and not for the pulse wings, leading to a shortening of the pulse. Only the high-intensity pulse can propagate stably in the resonator. The pulse can originate from a single spike in the initial noise background, which then builds up at successive resonator round-trips because of the lower losses. This technique is called Kerr lens mode-locking [2] and was first experimentally demonstrated by Spence *et al.* [3]. However, reliable self-starting is not easily achieved with this approach. Saturable absorbers have been developed to this end [4] and consist of an anti-reflection coating, a semiconductor layer and a high-reflectivity Bragg mirror. Saturable absorbers introduce high losses for low intensities and low losses for high intensities by means of saturation at a certain intensity leading to a bleaching of the absorption of the semiconductor layer. Therefore, as with the Kerr lens, they support the growth of distinct peaks in the noise at the expense of the weak noise background and consequently the oscillation of intense pulses that experience gain at each round-trip.

The actual pulse width is determined by a compromise between a pulse width narrowing effect of the mode-locking mechanism and a spectral narrowing effect of the laser gain medium. The shorter the circulating pulse becomes, the less loss it experiences within the mode-locking element. But the associated spectral broadening causes the spectral width to approach the gain bandwidth of the laser medium and the limit

will be reached. The ultimate pulse width is governed by the gain material, which is in favour of the leading pulse edge, because of the undepleted gain at the leading edge. This leads to a continuous decrease of the trailing edge and thus a temporal pulse shortening until the mentioned spectral broadening reaches the gain bandwidth. However, in very broad bandwidth materials, e.g. Ti:sapphire, group delay dispersion in the material typically limits the shortest pulse duration achievable.

In fibre-based ultrafast oscillators, other techniques for passive mode-locking are frequently applied. These include additive-pulse mode-locking [5] and nonlinear polarisation rotation [6]. In additive-pulse mode-locked lasers, a second cavity is coupled to the laser cavity by means of a semi-transparent mirror. This second cavity contains a single-mode fibre (SMF) and has the same round-trip time as the laser cavity. The SMF introduces a nonlinear phase shift to the pulses. The pulses propagating in the fibre cavity are coupled back to the laser cavity after one round-trip via the mirror and then interfere with the pulses there. For proper adjustment of the cavity lengths, the pulses from both cavities constructively interfere only near the pulse peak, but not at the pulse wings due to the intensity-dependent nonlinear phase shift. Long-term stability is an issue with such lasers, since a slight cavity mismatch or temperature drift lead to mode-locking instabilities. Nonlinear polarisation rotation in a doped fibre is a related method, however, without the need for a second cavity. The two different polarisation modes in the fibre (from a linearly polarised input beam) act as the two interferometer arms. Both modes undergo intensity-dependent nonlinear polarisation rotation, whose origins are SPM, cross-phase modulation and uncontrolled birefringence. An elliptically polarised beam emerges at the fibre output and therefore experiences a certain amount of loss at a subsequent polariser. The loss can be set to a minimum for the most intense central part of the pulse with a particular polarisation by just aligning the polariser and additional waveplates. The pulse wings are attenuated due to their different polarisation state. The most common dopants of active fibres are ytterbium- (Yb^{3+}) and erbium-ions (Er^{3+}) for the $1\,\mu\mathrm{m}$ and the $1.55\,\mu\mathrm{m}$ spectral region, respectively.

2.2.1.2 Gain-switched laser diodes

The repetition rate of mode-locked oscillators is limited by the length of the resonator, which is often determined by the components in the resonator and such oscillators often have to be set-up in a free-space configuration, which makes them prone to misalignment and instability. Features such as simplicity, low cost, ease of integration and reliability make modulated semiconductor laser diodes (LD) an attractive alternative. Since LDs can be electronically modulated, the pulse repetition rate is not dependent on resonator length anymore and thus much more tunable.

Gain-switching is a method, where optical pulses much shorter than the driving pump pulses can be produced, and is applicable to LD modulation [7–9]. It relies on isolating the first spike of LD relaxation oscillations triggered by the drive pulse. In order to achieve this, the drive pulse must be switched off before the second spike can build up. The physical process of gain-switching of an LD, as illustrated in figure 2.1(a), starts by biasing the LD with a direct current (DC) just below the threshold and superimposing it with the modulation current (black), typically a train of short electrical pulses. When such an electrical pulse is injected into the LD active region, the charge carrier density (blue) increases rapidly, but the photon density (red) remains close to zero as long as the lasing threshold is not reached. Once the threshold is reached, stimulated emission sets in with the photon density rising rapidly. This leads to a depletion of the charge carrier density until stimulated emission stops. If the electrical drive pulse is now terminated, the relaxation oscillation is interrupted and a single optical pulse much shorter than the electrical drive pulse is produced. However, if the drive pulse continues and more electrons are injected, the charge carrier density recovers until the lasing threshold is reached again and stimulated emission resumes. This transient behaviour leads to the generation of many more spikes with decreasing amplitude, eventually reaching a steady state. The pulse duration of the optical output pulse is determined by the time at which lasing threshold is reached relative to the drive pulse, by the level of inversion and by the rate of charge carrier depletion. Typical pulse durations are a few tens of picoseconds.

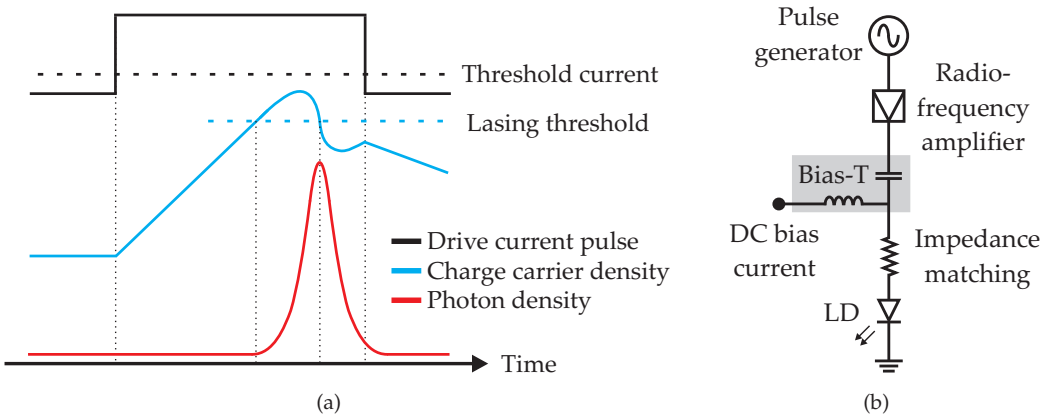

FIGURE 2.1: Physical process (a) and typical electronics architecture (b) of laser diode gain-switching. DC: Direct current, LD: Laser diode.

It is essential to precisely control the DC bias current and the timing of the modulation pulses. On the other hand, since the drive pulses are electronically generated and controlled, the repetition rate is variable over a wide range. Typical architectures (figure 2.1(b)) consist of a pulse generator plus a radio-frequency electronic amplifier to generate the drive pulses as well as a direct current source for the DC bias. The drive pulses

are superimposed on the DC bias in a bias-T-network. Impedance matching of the radio-frequency cable and the laser diode can be achieved with an additional resistor.

The output pulses of a gain-switched LD are inherently negatively chirped caused by the refractive index dependence of the active region on the varying drive current. The increase in charge carrier density just before lasing sets in reduces the refractive index and hence leads to a shorter optical path length of the active region. This in turn leads to a blue-shifted leading pulse edge, when stimulated emission begins, followed by a red-shift as the charge carrier density is reduced. Different pulse compression schemes (e.g. a fibre with normal dispersion at the wavelength of the pulses or a chirped fibre Bragg grating) can be exploited to compensate for this mainly linear chirp to generate shorter pulse durations.

2.2.2 Light amplification in ytterbium-doped fibres

The amplifiers must have a gain material, which offers a gain bandwidth broad enough to cover the seed pulse bandwidth. The minimum temporal width τ and the spectral bandwidth $\Delta\nu$ of a pulse (FWHM quantities) are related by the fundamental time-bandwidth product

$$\tau \cdot \Delta\nu = K \,, \tag{2.2}$$

K is a constant depending on the pulse shape (Gaussian: 0.441; Hyperbolic secant: 0.315). Femtosecond pulses correspond to bandwidths of up to a few hundred nanometres.

Gain materials for ultrafast pulse generation include materials such as dyes (e.g. Rhodamine 6G), bulk materials with transition metal dopants (e.g. Ti:sapphire) or optical fibres doped with rare-earth ions (e.g. ytterbium or erbium). Dyes are mostly toxic and therefore not often used anymore. The drawbacks of bulk material approaches are the beam quality deterioration during amplification, thermo-optical issues, difficult power scaling, low optical-to-optical conversion efficiency, high system complexity and poor stability. Despite all that, Ti:sapphire is still the workhorse in the ultrashort laser field generating pulses below $5\,\mathrm{fs}$ due to its high gain bandwidth of $\approx 230\,\mathrm{nm}$ (review publication: [10]). This may be achieved by Kerr lens mode-locking and dispersion compensation techniques.

Ytterbium (Yb^{3+}-ion) has distinct absorption bands at $910\,\mathrm{nm}$ and $975\,\mathrm{nm}$ and emission bands at $975\,\mathrm{nm}$ and around $1030\,\mathrm{nm}$ as shown in figure 2.2 [11]. The large gain bandwidth covers the spectral region $975 \ldots 1200\,\mathrm{nm}$ and has a FWHM of around $40\,\mathrm{nm}$. The laser gain coefficient is given by [12]

$$\gamma_g(\nu) = \Delta N \cdot \sigma_{21}(\nu) \,, \tag{2.3}$$

where ΔN is the population inversion density and $\sigma_{21}(\nu)$ the frequency-dependent emission cross-section of the dopant. The emission cross-section at $975\,\mathrm{nm}$ of ytterbium is $2.5 \cdot 10^{-20}\,\mathrm{cm}^2$, whereas it is $27 \cdot 10^{-20}\,\mathrm{cm}^2$ at $790\,\mathrm{nm}$ for Ti:sapphire [10]. So, assuming equal inversion and device length, Ti:sapphire gives a $\approx 10\times$ higher gain. However, the interaction length in Yb-doped fibres is typically much longer than in short Ti:sapphire crystals. Therefore, the gain can be orders of magnitude higher. Since the fluorescence lifetime is typically between $0.8\,\mathrm{ms}$ and $1.5\,\mathrm{ms}$, depending on the Germanium content of the fibre core, significant energy storage and population inversion is also possible. This compares to $3.2\,\mu\mathrm{s}$ in Ti:sapphire, which requires high pump beam intensities with good beam quality to achieve considerable population inversion. Furthermore, the long lifetime allows operation of ytterbium-doped fibre (YDF) amplifiers down to tens of kHz. In the widely used scheme with a pump wavelength of $975\,\mathrm{nm}$ and a lasing wavelength of around $1040\,\mathrm{nm}$, ytterbium exhibits a quasi-three level behaviour in that the lower laser level is very close to the ground level and gets thermally populated. The quantum defect is very low at 6% in this case, which is a positive aspect regarding thermal issues.

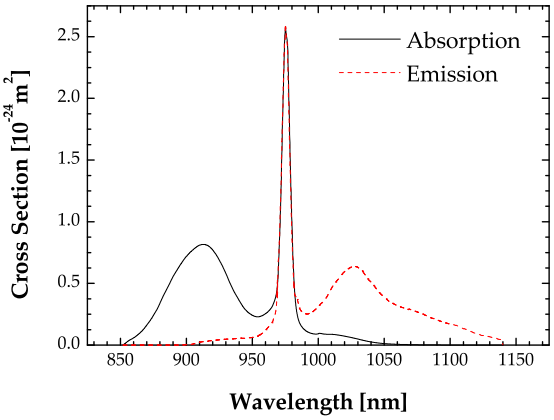

FIGURE 2.2: Absorption and emission cross sections of ytterbium in a germanosilicate host.

The process of gain narrowing [12] due to the finite gain bandwidth of ytterbium induces a reduction of the spectral pulse bandwidth and consequently a temporal broadening. The centre region of the pulse spectrum experiences a higher gain than the edges, causing it to grow stronger and the width of the pulse spectrum to become narrower. Furthermore, a shift of the pulse centre wavelength towards the gain peak wavelength can occur when the peaks do not coincide. These processes depend on the gain bandwidth and the magnitude of the gain.

YDFs show very good optical-to-optical conversion efficiencies of up to 80%. The single-pass gain is large because of the high interaction length in the fibre. Due to the distinct absorption lines, they can be pumped with readily available, cost-efficient, high-power LDs. In general, the beam characteristics of fibres are superior to bulk materials. Furthermore, thermal problems are significantly reduced because of the high

surface-to-volume ratio of fibres simplifying power scaling compared to bulk amplifier systems [13].

However, fibres possess inherently high nonlinearities, because of the relatively small mode area and long interaction length compared to bulk gain materials. As the pulse peak power increases the intensity-sensitive nonlinearities increase. To reduce this effect and to obtain higher damage thresholds, large-mode area (LMA) fibres [14] have been developed with mode areas reaching several thousand $\mu\mathrm{m}^2$ [15], while still maintaining single-mode behaviour. LMAs are fabricated by increasing the core radius and decreasing the numerical aperture such that the condition for single-mode guidance [16]

$$V = \frac{2\pi}{\lambda} \cdot a \cdot \mathrm{NA} = \frac{2\pi}{\lambda} \cdot a \cdot \sqrt{n_{core}^2 - n_{clad}^2} < 2.405 \tag{2.4}$$

is still fulfilled. V is the so-called V-number, a is the fibre core radius, NA is the numerical aperture and n_{core} and n_{clad} the refractive index of core and cladding, respectively. A result of the lowered difference between core and cladding index is a weaker guidance of the fundamental mode and increased losses. However, the properties of photonic crystal fibres (PCF) can largely avoid this (section 2.2.4).

Pump light delivery in high-power systems is typically performed with double-clad fibres [17, 18]. They have a doped core surrounded by a lower index inner cladding. The inner cladding and core constitute the waveguide for the single-mode signal beam. The pump beam is launched into the inner cladding and is confined by an outer cladding with even lower index. The pump propagates in the inner cladding and also in the core, where it is absorbed by the dopant ions. In order to increase the interaction overlap, the symmetry of the inner cladding is often broken (e.g. D-shape). The advantage of such double-clad fibres is that the inner cladding possesses a large NA and thus accepts multi-mode pump beams with high efficiency. Hence, high-power multi-mode LDs can be applied to pump the fibre device. Double-clad fibre amplifiers are sometimes referred to as brightness converters, where a low-brightness, high-power diode pump beam is converted to a high-brightness, high-power signal beam.

The setup of a fibre amplifier is relatively simple. It consists of the gain fibre to which a wavelength division multiplexer (WDM) is connected or spliced. The amplifier can be configured in a forward and / or backward pumping scheme, where the pump co- and / or counter-propagates with the signal. A WDM is a coupler with two input ports and one output port optimised to combine pump and signal light. Pigtailed pump LDs are connected to the WDM. Alternatively to WDMs, dichroic mirrors are used in case of free-space pump beam delivery. Optical isolators (OI) ensure that back-reflections into the seed source or pump LDs are blocked. Power scaling is achieved by using multiple setups of this kind in a cascade.

2.2.3 Pulse propagation in optical fibres

An ultrashort optical pulse can be described with

$$E(t) = A(t) \cdot e^{i(\omega_0 t + \varphi(t))} = \left(A_0 e^{-2\ln 2\left(\frac{t}{\tau}\right)^2} \right) \cdot e^{i(\omega_0 t + \varphi(t))} , \tag{2.5}$$

with $E(t)$ the time-dependent electric field, $A(t)$ the pulse amplitude consisting of the peak amplitude A_0 and a slowly varying envelope function, ω_0 the pulse carrier frequency, t the time and $\varphi(t)$ the temporal phase. The envelope function is assumed to have a Gaussian profile $e^{-2\ln 2\left(t^2/\tau^2\right)}$ with a full width at half maximum (FWHM) denoted with τ.

Dispersion means that the velocities of different frequency components within the pulse envelope vary during propagation in dispersive elements (caused by the frequency-dependent refractive index $n(\omega)$ of an optical medium or by geometrical path length differences of spatially separated frequency components). Thus, depending on the dispersion regime (normal or anomalous) a "red" component propagates faster compared to a "blue" component or vice versa. This is also referred to as pulse chirping. It is more convenient to describe dispersive effects in the frequency domain, therefore equation (2.5) is Fourier-transformed to

$$E(\omega) = A_0 \cdot e^{-2\ln 2\left(\frac{\omega-\omega_0}{\Delta\omega}\right)^2} \cdot e^{i\phi(\omega-\omega_0)} . \tag{2.6}$$

$\Delta\omega$ is the spectral FWHM of the pulse envelope, ω the light angular frequency and $\phi(\omega - \omega_0)$ is the spectral phase. The frequency detuning parameter $\Omega = \omega - \omega_0$ is introduced to indicate the detuning from the carrier frequency. It is common practice to expand the spectral phase into a Taylor series about the carrier frequency

$$\phi(\Omega) = \phi_0 + \frac{d\phi}{d\Omega} \cdot \Omega + \frac{1}{2!} \cdot \frac{d^2\phi}{d\Omega^2} \cdot \Omega^2 + \frac{1}{3!} \cdot \frac{d^3\phi}{d\Omega^3} \cdot \Omega^3 + \dots . \tag{2.7}$$

For $\Delta\omega \ll \omega_0$, the series can be truncated after the fourth term without considerable error. Taking the length L of the interacting medium into account and with the relation $\phi(\Omega) = \beta(\Omega) \cdot L$, we can also write

$$\beta(\Omega) = \beta_0 + \beta_1 \cdot \Omega + \frac{1}{2!} \cdot \beta_2 \cdot \Omega^2 + \frac{1}{3!} \cdot \beta_3 \cdot \Omega^3 + \dots , \tag{2.8}$$

where $\beta_m = \left(d^m\beta/d\omega^m\right)_{\omega=\omega_0}$ $(m = 1, 2, 3, \dots)$ correspond to the m-th order dispersion coefficients. β_0 is simply a constant offset and β_1 is the first-order dispersion coefficient giving the linear dispersion contribution, which is the inverse of the group velocity v_g and describes the velocity of the pulse envelope. β_2 is the GVD coefficient and describes

pulse broadening, because it adds a frequency-dependent delay to each frequency component within the pulse. β_3 is the TOD term and causes temporal oscillations [16, 19].

Self-phase modulation (SPM) is the most important nonlinear process when ultrashort pulses propagate in optical fibres, since it occurs at the lowest peak powers compared to other nonlinear processes and it does not exhibit a threshold. SPM stems from the third-order susceptibility in silica and leads to the intensity-dependence of the refractive index (Kerr effect, equation (2.1)). This causes a nonlinear phase shift, which adds to the linear phase

$$\varphi = \frac{2\pi}{\lambda_0} L \cdot (n_0 + n_2 I) = \frac{2\pi}{\lambda_0} L \cdot (n_L + n_{NL}) = \varphi_L + \varphi_{NL} \,, \tag{2.9}$$

with the linear φ_L and nonlinear φ_{NL} contribution to the temporal phase. A measure for the accumulated nonlinear phase shift in a medium of length L is

$$B = \frac{2\pi}{\lambda_0} \int_0^L n_2 I\,(z)\; dz \,, \tag{2.10}$$

commonly referred to as the B-integral [20]. λ_0 is the centre wavelength and $I(z)$ the pulse intensity. The B-integral can be calculated from the experimental parameters as described in Appendix B. An optical pulse acquires a chirp due to the action of the nonlinear phase on the instantaneous frequency

$$\nu_{inst} = \frac{1}{2\pi} \cdot \frac{d\varphi}{dt} = \nu_0 - \frac{1}{2\pi} \cdot \frac{d\varphi_{NL}}{dt} \,. \tag{2.11}$$

This temporal chirp leads to a modulation and broadening of the pulse spectrum allowing the possibility of reducing the temporal pulse width. However, an excessive amount of SPM induces a strong degradation of the pulse quality.

Pulse propagation in optical fibres is described by the nonlinear Schrödinger equation [16]

$$\frac{\partial A}{\partial z} = -\beta_1 \frac{\partial A}{\partial t} - \frac{i\beta_2}{2} \frac{\partial^2 A}{\partial t^2} + \frac{\beta_3}{6} \frac{\partial^3 A}{\partial t^3} - \frac{\alpha}{2} A + i\gamma \left|A\right|^2 A \,. \tag{2.12}$$

This equation describes the temporal and spatial dependence of the slowly varying amplitude of the pulse envelope $A\,(z,t)$ along an optical fibre. Here, we use a simplified equation considering only dispersion up to the third order and SPM as the only nonlinear effect, which is justified in this work due to the experimental parameters. In the equation, z denotes the propagation distance, α the loss coefficient and

$$\gamma = \frac{n_2 \omega_0}{c A_{eff}} \tag{2.13}$$

the nonlinear parameter, where c is the speed of light and A_{eff} the fibre effective mode area. One method to solve the nonlinear Schrödinger equation is the split-step Fourier

method. This method assumes that the fibre consists of many short segments in which nonlinear and dispersive processes occur independently and alternately and it then treats nonlinearities in the time domain and dispersion in the frequency domain.

Another class of nonlinear effects are stimulated inelastic scattering effects, where an energy transfer between the light pulse and the medium takes place. Stimulated Raman scattering (SRS) involves the excitation of optical phonons. The Stokes shift for SRS is $13\,\mathrm{THz}$ in silica and the threshold peak power is calculated with [16]

$$P_{peak,th} = \frac{16 A_{eff}}{g_R L_{eff}}\,, \tag{2.14}$$

where L_{eff} denotes the effective length of the fibre and g_R the Raman gain coefficient. Thus, SRS causes a rapid energy transfer to the frequency-downshifted Stokes wave from a certain peak power upwards.

2.2.4 Photonic crystal fibres

Photonic crystal fibres [21] with an LMA structure are preferably used in high-power CPA systems rather than standard SMFs. Due to the advantageous properties, the influence of nonlinear effects can be significantly reduced. Engineering of the microstructure in PCFs offers ways to design the dispersion properties, e.g. the zero-dispersion wavelength (ZDW) and the GVD profile. For example, anomalous dispersion well below $600\,\mathrm{nm}$ due to the strong waveguide contribution has been demonstrated [22]. A PCF in combination with a large-mode area also allows influence over the nonlinear properties, e.g. SPM.

The periodic structure of PCFs is normally a fine array of air holes that extends along the full fibre length. Many different types of microstructures have been developed, which are tailored to the specific application. An often used structure in high-power fibre amplifiers is shown in figure 2.3(a). It has a double-clad structure with a ring of airholes as outer cladding, a microstructured inner cladding and a solid core. The effective cladding refractive index of PCFs is determined by the ratio of the air hole diameter d and the pitch Λ, which are illustrated in figure 2.3(b).

The following properties can be incorporated into a single PCF and this is why they are so versatile [13]. The core can be doped with rare-earth ions, for example ytterbium, to generate gain with all the advantages mentioned in section 2.2.2. Short lengths of fibre are sufficient for efficient pump absorption of $10\,\mathrm{dB/m}$ or higher due to the small ratio of pump to active core (increased pump overlap) as well as for substantial gain. PCFs can be fabricated with large-mode areas, which still maintain single-mode behaviour

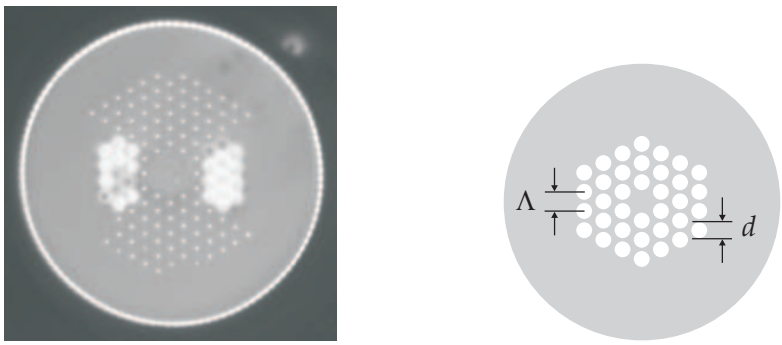

(a) (b)

FIGURE 2.3: Cross-section and parameter definition of a PCF. (a) Close-up image of the cross-section of a polarisation-maintaining, double-clad PCF with a ring of air holes as outer cladding, a microstructured inner cladding and an Yb-doped solid core. The stress-rods are located on both sides of the core. (b) Design parameters hole diameter d and pitch Λ of a PCF.

and strong guidance, due to the flexible effective cladding index. These features help to significantly reduce nonlinear effects.

In double-clad structures, the inner cladding is used as a multi-mode guide for the low brightness pump light (see figure 2.3(a)). The outer cladding with the ring of air holes gives a large index difference and hence a very high NA of up to 0.6. The pump coupling efficiency is thus relatively high even for multi-mode pump beams. Also, the increase in brightness from (multi-mode) pump to (single-mode) signal is significant.

Stress rods on opposite sides of the core can be used to introduce stress birefringence, where the refractive index on the axis rod–core–rod is much larger than the refractive index on the perpendicular axis (typically $\Delta n = 10^{-4}$). A large difference of the refractive index also means a large difference of the propagation constants of the two naturally occuring polarisation modes in these two orthogonal axes, which in turn considerably reduces the mutual coupling efficiency. Provided that the birefringence is high enough and that the input beam is linearly polarised along one of the two axes, the polarisation will be preserved and the output beam will be linearly polarised as well. The fibre is then said to be polarisation-maintaining (PM).

Furthermore, PCFs can be endlessly single-mode for all wavelengths, when the condition $d/\Lambda < 0.4$ is fulfilled [21, 23]. This behaviour can be understood with the picture of a modal "sieve". The wire mesh of the sieve are the air holes, where no light can be guided. Guidance is only possible in the silica gaps in between. If the hole spacing is large enough to only contain the single lobe of the spatial fundamental mode but not the smaller lobes of higher-order modes, then the latter slip through the silica gaps and are not guided (lobes basically mean effective wavelengths in the transverse plane). As the d/Λ-ratio is increased, more and more higher-order modes become trapped in the core.

An extreme example of an LMA PCF is the rod-type double-clad fibre with a $80\,\mu\mathrm{m}$ core and $200\,\mu\mathrm{m}$ inner cladding described in reference [15]. At $976\,\mathrm{nm}$ it has an inner cladding NA of 0.6 and a high absorption of $30\,\mathrm{dB/m}$ allowing very efficient pumping from multi-mode LDs. The effective mode area is $4000\,\mu\mathrm{m}^2$, thus the detrimental effect of SPM is strongly reduced.

2.2.5 Fibre-based chirped pulse amplification

Chirped pulse amplification (CPA) is a method to amplify ultrashort laser pulses up to high peak powers, while avoiding optical damage and keeping detrimental nonlinear effects and thus pulse distortions at a minimum. The technique can be classified into three main stages as shown in figure 2.4: (1) temporal stretching of the seed pulse by typically three to five orders of magnitude to avoid nonlinear effects during amplification, (2) amplification of the pulse by six to nine orders of magnitude to obtain high pulse energies and (3) temporal compressing of the amplified pulse back to the initial duration.

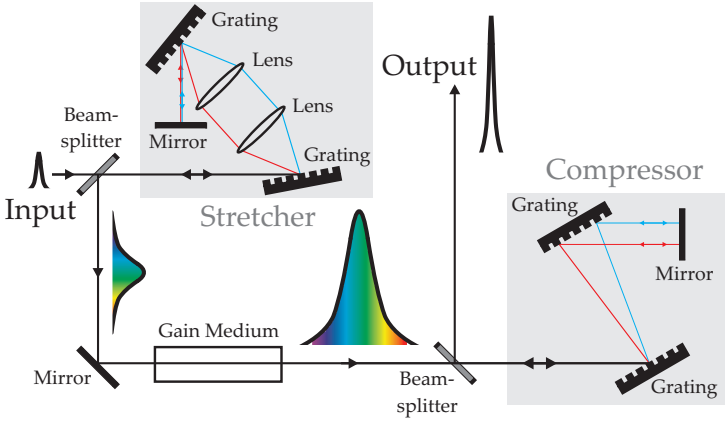

FIGURE 2.4: Schematic diagram of the CPA technique. An ultrashort pulse is stretched in time before the amplification and subsequently compressed to the original pulse duration.

The first CPA system was reported by Strickland and Mourou in 1985 [24]. CPA has been demonstrated in different bulk solid-state amplifier systems [10], amongst which Ti:sapphire is the most prominent. Multipass or regenerative amplifier systems are typically used. However, the complexity of such systems is high and the operation not trivial. Fibre-based CPA systems [13] became more popular due to the advantages of YDFs mentioned in section 2.2.2. The amplification often takes place in a multi-stage fibre amplifier using different fibre types, which is embedded between the stretcher and compressor. At the front end of the amplifier chain, where the average power is still low, ordinary ytterbium-doped single-mode fibres may still be used. However, further down the chain, where the (peak) power levels are much higher, other fibre types like LMA fibres, PCFs and / or double-clad fibres are employed to avoid pulse quality degradation by SPM.

A requirement for CPA is a means to accurately manage the dispersion of the stretcher, the amplifier and the compressor. The stretching and compressing of the pulses in the time domain is performed by intentionally influencing the dispersion of the broad-bandwidth pulse in the frequency domain. The stretcher unit strongly chirps the pulse leading to a temporal broadening. After amplification, the compressor unit inverts the chirp leading to a temporal re-compression. Components changing the pulse dispersion properties in this context are diffraction grating pairs [25], prism pairs, optical fibres [26, 27] or fibre Bragg gratings [28–30]. Fibre-based methods are mostly limited to the stretcher, because of the high peak powers in the compressor that would lead to high nonlinearities and hence pulses distortions. The sign of dispersion has to be opposite for the stretcher and the compressor. A grating pair has negative group delay dispersion (GDD, units of fs^2 or ps^2) of magnitude [25, 31]

$$\begin{aligned} \mathrm{GDD} &= \frac{d^2\phi}{d\omega^2} \\ &= 2 \cdot \frac{-4\pi^2 cb}{\omega^3 d^2 \left(1 - \left(\frac{2\pi c}{\omega d} - \sin\theta_{in}\right)^2\right)} \\ &= \frac{-\lambda^3 G}{\pi c^2 d^2 \left(1 - \left(\frac{\lambda}{d} - \sin\theta_{in}\right)^2\right)^{3/2}} , \end{aligned} \tag{2.15}$$

with d the grating period and θ_{in} the angle of incidence of the light beam to the first grating. $b = G/\cos\theta_d$ is the grating slant distance with G the perpendicular grating separation and θ_d the diffraction angle. Note that the factor of 2 accounts for the double-pass configuration of most grating compressor setups. GDD and GVD are related by

$$\mathrm{GDD} = \mathrm{GVD} \cdot L , \tag{2.16}$$

where L denotes the device length. The frequency derivative of the GDD equation (2.15) gives the equation for the cubic phase introduced by the grating pair (also in a double-pass setup)

$$\frac{d^3\phi}{d\omega^3} = -\frac{3\lambda}{2\pi c}\left(\frac{1 + \frac{\lambda}{d}\sin\theta_{in} - \sin^2\theta_{in}}{1 - \left(\frac{\lambda}{d} - \sin\theta_{in}\right)^2}\right)\frac{d^2\phi}{d\omega^2} . \tag{2.17}$$

It has units of ps^3 and is related to the TOD (with units of ps^3/m) in the same way as GDD and GVD above. This equation contains an error in the original publication [31], which has been altered here: The factor $\frac{-6\pi\lambda}{c}$ should read $\frac{-3\lambda}{2\pi c}$.

Standard optical fibres have positive GDD in the normal dispersion regime below approximately $1.3\,\mu\mathrm{m}$, therefore the combination of a grating pair and a fibre for pulse compressor and stretcher works well for GDD compensation. If grating pairs are used as stretcher and compressor, one pair must have positive GDD, which can be achieved

by inserting a 1-to-1 telescope between the gratings [32], where the lenses are positioned two focal lengths apart from each other and each grating is positioned between the respective lens and its focus point, so that a virtual image is generated. The GDD is then controlled by the effective distance between the second grating and the image of the first grating.

The design of stretcher and compressor requires a balance of the GDD of stretcher, amplifier(s) and compressor. This means that

$$\mathrm{GDD_S} + \mathrm{GDD_A} + \mathrm{GDD_C} = 0 \tag{2.18}$$

must be fulfilled, where $\mathrm{GDD_S}$, $\mathrm{GDD_A}$ and $\mathrm{GDD_C}$ are the group delay dispersion parameters of stretcher, amplifiers and compressor, respectively.

It has to be noted that the TOD contributions from a fibre stretcher and a grating compressor are both positive (in the normal dispersion regime again). That means they add up and can not easily be compensated for. This induces pulse distortions, e.g. a pulse pedestal and temporal oscillations that can contain a large amount of energy. To a certain extent, pulse shaping can compensate for the accumulated TOD. The quality of the output pulses from a CPA system is ultimately determined by the balance of stretcher and compressor dispersion, residual nonlinear effects and higher-order dispersion.

2.3 Femtosecond pulse shaping

2.3.1 Concept of femtosecond pulse shaping

Femtosecond pulse shaping is based on the linear filtering process, well-known from electronics. Linear filtering can be described in time or frequency. The input pulse $e_{in}(t)$ is altered by the filter, which is characterised by the impulse response function $h(t)$ (lower case letters used here to indicate the time domain). The output pulse is the convolution

$$e_{out}(t) = e_{in}(t) * h(t) \ . \tag{2.19}$$

For a delta function as input pulse, the output pulse is simply the impulse response of the filter. The frequency description of the filter is $H(\omega)$ and is related to the impulse response with the Fourier transform $H(\omega) = \frac{1}{\sqrt{2\pi}} \int_{-\infty}^{+\infty} h(t)\, e^{-i\omega t} dt$. The output of the linear filter is the product of the input signal $E_{in}(\omega)$ and $H(\omega)$

$$E_{out}(\omega) = E_{in}(\omega) \cdot H(\omega) \ , \tag{2.20}$$

since a convolution becomes a product after Fourier transform. This is easier to achieve experimentally, and hence many approaches of femtosecond pulse shaping use the frequency domain.

There are a number of techniques to control the phase and amplitude of an ultrashort pulse to achieve arbitrary waveforms. The most common setup is a 4-f-Fourier transform pulse shaper [33] and consists of the following components as shown in figure 2.5. The input pulse is dispersed into its spectral components by the first diffraction grating and subsequently collimated with a lens, which is one focal length f away from the grating. This corresponds to a spatial Fourier transform. The spatially separated spectral components are focused onto a masking element located in the back focal plane. The mask acts as filter $H(\omega)$ and modulates the phase and / or amplitude of each spectral component ω. A second lens and grating pair, with the same specifications and separated by f as well, recombines the spectral components back into an output beam with the desired temporal waveform. This corresponds to an inverse Fourier transform. The output pulse is shaped such that certain spectral components are temporally retarded (phase) and / or attenuated (amplitude) with respect to others. In the absence of the masking element, the setup should produce an output pulse, which is identical to the input pulse. This is the case, if all components are aligned in the 4-f-configuration. The lenses then act as a 1-to-1 telescope and the entire configuration is referred to as a zero-dispersion delay line.

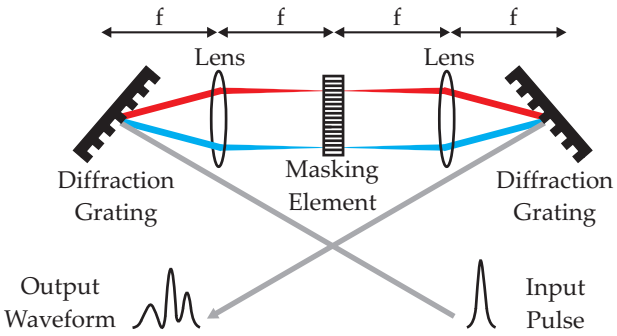

FIGURE 2.5: Schematic of a typical 4-f-Fourier transform pulse shaper setup with a masking element in the Fourier plane. The setup constitutes a zero-dispersion delay line without the mask being present. The input and output pulse shapes are then equal.

Spatial light modulators (SLM) discussed in section 2.3.3 are commonly used as the mask. The 4-f-Fourier transform approach is used in the experiments described in this work.

A radically different approach is the so-called acousto-optic programmable dispersive filter (AOPDF) [34, 35], which works in the time domain as given in equation (2.19). Here, the waveform of an acoustic wave is transferred to the optical pulse inside a birefringent acousto-optic crystal. A transducer driven by an arbitrary waveform generator launches the acoustic wave along the z-axis of the crystal. Hence, the radio-frequency

signal from the waveform generator is mapped onto space in the crystal and forms a temporary grating. Now the optical pulse enters this crystal along the z-axis as well. The pulse is polarised in the fast axis (mode 1) of the crystal. When the phases of both waves are matched, which is the case for a certain optical frequency ω at a specific position z in the crystal, this frequency component is diffracted to the slow axis (mode 2) via interaction with its acousto-optic counterpart (acousto-optic mode coupling). Depending on the position, where the transfer from fast to slow axis of the frequency component takes place, the optical path length is determined by the refractive indices of fast or slow axis. Thus, the pulse exiting the crystal in the slow axis is composed of spectral components that are diffracted at different points in the crystal. Because the crystal is birefringent, the velocities of the two axes differ and this leads to different time delays per frequency component and hence to the temporal shaping. Figure 2.6 shows a schematic of the working principle of an AOPDF. Here, an initially chirped pulse is de-chirped by the acousto-optic interaction and leaves the crystal as a compressed pulse.

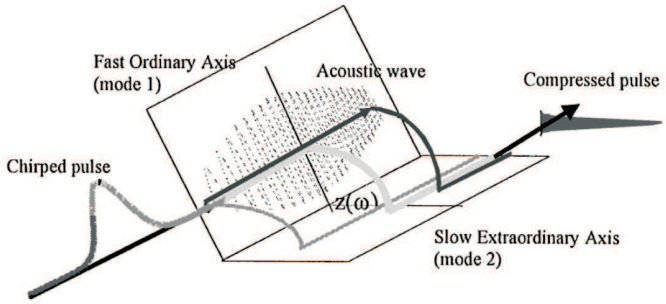

FIGURE 2.6: Working principle of an acousto-optic programmable dispersive filter. The frequency component ω is diffracted at a specific position z from the fast to the slow axis depending on the phase of the chirped acoustic wave. Because of the different refractive indices in the two axes of the birefringent crystal, the pulse changes the temporal profile (here: pulse compression). Source: [35].

The diffraction efficiency that determines the spectral amplitude of the output pulse is controlled by the acoustic power at the respective position. Since an AOPDF is an in-line device, the setup does not require a spatial dispersion of the pulse and thus the experimental complexity is considerably reduced. AOPDFs operate at repetition rates of tens of kHz. An overview and comparison of the two different techniques for pulse shaping, AOPDF and SLM, can be found in reference [36].

2.3.2 Frequency domain pulse shaping with spatial light modulators

Following the analysis of Weiner [33, 37], the resolution of a 4-f-pulse shaper in terms of frequency span per pixel can be calculated by starting with the grating equation [38]

$$\sin\theta_{in} + \sin\theta_d = \frac{m\lambda}{d}\,, \tag{2.21}$$

where θ_{in} and θ_d are the angle of incidence and the diffraction angle, respectively. The grating period is denoted with d, the wavelength with λ and the diffraction order with m. The angular dispersion D is found by differentiating equation (2.21).

$$D = \frac{d\theta_d}{d\lambda} = \frac{m}{d\cos\theta_d} \,. \tag{2.22}$$

With the FWHM pulse bandwidth $\Delta\lambda$ ($\approx d\lambda$), the approximation of small angles of θ_d the lens focal length f and with $m = 1$, we can write the expression

$$a = f \cdot d\theta_d = \frac{f\Delta\lambda}{d\cos\theta_d} \,, \tag{2.23}$$

which gives the total spatial span of the pulse spectrum on the SLM masking element. The spatial dispersion follows as

$$\alpha = \frac{a}{\Delta\omega} = \frac{f\lambda^2}{2\pi cd\cos\theta_d}. \tag{2.24}$$

$\Delta\omega$ is the pulse bandwidth expressed in angular frequency and c is the speed of light.

A relation between the filter function $H(\omega)$ in equation (2.20) and the actual masking function $M(x)$ describing the spatial distribution of amplitude and phase of the mask, can be found when we consider an electric field with a Gaussian profile directly after the mask

$$E_{mask}(x,\omega) \propto E_{in}(\omega) \cdot e^{-\frac{(x-\alpha\omega)^2}{w_0^2}} \cdot M(x) \,. \tag{2.25}$$

This equation describes the electric field as a function of space and frequency. The $1/e^2$-radius (of intensity) of each frequency component at the masking plane is

$$w_0 = \frac{\cos\theta_{in}}{\cos\theta_d} \cdot \frac{f\lambda}{\pi w_{in}} \,, \tag{2.26}$$

where the $1/e^2$-radius of the collimated input beam is denoted with w_{in}. In order to obtain the output electric field only as a function of frequency (or time), it is necessary to perform a spatial filtering operation. This can be achieved by expanding the masked field into a superposition of Hermite-Gaussian modes [38]. Higher-order modes, which describe spatial diffraction of the mask (inter-pixel gaps or pixel edges), are eliminated by spatial filtering, e.g. by coupling into a fibre or placing an iris after the pulse shaper. The shaped field is thus described by the lowest order Hermite-Gaussian mode (fundamental Gaussian mode), whose coefficient is defined as the filter function

$$H(\omega) = \sqrt{\frac{2}{\pi w_0^2}} \int_{-\infty}^{\infty} M(x) \cdot e^{-\frac{2(x-\alpha\omega)^2}{w_0^2}} dx \,. \tag{2.27}$$

It shows that the effective frequency domain filter is the mask function $M(x)$ convolved

with the Gaussian (intensity) profile of the beam. The FWHM of this Gaussian profile determines the spectral resolution limit of the shaper as

$$\delta\omega \approx \sqrt{\ln 2} \cdot \frac{w_0}{\alpha} \,. \tag{2.28}$$

Note that for pixellated devices, physical features smaller than w_0 are smeared out by the convolution and this ultimately limits the finest features that can be imprinted onto the filtered spectrum. The maximum achievable complexity η of the pulse shaper system can be defined as a function of the shaper resolution limit (equation (2.28)) and the pulse bandwidth $\Delta\omega$. With equations (2.24) and (2.26), we get

$$\eta = \frac{\Delta\omega}{\delta\omega} = \frac{\Delta\lambda}{\lambda_0} \frac{\pi}{\sqrt{\ln 2}} \frac{w_{in}}{d \cos\theta_{in}} \,. \tag{2.29}$$

The complexity is a measure of the number of distinct spectral features with width $\delta\omega$ that can be controlled within the pulse bandwidth $\Delta\omega$. Equivalently in the time domain, it means the number of temporal features with width τ that can be synthesised into a waveform within the time window T (see below). The complexity is typically between 100 and 400. Note that it is not only the optical components placed around the SLM that determine the complexity but also the applied SLM technology. An LC SLM with 128 pixels, for instance, limits the complexity to 128 and having a much higher complexity from the surrounding optical system is useless.

It is clear that the resolution limitation in the frequency domain infers a limitation in time as well due to the fundamental Fourier theory. The convolution of equation (2.27) yields the product $h(t) = m(t)\, g(t)$ for the impulse response $h(t)$, where $m(t)$ is the inverse Fourier transform of the mask function. The function

$$g(t) = e^{-\frac{w_0^2 t^2}{8\alpha^2}} \tag{2.30}$$

describes a Gaussian envelope that restricts the time window of the pulse shaper. The (intensity) FWHM of this envelope is

$$T = \frac{4\alpha\sqrt{\ln 2}}{w_0} = \frac{2\sqrt{\ln 2}\, w_{in}\lambda_0}{cd\cos\theta_{in}} \,, \tag{2.31}$$

Within this time window, the tailored output pulse can precisely reflect the response of the infinite-resolution mask. For a given grating, a larger time window can only be achieved with a larger input beam size. In a CPA system, the time window has no practical implications, since the stretched pulses are typically much longer than the calculated time window and it has been shown numerically that shaping of a linearly chirped and thus temporally stretched pulse beyond the time window is possible [39]. The time window is limited by the Fourier limit $T\delta\nu = 0.441$, where $\delta\nu = \delta\omega/2\pi$,

and is thus related to the spectral resolution of the pulse shaper in equation (2.28). The Fourier limit also applies to the full pulse bandwidth $\Delta\nu = \Delta\omega/2\pi$ and the finest temporal feature with width τ, i.e. $\Delta\nu\tau = 0.441$. The complexity can be expressed as $\eta = \Delta\nu/\delta\nu = T/\tau$. Hence, we get the maximum time-bandwidth product

$$T\Delta\nu = 0.441\eta\,. \tag{2.32}$$

All of the above quantities are given as FWHM. In general, the pulse shaper optics must be chosen such that its complexity is equal or higher than the complexity given by the masking element (for LC SLM: number of pixels).

We now discuss resolution issues of an SLM with a pixellated LC mask and its dispersion shaping capabilities. The discrete modulation of each frequency component in an LC SLM is limited by the sampling theorem after Nyquist-Shannon [40], which states that a signal must be sampled at least at twice the frequency of its highest frequency component. Applied to LC SLMs, two adjacent pixels must cover the total range of $0 \leq \phi \leq 2\pi$ of the spectral phase. In other words, a maximum number of $N_{pix}/2$ phase modulations can be synthesised with an LC mask with N_{pix} pixels. A sufficiently large effective phase range beyond only 2π is obtained, if phase wrapping is applied (instead of 0-π-2π-3π-4π-5π, the phase is wrapped to 0-π-2π-0-π-2π, for instance). Thus, with a maximum phase shift between two adjacent pixels of π and with the frequency span $\Delta\omega_{pix}$ on one pixel, the maximum rate of change of phase per angular frequency is $d\phi/d\omega = \pm\pi/\Delta\omega_{pix}$ (plus or minus symbolises pos. or neg. slope). With the spectral phase expanded to a Taylor series as in equation (2.7), one can deduce the maximum values of each individual dispersion parameter before reaching the Nyquist limit [39, 41]

$$\frac{d\phi}{d\omega} = \pm\frac{\lambda_0^2}{2c\Delta\lambda_{pix}}\,, \qquad \text{(Group delay)} \tag{2.33}$$

$$\frac{d^2\phi}{d\omega^2} = \pm\frac{\lambda_0^4}{2N_{pix}\pi c^2\Delta\lambda_{pix}^2}\,, \qquad \text{(GDD)} \tag{2.34}$$

$$\frac{d^3\phi}{d\omega^3} = \pm\frac{\lambda_0^6}{N_{pix}^2\pi^2 c^3\Delta\lambda_{pix}^3}\,, \qquad \text{(TOD)} \tag{2.35}$$

where $\Delta\lambda_{pix} = \Delta\omega_{pix}\lambda_0^2/2\pi c$ is the wavelength span per pixel and N_{pix} the number of used pixels. Each equation gives the maximum dispersion possible from this term only without the influence of the other terms. If more than one dispersion term acts on the pulse, the Nyquist limit may be reached sooner. Furthermore, if the LC SLM is used in reflection mode, the spatially dispersed beam traverses the device twice and hence the maximum dispersion values are doubled.

2.3.3 Spatial light modulators

To control phase and amplitude of a pulse, SLMs in 4-f-configurations are applied as spectral masking elements. Modern SLMs offer flexible modulation of both phase and amplitude, which can be controlled by an external signal, as opposed to a fixed mask modulator, where the experimental usability is strongly limited. A comprehensive review of SLM-based pulse shaping can be found in reference [37].

Deformable mirrors are mounted in two or more symmetric positions and a force is applied on both ends of the mirror membrane. The force can be of mechanical or electrostatic nature. In combination with a grating and a lens in a 2-f-configuration, the function is equal to a 4-f-setup using a transmissive masking element. Deformable mirrors are capable of performing a continuous phase modulation. The phase profile varies smoothly and the modulation is very precise. However, the actuators provide only a limited bending radius and hence phase shift. Also, arbitrary pulse shapes are not easily programmable. Deformable mirrors can, however, operate in spectral ranges not covered by other types including the MIR. This is achieved by state-of-the-art high-reflectivity coatings for the specific range.

In acousto-optic modulators, a piezo-electric transducer driven by a radio-frequency voltage generates a travelling acoustic wave in a crystal. This results in a periodic variation of the refractive index and thus a temporary diffraction grating. The optical pulse effectively sees a fixed diffraction grating as the acoustic wave velocity is much slower than the passing pulse light wave. The waveform of the radio-frequency signal determines the grating shape and therefore the diffraction angle and the delay per frequency component. The input beam is incident at the Bragg angle (highest efficiency) and each spatially dispersed frequency component diffracts off of this grating. The amplitude of the output waveform is directly related to the diffraction efficiency of the modulator grating, which is determined by the acoustic wave amplitude. The resolution is given by the minimum programmable acoustic wave feature and can be considered as continuous compared to pixellated devices (see below). The refresh rate of the grating pattern depends on the acoustic aperture time and is typically in the low microsecond range. Due to the finite speed of the acoustic wave, AOMs can not be used for high repetition rate pulse trains in the MHz-range and the efficiency of the AOM is only between 10% and 15%.

Liquid crystal (LC) arrays consist of transparent cells, referred to as pixels, which are filled with long, thin, rod-like molecules. Each pixel can be individually programmed by applying a voltage via transparent electrodes. With no voltage applied, the alignment direction of the molecules defines the extraordinary axis of the crystal. The molecules will tilt in the direction of the electric field when a voltage is applied. Thus,

light linearly polarised along the extraordinary axis, sees a voltage-dependent refractive index and consequently experiences a variable phase shift. The maximum phase shift is achieved when the light is subject to the full extraordinary index (no voltage and thus tilt). For independent phase and amplitude modulation, a combination of two LC-masks with a molecule orientation of $\pm 45^{\circ}$ relative to the light polarisation state is sandwiched between two polarisers. The retardance or optical path length of an LC-cell is nonlinearly dependent on the drive voltage. Amplitude modulation is expressed by the normalised transmission

$$T(V) = \cos^2\left(\frac{\pi}{\lambda}\left(R_1(V) - R_2(V)\right)\right), \tag{2.36}$$

where $R_1(V)$ an $R_2(V)$ are the retardances of LC-mask 1 and 2, respectively. The phase modulation is expressed by

$$\phi(V) = \frac{2\pi}{\lambda}\left(\frac{R_1(V) + R_2(V)}{2}\right). \tag{2.37}$$

The response time of the liquid crystals is considerably longer than with AOM SLMs and on the order of milliseconds, which makes adaptive pulse shaping with a feedback signal slow. But the efficiency is much higher due to the high transmission of the LC-cells of $> 80\%$. Once the liquid crystals are programmed, the phase and amplitude profile is fixed and all the pulses, even from a high repetition rate pulse train, see a permanent mask. Typical LC SLMs have 128 to 640 pixels [41], a $100\,\mu\mathrm{m}$ pixel spacing, $\approx 3\,\mu\mathrm{m}$ inter-pixel gaps and come with the electronic circuitry to control each pixel independently. They usually have an optical thickness corresponding to a maximum phase shift of several π. The most complex phase pattern is alternating phase values from one pixel to the next, e.g. 0-π-0-π and so on. A drawback of pixellated LC-masks is the non-continuous modulation and the ineffective gap between the pixels leading to abrupt phase changes and limited resolution. A direct result of this is the generation of temporal satellite pulses, which obviously extracts energy from the main pulse and significantly distorts the pulse train quality [33, 42].

Table 2.1 compares some properties of AOMs and LC-arrays for the purpose of femtosecond pulse shaping. Because of the ease of use and flexibility, an LC SLM is chosen for this project.

2.3.4 Adaptive pulse shaping algorithms

A further advance in programmable pulse shaping is adaptive pulse shaping, where a specific output parameter of the experiment serves as feedback for a computer algorithm to find the optimum pulse shape. This optimum is found by iteratively reducing

TABLE 2.1: Comparison of properties of liquid crystals and acousto-optics as modulators in femtosecond pulse shaping.

	LC	**AOM**
Refresh time	$\approx 10\,\mathrm{ms}$	μs-range
Repetition rate	any	low kHz-range
Modulation	independent grey-level spectral amplitude and phase	
Complexity	number of pixels (128, 640)	up to 1000
Efficiency	high ($> 80\%$)	low (10% to 15%)

the difference of a measured experimental parameter and a pre-set desired parameter. Possible feedback parameters in order to define a fitness function include the pulse spectrum [43], the FROG trace [36, 44], the autocorrelation peak-to-pedestal contrast [27], the second-harmonic signal [45] or the two-photon absorption (TPA) signal in a photodiode [46]. The TPA signal from a photodiode, which is proportional to $\int I^2\,(t)\,dt$ with the intensity I and the time t, can be used to maximise the pulse peak power and hence minimise the pulse width, since it is directly related to these two pulse parameters. The parameter search space in an LC SLM pulse shaping experiment is determined by the controlled LC-pixels from the two masks (phase and amplitude shaping).

In general, it is desirable to find the global optimum rather than just a local optimum, but the search process should not take too long to converge and finish. These contradictory desires can be expressed with the concepts of exploration and exploitation of the search space. Exploration means a random search over the whole search space. Exploitation means the rigorous use of a certain region where the optimum is assumed to be. In order to efficiently find the global optimum, a sensible balance of both has to be found. Several algorithms with different emphases have been developed. Simulated annealing [47], genetic algorithm [48] and differential evolution (DE) [49] are frequently used in pulse shaping.

Simulated annealing is analogous to the cooling and crystallisation process of metals. If the temperature is reduced slowly and in a controlled manner to allow relocation of molecules, the metal forms a single crystal and is therefore in the state of minimum energy. Translated to the field of optimisation algorithms, the optimum state of the system is found by starting to explore the entire search space and slowly reducing the search to a smaller region, where the global optimum is expected.

Genetic algorithms and differential evolution are members of the evolutionary algorithms family. They are derived from biological evolution laws such as mutation, crossover and selection. All of them have in common that they need (1) an initial population of individuals in a defined search space, (2) a fitness function evaluating the quality of each individual and defining the exiting condition, (3) particular processes

that alter the individuals and generate variety from the parent to the offspring generation as well as (4) decision parameters to select the individuals of the new generation. They require a continuous search space to avoid trapping in a local minimum and the search space must be reasonably sized to ensure fast convergence. The main difference between the evolutionary algorithms is the approach for the mutation step (see below).

In a genetic algorithm, the individuals are composed of genes that are represented as binary strings [50]. Crossover is performed by exchanging a subset of bits from certain genes between two individuals to generate offspring. Mutation is performed by randomly flipping bits of certain genes. Mutation ensures genetic diversity, prevents the domination of a particularly fit individual and avoids trapping in a local minimum.

The DE algorithm developed by Storn and Price [49] is chosen for this project, because it outperforms other algorithms both in theory and experiment [49, 51, 52]. The DE algorithm can be split up in the following sequence

(1) Initialisation of the population,

(2) Mutation operation,

(3) Crossover operation,

(4) Evaluation of the population with fitness function,

(5) Selection,

(6) Repetition of step (2) to (5).

Firstly, a random set $\mathbf{X}$ of N_p individuals, encoded as vectors with components made up of integer numbers, is generated in the initialisation step. They form the initial population $\mathbf{X}_{i,G}$, where $i = 1, 2, \ldots, N_p$ indexes the individual within the population and G the generation. Every individual is a vector of integers with the size $1 \times 2N_c$. Thus, an individual has $2N_c$ components $x_{j,i,G}$, indexed with j. N_c denotes the total number of actively controlled pixels in one of the two LC-masks in the dual mask SLM used in the experiments here. Each component can take a (digitised) voltage value corresponding to the phase shift required. The fitness function $f_{fit}(\mathbf{X})$ is programmed to maximise the experimental feedback signal.

Secondly, the mutation operator is implemented such that it randomly selects three individuals $\mathbf{X}_{r_1}$, $\mathbf{X}_{r_2}$, $\mathbf{X}_{r_3}$ and adds the weighted difference of two individuals to the third to form the i-th mutated individual

$$\mathbf{V}_{i,G+1} = \mathbf{X}_{r_3,G} + F \cdot (\mathbf{X}_{r_1,G} - \mathbf{X}_{r_2,G}) \ , \tag{2.38}$$

with the random indices $r_1, r_2, r_3 \in [1, N_p]$ and the condition $i \neq r_1 \neq r_2 \neq r_3$. The process is repeated N_p-times to produce the mutated population $\mathbf{V}_{i,G+1}$. The control parameter $F \in [0, 2]$ is called the scaling factor and controls the differential variation. F is controlled by the user. Note that r_1, r_2 and r_3 are chosen to be different from the running index i. Also, the mutated individual may not be a vector of integers. If this is true, the components are converted to integers first, before the crossover operation is started.

Thirdly, the "new" mutated individual $\mathbf{V}_{i,G+1} = (v_{1,i,G+1}, \ldots, v_{2N_c,i,G+1})$ and the "old" individual of the current population $\mathbf{X}_{i,G} = (x_{1,i,G}, \ldots, x_{2N_c,i,G})$ are subject to crossover on a component-by-component basis (indicated with lower case letters v, x, u) to form the crossover components

$$u_{j,i,G+1} = \begin{cases} v_{j,i,G+1} & \text{if } rand_j\,(0,1) \leq CR \text{ or } j = k\,, \\ x_{j,i,G} & \text{else,} \end{cases} \tag{2.39}$$

where $j = 1, 2, \ldots, 2N_c$ and $k \in [1, 2N_c]$. A uniform random number between 0 and 1, denoted by $rand_j\,(0,1)$, is newly generated at each step j. The crossover rate $CR \in [0, 1]$ is the other user control parameter of DE. The "or $j = k$" condition ensures that the crossover population $\mathbf{U}_{i,G+1}$ gets at least one parameter from $\mathbf{V}_{i,G+1}$. In case that one component $u_{j,i,G+1}$ goes beyond the search space boundary, the algorithm moves to a random integer between $x_{j,i,G}$ and the boundary. The crossover increases the diversity among the individuals and produces trial individuals $\mathbf{U}_{i,G+1} = (u_{1,i,G+1}, \ldots, u_{2N_c,i,G+1})$ that might be part of the next generation population.

Finally, the selection step selects the population for the next generation $G + 1$ by comparing the current individual $\mathbf{X}_{i,G}$ and its corresponding trial individual $\mathbf{U}_{i,G+1}$ using the greedy criterion. The greedy criterion states that a new individual is only accepted, if it maximises the value of the fitness function f_{fit}.

$$\mathbf{X}_{i,G+1} = \begin{cases} \mathbf{U}_{i,G+1} & \text{if } f_{fit}\,(\mathbf{U}_{i,G+1}) \geq f_{fit}\,(\mathbf{X}_{i,G})\ , \\ \mathbf{X}_{i,G} & \text{else.} \end{cases} \tag{2.40}$$

Note that the trial individual is not compared against all current individuals but only one individual, its direct counterpart. So $\mathbf{X}_{i,G}$ has been transformed to the next generation individual $\mathbf{X}_{i,G+1}$ through mutation, crossover and selection. The whole process repeats with this new generation as input until either a certain level of fitness is reached or a pre-set time period has elapsed.

We apply a modified operator in the mutation step (2) that is incorporated in the DE structure described above. This is called trigonometric mutation [52] and aims on speeding up and improving the convergence of the algorithm. Instead of taking the

weighted difference of two individuals (= vectors) and adding it to a third as in equation (2.38), the sum of three weighted vector differentials is added to the centre point of the geometric triangle spanned by these three vectors. The trigonometric mutation operator is rather greedy and can therefore be considered as a local search operator that speeds up the convergence. However, it is prone to converge prematurely and not necessarily to the global optimum. A user-defined control variable allows to set the probability of how often this mutation operator is used during the optimisation compared to the conventional operator. Thus, it is possible to keep a balance between fast convergence and finding the global maximum.

In order to improve the speed and reliability of convergence even more, a modification of DE is introduced, which (1) implements another mutation strategy and (2) self-adaptively adjusts the control parameters F and CR during the optimisation. The algorithm is called self-adaptive differential evolution (acronym used: JADE) [53]. The dynamic updating makes the initial setting of parameters and hence the user interaction obsolete. F and CR undergo natural selection themselves leading to better values and to individuals with a higher probability of survival. Every individual $\mathbf{X}_{i,G}$ is associated with its own control parameters CR_i and F_i rather than a single control parameter for all individuals. JADE combines a greedy mutation strategy with self-adaptive parameter control. The mutation utilises information of a certain percentage of very good individuals from the whole population. This is an advancement of the "best-so-far solution" strategy, where only the best individual propagates to the next stage.

Additionally to JADE, the population size N_p is successively reduced [54]. The advantage of dynamic population sizes is based on the fact that the outcome of the optimisation process is better, if the algorithm searches the search space in an exploiting manner towards the end stages. The aim is to improve the best-so-far individuals without considering weak individuals anymore. The algorithm starts with the full population in an exploration strategy and then gradually reduces the population to move to an exploitation strategy. The population is halved at certain generations during the optimisation by placing the fitter individuals in the first half of the population and deleting the second half.

It has also been shown that the convergence time is reduced by controlling only every n-th pixel with the optimisation algorithm. The phase state of the remaining unaffected pixels is subsequently determined by interpolation. Furthermore, a dynamic change of the number of algorithm-controlled pixels during optimisation is advantageous [55]. It is indicated in the specific experiment later, whether or not these two options have been applied.

The efficiency and robustness of JADE including population size reduction is greatly improved compared to conventional DE, where the choice of control parameters requires human intervention mostly based on experience.

2.4 Optical parametric oscillators

In an optical parametric oscillator, the frequency of a pump wave ω_p is converted by means of a parametric process in a nonlinear medium into two different frequencies ω_s (signal) and ω_i (idler). An OPO consist in its simplest form of a nonlinear crystal to perform the frequency conversion and to offer gain surrounded by two mirrors that build an optical resonator. The great interest in OPO devices originates from the compactness, the broad tunability from the ultra-violet (UV) to the mid-infrared (MIR), the temporal versatility from CW to femtoseconds and the high efficiencies of typically 50% to 90%. Thus, OPOs are an alternative to lasers or sometimes the only option in order to access certain operational regimes. However, there are stringent requirements on the nonlinear media and the pump lasers, which delayed scientific and technological progress in the early days of OPOs. The first demonstration of optical parametric oscillation in 1965 used lithium niobate and a nanosecond visible pump laser and achieved tuning around $1\,\mu\mathrm{m}$ [56]. Publications of OPOs in many operational regimes and with many different nonlinear crystals followed this demonstration, amongst which are the first picosecond SPOPO [57] and the first femtosecond SPOPO [58].

2.4.1 Fundamentals

2.4.1.1 Nonlinear optics

The electrons in a medium are forced into a dipole oscillation and hence become polarised, when an electric field $\mathbf{E}$ is applied to this medium. For weak electric fields the response of the medium is linear $\mathbf{P} = \epsilon_0 \chi^{(1)} \mathbf{E}$, where $\mathbf{P}$ is the polarisation, ϵ_0 the vacuum permittivity and $\chi^{(1)} = n_0^2 - 1$ the linear susceptibility. The linear susceptibility in crystalline media is a tensor, which obeys the symmetry properties of the crystal structure. If the electric field is very intense, the response of the medium is no longer linear and the polarisation must be expanded to a power series about the electric field to

$$\mathbf{P}(t) = \epsilon_0 \left[\chi^{(1)} \mathbf{E}(t) + \chi^{(2)} \mathbf{E}^2(t) + \chi^{(3)} \mathbf{E}^3(t) + \dots \right] , \tag{2.41}$$

where the first term on the right-hand side expresses the linear relation, the second the second-order relation and the third the third-order relation between the incident field $\mathbf{E}$ and the polarisation $\mathbf{P}$ [59, 60]. The second-order term gives rise to optical

phenomena such as second-harmonic generation, sum-frequency generation, the linear electro-optic effect or parametric oscillation, whereas the third-order term induces phenomena such as the Kerr effect, two-photon absorption or Raman scattering. $\chi^{(2)}$ is only non-zero in non-centrosymmetric media (without inversion symmetry), which applies for the crystals used in this thesis. In most other (isotropic) media, $\chi^{(2)}$ vanishes and this is the reason why in silica glasses $\chi^{(3)}$ is the dominating susceptibility, which is important in silica-based optical fibres. Nonlinear optics is closely linked to lasers, and in particular short pulse lasers, that can produce such intense electric fields to overcome the linear response.

A $\chi^{(2)}$ medium must also obey the crystal symmetry structure and therefore becomes a tensor $\chi^{(2)}_{ijk}$ in a non-centrosymmetric crystal (a discussion of crystal structure and nonlinear susceptibility tensors can be found in many textbooks, e.g. [59, 60]). However, if a certain crystal structure, a certain parametric interaction and a certain propagation direction of the involved fields is considered, the tensor character simplifies to a scalar and is typically represented by the effective nonlinear coefficient $d_{eff} = \frac{1}{2}\chi^{(2)}$ comprising the appropriate combination of nonlinear tensor elements.

Considering the combination of two electric fields of the form (c. c. denotes the complex conjugate)

$$E(z,t) = \frac{1}{2}\left(A_1 e^{i(k_1 z - \omega_1 t)} + A_2 e^{i(k_2 z - \omega_2 t)} + \text{c. c.}\right) \tag{2.42}$$

incident to a $\chi^{(2)}$ nonlinear media, the second-order term of equation (2.41) simultaneously produces mixing terms including the optical rectification, the second harmonic, the sum frequency and the difference frequency of the two fields. The dominating and most efficient effect is determined by the phase-matching condition as described in section 2.4.1.2.

The difference frequency generation can also be considered as an optical parametric amplification (OPA) process, where one input photon (signal) triggers the annihilation of one high-energy photon (pump) generating another signal photon and one additional photon (idler) at low energy. This shows that the pump field is depleted, a new field at the idler frequency is generated and the input signal field is amplified in the nonlinear medium. Energy conservation dictates that

$$\omega_p = \omega_s + \omega_i \,. \tag{2.43}$$

The gain that the signal field experiences in an OPA can be significantly enhanced, if the $\chi^{(2)}$ nonlinear crystal is placed in between two or more mirrors to form an optical resonator. The device is then called an optical parametric oscillator. Due to the feedback, it is not necessary to have an input signal photon to trigger the parametric process. A signal wave is generated from noise and grows rapidly in the resonator, when an intense

pump wave is present. An OPO resonator can offer feedback for either the signal or the idler, called singly resonant OPO, or for both, called doubly resonant OPO, depending on the mirror coatings. Singly resonant OPOs are typically easier to operate and more stable, since the additional condition of simultaneous resonance of both the signal and the idler besides the energy and phase-matching conditions must be fulfilled in a doubly resonant OPO. Small perturbations to the spacing of the resonant modes such as fluctuations of the cavity length, the temperature or the pump wavelength lead to amplitude instabilities [61–63]. Singly resonant operation, however, comes at the price of an order of magnitude higher threshold [60, 64], since the other, non-resonant field suffers high losses. This thesis solely deals with singly resonant OPOs for the signal.

2.4.1.2 Phase-matching

For an efficient conversion process and for achieving gain, it is essential that the photon momentum is conserved as well and this is expressed with the phase-matching condition for OPO

$$\Delta k = k_p - k_s - k_i = 0 \,, \tag{2.44}$$

with the wave vector $k_m = 2\pi n_m/\lambda_m$, the refractive index n_m and the wavelength λ_m of the respective waves ($m = p, s, i$). In a collinear arrangement, where all three fields propagate in the same direction, the wave vector can be treated as a scalar quantity, otherwise the vector property must be taken into account. For maximum conversion efficiency a phase-mismatch of $\Delta k = 0$ is required.

In order to obtain $\Delta k = 0$, several techniques have been developed, e.g. birefringent phase-matching (BPM) through angle-tuning or temperature-tuning, where the crystal birefringence is exploited to access appropriate indices of refraction for ordinarily and extraordinarily polarised beams.

BPM shall be discussed in the most simple case of second-harmonic generation (SHG), where the fundamental field with frequency ω is frequency-doubled to the second harmonic field with frequency 2ω. The phase-matching condition in this case requires $2k_\omega = k_{2\omega}$ or after substituting the correct frequencies

$$n(\omega) = n(2\omega) \,, \tag{2.45}$$

which cannot be fulfilled in materials with normal dispersion (refractive index increases with increasing frequency). In birefringent materials the refractive index depends on the polarisation direction of the incident light. It is distinguished between the ordinary and the extraordinary polarisation direction with the refractive indices n_o and n_e, respectively. The angles θ and ϕ and the light propagation direction k with respect to the

crystal axes are depicted in figure 2.7(a), with θ being the angle between k and the z-axis (optic axis) and ϕ being the angle between the x-axis and the projection of k on the xy-plane. The extraordinary refractive index n_e is a function of the angle θ and can be tuned between n_o at $\theta = 0°$ and the minimum n_e at $\theta = 90°$ (denoted with n_E here) as shown in the index ellipse of a negatively uniaxial, i.e. $n_o > n_e$, crystal in figure 2.7(b) [59]. Two waves with perpendicular polarisation propagate along the optic axis z at the same velocity, since both experience the ordinary refractive index, whereas if they propagate in the xy-plane the velocity difference is at a maximum. The angle tuning of the extraordinary index follows the relation

$$n_E(\theta) = \left[\frac{\sin^2\theta}{n_E^2} + \frac{\cos^2\theta}{n_o^2}\right]^{-1/2} , \tag{2.46}$$

which can be inserted in the birefringent phase-matching condition

$$n_o(\omega) = n_e(2\omega, \theta) . \tag{2.47}$$

The condition can now be fulfilled by means of angle tuning as shown in figure 2.8, if the fundamental wave is ordinarily polarised and the second-harmonic wave is extraordinarily polarised. Here, a $800\,\mathrm{nm}$ fundamental wave is frequency-doubled to $400\,\mathrm{nm}$ in a negatively uniaxial crystal by choosing the correct angle θ with respect to the light propagation direction.

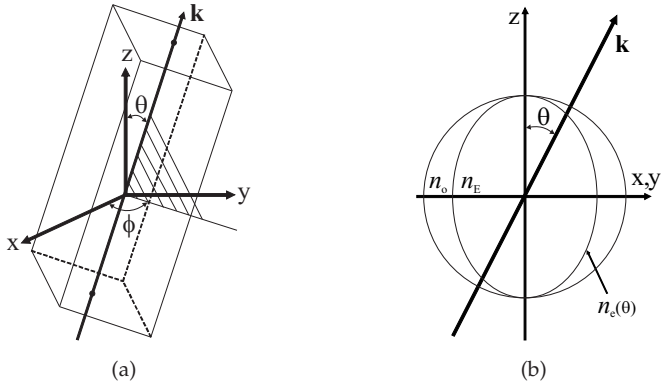

FIGURE 2.7: (a) Definition of crystal axes and phase-matching angles and (b) index ellipse of negatively uniaxial ($n_o > n_e$) birefringent crystal.

There are two choices of polarisations for the interacting waves to achieve phase-matching. In the case of SHG, the two input waves at the fundamental frequency can have the same (type I) or perpendicular (type II) polarisations with the second-harmonic wave having either ordinary or extraordinary polarisation (note that due to energy conservation, it requires two input photons generating one output photon at twice the frequency). In case of an OPO, the situation can be summarised as shown in table 2.2, where e denotes the extraordinary and o the ordinary polarisation.

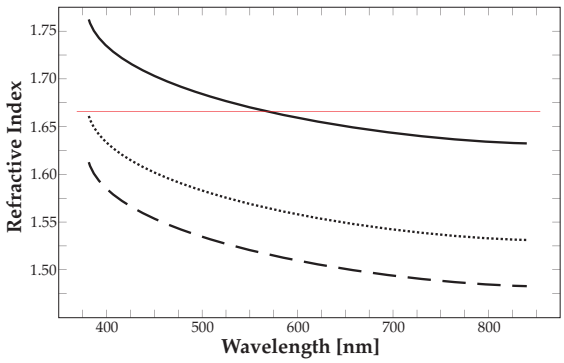

FIGURE 2.8: Dispersion curves for a negatively uniaxial crystal. Phase-matching is achieved by tuning the angle θ to obtain equal refractive indices for the ordinarily polarised fundamental and the extraordinarily polarised second-harmonic wave. n_o = solid curve, $n_e(\theta)$ = dotted curve, min. $n_e(90°)$ = dashed curve.

TABLE 2.2: Type I and type II phase-matching configurations in an OPO with e = extraordinary polarisation and o = ordinary polarisation.

	Pump		Signal		Idler	Crystal Type
Type I	e	$\rightarrow$	o	+	o	neg. birefringent
	o	$\rightarrow$	e	+	e	pos. birefringent
Type II	e	$\rightarrow$	e	+	o	neg. birefringent
	e	$\rightarrow$	o	+	e	neg. birefringent
	o	$\rightarrow$	e	+	o	pos. birefringent
	o	$\rightarrow$	o	+	e	pos. birefringent

The drawback of angle-tuning is a spatial walk-off of the interacting waves, if θ has a value other than $0°$ or $90°$, because the Poynting vector (direction of energy) and the propagation vector k (direction of the wavefront normal) are not parallel for the extraordinary wave. Thus the ordinary and extraordinary field with parallel k vectors walk-off each other inside the medium reducing the interaction length and the conversion efficiency. In order to avoid this, it is possible to exploit the temperature-dependence of the birefringence to set $\theta = 90°$, which is referred to as non-critical phase-matching (NCPM). The refractive indices in the different crystal axes can be derived from the temperature-dependent Sellmeier equations, which are available in the literature for many nonlinear crystals. Practical phase-matching temperatures vary typically between $20°\mathrm{C}$ and $400°\mathrm{C}$ depending on the crystal and interaction type.

Another method for phase-matching is QPM [65, 66]. Here, the nonlinear material is periodically poled such that the sign of the nonlinear coefficient is changed after a propagation distance, where a phase-mismatch of π has accumulated, corresponding to one coherence length $L_c = \pi/\Delta k$. The periodic poling is achieved by applying an electric field above the coercive field strength ($\approx 21\,\mathrm{kV/mm}$ for congruent lithium niobate) to a patterned electrode with period $\Lambda = 2L_c$, which is in contact with the surface of the nonlinear crystal over the entire length. The periodic field experienced by the crystal reverses the electric dipole domain orientation and hence the orientation of the

nonlinear coefficient. Due to the reversal after the phase shift π, the waves become in-phase again and the signal wave keeps growing as indicated in figure 2.9, where the domain reversal is depicted with arrows. The wavelengths of signal and hence idler are mainly determined by this poling period, which typically ranges from $\approx 5\,\mu\mathrm{m}$ for a NIR-to-visible SHG experiment to $\approx 30\,\mu\mathrm{m}$ for a NIR-to-MIR OPO experiment. The phase-matching condition in equation (2.44) must be modified by the poling period wave vector $k_G = 2\pi/\Lambda$ to

$$\Delta k_{QPM} = k_p - k_s - k_i - k_G\,. \tag{2.48}$$

The condition $\Delta k_{QPM} = 0$ can now be fulfilled by engineering of the domain period.

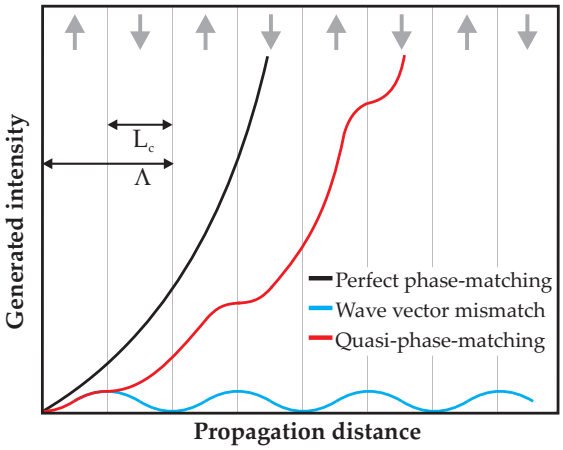

FIGURE 2.9: Generated parametric intensity as a function of propagation distance for the case of perfect phase-matching, quasi-phase-matching and non-phase-matching. L_c is the coherence length and Λ the poling period of the nonlinear material. The domain reversal is indicated with arrows.

An advantageous feature of QPM is that all three waves can have the same polarisation along the z-axis of the poled crystal and that this can be chosen to correspond to the largest tensor element of the effective nonlinear coefficient. It can be shown that for a domain duty cycle of $L_c/\Lambda = 0.5$, the effective nonlinear coefficient is reduced by $2/\pi$ compared to an unpoled crystal [65]. In lithium niobate, for instance, the d_{33}-coefficient with a value of $27\,\mathrm{pm/V}$ is utilised, which reduces to $17\,\mathrm{pm/V}$ after the poling process.

2.4.1.3 Parametric gain

The interaction of the pump wave at frequency ω_p, the signal wave at ω_s and the idler wave at ω_i in an OPO can be described with three coupled-wave equations, which are derived from the fundamental Maxwell equations and the nonlinear wave equation [59, 60, 64]. Each coupled-wave equation describes how the amplitude of one wave varies as a consequence of its coupling to the other two waves. In the simplest case with the approximation of a lossless nonlinear medium, collimated plane waves,

monochromatic waves, CW operation and the steady-state condition, the equations can be written as

$$\frac{dA_p}{dz} = i\frac{\omega_p d_{eff}}{n_p c} A_s A_i e^{-i\Delta kz} , \tag{2.49}$$

$$\frac{dA_s}{dz} = i\frac{\omega_s d_{eff}}{n_s c} A_p A_i^* e^{+i\Delta kz} , \tag{2.50}$$

$$\frac{dA_i}{dz} = i\frac{\omega_i d_{eff}}{n_i c} A_p A_s^* e^{+i\Delta kz} . \tag{2.51}$$

The slowly varying amplitude $A_m(z,t)$ is defined by the electric field

$$E_m(z,t) = A_m(z,t)e^{i(k_m z - \omega_m t)} + \text{c. c.} \tag{2.52}$$

of each involved wave ($m = p, s, i$). All three equations are coupled to each other through the effective nonlinear coefficient d_{eff}.

For perfect phase-matching with $\Delta k = 0$, with the boundary conditions $A_s(0) = \text{arb.}$ and $A_i(0) = 0$ and with the assumption of no pump depletion $dA_p/dz = 0$, the solutions to the coupled-wave equation of the signal and idler are given in the form of hyperbolic functions

$$A_s(z) \propto \cosh(\Gamma z) = \frac{1}{2}\left(e^{\Gamma z} + e^{-\Gamma z}\right) , \tag{2.53}$$

$$A_i(z) \propto \sinh(\Gamma z) = \frac{1}{2}\left(e^{\Gamma z} - e^{-\Gamma z}\right) , \tag{2.54}$$

where

$$\Gamma^2 = \frac{2\omega_s\omega_i d_{eff}^2}{n_s n_i n_p \epsilon_0 c^3} I_p = \frac{8\pi^2 d_{eff}^2}{n_s n_i n_p \epsilon_0 c \lambda_s \lambda_i} I_p \tag{2.55}$$

denotes the parametric gain coefficient and I_p the pump intensity. For a large interaction length z and / or high gain Γ^2, both waves experience exponential growth in the presence of an intense pump wave. In case of $\Delta k \neq 0$, the parametric gain coefficient is reduced according to $g = \sqrt{\Gamma^2 - (\Delta k/2)^2}$.

Based on the relation in (2.53), the single-pass incremental power gain of the signal wave in a nonlinear gain medium of length L at an arbitrary Δk can be derived as [64]

$$G_{inc,s}(L) = \frac{|A_s(L)|^2}{|A_s(0)|^2} - 1 = \Gamma^2 L^2 \frac{\sinh^2(gL)}{g^2 L^2} , \tag{2.56}$$

which becomes $G_{inc,s}(L) = \sinh^2(\Gamma L)$ under the condition of $\Delta k = 0$. OPOs can operate in different gain regimes depending on the magnitude of the parametric gain coefficient [64, 67]. We can re-write the incremental gain in the low gain limit $\Gamma^2 < (\Delta k/2)^2$ to

$$G_{inc,s}(L)\,|_{\text{low gain}} = \Gamma^2 L^2 \frac{\sin^2(g'L)}{g'^2 L^2} = \Gamma^2 L^2 \text{sinc}^2(g'L) \tag{2.57}$$

with $g' = ig = \sqrt{(\Delta k/2)^2 - \Gamma^2}$ and it can be approximated by $G_{inc,s}(L) \approx \Gamma^2 L^2$ for a phase-mismatch of $\Delta k = 0$. In the high gain limit $\Gamma^2 > (\Delta k/2)^2$, equation (2.56) becomes

$$G_{inc,s}(L)\,|_{\text{high gain}} \approx \frac{1}{4} e^{2\Gamma L} \,. \tag{2.58}$$

For completeness, the multiplicative gain in the case of plane waves is given by

$$G_{mult,s}(L) = \frac{|A_s(L)|^2}{|A_s(0)|^2} = 1 + \Gamma^2 L^2 \frac{\sinh^2(gL)}{g^2 L^2} \,, \tag{2.59}$$

which reduces to $G_{mult,s}(L) = \cosh^2(\Gamma L)$ for perfect phase-matching $\Delta k = 0$.

The theoretical treatment of OPO gain above assumes plane waves and CW operation. For a more realistic situation, where the pump and signal beams are focused and have Gaussian characteristics and where pulsed operation occurs, some modifications of the gain equations are required including diffraction and temporal walk-off. Guha derived threshold and efficiency expressions for the case of arbitrary focusing conditions of signal and pump of a singly resonant OPO in CW operation [68]. The results can easily be adapted for the case of plane waves in a collimated beam arrangement. McCarthy and Hanna derived expressions for a singly resonant OPO in pulsed operation, i.e. synchronously pumped, taking a reduced interaction length and a temporal overlap of signal and pump into account [69]. These expressions, however, only apply for the plane wave case. Both treatments were combined by Hanna *et al.* [70] for a synchronously pumped OPO with arbitrary focusing conditions. The final expression for the incremental signal gain is then

$$G^*_{inc,s} = \frac{128\pi^2 d_{eff}^2 l_{eff}}{n_p n_s \lambda_i^2 \lambda_s c \epsilon_0} P_p g_t \xi_s \Re(h_2) \,, \tag{2.60}$$

where l_{eff} is the effective parametric gain length, P_p is the pump power at the pulse peak,

$$\xi_s = \frac{L}{b_s} \tag{2.61}$$

is the signal focusing parameter (confocal parameter defined as $b = 2\pi n w^2/\lambda$ with n, λ and w the refractive index, the wavelength and the waist radius, respectively) and $\Re(h_2)$ is the real part of an integral h_2 describing the focusing conditions as defined in [68]. The parameter $g_t = \sqrt{\tau_p^2/\left(\tau_p^2 + \tau_s^2\right)}$ represents the effect of the Gaussian pulse shapes on the gain with the signal and pump FWHM pulse durations τ_s and τ_p, and the reduced gain length l_{eff} stems from the temporal walk-off between the interacting pulses, both parameters are defined in [69].

2.4.1.4 Signal gain bandwidth and pump acceptance bandwidth

The signal gain bandwidth in the low gain case is defined, where the sinc^2 function of equation (2.57) has its first zero and occurs when the argument $g'L$ equals π [60]

$$\left[\left(\frac{\Delta k}{2}\right)^2 - \Gamma^2\right]^{1/2} \cdot L = \pi \,. \tag{2.62}$$

For low gain such that $\Gamma^2 L^2 \ll \pi^2$, this expression reduces to $\Delta k L/2 = \pi$. Repeating this similarly for the high gain case yields a ratio of high gain to low gain bandwidth of

$$\frac{\Delta\omega_s\,|_{\text{high gain}}}{\Delta\omega_s\,|_{\text{low gain}}} = \sqrt{1 + \frac{\Gamma^2 L^2}{\pi^2}} \,. \tag{2.63}$$

For example, if an OPO has a high gain of $\Gamma^2 L^2 = 400$, the gain bandwidth is a factor of more than 6 higher than the low gain bandwidth. An analytical expression for the signal gain bandwidth can be obtained by expanding the phase-mismatch Δk in the definition of the bandwidth as in equation (2.62) to the second-order and introducing the group velocities at the three interacting waves (details in [60]). The signal gain bandwidth (low gain case), also often referred to as phase-matching bandwidth, then becomes

$$\Delta\omega_{PM} \approx \left|\frac{C}{\mathrm{GVM}_{s,i} \cdot L}\right| \,, \tag{2.64}$$

where $\mathrm{GVM}_{s,i} = 1/v_{g,s} - 1/v_{g,i}$ is the group velocity mismatch of signal and idler. C is a constant value that depends on the definition of the bandwidth. With the definition according to [60] used here, $C = 2\pi$. If the bandwidth is defined as the full width of the conversion efficiency curve, it is $C = 5.56$ [39].

If we are interested in the pump acceptance bandwidth at a fixed signal frequency under which the OPO can be operated, the GVM between signal and idler in equation (2.64) needs to be replaced by the GVM between pump and idler

$$\Delta\omega_{PA} \approx \left|\frac{C}{\mathrm{GVM}_{p,i} \cdot L}\right| \,. \tag{2.65}$$

2.4.1.5 Oscillation threshold

An OPO has a similar threshold behaviour as a laser oscillator, above which the gain overcomes the resonator losses. In the case of arbitrarily focused Gaussian beams and pulsed operation of the OPO, the peak pump power at the oscillation threshold $P^*_{th,p}$ can be calculated by setting $G^*_{inc,s} = \epsilon_s$. The gain $G^*_{inc,s}$ is given in equation (2.60) and ϵ_s denotes the fractional signal power loss per round-trip. The required threshold peak

pump power then becomes

$$P^*_{th,p} = \frac{n_p n_s \lambda_i^2 \lambda_s c \epsilon_0}{128\pi^2 d_{eff}^2 l_{eff}} \frac{\epsilon_s}{g_t \xi_s \Re\left(h_2\right)} \,. \tag{2.66}$$

This is a useful equation to estimate the expected OPO threshold for an assumed (or measured, see section 2.4.1.6) round-trip signal loss. Values of the integral h_2 for different focusing conditions and operating wavelengths are tabulated in [68].

2.4.1.6 Findlay-Clay analysis of resonator loss

In order to reach the oscillation threshold at which the gain equals the loss, it is important to know the exact losses of an OPO resonator. Findlay and Clay developed a method to measure the internal loss of a 4-level laser [71]. This method can be extended to determine the internal loss of an OPO resonator. In a 4-level laser, the relation between the gain exponent and the pump power is usually linear. This only applies for an OPO, if all cavity mirrors have a high reflectivity, i.e. no effective output coupling, and if all other losses are low corresponding to a low gain device. In the high gain regime, the relation of gain and pump power is not linear and the Findlay-Clay method needs to be extended. The experimental procedure involves changing the output coupling mirror with reflectivity R_{OC} and measuring the change of the oscillation threshold power P_{th}. Note that the following analysis applies only to plane waves and not to focused Gaussian beams.

Equating the plane wave multiplicative gain (equation (2.59)) for perfect phase-matching and the resonator loss, we can write an expression at threshold as

$$\cosh^2\left(\Gamma L\right) = \frac{1}{R_{OC} R_C} \,, \tag{2.67}$$

where R_C is the effective reflectivity of all other cavity elements apart from the output coupler.

For a low loss cavity, i.e. $(1 - R_{OC}) \ll 1$ and $(1 - R_C) \ll 1$ and $\Gamma L \ll 1$, equation (2.67) can be rearranged

$$\begin{aligned} \ln\left(\cosh^2\left(\Gamma L\right)\right) &= -\ln R_C - \ln R_{OC} && (2.68)\\ \Gamma^2 L^2 &\approx -\ln R_C - \ln R_{OC} && (2.69)\\ K P_{th} &\approx -\ln R_C - \ln R_{OC} \,, && (2.70) \end{aligned}$$

where $K P_{th}$ replaces $\Gamma^2 L^2$, because the parametric gain coefficient Γ^2 is proportional to the pump intensity I_p and thus the pump power P_p. K is a simple proportionality constant. It is now possible to obtain a value for the effective cavity reflectivity R_C

by plotting $-\ln R_{OC}$ as a function of P_{th}. The gradient of the linear curve of equation (2.70) is K and the ordinate intercept is $\ln R_C$. The effective loss of the cavity is then $1 - R_C$. This corresponds to the original Findlay-Clay analysis.

For a cavity that has higher losses, for example due to a large output coupling transmission, the accurate equation (2.68) must be used, where ΓL is replaced by $\sqrt{KP_{th}}$. The plot is no longer linear, however the effective cavity loss can still be obtained from the ordinate intercept $\ln R_C$.

2.4.2 Nonlinear crystals

2.4.2.1 Periodically poled lithium niobate

For the experiments with QPM nonlinear materials, periodically poled lithium niobate (PPLN) was used in this thesis due to its mature producibility and because it is cheaply and widely available. Lithium niobate, $LiNbO_3$, was one of the first crystal materials designed for nonlinear optics applications in the 1960s, for example in the first OPO demonstration by Giordmaine and Miller [56], but was later replaced by more damage-resistant and more effective materials such as KTP, LBO and BBO. It is a negatively uniaxial ($n_e < n_o$) ferroelectric crystal with a transparency range from $\approx 0.4\,\mu\mathrm{m}$ to $\approx 4.5\,\mu\mathrm{m}$ and large nonlinear tensor elements up to $27\,\mathrm{pm/V}$ (congruent) and $42\,\mathrm{pm/V}$ (stoichiometric) [72]. Lithium niobate had its renaissance in the 1990s when it was successfully periodically poled to be used as a QPM material with very attractive features. These include the freedom of choosing the polarisation of the interacting waves, mostly $e \rightarrow e + e$, the accessed tensor elements of the nonlinear coefficient for maximum gain (up to $17\,\mathrm{pm/V}$), the non-critical phase-matching of almost any nonlinear interaction without the confinement of dispersion and birefringence, as well as a higher damage threshold due to reduced photo-refraction (see below). Good reviews of PPLN and its application in OPOs were published from the Stanford University group, for instance Myers *et al.* [61, 73, 74]. PPLN crystals with a thickness of up to $2\,\mathrm{mm}$ are commercially available with multiple, fan out, cascaded or aperiodic gratings in one device. The poling of larger thicknesses is technologically challenging due to the electric fields that have to be applied, which must exceed the coercive field strength of $21\,\mathrm{kV/mm}$ in congruent lithium niobate, but only $2\,\mathrm{kV/mm}$ for stoichiometric lithium niobate. A microscope image of a multiple-grating PPLN sample is depicted in figure 2.10.

Wavelength tuning of a QPM crystal such as PPLN is conveniently performed by translating a multiple-grating crystal up or down so that the pump beam enters different poling periods. For a fixed pump wavelength, the signal and idler wavelengths are then determined by the quasi-phase-matching condition of equation (2.48). The poling

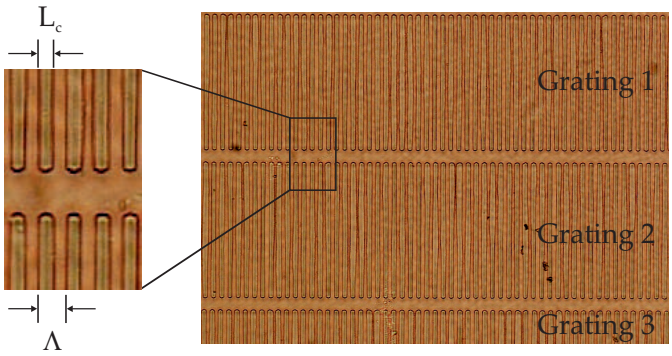

FIGURE 2.10: Microscope image of a multiple-grating PPLN sample showing three different gratings with periods of around $30\,\mu\mathrm{m}$.

periods range from $25\,\mu\mathrm{m}$ to $32\,\mu\mathrm{m}$ in a typical OPO experiment with a pump at $1\,\mu\mathrm{m}$, a signal at around $1.5\,\mu\mathrm{m}$ and the corresponding idler in the MIR. Continuous tuning is achieved by additional temperature variation or alternatively by the application of a PPLN device with a fan out structure rather than stacked discrete gratings.

Lithium niobate suffers from the photo-refractive effect [59, 75, 76], which is induced by a spatially varying light intensity leading to free carriers in the crystal medium through photo-ionisation. The free carriers generate an electric field, which in turn generates a refractive index variation via the linear electro-optic effect. Photo-refraction generally leads to a compromised OPO performance (reduced conversion efficiency, higher threshold, degraded beam quality, temporal instabilities) or even crystal damage and is stronger at visible wavelengths. A further damage effect is green-induced infrared absorption (GRIIRA) [77, 78], where absorption in the IR is induced by visible light. The visible light can stem from the parasitic non-phase-matched second harmonic of the pump in a NIR-pumped OPO or from the pump directly in a visible-pumped OPO. GRIIRA originates from colour centre creation, crystal impurities (mainly iron ions) and intrinsic defects (niobium ions occupying lithium sites). The absorbed energy is converted to heat and thus causes thermal problems like thermal lensing, resonator instabilities or a degraded beam quality. Both effects are usually reversible, but can lead to permanent damage depending on the particular operating conditions. One way to reduce the photo-refractive effect is the operation of the crystal at elevated temperature so that the free charge carriers causing the refractive index perturbation are diffused [73]. Typical operating temperatures are between $100^{\circ}\mathrm{C}$ and $200^{\circ}\mathrm{C}$. Another measure mitigating both photo-refraction and GRIIRA, is the doping of lithium niobate with magnesium oxide (MgO), which increases the photo-conductivity of the crystal structure hundredfold [79–81]. The niobium anti-site defects are reduced, because magnesium ions replace these niobium ions in the lattice structure. MgO-doping with a concentration of typically 5% allows for room-temperature operation and increases the transparency range especially in the MIR up to $\approx 5.5\,\mu\mathrm{m}$ [82]. Furthermore, investigations with stoichiometric and congruent PPLN and periodically poled lithium tantalate

(PPLT) have shown that stoichiometric crystals, i.e. with a balanced concentration of lithium and niobium ions, have significantly reduced optical damage thresholds with stoichiometric PPLT being the most suited material to avoid photo-refraction and GRIIRA [81, 83].

Not much research has been undertaken with pulsed OPO devices based on MgO:PPLN and pumped at multi-Watt average power levels in the visible due to the mentioned damage effects. Green-pumped CW OPOs [84, 85] and frequency-doubling [86] experiments have been reported using MgO:PPLN with Watt-level pump powers, but no pulsed systems.

2.4.2.2 Lithium triborate

Lithium triborate (LBO) is an attractive alternative to PPLN for visible-pumped OPOs, since it does not suffer from photo-refraction and GRIIRA and has better optical damage properties. LBO with the chemical formula LiB_3O_5 is negatively biaxial, suitable for type I and type II NCPM and transparent from around $160\,\mathrm{nm}$ to $3.2\,\mu\mathrm{m}$. Furthermore, it has a high optical damage threshold of $> 10\,\mathrm{GW/cm^2}$, a large spectral acceptance bandwidth and a low group velocity dispersion. For a type I interaction $e \rightarrow o + o$ in the xy-plane with $\theta = 90°$, the effective nonlinear coefficient of LBO is $d_{eff} = d_{32}\cos\phi$, where $d_{32} = 1.17\,\mathrm{pm/V}$. If the crystal is cut such that the beams propagate along the x-axis, $\phi = 0°$ and hence $d_{eff} = d_{32}$ is at its maximum. However, this value is significantly lower than the highest value accessible with PPLN of $d_{eff} = 17\,\mathrm{pm/V}$.

There is a large number of publications of nonlinear frequency conversion experiments using LBO including demonstrations of OPOs pumped in the visible in the nanosecond [87], picosecond [63, 88–91] and femtosecond [92] regime with average output powers from hundreds of mW to several Watts. Thus, LBO is a well-proven nonlinear medium for a wide range of OPO operational regimes.

2.4.3 Typical resonator configurations

The OPOs described in this thesis are all synchronously pumped by a train of ultrashort pulses, which means that the resonating signal pulse experiences gain as it coincides with a pump pulse inside the nonlinear crystal. This requires that the signal pulse repetition rate matches the pump pulse repetition rate.

A schematic diagram of a synchronously pumped OPO (SPOPO) in a bow-tie standing-wave configuration is shown in figure 2.11. The resonator consists of two plane mirrors (M) and two curved mirrors (CM). The curved mirrors generate a beam waist for the

resonating signal beam in the centre of the nonlinear crystal. Optimum operation of an OPO is typically obtained with confocal focusing of the signal beam described by a focusing parameter $\xi_s = 1$ (see equation (2.61)). In this condition, the product of intensity and interaction length is maximised and leads to maximum gain and efficiency. In order to yield $\xi_p = 1$ as well, a lens with a focal length of typically $100\,\mathrm{mm}$ to $200\,\mathrm{mm}$ is used to focus the pump beam into the crystal. The additional two plane mirrors allow for simple discrimination of the three beams at different wavelengths but also for independent adjustment of the cavity length to achieve synchronism.

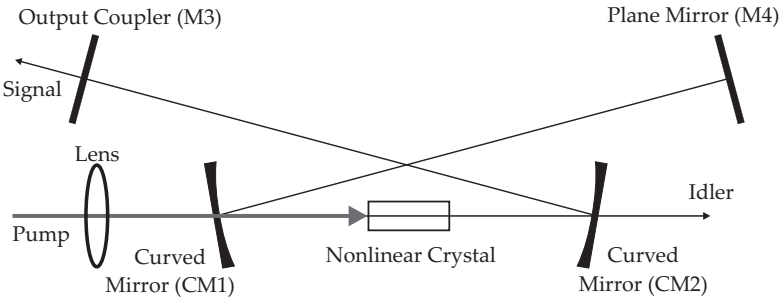

FIGURE 2.11: Synchronously pumped OPO in a bow-tie, standing-wave configuration. The poling period of the nonlinear crystal mainly determines the signal and thus the idler wavelength. The curved mirrors (CM) and the plane mirrors (M) are highly reflective for the signal. M 3 acts as the signal output coupler (OC). The idler is not oscillating in the resonator and is transmitted through CM 2. The pump beam is focused into the nonlinear crystal with a lens.

Depending on the mirror coatings, an SPOPO can be singly resonant or doubly resonant as described in section 2.4.1.1. Because of the convenience of singly resonant OPOs as described earlier and the sufficiently high pump powers available, the SPOPOs described in this thesis are all singly resonant for the signal wave. The curved mirrors and the plane mirror M 4 have coatings such that they are highly reflective for the signal tuning range, but highly transmissive for the pump and idler. Therefore, the idler output coupling is obtained predominantly from CM 2. The mirror M 3 is the output coupler (OC) for the signal and is interchangeable according to the required output coupling transmission for optimum efficiency.

In a standing-wave configuration as in figure 2.11, each signal pulse passes twice through the crystal per resonator round-trip. This leads to increased losses because the signal pulse, after returning from the resonator arm with the OC, passes through the crystal without a new pump pulse present and thus is not amplified but suffers from Fresnel reflection loss. The signal pulse is amplified only after returning from the arm with mirror M 4, when a new pump pulse has arrived at the crystal. It is therefore important to use nonlinear crystals with good anti-reflection coatings to minimise signal loss. An improved resonator setup is a ring cavity, where the beam follows the sequence 'crystal – CM 2 – M 3 – M 4 – CM 1 – crystal' rather than travelling back and forth in the bow-tie arms. The single pass of each signal pulse through the crystal per round-trip leads to a reduced loss and a correspondingly lower threshold. However,

the alignment is complicated since the plane mirrors can not simply be translated along the beam direction for cavity length fine tuning.

Wavelength tuning is typically achieved either by changing the pump wavelength, by changing the crystal temperature (QPM and BPM), by changing the crystal angle (BPM) or by changing the period of the crystal (QPM). For reasons of temperature tuning and mitigation of photo-refraction, the nonlinear crystal is often held in an oven at elevated temperature.

Other resonator designs with fewer degrees of freedom (cavity length, wavelength discrimination) but with improved stability and compactness include monolithic cavities with the mirrors directly coated onto the crystal end-facets, semi-monolithic cavities with one discrete mirror (often in a V-cavity layout) and linear cavities with two discrete plane and / or curved mirrors. Another development is the insertion of a nonlinear crystal into the pump laser resonator utilising the laser resonator mirrors for the OPO as well.

2.5 Conclusions

In this chapter, we reviewed the theoretical and technological background of the work that is presented in this thesis. It begins with an introduction to fibre laser and amplifier systems for the generation and amplification of ultrashort pulses at high pulse energy and average power including the mode-locking principle, the gain-switching technique, ultrashort pulse propagation in optical fibres, specialty doped amplifier fibres (LMA, PCF or double-clad structures) as well as chirped pulses amplification. The concept of femtosecond pulse shaping in liquid-crystal-based spatial light modulators was described in the following section. In such devices the amplitude and phase of a spectrally dispersed pulse can be controlled to generate arbitrary pulse shapes. Computer-based optimisation algorithms used in a feedback loop for adaptive pulse shaping were described, particularly the differential evolution algorithm, which is part of the family of genetic algorithms. In the final section, we introduced the theory of nonlinear optics with the emphasis on optical parametric oscillation. Phase-matching, paramatric gain, gain bandwidth, oscillation threshold and a resonator loss estimation were described. The two nonlinear crystals used in this thesis, namely PPLN and LBO, were then discussed, followed by typical resonator configurations of synchronously pumped OPOs.

References

[1] H. A. Haus, "Mode-locking of lasers," IEEE Journal of Selected Topics in Quantum Electronics **6**(6), 1173–1185 (2000).

[2] T. Brabec, C. Spielmann, P. F. Curley, and F. Krausz, "Kerr lens mode locking," Opt. Lett. **17**(18), 1292–1294 (1992).

[3] D. E. Spence, P. N. Kean, and W. Sibbett, "60-fsec pulse generation from a self-mode-locked Ti:sapphire laser," Opt. Lett. **16**(1), 42–44 (1991).

[4] U. Keller, K. J. Weingarten, F. X. Kärtner, D. Kopf, B. Braun, I. D. Jung, R. Fluck, C. Hönninger, N. Matuschek, and J. Aus der Au, "Semiconductor saturable absorber mirrors (SESAM's) for femtosecond to nanosecond pulse generation in solid-state lasers," IEEE Journal of Selected Topics in Quantum Electronics **2**(3), 435–453 (1996).

[5] E. P. Ippen, H. A. Haus, and L. Y. Liu, "Additive pulse mode locking," J. Opt. Soc. Am. B **6**(9), 1736–1745 (1989).

[6] M. E. Fermann, M. J. Andrejco, Y. Silberberg, and M. L. Stock, "Passive mode locking by using nonlinear polarization evolution in a polarization-maintaining erbium-doped fiber," Opt. Lett. **18**(11), 894 (1993).

[7] H. Ito, H. Yokoyama, S. Murata, and H. Inaba, "Generation of picosecond optical pulses with highly RF modulated AlGaAs DH laser," IEEE Journal of Quantum Electronics **17**(5), 663–670 (1981).

[8] K. Y. Lau, "Gain switching of semiconductor injection lasers," Applied Physics Letters **52**(4), 257–259 (1988).

[9] A. Piper, "The Development Of High Power, Pulsed Fiber Laser Systems And Their Applications," Ph.D. thesis, Optoelectronics Research Centre, University of Southampton, Southampton (2005).

[10] S. Backus, C. G. Durfee, M. M. Murnane, and H. C. Kapteyn, "High power ultrafast lasers," Review of Scientific Instruments **69**(3), 1207–1223 (1998).

[11] R. Paschotta, J. Nilsson, A. C. Tropper, and D. C. Hanna, "Ytterbium-doped fiber amplifiers," IEEE Journal of Quantum Electronics **33**(7), 1049–1056 (1997).

[12] A. E. Siegman, *Lasers*, 1st ed. (University Science Books, Sausalito, California, 1986).

[13] J. Limpert, F. Röser, T. Schreiber, and A. Tünnermann, "High-Power Ultrafast Fiber Laser Systems," IEEE Journal of Selected Topics in Quantum Electronics **12**(2), 233–244 (2006).

[14] N. G. R. Broderick, H. L. Offerhaus, D. J. Richardson, R. A. Sammut, J. Caplen, and L. Dong, "Large Mode Area Fibers for High Power Applications," Optical Fiber Technology **5**(2), 185–196 (1999).

[15] J. Limpert, F. Röser, D. N. Schimpf, E. Seise, T. Eidam, S. Hädrich, J. Rothhardt, C. J. Misas, and A. Tünnermann, "High Repetition Rate Gigawatt Peak Power Fiber Laser-Systems: Challenges, Design, and Experiment," IEEE Journal of Selected Topics in Quantum Electronics **15**(1), 159–169 (2009).

[16] G. P. Agrawal, *Nonlinear Fiber Optics*, Optics and Photonics, 3rd ed. (Academic Press, San Diego, 2001).

[17] E. Snitzer, H. Po, F. Hakimi, R. Tumminelli, and B. C. McCollum, "Double clad, offset core Nd fiber laser," in *Optical Fiber Sensors*, vol. PD5 (New Orleans, LA, USA, 1988).

[18] L. Zenteno, "High-power double-clad fiber lasers," Journal of Lightwave Technology **11**(9), 1435–1446 (1993).

[19] R. Trebino, *Frequency-Resolved Optical Gating: The Measurement of Ultrashort Laser Pulses*, 1st ed. (Kluwer Academic Publishers, Boston, 2002).

[20] M. D. Perry, T. Ditmire, and B. C. Stuart, "Self-phase modulation in chirped-pulse amplification," Opt. Lett. **19**(24), 2149–2151 (1994).

[21] P. S. J. Russell, "Photonic Crystal Fibers," Science **299**(5605), 358–362 (2003).

[22] J. C. Knight, J. Arriaga, T. A. Birks, A. Ortigosa-Blanch, W. J. Wadsworth, and P. S. J. Russell, "Anomalous dispersion in photonic crystal fiber," IEEE Photonics Technology Letters **12**(7), 807–809 (2000).

[23] T. A. Birks, J. C. Knight, and P. S. J. Russell, "Endlessly single-mode photonic crystal fiber," Opt. Lett. **22**(13), 961–963 (1997).

[24] D. Strickland and G. Mourou, "Compression of amplified chirped optical pulses," Optics Communications **56**(3), 219–221 (1985).

[25] E. B. Treacy, "Optical pulse compression with diffraction gratings," IEEE Journal of Quantum Electronics **5**(9), 454–458 (1969).

[26] J. Limpert, T. Clausnitzer, A. Liem, T. Schreiber, H. J. Fuchs, H. Zellmer, E. B. Kley, and A. Tünnermann, "High-average-power femtosecond fiber chirped-pulse amplification system," Opt. Lett. **28**(20), 1984–1986 (2003).

[27] F. He, H. S. S. Hung, J. H. V. Price, N. K. Daga, N. A. Naz, J. Prawiharjo, D. C. Hanna, D. P. Shepherd, D. J. Richardson, J. W. Dawson, C. W. Siders, and C. P.

Barty, "High energy femtosecond fiber chirped pulse amplification system with adaptive phase control," Opt. Express **16**(8), 5813–5821 (2008).

[28] G. Imeshev, I. Hartl, and M. E. Fermann, "Chirped pulse amplification with a nonlinearly chirped fiber Bragg grating matched to the Treacy compressor," Opt. Lett. **29**(7), 679–681 (2004).

[29] N. G. R. Broderick, D. J. Richardson, D. Taverner, J. E. Caplen, L. Dong, and M. Ibsen, "High-power chirped-pulse all-fiber amplification system based on large-mode-area fiber gratings," Opt. Lett. **24**(8), 566–568 (1999).

[30] J. H. V. Price, "The Development of High Power, Pulsed Fiber Laser Systems and their Applications," Ph.D. thesis, Optoelectronics Research Centre, University of Southampton, Southampton (2003).

[31] R. L. Fork, C. H. B. Cruz, P. C. Becker, and C. V. Shank, "Compression of optical pulses to six femtoseconds by using cubic phase compensation," Opt. Lett. **12**(7), 483–485 (1987).

[32] O. E. Martinez, "3000 Times Grating Compressor with Positive Group Velocity Dispersion: Application to Fiber Compensation in 1.3-1.6μm Region," IEEE Journal of Quantum Electronics **23**(1), 59–64 (1987).

[33] A. M. Weiner, "Femtosecond pulse shaping using spatial light modulators," Review of Scientific Instruments **71**(5), 1929–1960 (2000).

[34] P. Tournois, "Acousto-optic programmable dispersive filter for adaptive compensation of group delay time dispersion in laser systems," Optics Communications **140**(4-6), 245–249 (1997).

[35] F. Verluise, V. Laude, Z. Cheng, C. Spielmann, and P. Tournois, "Amplitude and phase control of ultrashort pulses by use of an acousto-optic programmable dispersive filter: pulse compression and shaping," Opt. Lett. **25**(8), 575–577 (2000).

[36] T. Tanabe, K. Ohno, T. Okamoto, M. Yamanaka, and F. Kannari, "Feedback control for accurate shaping of ultrashort optical pulses prior to chirped pulse amplification," Japanese Journal of Applied Physics Part 1-Regular Papers Short Notes & Review Papers **43**(4A), 1366–1375 (2004).

[37] A. M. Weiner, "Femtosecond Optical Pulse Shaping and Processing," Progress in Quantum Electronics **19**(3), 161–237 (1995).

[38] R. N. Thurston, J. P. Heritage, A. M. Weiner, and W. J. Tomlinson, "Analysis of Picosecond Pulse Shape Synthesis by Spectral Masking in a Grating Pulse Compressor," IEEE Journal of Quantum Electronics **22**(5), 682–696 (1986).

[39] H. S. S. Hung, "An Adaptive Mid-Infrared Ultrashort Pulse Source for Applications in Coherent Control," Ph.D. thesis, Optoelectronics Research Centre, University of Southampton, Southampton (2008).

[40] C. E. Shannon, "Communication in the Presence of Noise," Proceedings of the IRE **37**(1), 10–21 (1949).

[41] G. Stobrawa, M. Hacker, T. Feurer, D. Zeidler, M. Motzkus, and F. Reichel, "A new high-resolution femtosecond pulse shaper," Applied Physics B: Lasers and Optics **72**(5), 627–630 (2001).

[42] J. Vaughan, T. Feurer, K. Stone, and K. Nelson, "Analysis of replica pulses in femtosecond pulse shaping with pixelated devices," Opt. Express **14**(3), 1314–1328 (2006).

[43] D. N. Schimpf, E. Seise, T. Eidam, J. Limpert, and A. Tünnermann, "Control of the optical Kerr effect in chirped-pulse-amplification systems using model-based phase shaping," Opt. Lett. **34**(24), 3788–3790 (2009).

[44] K. Ohno, T. Tanabe, and F. Kannari, "Adaptive pulse shaping of phase and amplitude of an amplified femtosecond pulse laser by direct reference to frequency-resolved optical gating traces," J. Opt. Soc. Am. B **19**(11), 2781–2790 (2002).

[45] F. G. Omenetto, A. J. Taylor, M. D. Moores, and D. H. Reitze, "Adaptive control of femtosecond pulse propagation in optical fibers," Opt. Lett. **26**(12), 938–940 (2001).

[46] J. Prawiharjo, N. K. Daga, R. Geng, J. H. Price, D. C. Hanna, D. J. Richardson, and D. P. Shepherd, "High fidelity femtosecond pulses from an ultrafast fiber laser system via adaptive amplitude and phase pre-shaping," Opt. Express **16**(19), 15,074–15,089 (2008).

[47] S. Kirkpatrick, J. Gelatt, C. D., and M. P. Vecchi, "Optimization by Simulated Annealing," Science **220**(4598), 671–680 (1983).

[48] D. E. Goldberg, *Genetic Algorithms in Search, Optimization and Machine Learning* (Addison-Wesley Longman Publishing Co., Inc., Boston, 1989).

[49] R. Storn and K. Price, "Differential evolution – A simple and efficient heuristic for global optimization over continuous spaces," Journal of Global Optimization **11**(4), 341–359 (1997).

[50] A. Efimov, M. D. Moores, B. Mei, J. L. Krause, C. W. Siders, and D. H. Reitze, "Minimization of dispersion in an ultrafast chirped pulse amplifier using adaptive learning," Applied Physics B: Lasers and Optics **70**(0), S133–S141 (2000).

[51] M. M. Ali, C. Khompatraporn, and Z. B. Zabinsky, "A numerical evaluation of several stochastic algorithms on selected continuous global optimization test problems," Journal of Global Optimization **31**(4), 635–672 (2005).

[52] H. Y. Fan and J. Lampinen, "A trigonometric mutation operation to differential evolution," Journal of Global Optimization **27**(1), 105–129 (2003).

[53] J. Zhang and A. C. Sanderson, "JADE: Self-adaptive differential evolution with fast and reliable convergence performance," in *IEEE Congress on Evolutionary Computation (CEC 2007)*, pp. 2251–2258 (2007).

[54] J. Brest and M. S. Maučec, "Population size reduction for the differential evolution algorithm," Applied Intelligence **29**(3), 228–247 (2008).

[55] R. Mizoguchi, K. Onda, S. S. Kano, and A. Wada, "Thinning-out in optimized pulse shaping method using genetic algorithm," Review of Scientific Instruments **74**(5), 2670–2674 (2003).

[56] J. A. Giordmaine and R. C. Miller, "Tunable Coherent Parametric Oscillation in $LiNbO_3$ at Optical Frequencies," Physical Review Letters **14**(24), 973 (1965).

[57] A. Piskarskas, V. Smil'gyavichyus, and A. Umbrasas, "Continuous parametric generation of picosecond light pulses," Soviet Journal of Quantum Electronics **18**(2), 155 (1988).

[58] D. C. Edelstein, E. S. Wachman, and C. L. Tang, "Broadly tunable high repetition rate femtosecond optical parametric oscillator," Applied Physics Letters **54**(18), 1728–1730 (1989).

[59] R. W. Boyd, *Nonlinear Optics*, 2nd ed. (Academic Press, San Diego, 2002).

[60] R. L. Byer, "Parametric Oscillators and Nonlinear Materials," in *Nonlinear Optics*, P. G. Harper and B. S. Wherrett, eds., chap. 2, pp. 47–117 (Academic Press, New York, 1977).

[61] L. E. Myers and W. R. Bosenberg, "Periodically Poled Lithium Niobate and Quasi-Phase-Matched Optical Parametric Oscillators," IEEE Journal of Quantum Electronics **33**(10), 1663–1672 (1997).

[62] A. J. Henderson, M. J. Padgett, F. G. Colville, J. Zhang, and M. H. Dunn, "Doubly-resonant optical parametric oscillators: tuning behaviour and stability requirements," Optics Communications **119**(1-2), 256–264 (1995).

[63] S. D. Butterworth, S. Girard, and D. C. Hanna, "High-power, broadly tunable all-solid-state synchronously pumped lithium triborate optical parametric oscillator," J. Opt. Soc. Am. B **12**(11), 2158–2167 (1995).

[64] R. L. Byer and R. L. Herbst, "Parametric Oscillation and Mixing," in *Nonlinear Infrared Generation*, Y. R. Shen, ed., vol. 16 of *Topics in Applied Physics*, chap. 3, pp. 81–137 (Springer, Berlin, 1977).

[65] R. L. Byer, "Quasi-phasematched nonlinear interactions and devices," Journal of Nonlinear Optical Physics & Materials **6**(4), 549–592 (1997).

[66] M. M. Fejer, G. A. Magel, D. H. Jundt, and R. L. Byer, "Quasi-Phase-Matched Second Harmonic Generation: Tuning and Tolerances," IEEE Journal of Quantum Electronics **28**(11), 2631–2654 (1992).

[67] M. Ebrahim-Zadeh, "Mid-Infrared Ultrafast and Continuous-Wave Optical Parametric Oscillators," in *Solid-State Mid-Infrared Laser Sources*, vol. 89 of *Topics in Applied Physics*, pp. 184–224 (Springer, Berlin / Heidelberg, 2003).

[68] S. Guha, "Focusing dependence of the efficiency of a singly resonant optical parametric oscillator," Applied Physics B: Lasers and Optics **66**(6), 663–675 (1998).

[69] M. J. McCarthy and D. C. Hanna, "All-solid-state synchronously pumped optical parametric oscillator," J. Opt. Soc. Am. B **10**(11), 2180 (1993).

[70] D. C. Hanna, M. V. O'Connor, M. A. Watson, and D. P. Shepherd, "Synchronously pumped optical parametric oscillator with diffraction-grating tuning," Journal of Physics D-Applied Physics **34**(16), 2440–2454 (2001).

[71] D. Findlay and R. A. Clay, "The measurement of internal losses in 4-level lasers," Physics Letters **20**(3), 277–278 (1966).

[72] D. N. Nikogosyan, *Nonlinear optical crystals: a complete survey*, 1st ed. (Springer, Berlin / Heidelberg, 2005).

[73] L. E. Myers, R. C. Eckardt, M. M. Fejer, R. L. Byer, W. R. Bosenberg, and J. W. Pierce, "Quasi-phase-matched optical parametric oscillators in bulk periodically poled $LiNbO_3$," J. Opt. Soc. Am. B **12**(11), 2102–2116 (1995).

[74] L. E. Myers, R. C. Eckardt, M. M. Fejer, R. L. Byer, and W. R. Bosenberg, "Multigrating quasi-phase-matched optical parametric oscillator in periodically poled $LiNbO_3$," Opt. Lett. **21**(8), 591–593 (1996).

[75] A. Ashkin, G. D. Boyd, J. M. Dziedzic, R. G. Smith, A. A. Ballman, J. J. Levinstein, and K. Nassau, "Optically-induced refractive index inhomogeneities in $LiNbO_3$ and $LiTaO_3$," Applied Physics Letters **9**(1), 72–74 (1966).

[76] F. Jermann, M. Simon, and E. Krätzig, "Photorefractive properties of congruent and stoichiometric lithium niobate at high light intensities," J. Opt. Soc. Am. B **12**(11), 2066–2070 (1995).

[77] Y. Furukawa, K. Kitamura, A. Alexandrovski, R. K. Route, M. M. Fejer, and G. Foulon, "Green-induced infrared absorption in MgO doped $LiNbO_3$," Applied Physics Letters **78**(14), 1970–1972 (2001).

[78] R. G. Batchko, D. R. Weise, T. Plettner, G. D. Miller, M. M. Fejer, and R. L. Byer, "Continuous-wave 532-nm-pumped singly resonant optical parametric oscillator based on periodically poled lithium niobate," Opt. Lett. **23**(3), 168–170 (1998).

[79] D. A. Bryan, R. Gerson, and H. E. Tomaschke, "Increased optical damage resistance in lithium niobate," Applied Physics Letters **44**(9), 847–849 (1984).

[80] M. Nakamura, M. Kotoh, H. Taniguchi, and K. Tadatomo, "Bulk periodically poled MgO-doped $LiNbO_3$ by external electric field application," Japanese Journal of Applied Physics Part 2-Letters **38**(5A), L512–L514 (1999).

[81] M. Nakamura, S. Higuchi, S. Takekawa, K. Terabe, Y. Furukawa, and K. Kitamura, "Optical damage resistance and refractive indices in near-stoichiometric MgO-doped $LiNbO_3$," Japanese Journal of Applied Physics Part 2-Letters **41**(1AB), L49–L51 (2002).

[82] T. Andres, P. Haag, S. Zelt, J. P. Meyn, A. Borsutzky, R. Beigang, and R. Wallenstein, "Synchronously pumped femtosecond optical parametric oscillator of congruent and stoichiometric MgO-doped periodically poled lithium niobate," Applied Physics B: Lasers and Optics **76**(3), 241–244 (2003).

[83] K. Kitamura, Y. Furukawa, S. Takekawa, T. Hatanaka, H. Ito, and V. Gopalan, "Non-stoichiometric control of $LiNbO_3$ and $LiTaO_3$ in ferroelectric domain engineering for optical devices," in *5th European Conference on Applications of Polar Dielectrics (ECAPD-V)*, pp. 235–243 (Jurmala, Latvia, 2000).

[84] S. Zaske, D. H. Lee, and C. Becher, "Green-pumped cw singly resonant optical parametric oscillator based on MgO:PPLN with frequency stabilization to an atomic resonance," Applied Physics B: Lasers and Optics **98**(4), 729–735 (2010).

[85] D.-H. Lee, S. K. Kim, S.-N. Park, H. Su Park, J. Y. Lee, and S.-K. Choi, "Continuous-wave 532nm pumped MgO:PPLN optical parametric oscillator with external power regulation and spatial mode filtering," Appl. Opt. **48**(1), 37–42 (2009).

[86] H. Furuya, A. Morikawa, K. Mizuuchi, and K. Yamamoto, "High-beam-quality continuous wave 3 W green-light generation in bulk periodically poled MgO:$LiNbO_3$," Japanese Journal of Applied Physics Part 1-Regular Papers Brief Communications & Review Papers **45**(8B), 6704–6707 (2006).

[87] Y. Cui, M. H. Dunn, C. J. Norrie, W. Sibbett, B. D. Sinclair, Y. Tang, and J. A. C. Terry, "All-solid-state optical parametric oscillator for the visible," Opt. Lett. **17**(9), 646–648 (1992).

[88] M. Jurna, J. P. Korterik, H. L. Offerhaus, and C. Otto, "Noncritical phase-matched lithium triborate optical parametric oscillator for high resolution coherent anti-Stokes Raman scattering spectroscopy and microscopy," Applied Physics Letters **89**(25), 251,116–3 (2006).

[89] T. W. Tukker, C. Otto, and J. Greve, "Design, optimization, and characterization of a narrow-bandwidth optical parametric oscillator," J. Opt. Soc. Am. B **16**(1), 90–95 (1999).

[90] J. D. Kafka, M. L. Watts, and J. W. Pieterse, "Synchronously pumped optical parametric oscillators with LiB_3O_5," J. Opt. Soc. Am. B **12**(11), 2147–2157 (1995).

[91] K. Kieu, B. G. Saar, G. R. Holtom, X. S. Xie, and F. W. Wise, "High-power picosecond fiber source for coherent Raman microscopy," Opt. Lett. **34**(13), 2051–2053 (2009).

[92] C. Cleff, J. Epping, P. Gross, and C. Fallnich, "Femtosecond OPO based on LBO pumped by a frequency-doubled Yb-fiber laser-amplifier system for CARS spectroscopy," Applied Physics B: Lasers and Optics **103**(4), 795–800 (2011).

Chapter 3

High-power, variable-repetition-rate, picosecond optical parametric oscillator

3.1 Introduction

Synchronously pumped optical parametric oscillators (SPOPOs) are of general interest as broadly tunable sources of ultrashort pulses. In the past, mode-locked bulk solid-state laser systems with fixed pulse repetition rates around $100\,\mathrm{MHz}$ have typically been used to pump SPOPOs. However, the emergence of novel ultrashort pulse sources has led to various demonstrations of SPOPOs with high repetition rates up to $82\,\mathrm{GHz}$ [1] and high average powers up to $\approx 27\,\mathrm{W}$ (combined signal and idler) [2]. These novel pump sources have also become more compact, leading to reports of SPOPOs pumped by amplified mode-locked diode sources [3], fibre lasers [4, 5] or passively mode-locked miniature bulk lasers [1, 6]. High average output powers from SPOPOs have been achieved with pump sources based on Nd:YAG bulk solid-state lasers ($80\,\mathrm{ps}$, $18\,\mathrm{W}$, $1064\,\mathrm{nm}$, $76\,\mathrm{MHz}$) obtaining $8\,\mathrm{W}$ of signal and $5\,\mathrm{W}$ of idler from a PPLN OPO [7], YDF lasers ($21\,\mathrm{ps}$, $16\,\mathrm{W}$, $1064\,\mathrm{nm}$, $81\,\mathrm{MHz}$) obtaining $7.4\,\mathrm{W}$ of signal and $4.9\,\mathrm{W}$ of idler from an MgO:PPLN OPO [5] or Yb:YAG thin-disk lasers ($780\,\mathrm{fs}$, $58\,\mathrm{W}$, $1030\,\mathrm{nm}$, $56\,\mathrm{MHz}$) obtaining $19\,\mathrm{W}$ of signal and $7.8\,\mathrm{W}$ of idler from a PPsLT OPO [2].

This chapter describes an SPOPO based on an MgO-doped PPLN crystal pumped by a gain-switched laser diode, whose output is amplified by a chain of ytterbium-doped fibre amplifiers. This pump system benefits from a highly compact, simple and all-fiberised design, a user-controllable repetition rate up to the GHz-regime and the potential for scaling to high average powers [8]. MgO-doping has several advantageous effects over undoped PPLN in terms of optical damage as described in section 2.4.2.1.

Possible applications for high repetition rate, ultrashort pulse sources include research fields such as telecommunications [1], ablation and deposition of polymer materials [9], non-invasive nonlinear microscopy [10, 11] and, in particular, coherent anti-Stokes Raman scattering (CARS) spectroscopy and microscopy [12–14]. Synchronised ultrashort pulses at different wavelengths are required in CARS and this is what an SPOPO naturally produces. High repetition rates generally offer the advantages of higher acquisition frame rates in imaging applications and reduced nonlinear damage of biological samples.

The pump source for the SPOPO in this work was developed and operated by Kang Kang Chen. The SPOPO was set-up and all the experiments were carried out by the author.

3.2 Pump source experimental setup

The pump laser [8] for the SPOPO is shown in figure 3.1. It consists of a gain-switched laser diode and a chain of diode-pumped Yb-doped fibre amplifiers in a MOPA architecture.

The seed pulses at $1060\,\mathrm{nm}$ were generated in a Fabry-Perot fibre-pigtailed laser diode (LD) that was gain-switched with a modulation signal from a pulse generator superimposed on a DC bias. 10% of each pulse was reflected back with a tunable grating in synchronism with the following pulse to ensure stable pulse-to-pulse operation. This mechanism of self-seeding yielded purely single longitudinal mode operation with a suppression ratio of $> 40\,\mathrm{dB}$. The chirp of the output pulses from the laser diode was compensated for with a chirped fibre Bragg grating (CFBG). The repetition rate was controlled with a pulse picker consisting of a fibre-pigtailed EOM and a pulse generator externally triggered by the modulation signal of the LD. The polarisation after each component in the seed source was controlled by three-paddle manual polarisation controllers (PC).

The amplification of the seed pulses took place in a three-stage YDF amplifier chain. The fibre of the first core-pumped amplifier YDF was $4.5\,\mathrm{m}$ long and had a core and cladding diameter of $6\,\mu\mathrm{m}$ and $125\,\mu\mathrm{m}$, respectively. It was bi-directionally pumped via WDMs with two $160\,\mathrm{mW}$ pump diodes at $975\,\mathrm{nm}$. The second YDF consists of a $3.5\,\mathrm{m}$, single-mode, double-clad fibre (core: $6\,\mu\mathrm{m}$, NA 0.12; inner cladding: $125\,\mu\mathrm{m}$, NA 0.45) forward-pumped into the inner cladding by two 7 W pump diodes at $915\,\mathrm{nm}$. The lengths of the fibres were carefully chosen to get optimum performance in terms of centre wavelength, nonlinearities and ASE [8]. The final power amplifier used a $5.7\,\mathrm{m}$-long, polarisation-maintaining (PM), double-clad fibre with a core diameter of $25\,\mu\mathrm{m}$

and an inner cladding diameter of $350\,\mu\mathrm{m}$. The respective NAs were 0.055 and 0.45. Robust single-mode operation (spatially) was obtained by tapering the input side of the (otherwise multi-modal) fibre to a diameter of $125\,\mu\mathrm{m}$. This measure also reduced the splice loss between the polarisation-maintaing, fiberised optical isolator (OI) with a smaller core and the final amplifier. The output side of the fibre had a $2\,\mathrm{mm}$, core-less, angle-polished end-cap to allow for mode expansion and hence an intensity reduction to avoid fibre facet damage. A $170\,\mathrm{W}$, $975\,\mathrm{nm}$, water-cooled diode stack was used to backward-pump the YDF in a free-space configuration. Cylindrical and aspherical lenses were used to obtain a launch efficiency of 83% and dichroic mirrors (DM) separated the signal from the pump light. Each amplification stage was protected from back-reflections of the following stage by OIs, which also prevented leakage of ASE between the stages.

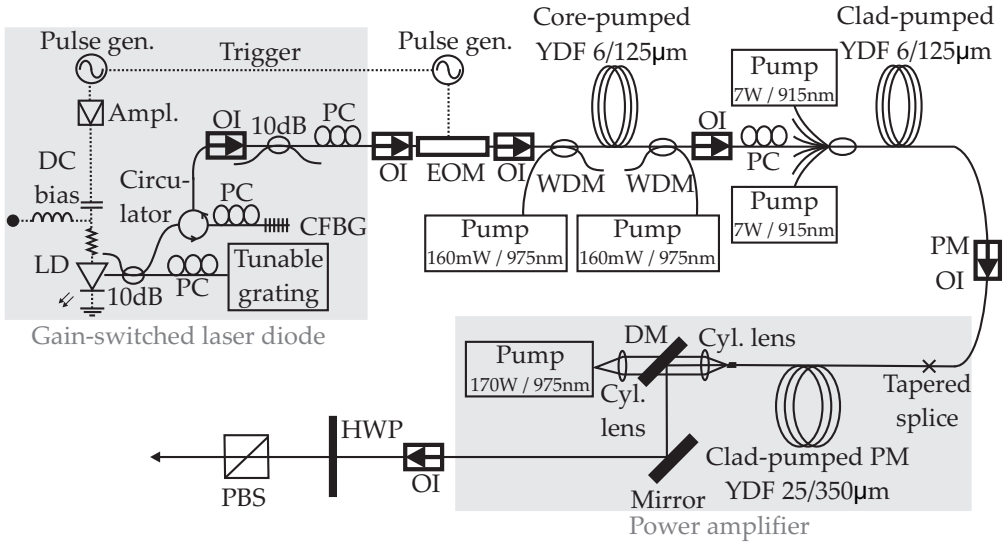

FIGURE 3.1: Schematic diagram of the fibre-amplified gain-switched laser diode pump source. DC: Direct current, LD: Laser diode, PC: Polarisation controller, CFBG: Chirped fibre Bragg grating, OI: Optical isolator, EOM: Electro-optical modulator, WDM: Wavelength division multiplexer, YDF: Ytterbium-doped fibre, PM: Polarisation-maintaining, DM: Dichroic mirror, HWP: $\lambda/2$-plate, PBS: Polarising beam splitter. Dashed and solid lines represent electrical and optical connections, respectively.

The system delivered linearly polarised, $21\,\mathrm{ps}$ pulses with average powers up to $100\,\mathrm{W}$ at a centre wavelength of $1060\,\mathrm{nm}$. The repetition rate could be varied between $100\,\mathrm{MHz}$ and $1\,\mathrm{GHz}$ with the EOM pulse picker and the output beam had an excellent beam quality with a stable M^2-value of 1.02. The polarisation extinction ratio of the final power amplifier output was $19\,\mathrm{dB}$ but this was degraded by the OI due to thermal depolarisation effects [15, 16]. To restore the linear polarisation of the pump beam as required for an efficient parametric interaction and to control the pump power delivered to the SPOPO, a $\lambda/2$ waveplate and a polarising beam splitter were applied. A two-lens telescope and a focusing lens were used after the polarising beam splitter to obtain the required pump waist radius inside the nonlinear crystal of the SPOPO.

3.3 Nonlinear crystal specifications

A periodically poled, congruent $LiNbO_3$ crystal with a 5% magnesium oxide doping concentration (MgO:PPLN) was used in the SPOPO as the nonlinear gain medium. The slab-like MgO:PPLN crystal (Covesion Ltd., United Kingdom) had physical dimensions of $L = 40\,\mathrm{mm}$ (pump beam propagation direction), $H = 10\,\mathrm{mm}$ and $W = 0.5\,\mathrm{mm}$ with eleven $0.5\,\mathrm{mm}$-wide poled gratings ranging from $26.5\,\mu\mathrm{m}$ to $31.5\,\mu\mathrm{m}$. The transmission along the z-axis (i.e. $0.5\,\mathrm{mm}$ thickness) of this crystal as a function of wavelength measured with a Fourier-transform IR spectrophotometer is shown in figure 3.2. This demonstrates that absorption in the MIR does not occur up to $5.5\,\mu\mathrm{m}$, which is a higher value compared to undoped PPLN [17]. The small dip at $\approx 2.8\,\mu\mathrm{m}$ is due to OH-absorption and was reported in [17] as well. It is believed that the feature at around $4.2\,\mu\mathrm{m}$ is an artefact caused by the spectrophotometer and is not related to the crystal sample. As an additional precaution against photo-refraction, the crystal was mounted in an oven with a resolution of $0.1^{\circ}\mathrm{C}$ and heated to $150^{\circ}\mathrm{C}$. The MgO:PPLN was anti-reflection (AR) coated with a single quarter-wave layer of magnesium fluoride (MgF_2) optimised for a signal wavelength of $1.75\,\mu\mathrm{m}$, which is roughly the centre of the signal wavelength range feasible with the grating periods of this crystal. Since the beams are focused in the centre of the crystal and are therefore subject to a certain divergence and since the clear aperture of each poled grating is limited to $0.5\,\mathrm{mm} \times 0.5\,\mathrm{mm}$, the crystal can only have a limited length to avoid beam clipping at the crystal surfaces. However, a long crystal is desired for high nonlinear conversion. The $40\,\mathrm{mm}$-long MgO:PPLN sample is a compromise between both effects. Furthermore, the group velocity mismatches (GVM) of the interacting waves for a $1.06\,\mu\mathrm{m}$ pump, a $1.4\,\mu\mathrm{m}$ to $1.7\,\mu\mathrm{m}$ signal and a $3\,\mu\mathrm{m}$ to $4\,\mu\mathrm{m}$ idler are small enough to give a pump acceptance bandwidth that copes with the nonlinearly broadened pump spectrum and a minimal temporal walk-off. For instance, the calculated GVM between a $1.06\,\mu\mathrm{m}$ pump and a $1.5\,\mu\mathrm{m}$ signal is $1\,\mathrm{ps/cm}$ in MgO:PPLN.

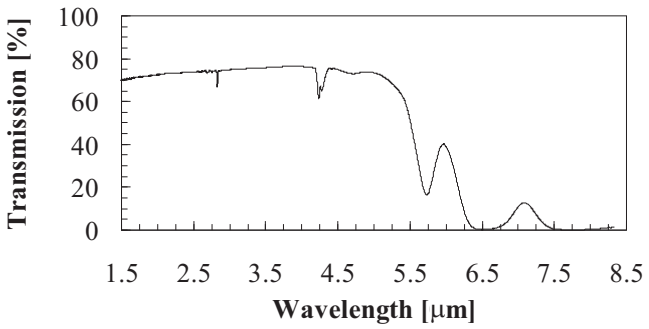

FIGURE 3.2: Transmission as a function of wavelength of a $0.5\,\mathrm{mm}$-thick MgO:PPLN crystal.

3.4 Experiments and results

3.4.1 Standing-wave cavity optical parametric oscillator

The first experiments were carried out with a standing-wave cavity in a bow-tie configuration (see figure 2.11). The MgO:PPLN was aligned such that its optic axis (z-axis) coincided with the plane of the resonator. The polarisation of the pump beam was set to the same axis for optimum nonlinear conversion efficiency as can be seen in figure 3.3.

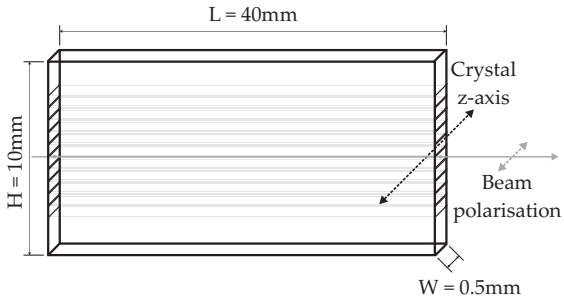

FIGURE 3.3: Three-dimensional illustration of the MgO:PPLN, its crystal axes and the beam polarisations (signal, idler and pump).

There are two limitations regarding the choice of waist size for the signal inside the nonlinear crystal. Firstly, it is important to avoid damage of the crystal during high-power operation and therefore a signal waist as large as possible is required to reduce the peak intensity. Secondly, the ultimate physical beam size limit is the clear aperture of an individual poled grating of the nonlinear crystal, which is $0.5\,\mathrm{mm} \times 0.5\,\mathrm{mm}$ for the MgO:PPLN used here. Since the idler beam with the highest wavelength of all three beams has the largest divergence (Gaussian beams: divergence proportional to wavelength) and since its beam waist radius w_i is coupled to the pump waist radius w_p and signal waist radius w_s by the relation [18]

$$w_i^{-2} = w_s^{-2} + w_p^{-2}\,, \tag{3.1}$$

it will be the idler beam that first suffers from clipping. This equation, which may be counterintuitive, originates from the nonlinear mixing of the signal and pump electric field with a Gaussian spatial profile via the driving polarisation $\mathbf{P}_i = 2\epsilon_0 d_{eff}\mathbf{E}_s^*\mathbf{E}_p$ and thus the driving polarisation for the idler will also have a Gaussian spatial profile. Furthermore, the generated idler field is non-resonant and therefore not determined by the resonator design, but will assume a waist size that yields maximum conversion efficiency. The definition for clipping adopted here is when a beam waist radius grows larger than $1/3$ of the grating aperture at any point in the crystal, which will be at the crystal end facets, if the waist is located in the centre. If diffraction-limited beams are assumed and if the signal and pump beam waist radii in the centre of the nonlinear

crystal are assumed to be equal, a signal waist radius range between approximately $90\,\mu\mathrm{m}$ and $160\,\mu\mathrm{m}$ was found before the idler beam radius multiplied by 3, i.e. $3w_i$, exceeds the $0.5\,\mathrm{mm} \times 0.5\,\mathrm{mm}$ grating aperture at the end facets. The OPO cavity was then numerically modelled such that a maximally large signal waist radius within these boundaries was obtained to prevent optical damage. The well-known ABCD matrix formalism was used for the resonator modelling [19]. The model yielded a maximum signal waist radius of $98\,\mu\mathrm{m}$ ($1/e^2$-intensity) by using concave curved mirrors CM 1 and CM 2 with a radius of curvature of $-250\,\mathrm{mm}$. Mirrors with a larger radius of curvature, which would produce larger signal waists, were not available at the time. The confocal parameter corresponding to the $98\,\mu\mathrm{m}$ waist radius was $b_s = 86\,\mathrm{mm}$ with a refractive index of $n = 2.145$ at the signal wavelength of $\lambda_s = 1.5\,\mu\mathrm{m}$. Hence, the focusing parameter was $\xi_s = 0.47$, which means that the signal beam deviates from the ideal condition of confocal focusing with $\xi_s = 1$. But the higher priority was given to the prevention of optical damage rather than achieving optimum gain and efficiency. Using a telescope with $f_1 = 200\,\mathrm{mm}$ and $f_2 = 175\,\mathrm{mm}$ lenses to slightly reduce the collimated beam radius from the final amplifier and a focusing lens with a focal length of $250\,\mathrm{mm}$, the pump spot size was set to $125\,\mu\mathrm{m}$ (measured with a beam profiler) resulting in a confocal parameter of $b_p = 200\,\mathrm{mm}$ and thus relatively weak focusing expressed by a focusing parameter of $\xi_p = 0.2$, i.e. a nearly collimated pump beam along the crystal length. The idler waist radius of $77\,\mu\mathrm{m}$ was then calculated with the relation in equation 3.1. Due to mechanical limitations with crystal and mirror mounts, it was necessary to set the bow-tie folding angle to $12°$. The astigmatism introduced by the curved mirrors [20] in conjunction with the folding angle leads to an elliptical signal beam with its major and minor axes normal to and in the resonator plane, respectively. However, this astigmatism and associated beam ellipticity was calculated with the ABCD matrix model to be insignificant regarding the resonator stability. In the worst case, the resonator may become unstable in one axis (major axis of the elliptical beam), but not in the other.

All of the cavity mirrors were highly reflective for the signal wavelength, except for the OC mirror M 3. CM 1 served as the input coupler for the pump and had a transmission of 92% at the pump wavelength, the other mirrors had a similar pump transmission. Mirror CM 2 was the output coupler for the idler with a measured transmission of 88%, and therefore the SPOPO was singly resonant only for the signal. All mirrors were based on CaF_2 substrates with a high MIR transmission and hence additionally ensured that the idler was not resonant. A round-trip signal loss excluding the output coupling of 9.5% was measured by means of the modified Findlay-Clay analysis described in section 2.4.1.6 [21]. This loss is dominated by the Fresnel reflection at the crystal surfaces. The MgO:PPLN was AR-coated in-house with a simple MgF_2-layer.

The measured transmission of these coatings and through the entire length of the crystal was approximately 95% at $1.5\,\mu\mathrm{m}$ and, furthermore, the signal passes twice through the crystal per round-trip in a standing-wave cavity explaining the 9.5% internal loss.

Figure 3.4 shows the initial results of output power and pump depletion as a function of input pump power with an optimum reflectivity of the OC of $R = 95\%$ and a repetition rate of $918.4\,\mathrm{MHz}$ at a signal wavelength of $1.5\,\mu\mathrm{m}$. The SPOPO cavity length was not changed from the $114.8\,\mathrm{MHz}$, but it was accepted that 8 signal pulses were circulating in the cavity at the same time. As reported before [3, 6, 22, 23], this is not problematic as each signal pulse acts independently and is in synchronism with a separate pump pulse. The pump depletion reached values of up to 50% with maximum signal and idler powers of $1.2\,\mathrm{W}$ and $1.3\,\mathrm{W}$, respectively, for an input power of $11.4\,\mathrm{W}$. The oscillation threshold was just over $2\,\mathrm{W}$. The M^2-beam quality was measured to be 1.02 parallel to the resonator plane and 1.30 perpendicular to the resonator plane. The signal FWHM pulse duration was $20.4\,\mathrm{ps}$ determined with an intensity autocorrelator and assuming a Gaussian pulse profile.

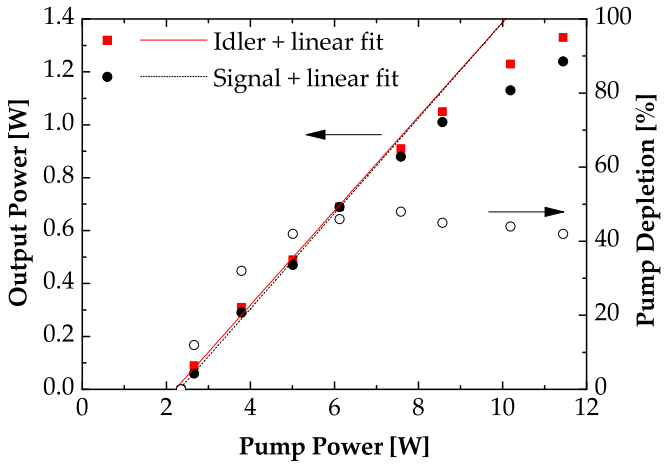

FIGURE 3.4: Output power and pump depletion as a function of pump power of the standing-wave cavity SPOPO using an $R = 95\%$ OC mirror. The linear curve fits used only the first 5 data points that showed a linear behaviour. The repetition rate was $918.4\,\mathrm{MHz}$.

Using an $R = 65\%$ OC and pumping with higher powers, the output characteristic rolled-off and oscillation ceased at around $21\,\mathrm{W}$ of pump power as can be seen in figure 3.5. Due to the higher output coupling, the threshold power of $8\,\mathrm{W}$ was higher compared to the previous case. There is already a trend for a roll-off effect apparent in figure 3.4. It appears that thermal effects were, at least in part, responsible for the roll-off, because an experiment with a 50% duty cycle chopper (frequency of $150\,\mathrm{Hz}$) placed in the pump beam [24] to reduce the thermal input led to a recovery of the oscillation at the high pump power level. This fact is not in agreement with the simplistic notion that an OPO should in theory not exhibit any significant thermal input. Also, previous publications of high-power OPOs based on periodically poled lithium tantalate [2] and

lithium niobate [7] did not report such effects. Thermal input due to increased idler absorption can be ruled out, since an experiment, where the idler wavelength was tuned away from the transparency boundary to a wavelength of $2.9\,\mu\mathrm{m}$, did not reduce the roll-off effect. Furthermore, measurement of the pump bandwidth showed no increase at the higher power levels at this repetition rate, which could potentially have reduced the conversion efficiency, if it extended beyond the pump acceptance bandwidth. As the MgO:PPLN was held in a temperature-controlled oven, any physical beam clipping due to non-diffraction-limited performance should not trigger significant temperature variations. On the other hand, the observation of a linear increase of the signal centre wavelength with pump power at a rate of $0.155\,\mathrm{nm/W}$ did indicate a thermal input. For an increase from $2.6\,\mathrm{W}$ to $23.8\,\mathrm{W}$, the signal wavelength increased by $\approx 3.3\,\mathrm{nm}$, which would correspond to a $6^{\circ}\mathrm{C}$ rise within the crystal at the location of the interacting beams, if it was only due to a temperature change (based on the temperature-dependent Sellmeier equation [25]).

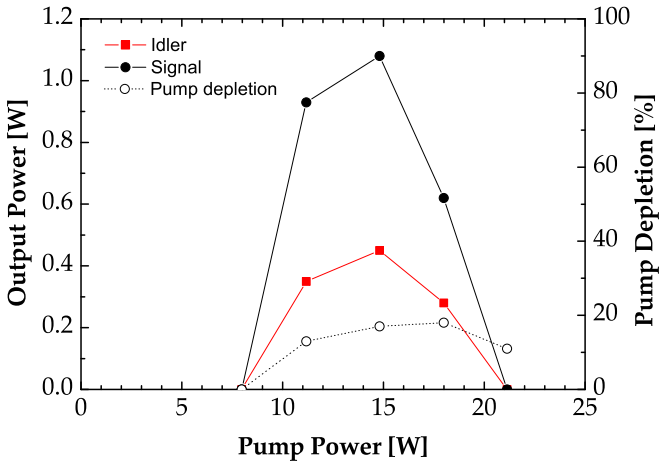

FIGURE 3.5: Output power and pump depletion as a function of pump power of the standing-wave cavity SPOPO using an $R = 65\%$ OC mirror (repetition rate $918.4\,\mathrm{MHz}$). The lines between the experimental data points are only a guide for the eye. A roll-off effect was observed that led to a cessation of the oscillation at a pump power of approximately $21\,\mathrm{W}$. Thermal effects were assumed to be responsible for this.

Thus, although the nature of the thermal input is not clear, there is evidence for its presence. It is now interesting to discuss how well lithium niobate can cope with such a thermal input. $LiNbO_3$ (MgO-doped or undoped) has a large value of $(dn_e/dT)/\kappa$, where dn_e/dT is the thermo-optic coefficient and gives the rate of change of the extraordinary refractive index with temperature [26] and κ is the thermal conductivity. These two parameters are the dominant material parameters that influence the focal length of the thermal lens generated by a Gaussian beam [27]

$$f_{th} = \frac{\pi \kappa w_p^2}{P_p \gamma_{heat} \frac{dn}{dT}} \,. \tag{3.2}$$

The fraction of absorbed pump power dissipated as heat is denoted with γ_{heat}. This is close to 0 in a parametric device unlike in a laser, where the quantum defect mainly determines γ_{heat}. The other parameters in the equation are the absorbed (or depleted) pump power P_p and the waist radius w_p. The value of $(dn_e/dT)/\kappa$ in a high-power laser medium such as yttrium aluminium garnet (YAG) is roughly 20× smaller than in $LiNbO_3$, where the thermo-optic coefficients at $1.064\,\mu\mathrm{m}$ are $dn_e/dT = 39{\cdot}10^{-6}\,\mathrm{K}^{-1}$ and $dn_o/dT = 1.4 \cdot 10^{-6}\,\mathrm{K}^{-1}$ and the thermal conductivity is $4.6\,\mathrm{W/mK}$ [28]. Using these material parameters in a simple model for a cylindrical rod geometry [27] rather than a thin slab, leads to predictions that a thermal lens with a focal length of approximately $1\,\mathrm{cm}$ would be generated, if less than 1% of the pump power were converted to heat within the beam volume. Such a thermal lens is sufficient to make the OPO resonator unstable.

3.4.2 Ring cavity optical parametric oscillator

A ring cavity was then set-up as shown in figure 3.6, where the signal passes only once per round-trip through the MgO:PPLN crystal. This was motivated by the fact that a single pass through the crystal would reduce the round-trip losses for the signal, any signal-induced thermal effects and also the aberration imposed upon the signal by any thermal lensing present. An increase of the total cavity length by a factor of two was required to continue matching the fundamental repetition rate of $114.8\,\mathrm{MHz}$ with the OPO cavity (ring cavity: $L = c/f_{rep}$). This, however, led to a smaller and more asymmetric signal waist within the crystal of $47\,\mu\mathrm{m} \times 59\,\mu\mathrm{m}$ (parallel and perpendicular to the cavity plane). The lack of appropriate curved mirrors did not allow the production of the same waist radius as in the standing-wave cavity. The pump waist radius was adapted to $50\,\mu\mathrm{m}$ to maintain a good spatial overlap of pump and signal waist by using a telescope with a $f_1 = 100\,\mathrm{mm}$ and a $f_2 = 175\,\mathrm{mm}$ lens as well as a $250\,\mathrm{mm}$ focusing lens. The resulting idler waist was therefore only $\approx 34\,\mathrm{um} \times 38\,\mu\mathrm{m}$ and, consequently, it was expected that the idler beam was significantly clipped at the crystal edges due to the increased beam divergence, even if the beam was considered diffraction-limited. The round-trip losses were determined to be 15.7% by performing a Findlay-Clay analysis. This is actually higher than in the standing-wave cavity, despite the single pass through the MgO:PPLN crystal. However, the assumption of additional losses from diffraction and clipping of the idler beam would explain a reduction in the parametric gain [29, 30] and thus an increase of the effective loss as determined by the Findlay-Clay analysis.

Figure 3.7 shows the output power and the pump depletion as a function of the pump power for 1, 4 and 8 pulses circulating in the cavity, corresponding to repetition rates of $114.8\,\mathrm{MHz}$, $459.2\,\mathrm{MHz}$ and $918.4\,\mathrm{MHz}$, and for pump average powers up to $24\,\mathrm{W}$.

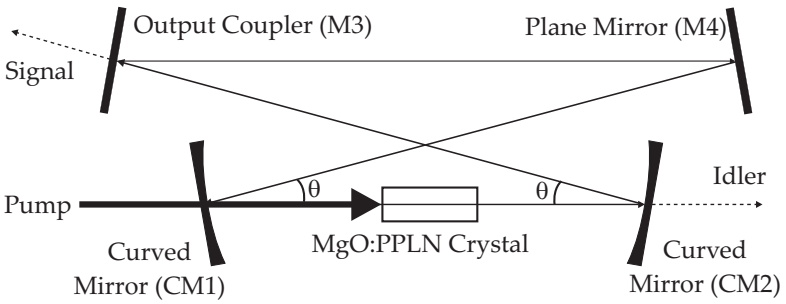

FIGURE 3.6: Ring cavity bow-tie SPOPO configuration. The curved mirrors (CM 1 and CM 2) and the plane mirror (M 4) were highly reflective for the signal. The output coupler (M 3) had a reflectivity of 65% at the signal wavelength. The idler was not oscillating in the resonator and was transmitted through CM 2. The bow-tie folding angle θ was 12°.

The maximum available pump power was limited by the maximum power rating of the polarising beam splitter used at that time between the pump source and the OPO (see figure 3.1). A first observation was that the roll-off effect was not present for the lower repetition rates and while still present at $918.4\,\mathrm{MHz}$, oscillation was maintained up to the maximum $24\,\mathrm{W}$ of pump power at this repetition rate. For the fundamental repetition rate of $114.8\,\mathrm{MHz}$, a maximum signal output power of $7.3\,\mathrm{W}$ at $1.54\,\mu\mathrm{m}$ and idler power of $3.1\,\mathrm{W}$ at $3.4\,\mu\mathrm{m}$ was obtained for $24\,\mathrm{W}$ of pump power corresponding to efficiencies of 30.4% and 12.9%, respectively (the slope efficiencies of the linear curve fits were 33.3% and 13.6%). The pump depletion saturated at around 70%. All the results in figure 3.7 were obtained by using an output coupler (M 3) with a reflectivity of $R = 65\%$. In order to double-check with the round-trip loss value of 15.7% from the Findlay-Clay analysis, the photon budget for the signal is estimated. Equating the product of the maximum pump power inside the crystal of $20.3\,\mathrm{W}$ (coating losses), the maximum pump depletion of 70%, the quantum defect of $1.06\,\mu\mathrm{m}/1.54\,\mu\mathrm{m}$ and the approximate total cavity loss factor $T_{OC}/\left(T_{OC}+\epsilon_s\right)$ to the measured signal power of $7.3\,\mathrm{W}$, a value of $\epsilon_s \approx 0.12$, i.e. 12% is calculated, which is in good agreement with the Findlay-Clay analysis (ϵ_s denotes the signal round-trip loss and $T_{OC} = 0.35$ the output coupler transmission). Considering that the SPOPO was operated at $33\times$ above threshold at the maximum pump power and at the fundamental repetition rate, it is likely that an OC with a much lower reflectivity could have provided more signal output power.

The significantly improved performance of the ring cavity SPOPO suggested that it benefited from the single pass per round-trip of the signal through the nonlinear crystal. A simple modelling of the ring and standing-wave cavities suggested that they would both require thermal lenses of similar strength to drive them into instability. It is thus speculated that the reduction of the aberrations imposed on the signal by only passing once through the MgO:PPLN was the likely dominant effect. The single pass of the signal through the crystal could also lead to less heat being deposited, although the mechanism by which any such absorption occurs is not entirely clear. Henderson and

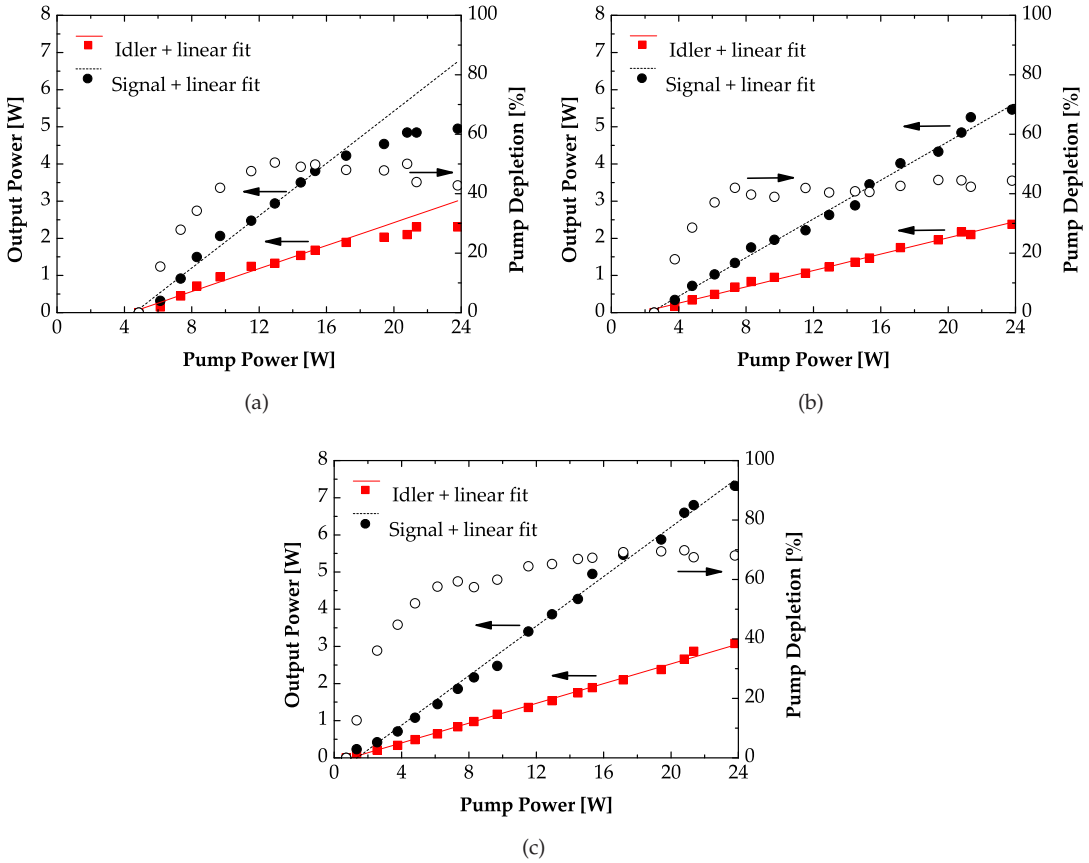

FIGURE 3.7: Output power and pump depletion as a function of pump power of the ring cavity SPOPO at repetition rates of (a) 918.4 MHz, (b) 459.2 MHz and (c) 114.8 MHz. The linear curve fits in (a) used only the first 10 data points that showed a linear behaviour. The signal output coupler had a reflectivity of 65%.

Stafford report a low-level signal absorption of $0.08\%/cm$ at $1.7\,\mu\mathrm{m}$ [31], which could lead to several Watts of intracavity signal power absorbed and converted to heat in the crystal. The diverging idler beam being clipped at the crystal input and output facets, as expected, apparently did not hinder improved performance of the ring cavity SPOPO.

It is intriguing that the power roll-off for the high repetition rate results was still present, because the thermal load imposed on the crystal should be the same independent of the repetition rate. The only difference was the lower gain due to the reduced peak intensity of the pump pulse, which was reflected in the higher threshold.

Wavelength tunability of the SPOPO was achieved by translating the MgO:PPLN slab to access gratings with different poling periods. Additional temperature tuning was not performed but the crystal was kept at an elevated temperature of $150^{\circ}\mathrm{C}$. The tuning curve is shown in figure 3.8, where the black dots indicate the measured signal centre wavelengths (using a standard OSA with a resolution of $0.1\,\mathrm{nm}$), the red squares indicate the inferred idler centre wavelengths and the dashed curve is the theoretical

tuning curve calculated with the temperature-dependent Sellmeier equation of MgO-doped $LiNbO_3$ [25]. The repetition rate was set to $918.4\,\mathrm{MHz}$ during the measurement and the pump power was adjusted to be approximately 15% higher than the threshold level, which increases with decreasing signal wavelength due to higher mirror coating losses, operation further away from the degeneracy point (see equation (2.66): threshold power $P^*_{th,p} \propto \lambda_i^2 \lambda_s$, thus minimum at degeneracy) and increasing idler absorption [32]. The signal was tuned from $1.40\,\mu\mathrm{m}$ to $1.68\,\mu\mathrm{m}$ and the idler from $2.87\,\mu\mathrm{m}$ to $4.36\,\mu\mathrm{m}$. The MgO:PPLN gratings with periods of $26.5\,\mu\mathrm{m}$ and $27.0\,\mu\mathrm{m}$ were not accessed to avoid idler absorption at wavelengths $> 4.5\,\mu\mathrm{m}$ and the $31.5\,\mu\mathrm{m}$ yielded a signal wavelength beyond the OSA sensitivity and could therefore not be measured.

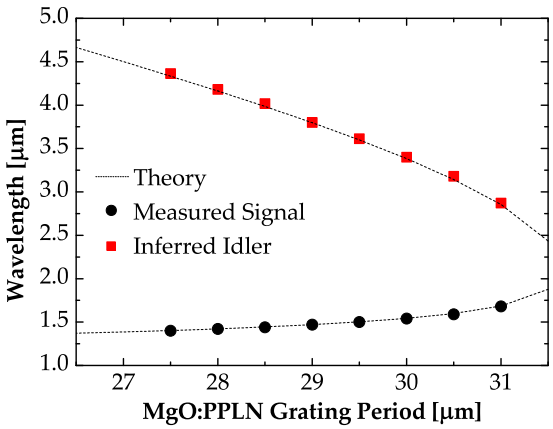

FIGURE 3.8: Signal and idler wavelength as a function of the MgO:PPLN grating period of the ring cavity SPOPO. The idler wavelength was inferred from the measured signal wavelength. The repetition rate was $918.4\,\mathrm{MHz}$ and the crystal was heated up to a constant temperature of $150^\circ\mathrm{C}$. The dashed curve is the theoretical tuning curve.

The duration of the signal and idler pulses was measured by using intensity and interferometric autocorrelation, repectively. The signal intensity autocorrelator used a TPA silicon photodiode, whereas the idler interferometric autocorrelator used a TPA InGaAs photodiode with extended sensitivity up to $2.1\,\mu\mathrm{m}$. The autocorrelation traces recorded at a pump power of $\approx 10\,\mathrm{W}$ and at a repetition rate of $918.4\,\mathrm{MHz}$ are shown in figure 3.9. Assuming a Gaussian pulse profile, the FWHM pulse durations were $17.0\,\mathrm{ps}$ and $17.2\,\mathrm{ps}$ for signal and idler, respectively. With a FWHM signal bandwidth of $\approx 0.6\,\mathrm{nm}$ at $1.542\,\mu\mathrm{m}$, the time-bandwidth product was 1.28 and hence almost $3\times$ higher than the bandwidth limit 0.441. The time-bandwidth product of the pump, for comparison, was 0.84 with a FWHM pulse duration of $21\,\mathrm{ps}$ and a FWHM bandwidth of $0.15\,\mathrm{nm}$, also at $10\,\mathrm{W}$ and $918.4\,\mathrm{MHz}$. The idler spectrum could not be measured due to the lack of a suitable MIR spectrometer and thus the exact time-bandwidth product could not be calculated. However, the shape of the idler autocorrelation trace, especially the fully filled-out fringes, suggest that the pulses are nearly bandwidth-limited.

The spectra of the input pump and the residual pump after depletion at high average

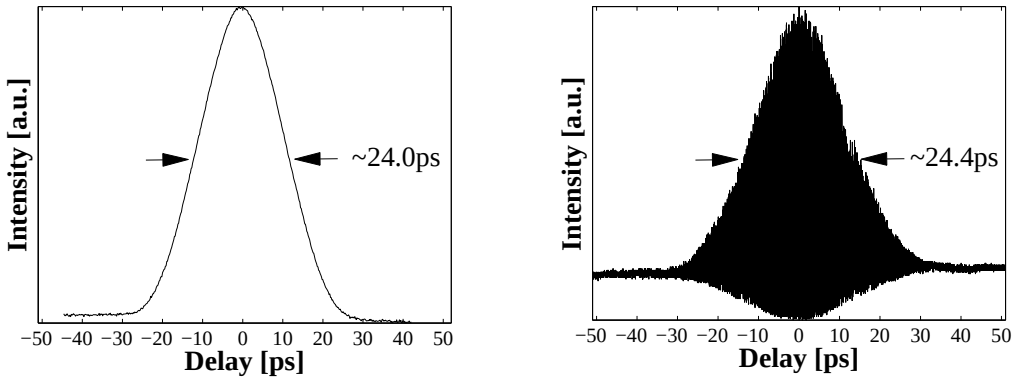

FIGURE 3.9: Pulse autocorrelations of (a) the signal (intensity) and (b) the idler (interferometric) of the ring cavity SPOPO. The pump power was $\approx 10\,\mathrm{W}$ and the repetition rate was $918.4\,\mathrm{MHz}$. The FWHM pulse durations derived from the autocorrelations were $17.0\,\mathrm{ps}$ and $17.2\,\mathrm{ps}$ for the signal at $1.54\,\mu\mathrm{m}$ and the idler at $3.40\,\mu\mathrm{m}$, respectively, if a Gaussian pulse shape is assumed (deconvolution factor $1/\sqrt{2}$).

powers in the two repetition rate extremes were also measured, where nonlinear broadening was either absent or at its strongest. This was carried out to investigate, whether all of the pump spectrum is within the MgO:PPLN phase-matching bandwidth and is efficiently converted to signal and idler. The spectra are shown in figure 3.10(a) and 3.10(b) and confirm that depletion occurred across the entire spectrum. Therefore, the phase-matching bandwidth was not limiting the pump depletion, even when the spectrum is broadened due to SPM in the fibre amplifiers at the low repetition rate. The areas under the curves were adjusted to represent the measured average powers of the input pump and the residual pump after depletion to allow a direct comparison. The corresponding signal spectra at the two extreme repetition rates are shown in figure 3.10(c) and 3.10(d). Both spectra had similar FWHM bandwidths and had a certain structured shape, although this was much more pronounced at the lower repetition rate of $114.8\,\mathrm{MHz}$.

The signal and idler beam quality (M^2-value) at $918.4\,\mathrm{MHz}$ was measured at $10\,\mathrm{W}$ and $24\,\mathrm{W}$ of pump power. The signal M^2 was measured by translating a beam profiler through the beam waist, produced with a lens, and recording the $1/e^2$-radius at points along the beam. The beam profiler was not sensitive in the MIR spectral region of the idler and therefore a knife-edge method [33] was used to determine the 15% and 85% power transmission points giving an estimate of the $1/e^2$-radius. This was repeated for several points along the beam spanning the waist region. In both cases, a Gaussian curve fit was applied to the experimental data, which gave the M^2-values. The beam caustic plots of these measurements are shown in figure 3.11 for both signal and idler at the power levels indicated and for the planes parallel (denoted with x) and perpendicular (denoted with y) to the ring resonator plane. The M^2-values from the curve fits are summarised in table 3.1. The repetition rate was $918.4\,\mathrm{MHz}$, the signal

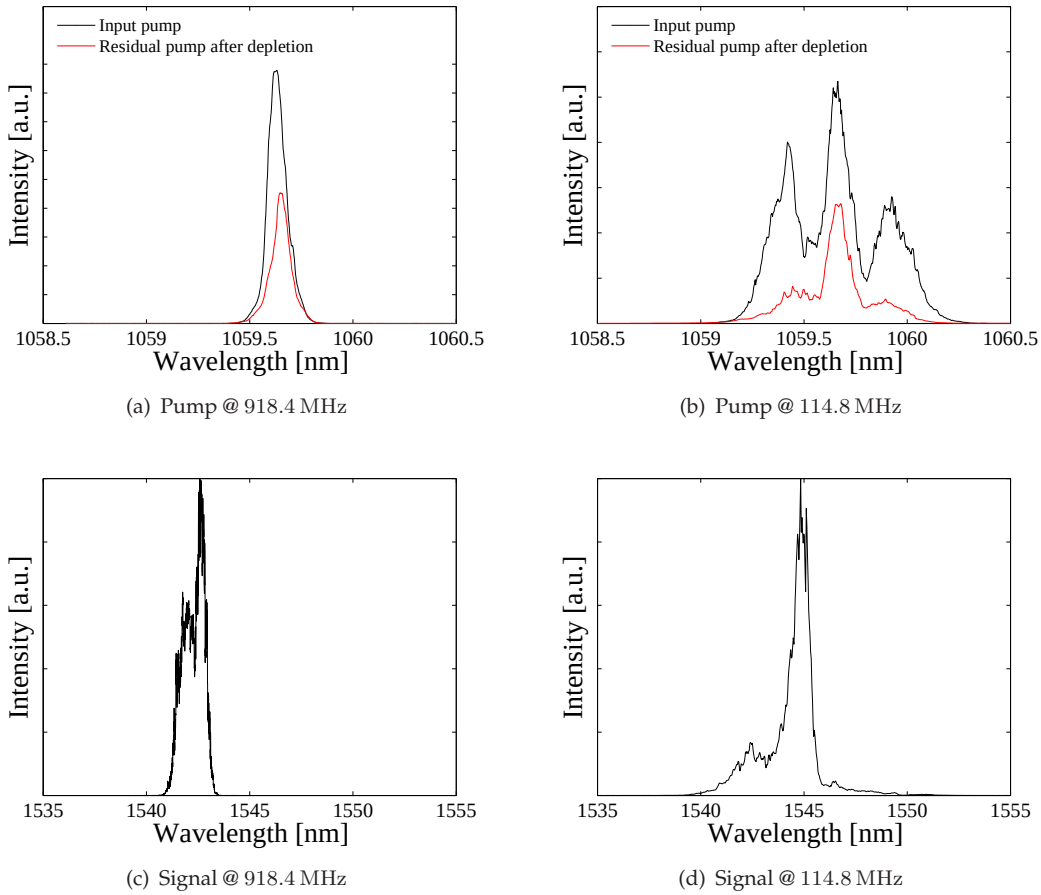

(a) Pump @ 918.4 MHz

(b) Pump @ 114.8 MHz

(c) Signal @ 918.4 MHz

(d) Signal @ 114.8 MHz

FIGURE 3.10: (a), (b) Comparison of the spectra of the input pump and the residual pump (after depletion) at the two extreme repetition rates. The curves are scaled according to the ratio of the measured average powers. The signal spectra are shown in (c) and (d) for the same repetition rates. The spectra at the low repetition rate show a broadening caused by SPM in the fibre amplifiers. All spectra were taken at a pump power of 24 W.

wavelength $1.54\,\mu\mathrm{m}$ and the idler wavelength $3.40\,\mu\mathrm{m}$. The resonant signal beam was close to the diffraction limit with a minor degradation at higher pump powers. The non-resonant idler beam deviated significantly from the diffraction limit, which is not surprising since it was composed of an addition of the idler radiation generated from all points along the $40\,\mathrm{mm}$ crystal length. This length is much greater than the idler confocal parameter of approximately $5\,\mathrm{mm}$. Another observation was that the M^2 was consistently worse in the x-plane for both the signal and idler beam. There were various factors that distinguish the x- and the y-plane and that may be responsible for the degraded beam quality in the x-plane: (1) the asymmetry of the signal beam waist due to the astigmatism introduced by the folding angle θ, (2) stronger thermal lensing in the x-plane as this axis corresponds to the heat dissipation axis of the slab geometry of the crystal and to the axis with the higher thermo-optic coefficient dn_e/dT and (3) the presence of a hard aperture in the x-plane due to the crystal oven.

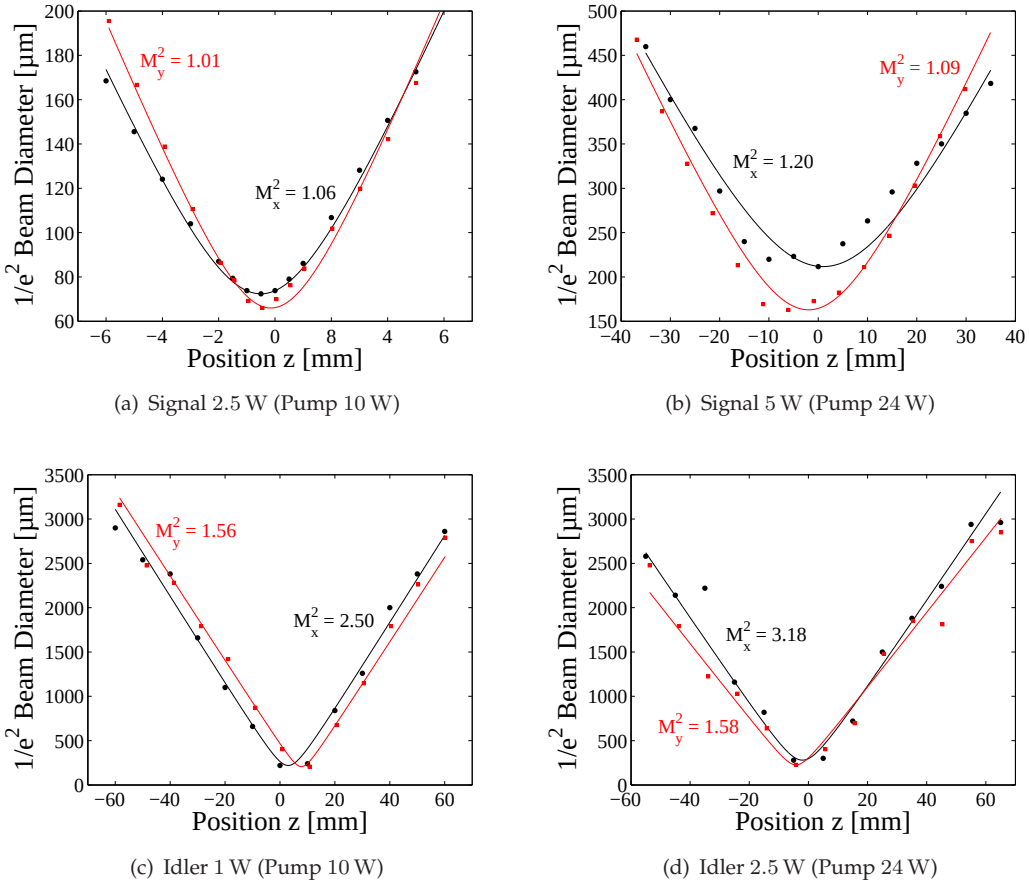

(a) Signal 2.5 W (Pump 10 W)

(b) Signal 5 W (Pump 24 W)

(c) Idler 1 W (Pump 10 W)

(d) Idler 2.5 W (Pump 24 W)

FIGURE 3.11: Beam caustic plots and curve fits for the M^2-measurement of (a), (b) signal and (c), (d) idler of the ring cavity SPOPO at two different pump power levels. The M^2-values are indicated in the plots and summarised in table 3.1. The repetition rate was 918.4 MHz.

TABLE 3.1: M^2-beam quality measurement of the ring cavity SPOPO at two different pump power levels. The repetition rate was 918.4 MHz, the signal wavelength 1.54 μm and the idler wavelength 3.40 μm (*corresponds to 2.5 W signal, 1.0 W idler; †corresponds to 5.0 W signal, 2.5 W idler).

	Signal		**Idler**	
	M_x^2	M_y^2	M_x^2	M_y^2
Pump 10 W*	1.06	1.01	2.50	1.56
Pump 24 W†	1.20	1.09	3.18	1.58

3.5 Conclusions

In this chapter, a high average power, ring cavity OPO synchronously pumped by a 21 ps, up to 100 W, 1.06 μm fibre-amplified gain-switched laser diode was demonstrated. The pump source was very compact and, except for one component (diode pumping of final fibre amplifier), all-fiberised. The repetition rate could be electronically set to values of $i \times 114.8$ MHz with $i = 1, 2, 4, 8$ using an EOM pulse picker. The SPOPO had a fixed cavity length that matched the fundamental repetition rate of

$114.8\,\mathrm{MHz}$ with multiple pulses circulating in the cavity at higher pump source repetition rate, i.e. 2, 4 or 8 pulses.

At the fundamental repetition rate of $114.8\,\mathrm{MHz}$, maximum output powers of $7.3\,\mathrm{W}$ at $1.54\,\mu\mathrm{m}$ and $3.1\,\mathrm{W}$ at $3.40\,\mu\mathrm{m}$ were obtained at a maximum pump power of $24\,\mathrm{W}$ corresponding to efficiencies of 30% and 13%, respectively. Wide tunability for the signal ($1.4\,\mu\mathrm{m} \ldots 1.7\,\mu\mathrm{m}$) and the idler ($2.9\,\mu\mathrm{m} \ldots 4.4\,\mu\mathrm{m}$) was demonstrated by translating the MgO:PPLN to access different poled periods with the pump beam. The FWHM pulse duration of the signal and idler was $17\,\mathrm{ps}$ and slightly shorter than the pump pulses with a duration of $21\,\mathrm{ps}$. The beam quality of the signal was close to the diffraction limit indicated by M^2-values close to 1. The idler beam quality, however, departed strongly from the diffraction limit, especially in the plane of the resonator ($M^2 > 2$).

In initial experiments with a standing-wave cavity and in the experiments with the ring cavity at high repetition rates, a power roll-off effect was observed, which was attributed to a thermal input to the nonlinear crystal. In the standing-wave cavity a complete cessation of oscillation occurred as the pump power was increased, whereas in the ring cavity, where the signal just passes once through the crystal per round-trip, oscillation was maintained up to the maximum pump power, however with a roll-off setting in. The origin of the thermal input is not completely understood yet but could lead to strong thermal lensing and beam aberrations, which is enhanced by adverse thermal coefficients of the MgO:PPLN material. In order to exploit the full power scaling capability of the pump source up to $100\,\mathrm{W}$ for the OPO in the future, it will be necessary to get a good understanding of this thermal effect.

Such a high-power OPO pumped with a compact fibre-amplified gain-switched LD source is an interesting replacement for complex and expensive Ti:sapphire-pumped OPO systems and especially the high repetition rates towards the gigahertz regime are an advantage in terms of specimen damage [10, 34]. The pump source also has the potential for pulse compression down to approximately $1\,\mathrm{ps}$ [35] and thus accessing the most interesting pulse regime for CARS (characteristic relaxation times of molecular systems, trade-off between signal strength and spectral resolution) [36, 37].

References

[1] S. Lecomte, R. Paschotta, S. Pawlik, B. Schmidt, K. Furusawa, A. Malinowski, D. J. Richardson, and U. Keller, "Synchronously pumped optical parametric oscillator with a repetition rate of 81.8 GHz," IEEE Photonics Technology Letters **17**(2), 483–485 (2005).

[2] T. Südmeyer, E. Innerhofer, F. Brunner, R. Paschotta, T. Usami, H. Ito, S. Kurimura, K. Kitamura, D. C. Hanna, and U. Keller, "High-power femtosecond fiber-feedback optical parametric oscillator based on periodically poled stoichiometric $LiTaO_3$," Opt. Lett. **29**(10), 1111–1113 (2004).

[3] A. Robertson, M. E. Klein, M. A. Tremont, K. J. Boller, and R. Wallenstein, "2.5-GHz repetition-rate singly resonant optical parametric oscillator synchronously pumped by a mode-locked diode oscillator amplifier system," Opt. Lett. **25**(9), 657–659 (2000).

[4] M. V. O'Connor, M. A. Watson, D. P. Shepherd, D. C. Hanna, J. H. V. Price, A. Malinowski, J. Nilsson, N. G. R. Broderick, D. J. Richardson, and L. Lefort, "Synchronously pumped optical parametric oscillator driven by a femtosecond mode-locked fiber laser," Opt. Lett. **27**(12), 1052–1054 (2002).

[5] O. Kokabee, A. Esteban-Martin, and M. Ebrahim-Zadeh, "Efficient, high-power, ytterbium-fiber-laser-pumped picosecond optical parametric oscillator," Opt. Lett. **35**(19), 3210–3212 (2010).

[6] S. Lecomte, R. Paschotta, M. Golling, D. Ebling, and U. Keller, "Synchronously pumped optical parametric oscillators in the 1.5-μm spectral region with a repetition rate of 10 GHz," J. Opt. Soc. Am. B **21**(4), 844–850 (2004).

[7] C. W. Hoyt, M. Sheik-Bahae, and M. Ebrahim-Zadeh, "High-power picosecond optical parametric oscillator based on periodically poled lithium niobate," Opt. Lett. **27**(17), 1543–1545 (2002).

[8] K. K. Chen, S.-U. Alam, J. Hayes, D. Lin, A. Malinowski, and D. J. Richardson, "100W, Single Mode, Single Polarization, Picosecond, Ytterbium Doped Fibre MOPA Frequency Doubled to 530nm," in *Conference on Lasers and Electro-Optics (CLEO) Pacific Rim*, vol. TuF4-4 (Shanghai, China, 2009).

[9] V. Z. Kolev, M. W. Duering, B. Luther-Davies, and A. V. Rode, "Compact high-power optical source for resonant infrared pulsed laser ablation and deposition of polymer materials," Opt. Express **14**(25), 12,302–12,309 (2006).

[10] S.-W. Chu, T.-M. Liu, C.-K. Sun, C.-Y. Lin, and H.-J. Tsai, "Real-time second-harmonic-generation microscopy based on a 2-GHz repetition rate Ti:sapphire laser," Opt. Express **11**(8), 933–938 (2003).

[11] A. Vogel, J. Noack, G. Hüttman, and G. Paltauf, "Mechanisms of femtosecond laser nanosurgery of cells and tissues," Applied Physics B: Lasers and Optics **81**(8), 1015–1047 (2005).

[12] C. L. Evans, E. O. Potma, M. Puoris'haag, D. Côté, C. P. Lin, and X. S. Xie, "Chemical imaging of tissue in vivo with video-rate coherent anti-Stokes Raman scattering microscopy," Proceedings of the National Academy of Sciences of the United States of America **102**(46), 16,807–16,812 (2005).

[13] C. L. Evans and X. S. Xie, "Coherent Anti-Stokes Raman Scattering Microscopy: Chemical Imaging for Biology and Medicine," Annual Review of Analytical Chemistry **1**(1), 883–909 (2008).

[14] F. Ganikhanov, S. Carrasco, X. Sunney Xie, M. Katz, W. Seitz, and D. Kopf, "Broadly tunable dual-wavelength light source for coherent anti-Stokes Raman scattering microscopy," Opt. Lett. **31**(9), 1292–1294 (2006).

[15] E. A. Khazanov, O. V. Kulagin, S. Yoshida, D. B. Tanner, and D. H. Reitze, "Investigation of Self-Induced Depolarization of Laser Radiation in Terbium Gallium Garnet," IEEE Journal of Quantum Electronics **35**(8), 1116–1122 (1999).

[16] E. Khazanov, N. F. Andreev, A. Mal'shakov, O. Palashov, A. K. Poteomkin, A. Sergeev, A. A. Shaykin, V. Zelenogorsky, I. A. Ivanov, R. Amin, G. Mueller, D. B. Tanner, and D. H. Reitze, "Compensation of Thermally Induced Modal Distortions in Faraday Isolators," IEEE Journal of Quantum Electronics **40**(10), 1500–1510 (2004).

[17] L. E. Myers, R. C. Eckardt, M. M. Fejer, R. L. Byer, and W. R. Bosenberg, "Multigrating quasi-phase-matched optical parametric oscillator in periodically poled $LiNbO_3$," Opt. Lett. **21**(8), 591–593 (1996).

[18] M. J. McCarthy and D. C. Hanna, "All-solid-state synchronously pumped optical parametric oscillator," J. Opt. Soc. Am. B **10**(11), 2180 (1993).

[19] A. E. Siegman, *Lasers*, 1st ed. (University Science Books, Sausalito, California, 1986).

[20] D. C. Hanna, "Astigmatic Gaussian Beams Produced by Axially Asymmetric Laser Cavities," IEEE Journal of Quantum Electronics **5**(10), 483–488 (1969).

[21] D. Findlay and R. A. Clay, "The measurement of internal losses in 4-level lasers," Physics Letters **20**(3), 277–278 (1966).

[22] X. P. Zhang, J. Hebling, A. Bartels, D. Nau, J. Kuhl, W. W. Rühle, and H. Giessen, "1-GHz-repetition-rate femtosecond optical parametric oscillator," Applied Physics Letters **80**(11), 1873–1875 (2002).

[23] S. Lecomte, R. Paschotta, S. Pawlik, B. Schmidt, K. Furusawa, A. Malinowski, D. J. Richardson, and U. Keller, "Optical parametric oscillator with a pulse repetition rate of 39 GHz and 2.1-W signal average output power in the spectral region near 1.5μm," Opt. Lett. **30**(3), 290–292 (2005).

[24] R. G. Batchko, D. R. Weise, T. Plettner, G. D. Miller, M. M. Fejer, and R. L. Byer, "Continuous-wave 532-nm-pumped singly resonant optical parametric oscillator based on periodically poled lithium niobate," Opt. Lett. **23**(3), 168–170 (1998).

[25] O. Gayer, Z. Sacks, E. Galun, and A. Arie, "Temperature and wavelength dependent refractive index equations for MgO-doped congruent and stoichiometric $LiNbO_3$," Applied Physics B: Lasers and Optics **91**(2), 343–348 (2008).

[26] L. Moretti, M. Iodice, F. G. Della Corte, and I. Rendina, "Temperature dependence of the thermo-optic coefficient of lithium niobate, from 300 to 515 K in the visible and infrared regions," Journal of Applied Physics **98**(3), 036,101–3 (2005).

[27] W. A. Clarkson, "Thermal effects and their mitigation in end-pumped solid-state lasers," Journal of Physics D-Applied Physics **34**(16), 2381–2395 (2001).

[28] D. N. Nikogosyan, *Nonlinear optical crystals: a complete survey*, 1st ed. (Springer, Berlin / Heidelberg, 2005).

[29] D. D. Lowenthal, "CW periodically poled $LiNbO_3$ optical parametric oscillator model with strong idler absorption," IEEE Journal of Quantum Electronics **34**(8), 1356–1366 (1998).

[30] L. Lefort, K. Puech, G. W. Ross, Y. P. Svirko, and D. C. Hanna, "Optical parametric oscillation out to 6.3μm in periodically poled lithium niobate under strong idler absorption," Applied Physics Letters **73**(12), 1610–1612 (1998).

[31] A. Henderson and R. Stafford, "Intra-cavity power effects in singly resonant cw OPOs," Applied Physics B: Lasers and Optics **85**(2), 181–184 (2006).

[32] L. E. Myers and W. R. Bosenberg, "Periodically Poled Lithium Niobate and Quasi-Phase-Matched Optical Parametric Oscillators," IEEE Journal of Quantum Electronics **33**(10), 1663–1672 (1997).

[33] A. E. Siegman, M. W. Sasnett, and T. F. Johnston, "Choice of Clip Levels for Beam Width Measurements Using Knife-Edge Techniques," IEEE Journal of Quantum Electronics **27**(4), 1098–1104 (1991).

[34] K. König, T. W. Becker, P. Fischer, I. Riemann, and K. J. Halbhuber, "Pulse-length dependence of cellular response to intense near-infrared laser pulses in multiphoton microscopes," Opt. Lett. **24**(2), 113–115 (1999).

[35] K. K. Chen, J. H. V. Price, S.-U. Alam, J. R. Hayes, D. J. Lin, A. Malinowski, and D. J. Richardson, "Polarisation maintaining 100W Yb-fiber MOPA producing μJ pulses tunable in duration from 1 to 21 ps," Opt. Express **18**(14), 14,385–14,394 (2010).

[36] K. Kieu, B. G. Saar, G. R. Holtom, X. S. Xie, and F. W. Wise, "High-power picosecond fiber source for coherent Raman microscopy," Opt. Lett. **34**(13), 2051–2053 (2009).

[37] A. M. Zheltikov, "Coherent anti-Stokes Raman scattering: from proof-of-the-principle experiments to femtosecond CARS and higher order wave-mixing generalizations," Journal of Raman Spectroscopy **31**(8-9), 653–667 (2000).

Chapter 4

High-pulse-energy, compact, picosecond optical parametric oscillator

4.1 Introduction

Ultrashort-pulse, NIR and MIR tunable laser sources with high pulse energies in the μJ- and mJ-range are required in the field of materials processing in general and in resonant IR pulsed laser deposition of polymers [1, 2] in particular. Also, ultrafast waveguide inscription in IR materials such as silicon or germanium requires high-energy sources with megahertz repetition rates that cover the $1\,\mu\mathrm{m}$ to $2\,\mu\mathrm{m}$ region and beyond [3]. Bulk solid-state amplifier systems at low repetition rates in the kilohertz range have been used in the past to generate high pulse energies, where Ti:sapphire offered the widest tunability. However, important wavelength regions in the NIR and MIR could not be accessed. Optical parametric amplifiers (OPA) pumped by Ti:sapphire sources can extend the wavelength range into the MIR with millijoule pulse energies [4], but at kilohertz repetition rates. Therefore, in resonant IR pulsed laser deposition and ablation, expensive and complex free-electron lasers are still used today.

An attractive alternative to the described high-pulse-energy systems are compact and pulsed OPOs using periodically poled materials that allow convenient access to the desired wavelength regions at multi-megahertz repetition rates. MgO:PPLN OPOs pumped with nanosecond Q-switched or directly modulated laser diodes (LD) producing (combined signal and idler) pulse energies of $220\,\mu\mathrm{J}$ [5], $9\,\mathrm{mJ}$ [6] and $77\,\mathrm{mJ}$ [7] have been demonstrated. However, these OPOs did not deliver ultrashort pulses required in many materials processing applications. Ultrashort, synchronously pumped

OPOs based on periodically poled crystals with pulse durations in the nJ-region include 77 ps pulses at 76 MHz from an Nd:YAG-laser-pumped, standing-wave-cavity, MgO:PPLN SPOPO [8] with signal and idler energies of 105 nJ and 66 nJ, respectively; 1.5 ps pulses at 15.3 MHz from a YDF-laser-pumped, MgO:PPLN SPOPO using a relay-imaging cavity [3] with a signal energy of 71 nJ; and 840 fs pulses at 56 MHz from a thin-disk-laser-pumped, fibre-feedback-cavity, PPsLT SPOPO [9] with signal and idler energies of 339 nJ and 139 nJ. Lamour *et al.* reported 650 nJ from an optimised version of the relay-imaging cavity SPOPO employing a cavity-dumping scheme [10, 11].

The experiments presented in this chapter investigate high-pulse-energy operation of a picosecond SPOPOs with a similar fibre-feedback resonator to that reported in [9, 12], although the motivation to apply such a resonator was different. Rather than exploiting a high gain and large output coupling to achieve stable femtosecond operation insensitive to external perturbations, the goal of this work was to build a compact, robust and stable SPOPO system producing high pulse energies. This required a relatively low repetition rate of 7.19 MHz and thus a much longer fibre with a length of ≈ 27 m. Another possibility to achieve a compact SPOPO cavity generating high pulse energies is to match the repetition rate to the pump source and use relay-imaging optics to reduce the cavity footprint as described in [3, 11]. However, the system complexity grows with each additional imaging component and alignment and stability is impaired.

The fibre-amplified, gain-switched LD source used to pump the SPOPO was similar to that described in chapter 3.2 but operated at much lower repetition rate and hence much higher pulse energy. Furthermore, the fibre-amplifier chain was up-graded to an all-polarisation-maintaining (PM) setup [13].

The pump source for the SPOPO in this work was developed by Kang Kang Chen and operated by Peh Siong Teh. The SPOPO was set-up and all the experiments were carried out by the author.

4.2 Pump source experimental setup

The 1.06 μm pump source has been modified to an all-PM setup as compared to the system described in chapter 3.2, which improves the polarisation stability of the output needed for certain materials processing applications and frequency-doubling experiments undertaken with this source [13]. The first fibre amplifier now incorporated a 3 m-long, core-pumped, single-mode, Yb-doped, PM fibre with a 5 μm core and a 130 μm cladding. It was pumped in the same configuration as described in 3.2. The second amplifier incorporated a 7 m-long, cladding-pumped, single-mode, Yb-doped, PM fibre with a 5 μm core (NA 0.13) and a 130 μm inner cladding (NA 0.46), which was now

cladding-pumped only by one diode ($10\,\mathrm{W}$, $975\,\mathrm{nm}$) and in a backwards configuration. The final amplifier remained unaltered. The second modification to the pump source was that the CFBG was by-passed so that the output pulses from the gain-switched LD seed were not chirp-compensated leading to an increase in pulse duration from $21\,\mathrm{ps}$ to $\approx 100\,\mathrm{ps}$. As a result of this, the peak intensity was sufficiently reduced to avoid non-linear effects such as SRS or SPM in the fibre amplifiers. Pulse energies of up to $8.6\,\mu\mathrm{J}$ corresponding to $62\,\mathrm{W}$ of average power at the operating repetition rate of $7.19\,\mathrm{MHz}$ in a near-diffraction-limited ($M^2 = 1.2$ at any power level), linearly polarised beam could be obtained from this system.

4.3 Fibre-feedback, ring cavity optical parametric oscillator setup

A schematic diagram of the fibre-feedback bow-tie SPOPO ring cavity used in this work is shown in figure 4.1. A ring cavity is better compared to a standing-wave cavity, since in a standing-wave arrangement with the fibre in one arm, launch losses, chromatic dispersion and potential nonlinear effects would be doubled due to the double pass of the signal pulses through the fibre. An MgO:PPLN piece (Covesion Ltd., United Kingdom) with dimensions of $L = 40\,\mathrm{mm}$, $H = 10\,\mathrm{mm}$ and $W = 1\,\mathrm{mm}$ and with five periodically poled gratings ranging from $29.5\,\mu\mathrm{m}$ to $31.5\,\mu\mathrm{m}$ was used. Each grating had a $1\,\mathrm{mm} \times 1\,\mathrm{mm}$ wide aperture. The $40\,\mathrm{mm}$ length had a sufficient phase-matching bandwidth and minimal temporal walk-off for the involved wavelengths compared to the $100\,\mathrm{ps}$ pump pulses. The calculated GVM for a $1.5\,\mu\mathrm{m}$ signal and the $1.06\,\mu\mathrm{m}$ pump is $95\,\mathrm{fs/mm}$, which leads to an acceptable walk-off of $3.8\,\mathrm{ps}$ along the entire crystal length. In order to eliminate any residual photo-refraction, the crystal was held in an oven at an elevated temperature of $150^{\circ}\mathrm{C}$.

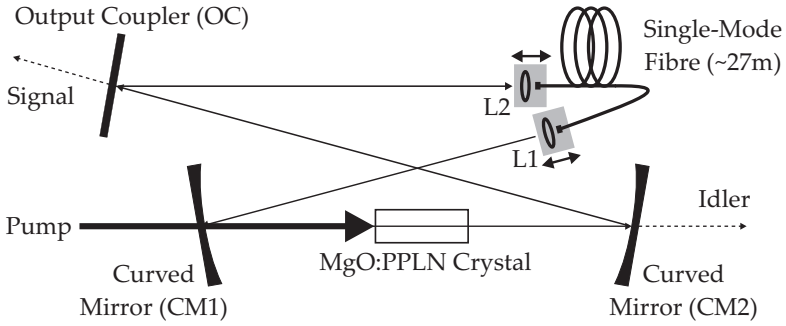

FIGURE 4.1: Schematic diagram of the fibre-feedback bow-tie SPOPO cavity. The curved mirrors CM 1 and CM 2 have radii of curvature of $-250\,\mathrm{mm}$ and the fibre coupling lenses L 1 and L 2 (aspherical) have focal lengths of $4.5\,\mathrm{mm}$.

The two main criteria of the resonator design, namely obtaining large waist sizes to reduce the peak intensities and obtaining synchronism with the pump source repetition

rate, were separated by choosing a free-space section of the resonator first in order to model the waist sizes (no fibre in the setup, but a plane "dummy" mirror model) and then removing the "dummy" mirror and inserting the fibre into the resonator, cut to the right length, to achieve synchronism.

Similar resonator design consideration as for the SPOPO in chapter 3, i.e. (1) avoiding the physical clipping of the beams at the crystal clear aperture, (2) obtaining the largest possible beam waist radii to reduce the peak intensities and (3) considering the limitations due to the availability of curved mirrors with different radii of curvature, limited the design options to a signal waist radius around $100\,\mu\mathrm{m}$. A Gaussian beam propagation model and the well-known ABCD matrix formalism [14] were used to model the ring resonator, which resulted in calculated beam waist radii ($1/e^2$-intensity) of the signal in the centre of the MgO:PPLN of $99.4\,\mu\mathrm{m}$ and $98.0\,\mu\mathrm{m}$ (parallel and perpendicular to the resonator plane) using curved mirrors (CM 1, CM 2) with a radius of curvature of $-250\,\mathrm{mm}$. The signal waist asymmetry in the two orthogonal resonator planes was caused by astigmatism due to the bow-tie angle of $10.2°$, which was necessary because of mechanical limits set by the physical dimensions of mirror and crystal mounts. The signal focusing parameter was $\xi_s \approx 0.45$, which deviates significantly from the ideal case of $\xi_s = 1$, but this was again accepted in favour of reducing the peak intensities to a minimum. The cavity model produced a total free-space section of $1.35\,\mathrm{m}$ for a stable ring resonator with the $\approx 99\,\mu\mathrm{m}$ signal waist resulting in an arbitrary repetition rate of $222\,\mathrm{MHz}$ when neglecting the fibre section (with dummy mirror in the model). In order to obtain a good match of the signal and the pump inside the nonlinear crystal, a telescope with a $150\,\mathrm{mm}$ and a $200\,\mathrm{mm}$ lens and a $250\,\mathrm{mm}$ focusing lens formed the pump beam to generate a waist of $104\,\mu\mathrm{m}$.

The feedback fibre covering the majority of the $41.72\,\mathrm{m}$ ring cavity optical path length (corresponds to $7.19\,\mathrm{MHz}$) was a standard single-mode fibre (SMF 28e, Corning Inc., USA) for the telecommunications C-band around $1.55\,\mu\mathrm{m}$, which coincides with the typical signal wavelength range of this SPOPO. To obtain synchronism with the pump pulse repetition rate, the fibre was inserted in the resonator and must have a physical length of $41.72\,\mathrm{m}$ minus the free-space section and divided by the group index of a signal pulse in silica at the correct wavelength. The two fibre ends were positioned at points between CM 1 and the OC close to where the dummy mirror of the model was located, so that a good fibre launch efficiency could be achieved taking the propagation of the signal beam in the resonator into account. The beam radius at these points (as calculated by the model) was $0.5\,\mathrm{mm}$. For a good launch efficiency, the numerical aperture (NA) of the focused beam going into the fibre core should ideally be equal to the NA of the fibre core, which is approximately 0.14 and corresponds to an angle of $8.05°$. Using simple trigonometry, a lens with a focal length of $\approx 3.6\,\mathrm{mm}$ or larger is required to achieve an NA that matches 0.14. Aspherical lenses with $f = 4.5\,\mathrm{mm}$ were chosen

(L 1, L 2). Both the fibre input / output ends and the aspherical lenses were mounted on three-axis translation stage assemblies to allow for launch alignment on the input side and for beam collimation on the output side. Fibre throughput efficiencies, including launch efficiency and fibre loss, were typically around 50% as measured for the pump beam after it had passed through the cavity to the fibre (see figure 4.1). As a first approximation, the launch efficiency of the resonating signal was assumed to be similar to this, because the cavity model delivers a beam radius at the fibre input of around $0.4\,\mathrm{mm}$ for the pump compared to $0.5\,\mathrm{mm}$ for the signal, where both numbers yield NAs of 0.11 and 0.09, respectively, well within the NA limit of 0.14 of the fibre. Since the fibre section is relatively long and vital to achieve synchronism, accurate values of the refractive indices $n(\lambda, T)$ and group indices

$$n_g\,(\lambda, T) = n(\lambda, T) - \lambda \frac{dn(\lambda, T)}{d\lambda} \tag{4.1}$$

were calculated with the temperature-dependent Sellmeier equation of such a single-mode fibre (GeO_2-doped SiO_2 core and pure SiO_2 cladding) as given in [15]. The dispersion curves at $20^\circ\mathrm{C}$ are shown in figure 4.2(a). With the exact fibre core group index of $n_{g,core}(1.504\,\mu\mathrm{m}, 20^\circ\mathrm{C}) = 1.481738$, which reflects how fast a signal pulse travels inside the fibre at this centre wavelength (given by the MgO:PPLN grating), a fibre length of $27.24\,\mathrm{m}$ was calculated.

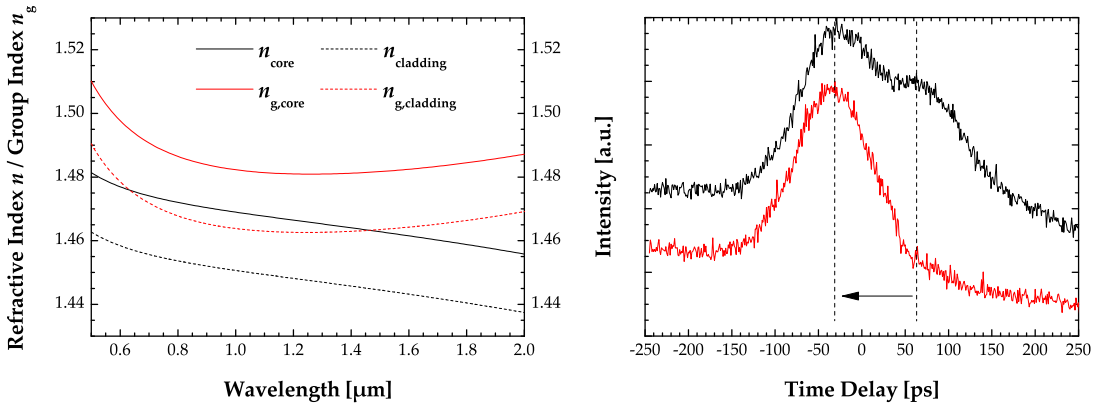

FIGURE 4.2: (a) Refractive index $n(\lambda, T)$ and group index $n_g(\lambda, T)$ as a function of wavelength of a silica fibre. The group velocity of a pulse propagating in the fibre can be determined with the group index. The SiO_2 core is doped with GeO_2 to raise the refractive index, the cladding is pure SiO_2. (b) Time delay of the reflected and resonating pump pulse. The red curve shows only the input pulse, while the black curve shows both the input pulse and the resonating pulse. The time delay was $\approx 90\,\mathrm{ps}$ here. The cavity length had to be tuned to shift the resonating pulse towards the input pulse to achieve synchronism as indicated by the arrow.

Coarse spatial alignment of the cavity was undertaken by exploiting the low-level, non-phase-matched second harmonic of the pump beam generated in the MgO:PPLN. Fine tuning to achieve synchronism was carried out by directing the pump pulse reflected from the curved surface of CM 1 and the weak pump pulse transmitted through CM 1

after completing one round trip in the cavity onto a $32\,\mathrm{GHz}$ InGaAs photodiode and observing their mutual time delay on a $50\,\mathrm{GHz}$ communication signal analyzer (CSA). In order to get similar intensities for both pulses on the detector, the reflected beam from CM 1 was intentionally misaligned away from the centre of the sensitive area of the detector. It has to be taken into account that the group delay of a signal pulse is different to the group delay of a pump pulse and hence the described procedure only helps to obtain synchronism of the resonating pump pulse. However, the difference in cavity length between a pump pulse at $1.06\,\mu\mathrm{m}$ and a signal pulse at $1.504\,\mu\mathrm{m}$ was only a few millimetres as determined from the dispersion curves in figure 4.2(a) and can readily be covered by movement of the translation stages along the signal beam path. Typical CSA traces are shown in figure 4.2(b), where the red curve shows only the input pulse reflected from CM 1 and the black curve shows both the input pulse and the resonating pulse. The time delay in this case was roughly $90\,\mathrm{ps}$. Thus, the cavity length had to be tuned by the corresponding length of $2.7\,\mathrm{cm}$ to shift the resonating pulse towards the input pulse to achieve synchronism as indicated by the arrow.

The MgO:PPLN input and output surfaces were broadband AR-coated for the signal wavelength range and the pump wavelength. The curved mirrors, based on CaF_2 substrates, were highly transmissive at the pump wavelength and in the MIR, which led to singly resonant operation additionally supported by the fact that the SMF 28e fibre does not transmit MIR wavelengths. A large signal OC transmission of 90% provided efficient output power extraction and also ensured that relatively low power levels were propagating in the feedback fibre to avoid unwanted nonlinear effects. Nevertheless, it has been found experimentally that the fibre input side must be placed in a heat sink arrangement to avoid gradual damage of the end facet. Furthermore, the coiled fibre was enclosed in a box to reduce the sensitivity to ambient temperature fluctuations. Lenses L 1 and L 2 also had broadband AR coatings for the pump and the signal range.

4.4 Experiments

4.4.1 Results

Figure 4.3 shows the signal and idler output power and the pump depletion versus pump power incident upon CM 1 (92% transmission at $1.06\,\mu\mathrm{m}$) of the fibre-feedback SPOPO using a signal OC with 90% transmission. Figure 4.4 shows the same results but in terms of pulse energies rather than average powers. From the range of available signal OCs, this OC gave the best performance and the highest output power as can be seen in figure 4.5, where the signal output power is plotted as a function of OC transmission. The SPOPO did not oscillate when a simple glass window with $\approx 4\%$

reflection was used as OC. The idler beam was extracted through CM 2, which had a transmission of around 88% for the idler wavelengths. All values given in the figures were external to the cavity. The oscillation threshold was reached at an average pump power of $3.94\,\mathrm{W}$ and was evident by observing the small amount of pump and signal sum-frequency red light. The SPOPO generated a maximum of $3.51\,\mathrm{W}$ and $1.37\,\mathrm{W}$ at $1.504\,\mu\mathrm{m}$ and $3.591\,\mu\mathrm{m}$, respectively, when pumped with $20\,\mathrm{W}$. The pump depletion saturated at a relatively low level of approximately 35%. The signal and idler pulse energies corresponding to the average powers above were $488\,\mathrm{nJ}$ and $191\,\mathrm{nJ}$, respectively. The obtained signal pulse energy was below the highest energy of $650\,\mathrm{nJ}$ demonstrated with an MgO:PPLN SPOPO [10, 11], but the combined energy of signal and idler was, to the best of the author's knowledge, a new record and has many useful applications.

The feedback fibre was not polarisation-maintaining and possibly led to a de-polarisation of the signal beam. In an attempt to deliver a linearly polarised beam of the correct (extraordinary) orientation to the nonlinear crystal for maximum conversion efficiency, a three-paddle manual fibre polarisation controller was inserted at the fibre output end, but did not lead to significantly improved output powers, which could be explained by the fact that such a polarisation controller can not generate perfectly linear polarisation along the correct axis with respect to the nonlinear crystal.

The SPOPO operated in the high small-signal gain regime, as estimated from the threshold level and the high OC transmission as follows. The estimated parametric gain required to reach the oscillation threshold (gain equals loss) was ≈ 40 ($16\,\mathrm{dB}$), mainly due to the high OC transmission (round-trip signal power attenuation factor 0.1), the loss at fibre launching (factor 0.5) and the incorrect polarisation at the fibre output (factor 0.5). In a steady-state oscillator, the gain should saturate at this value. The equation for high gain is given by (2.58), therefore the threshold gain exponent $2\Gamma L$ becomes ≈ 5. At the highest pump power, which corresponded to operation at $\approx 5\times$ above threshold, this exponent was $\sqrt{5}\times$ greater due to Γ^2 being proportional to the pump power. Thus, $2\Gamma L = 11.2$ corresponding to an effective small-signal gain of $\approx 43\,\mathrm{dB}$ at this operating point. A more accurate calculation of the effective gain exponent is complicated by the uncertainty over the effective pump intensity, because it had a Gaussian rather than a plane-wave form. The high parametric gain resulted in a remarkable insensitivity to additional intracavity losses as reported before [9, 12]. This was shown in an initial SPOPO setup with an $R = 95\%$ OC, i.e. a low output coupling of only 5%, where oscillation was maintained and the threshold stayed constant even with a 50 / 50 beam splitter inserted between the fibre output end and the OC to extract 50% of the signal light from the resonator.

As can be seen in figure 4.3 and 4.4, a power roll-off was setting in with increasing

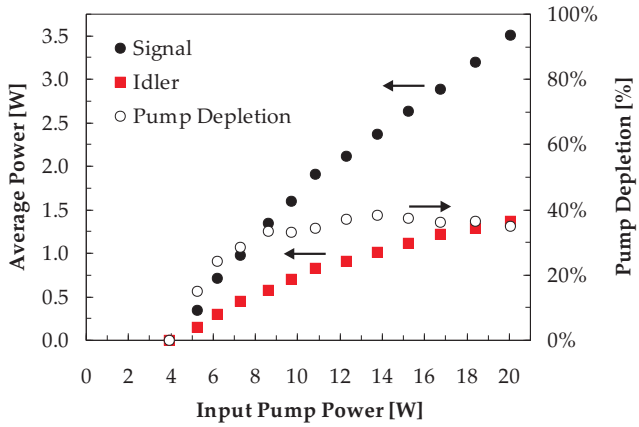

FIGURE 4.3: Output power and pump depletion as a function of input pump power of the fibre-feedback SPOPO using a signal output coupler with a transmission of 90%.

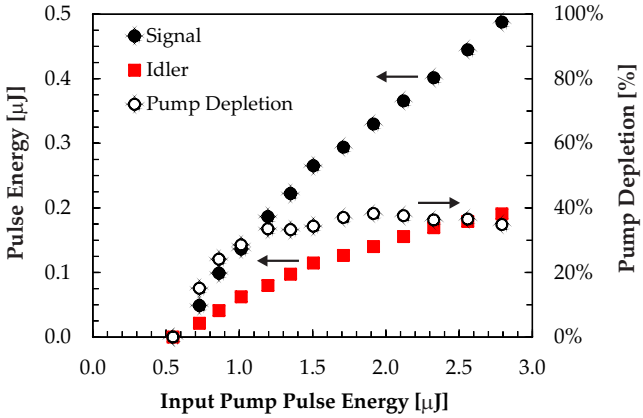

FIGURE 4.4: Signal and idler pulse energy and pump depletion as a function of input pump pulse energy of the fibre-feedback SPOPO using a signal output coupler with a transmission of 90% (same experimental data as in figure 4.3).

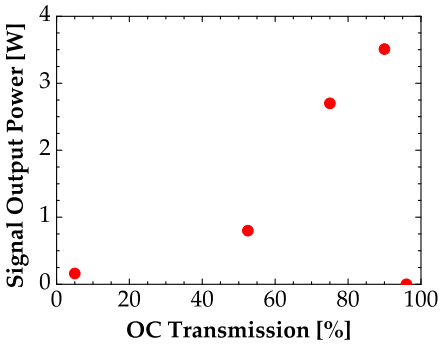

FIGURE 4.5: Signal output power as a function of OC transmission of the fibre-feedback SPOPO. The highest output power was obtained at 90% output coupling.

pump power. This became more apparent, when the pump power was further increased beyond $20\,\mathrm{W}$ and resulted in significant instabilities and a complete output power drop. The origin of this effect was not completely understood, as already mentioned in chapter 3, where a very similar effect was observed. Unlike the findings in that chapter, the effect did not appear to be correlated with MgO:PPLN average power limitations in this experiment, since a reduction of the pump average power with a 50% duty cycle mechanical chopper did not improve the performance as shown in figure 4.6, where the displayed values are average power values during the "transmit" cycle of the chopper, i.e. the measured average power multiplied by 2. The oscillation ceased altogether at a pump power of around $35\,\mathrm{W}$. It is worth mentioning that no visible damage was observed, when the crystal was examined under a microscope. There are indications that the limitation may lie in the pump source and particularly in the Faraday rotator crystal of the optical isolator [16, 17] used to protect the pump source from back-reflections, which is known to suffer from thermal effects at power levels $> 20\,\mathrm{W}$.

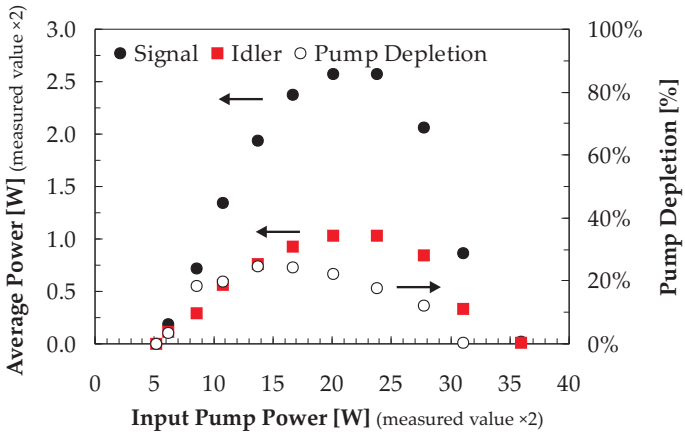

FIGURE 4.6: Power roll-off at pump powers higher than $20\,\mathrm{W}$ of the fibre-feedback SPOPO. The output coupling was 90% and a mechanical chopper (50% duty cycle, $\approx 50\,\mathrm{Hz}$ frequency) was placed in the pump beam to reduce the average power incident on the nonlinear crystal. The values displayed in the graph are the average power values during the "transmit" cycle of the chopper, i.e. the measured average power multiplied by 2.

Spectral tuning of the SPOPO was demonstrated by accessing different poled gratings of the MgO:PPLN crystal at a constant temperature of $150^{\circ}\mathrm{C}$ and at the highest pump power as shown in figure 4.7. Due to the changing group velocity of the signal pulses, it was necessary to adjust the cavity length of the relatively long resonator to maintain synchronism. The signal could be tuned from $1.50\,\mu\mathrm{m}$ to $1.69\,\mu\mathrm{m}$ by using 4 of the 5 poled gratings, which corresponds to an idler range from $2.84\,\mu\mathrm{m}$ to $3.61\,\mu\mathrm{m}$. The signal wavelengths were measured using an OSA with a resolution of $0.02\,\mathrm{nm}$ and the idler wavelengths were inferred, although separate measurements of the idler wavelength using an MIR monochromator (resolution $0.5\,\mathrm{nm}$) confirmed their accuracy. The signal wavelength of the fifth poled grating with a period of $31.5\,\mu\mathrm{m}$ could not be measured,

because the OSA was not sensitive beyond $1.7\,\mu\mathrm{m}$. Continuous tuning can be achieved by additionally varying the temperature. The dashed curve indicates the theoretical tuning behaviour derived from the temperature-dependent Sellmeier equation [18].

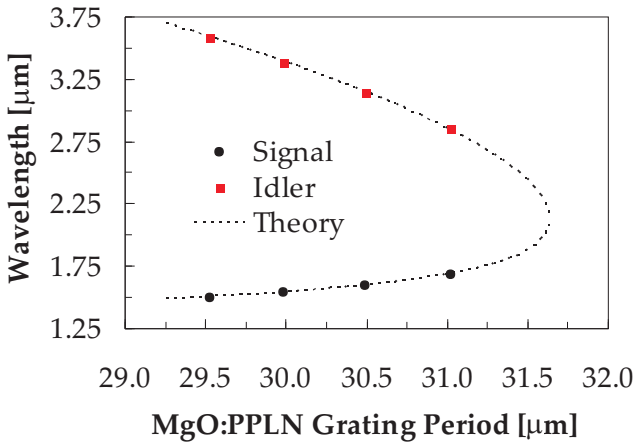

FIGURE 4.7: Signal and idler tuning curve of the fibre-feedback SPOPO. Different MgO:PPLN grating periods were accessed at a constant temperature of $150^{\circ}\mathrm{C}$. The idler wavelengths were inferred from the measured signal wavelengths and the dashed curve is the theoretical tuning curve. No measurement of the signal wavelength for the $31.5\,\mu\mathrm{m}$ poled grating was carried out, since the upper wavelength limit of the OSA was $1.7\,\mu\mathrm{m}$.

Characteristic spectra of the pump, the signal and the idler are plotted in figure 4.8 at the highest pump power of $20\,\mathrm{W}$. The amplified pump FWHM bandwidth was $0.25\,\mathrm{nm}$, which with the $100\,\mathrm{ps}$ pulse duration gives a time-bandwidth product of 6.67 and this is more than $15\times$ higher than the bandwidth limit. The signal and idler bandwidths were $\approx 2\,\mathrm{nm}$ at a centre wavelength of $1.504\,\mu\mathrm{m}$ and $\approx 12\,\mathrm{nm}$ at $3.61\,\mu\mathrm{m}$, respectively, indicating strongly chirped pulses. The noise on the idler spectrum was mainly caused by the slow acquisition speed of the monochromator and the low idler power after passing through the device leading to a reduced signal-to-noise ratio. From equations (2.64) and (2.65), with $C = 5.56$ (full width definition) and with the centre wavelengths above, the signal gain bandwidth and the pump acceptance bandwidth become $\Delta\omega_{PM} = 1.16 \cdot 10^{12}\,\mathrm{rad/s}$ and $\Delta\omega_{PA} = 5.82 \cdot 10^{12}\,\mathrm{rad/s}$, respectively. The $2\,\mathrm{nm}$ signal bandwidth expressed in angular frequency is $1.67 \cdot 10^{12}\,\mathrm{rad/s}$ and hence slightly higher compared to the signal gain bandwidth. However, the gain bandwidth increases in the high gain condition according to equation (2.63). Solving the gain exponent $2\Gamma L = 11.2$ as determined earlier for Γ and inserting this value and the crystal length $L = 40\,\mathrm{mm}$ into equation (2.63), a ratio of high gain to low gain bandwidth of 2.0 is calculated. Therefore, the signal gain bandwidth $\Delta\omega_{PM}$ is $2\times$ higher in the high gain case, so that the actual signal bandwidth of $1.67 \cdot 10^{12}\,\mathrm{rad/s}$ does not exceed it. The $0.25\,\mathrm{nm}$ pump bandwidth corresponds to $0.42 \cdot 10^{12}\,\mathrm{rad/s}$ and is therefore well within the acceptable pump bandwidth. A Raman peak on the long wavelength side of the signal spectrum was not observed and this was not expected, since the SRS peak power threshold as given in equation (2.14) was approximately $500\,\mathrm{W}$ with the

mode-field area $A_{eff} = 85\,\mu\mathrm{m}^2$ (mode-field diameter $10.4\,\mu\mathrm{m}$ at $1550\,\mathrm{nm}$), the Raman gain coefficient $g_R = 10^{-13}\,\mathrm{m/W}$ [19] and the fibre length $L_{eff} = 27.24\,\mathrm{m}$, whereas the signal pulse peak power inside the fibre was only $278\,\mathrm{W}$. This pulse peak power was calculated assuming that $0.4\,\mathrm{W}$ of the signal was reflected by the OC towards the fibre, as $3.5\,\mathrm{W}$ was extracted from the resonator through the 90% transmission OC, and it was assumed that only 50% of the remaining power was launched into the fibre. Comparing the frequency bandwidths of the signal ($\Delta\omega_s = 1.67 \cdot 10^{12}\,\mathrm{rad/s}$) and idler ($\Delta\omega_i = 1.74 \cdot 10^{12}\,\mathrm{rad/s}$) to the pump bandwidth ($\Delta\omega_p = 0.42 \cdot 10^{12}\,\mathrm{rad/s}$) shows that both signal and idler were spectrally broadened by around a factor of 4. The B-integral of the signal pulse in the SMF is calculated to be 2.9π and indicates operation in the nonlinear regime, where spectral broadening due to SPM is expected. Simulations of the signal pulse propagation in the SMF show, however, that the signal spectrum and pulse duration remain relatively unaffected by the SPM (this is further discussed in the following section).

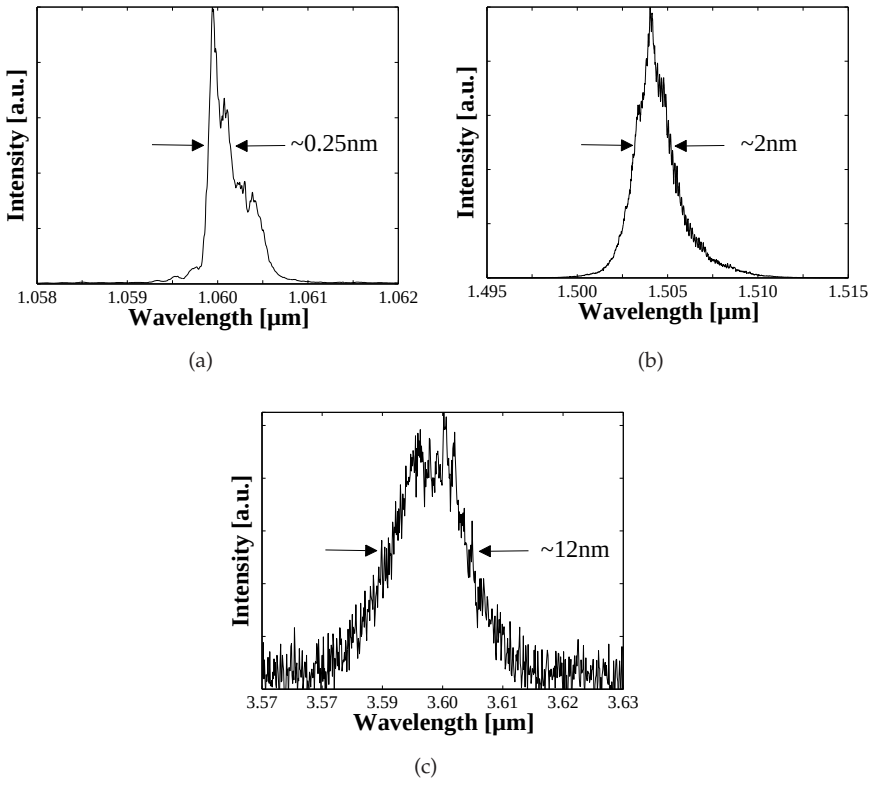

FIGURE 4.8: (a) Pump, (b) signal and (c) idler spectra of the fibre-feedback SPOPO at the highest pump power of $20\,\mathrm{W}$. The FWHM bandwidths are indicated in the graphs.

The pulse duration of the signal pulses was measured with the $32\,\mathrm{GHz}$ InGaAs photodiode and the $50\,\mathrm{GHz}$ CSA. The combination of the two devices had an experimentally determined minimum measurable pulse duration of $30\,\mathrm{ps}$. The measured $100\,\mathrm{ps}$ signal pulse duration was the same as the pump pulse duration. No pulse diagnostics were

available for the idler pulses in the MIR, but it is expected that they also have a similar duration.

The M^2-beam quality of the signal and the idler was determined at $20\,\mathrm{W}$ of average pump power with the same techniques as described in 3.4.2. The signal M^2 was 1.53×1.29 and the idler M^2 was 2.80×1.88 in the planes parallel (x) and perpendicular (y) to the ring cavity plane, respectively. Figure 4.9 shows the caustic plots of the measurements. These M^2-value values were worse than the value of the input pump beam of 1.20. The higher values in each case occurred in the plane, which was perpendicular to the nonlinear crystal plane corresponding again to the situation described in chapter 3, where it was speculated that thermal lensing effects and / or spot size asymmetry deteriorate the beam quality.

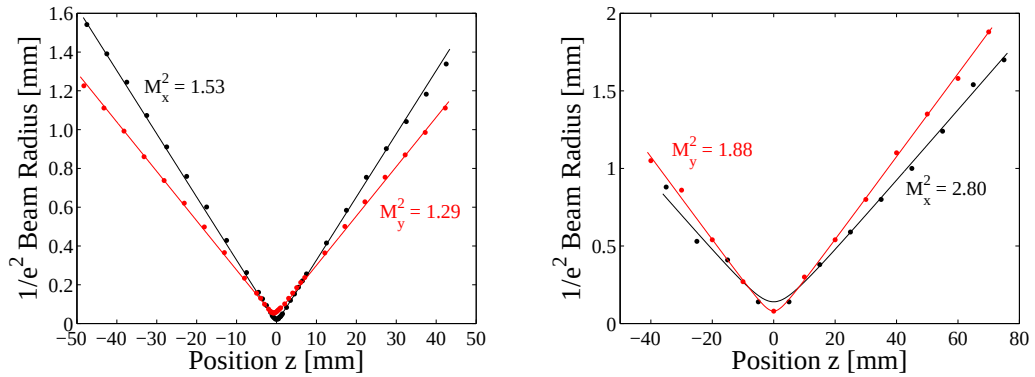

(a) Signal (b) Idler

FIGURE 4.9: Beam caustic plots and curve fits for the M^2-measurement of the fibre-feedback SPOPO for (a) the signal beam and (b) the idler beam at a pump power of $20\,\mathrm{W}$.

4.4.2 Discussion

A treatment of the SPOPO efficiency and loss is based on a simple photon budget calculation at the highest pump power. The $20\,\mathrm{W}$ of pump power are reduced to $17.14\,\mathrm{W}$ inside the crystal due to reflection losses of the CM 1 and crystal coatings. The pump depletion of 35% means that a power of only $6.00\,\mathrm{W}$ of the $17.14\,\mathrm{W}$ is converted into signal and idler. Taking the quantum defects into account, the theoretical maximum powers inside the resonator are $4.23\,\mathrm{W}$ and $1.77\,\mathrm{W}$ for the signal and idler, respectively. This signal power must be multiplied by $-\ln R_{OC}/\left(-\ln R_{OC} - \ln R_C\right)$, which accounts for the resonator losses during one round-trip (R_{OC} is the output coupler reflectivity and R_C the effective cavity reflectivity). Note that the negative logarithmic values are required here, since the output coupling transmission of $T_{OC} = 0.9$ is very high and hence the approximation $T_{OC} \approx -\ln R_{OC}$ is no longer valid. A value for the signal round-trip loss $\epsilon_s = 1 - R_C$ can be found by comparing the measured signal power

(3.51 W) and the theoretical power (4.23 W) including the loss factor above, which results in a value of $\epsilon_s = 0.38$. These high losses can be explained with the loss during launching of the signal beam into the SMF and the reduced parametric conversion efficiency due to the incorrect polarisation of the signal beam after propagating through the fibre. The situation could be improved by using a polarisation-maintaining fibre in future experiments. In terms of the non-resonating idler, the theoretical power of 1.77 W inside the nonlinear crystal is multiplied by the coating transmission of the crystal (90%, estimated) and CM 2 (88.4%, measured) to yield a value of 1.41 W, which is in good agreement with the measured 1.37 W.

The fact that the signal and idler spectrum was about $4\times$ broader than the pump spectrum suggests spectral broadening in the intracavity SMF. With 0.2 W of signal input power, $n_2 = 2.45 \cdot 10^{-20}\, m^2/W$ and the mode-field diameter of $10.4\,\mu$m, the accumulated nonlinearity of the signal pulses along the 27.24 m-long fibre is $B \approx 2.9\pi$. Simulations of the signal pulse propagation in the SMF show that if the signal pulse spectrum initially has a bandwidth similar to the pump, it will be broadened by SPM. However, these simulations also show that once the spectrum is broadened to the extent measured experimentally, there will be negligible change on further propagation in the fibre. Hence, a steady-state condition will be reached. In addition, the phase-matching bandwidth of the MgO:PPLN may impose a final limit in that gain narrowing and SPM broadening balance each other. Note that the contribution of the fibre dispersion to the temporal chirp is negligible compared to the strong initial negative chirp imposed on the signal pulses, where it is assumed that the negative chirp of the pump pulses (originating from the gain-switched laser diode, see section 2.2.1.2) is transferred to the signal pulses. Furthermore, the dispersion length $L_D = \tau^2/|\beta_2|$ is four orders of magnitude larger than the nonlinear length $L_{NL} = 1/\gamma P_0$ and three orders of magnitude larger than the fibre length, so that dispersion can not dominate here [19].

The use of an LMA fibre would help to increase the threshold peak power for Raman generation, if further pulse energy scaling is undertaken. Currently, with this setup, the threshold of 500 W is high enough to avoid SRS, but it could be increased to 4 kW by simply employing a LMA fibre with a mode-field diameter of $30\,\mu$m. To reach this threshold, signal pulse energies of up to 400 nJ in the fibre could be accepted, corresponding to $7.2\,\mu$J output-coupled with a $T = 90\%$ OC mirror. This is approximately $15\times$ higher than the maximum pulse energy of 488 nJ measured with the current setup. Simultaneously, the B-integral would be reduced from 2.9π to 0.3π.

Additional to the use of an LMA fibre in the cavity, further energy scaling to pulse energies of more than $1\,\mu$J and shorter pulse durations could also be achieved by scaling the beam waist sizes inside the MgO:PPLN crystal in order to reduce the peak intensities. A set of curved mirrors with a $2\times$ larger radius of curvature than the -250 mm

mirrors used here, for instance, would allow signal beam radii between $\approx 120\,\mu\mathrm{m}$ and $\approx 230\,\mu\mathrm{m}$ by varying the free-space length of the cavity by only $1\,\mathrm{m}$ (distance between CM and OC is changed, distance between CMs and crystal is kept constant). As before, synchronism with the pump repetition rate can then be achieved by cutting the fibre to the correct length. The boundaries regarding beam divergence and beam clipping are more relaxed with the $1\,\mathrm{mm}$-wide MgO:PPLN sample and clipping does not occur for the waist radius range above. An increase of the waist size inside the crystal by changing the free-space resonator length corresponds to a decrease of the beam size in the bow-tie arms of the ring cavity and thus at the location of the fibre input and output ends. But with the appropriate choice of the focal length of the aspherical lenses with respect to the fibre geometry, mainly the core NA, a good launch efficiency at the fibre input side and a good beam collimation at the fibre output side can be maintained.

4.5 Conclusions

This chapter described a $100\,\mathrm{ps}$, MgO:PPLN, ring cavity SPOPO operating at a low repetition rate of $7.19\,\mathrm{MHz}$ and producing $488\,\mathrm{nJ}$ and $191\,\mathrm{nJ}$ of signal and idler pulse energies at a pump pulse energy of $2.79\,\mu\mathrm{J}$ (average pump power of $20\,\mathrm{W}$). The combined idler and signal pulse energy was the highest reported in literature to date. The majority of the optical path length of the resonator was represented by a $\approx 27\,\mathrm{m}$ single-mode optical fibre resulting in a small and compact resonator. The SPOPO was tunable from $1.50\,\mu\mathrm{m}$ to $1.69\,\mu\mathrm{m}$ and from $2.84\,\mu\mathrm{m}$ to $3.61\,\mu\mathrm{m}$ and the M^2-beam quality was 1.53×1.29 and 2.80×1.88 for signal and idler, respectively.

The SPOPO was pumped by a gain-switched YDF-amplified LD generating predominantly linearly chirped $100\,\mathrm{ps}$, up to $8.6\,\mu\mathrm{J}$, $1.06\,\mu\mathrm{m}$, $M^2 < 1.2$, single-polarisation output. The pump source has the potential for higher pulse energies, if the LMA fibre of the final amplifier is replaced by a fibre with an even larger core size to avoid nonlinear broadening. The current fibre with a core diameter of $25\,\mu\mathrm{m}$ limits the pulse energies to $8.6\,\mu\mathrm{J}$ before SPM starts degrading the pulse quality.

The combination of the compact, user-friendly, flexible, all-fibre pump source and the tunable, fibre-feedback, picosecond, high-pulse-energy SPOPO approaching the $1\,\mu\mathrm{J}$ regime is an attractive solution for applications in IR materials processing, for instance in resonant IR pulsed laser deposition and ablation of polymer films [1, 2] or ultrafast IR waveguide inscription [3].

References

[1] V. Z. Kolev, M. W. Duering, B. Luther-Davies, and A. V. Rode, "Compact high-power optical source for resonant infrared pulsed laser ablation and deposition of polymer materials," Opt. Express **14**(25), 12,302–12,309 (2006).

[2] D. M. Bubb and R. F. Haglund Jr., "Resonant Infrared Pulsed Laser Ablation and Deposition of Thin Polymer Films," in *Pulsed Laser Deposition of Thin Films*, R. W. Eason, ed., pp. 35–60 (John Wiley & Sons, Hoboken, New Jersey, 2006).

[3] T. P. Lamour, L. Kornaszewski, J. H. Sun, and D. T. Reid, "Yb:fiber-laser-pumped high-energy picosecond optical parametric oscillator," Opt. Express **17**(16), 14,229–14,234 (2009).

[4] G. Cerullo and S. De Silvestri, "Ultrafast optical parametric amplifiers," Review of Scientific Instruments **74**(1), 1–18 (2003).

[5] Y. Shen, S.-U. Alam, K. K. Chen, D. Lin, S. Cai, B. Wu, P. Jiang, A. Malinowski, and D. J. Richardson, "PPMgLN-Based High-Power Optical Parametric Oscillator Pumped by Yb^{3+}-Doped Fiber Amplifier Incorporates Active Pulse Shaping," IEEE Journal of Selected Topics in Quantum Electronics **15**(2), 385–392 (2009).

[6] Y. Peng, W. Wang, X. Wei, and D. Li, "High-efficiency mid-infrared optical parametric oscillator based on PPMgO:CLN," Opt. Lett. **34**(19), 2897–2899 (2009).

[7] H. Ishizuki and T. Taira, "High-energy quasi-phase-matched optical parametric oscillation in a periodically poled $MgO:LiNbO_3$ device with a 5mm x 5mm aperture," Opt. Lett. **30**(21), 2918–2920 (2005).

[8] C. W. Hoyt, M. Sheik-Bahae, and M. Ebrahim-Zadeh, "High-power picosecond optical parametric oscillator based on periodically poled lithium niobate," Opt. Lett. **27**(17), 1543–1545 (2002).

[9] T. Südmeyer, E. Innerhofer, F. Brunner, R. Paschotta, T. Usami, H. Ito, S. Kurimura, K. Kitamura, D. C. Hanna, and U. Keller, "High-power femtosecond fiber-feedback optical parametric oscillator based on periodically poled stoichiometric $LiTaO_3$," Opt. Lett. **29**(10), 1111–1113 (2004).

[10] T. P. Lamour, J. H. Sun, and D. T. Reid, "High-pulse-energy cavity-dumped optical parametric oscillator in the near- and mid-infrared," in *International Summer School in Ultrafast Nonlinear Optics, SUSSP 66, August 11–21*, Edinburgh, Scotland (Heriot-Watt University, 2010).

[11] T. P. Lamour and D. T. Reid, "650-nJ pulses from a cavity-dumped Yb:fiber-pumped ultrafast optical parametric oscillator," Opt. Express **19**(18), 17,557–17,562 (2011).

[12] T. Südmeyer, J. Aus der Au, R. Paschotta, U. Keller, P. G. R. Smith, G. W. Ross, and D. C. Hanna, "Femtosecond fiber-feedback optical parametric oscillator," Opt. Lett. **26**(5), 304–306 (2001).

[13] K. K. Chen, J. H. V. Price, S.-U. Alam, J. R. Hayes, D. J. Lin, A. Malinowski, and D. J. Richardson, "Polarisation maintaining 100W Yb-fiber MOPA producing μJ pulses tunable in duration from 1 to 21 ps," Opt. Express **18**(14), 14,385–14,394 (2010).

[14] A. E. Siegman, *Lasers*, 1st ed. (University Science Books, Sausalito, California, 1986).

[15] M. Medhat, S. Y. El-Zaiat, A. Radi, and M. F. Omar, "Application of fringes of equal chromatic order for investigating the effect of temperature on optical parameters of a GRIN optical fibre," Journal of Optics A: Pure and Applied Optics **4**(2), 174 (2002).

[16] E. Khazanov, N. Andreev, O. Palashov, A. Poteomkin, A. Sergeev, O. Mehl, and D. H. Reitze, "Effect of terbium gallium garnet crystal orientation on the isolation ratio of a Faraday isolator at high average power," Appl. Opt. **41**(3), 483–492 (2002).

[17] E. Khazanov, N. F. Andreev, A. Mal'shakov, O. Palashov, A. K. Poteomkin, A. Sergeev, A. A. Shaykin, V. Zelenogorsky, I. A. Ivanov, R. Amin, G. Mueller, D. B. Tanner, and D. H. Reitze, "Compensation of Thermally Induced Modal Distortions in Faraday Isolators," IEEE Journal of Quantum Electronics **40**(10), 1500–1510 (2004).

[18] O. Gayer, Z. Sacks, E. Galun, and A. Arie, "Temperature and wavelength dependent refractive index equations for MgO-doped congruent and stoichiometric $LiNbO_3$," Applied Physics B: Lasers and Optics **91**(2), 343–348 (2008).

[19] G. P. Agrawal, *Nonlinear Fiber Optics*, Optics and Photonics, 3rd ed. (Academic Press, San Diego, 2001).

Chapter 5

Green-pumped, picosecond, high-repetition-rate optical parametric oscillators

5.1 Introduction

Tunable ultrashort pulses in the visible and the NIR region have a multitude of applications including coherent anti-Stokes Raman scattering (CARS) spectroscopy / microscopy [1–5], stimulated Raman scattering microscopy [6] or stimulated-emission-depletion (STED) microscopy [7]. In the past, Ti:Sapphire lasers have been the preferred choice to deliver tunable, femtosecond pulses, but cheaper, more compact, more user-friendly alternatives are increasingly sought after. Particularly for CARS, synchronously pumped OPOs are an ideal solution in that they generate two temporally synchronous pulses at different (and tunable) wavelengths. The pump sources used for such SPOPOs are typically ultrashort, solid-state laser systems operating at around $1\,\mu\mathrm{m}$ and subsequently frequency-doubled to the green spectral region.

There is a host of nonlinear crystals applicable for SPOPOs pumped in the visible and factors such as the phase-matching condition (birefringent phase-matching (BPM) or quasi-phase-matching (QPM)), the required phase-matching bandwidth, the parametric gain, the transparency range and the damage threshold influence the choice. Two crystals, namely LBO and MgO:PPLN, are investigated in this chapter.

Bulk nonlinear crystals, e.g. LBO, BBO, KTP, generally have high damage thresholds and wide transparency ranges, but only moderate values of the effective nonlinearity and therefore gain. In high-power pulsed OPOs, bulk crystals are usually preferred

mainly due to their high damage threshold. Lithium triborate (LBO) is the most prominent type with a damage threshold of $> 10\,\mathrm{GW/cm^2}$ and the possibility of non-critical BPM [8–11]. The highest signal output power of $1.6\,\mathrm{W}$ tunable from $740\,\mathrm{nm}$ to $930\,\mathrm{nm}$ from an LBO-based, picosecond SPOPO was reported by Tukker *et al.* [11] using $5.6\,\mathrm{W}$ of pump power from a frequency-doubled, $50\,\mathrm{ps}$ Nd:YLF laser. MOPA configurations based on ytterbium-doped fibres (YDF), rather than bulk solid-state laser systems, have also been used as OPO pump sources in recent years including reports of picosecond [12] and femtosecond [13] systems delivering hundreds of milliwatts of signal output power tunable over $\approx 200\,\mathrm{nm}$ in the NIR.

The results of a high-power, green-pumped, picosecond SPOPO based on LBO and operated at high repetition rate are described in section 5.4. The ring cavity, singly resonant LBO SPOPO is pumped with the second-harmonic at $530\,\mathrm{nm}$ of a fibre-amplified, gain-switched laser diode MOPA system operating at a repetition rate of $230\,\mathrm{MHz}$. The $20\,\mathrm{ps}$-long output pulses at $1060\,\mathrm{nm}$ from the MOPA are compressed to $4.4\,\mathrm{ps}$ in a transmission grating compressor before frequency-doubling in an LBO crystal. At a pump power of $17\,\mathrm{W}$ and with the SPOPO tuned to a signal wavelength of $877\,\mathrm{nm}$ (idler at $1.34\,\mu\mathrm{m}$), record powers of $2.5\,\mathrm{W}$ of signal and $1.7\,\mathrm{W}$ of idler are generated. The SPOPO is widely tunable from $651\,\mathrm{nm}$ to $1040\,\mathrm{nm}$ (signal) and from $1081\,\mathrm{nm}$ to $2851\,\mathrm{nm}$ (idler) and its signal pulse duration is around $3.2\,\mathrm{ps}$.

Despite the impressive results with bulk crystals in BPM arrangements, QPM with periodically poled lithium niobate remains interesting for green-pumped, ultrashort SPOPOs because of its attractive QPM properties (e.g. a high effective nonlinear coefficient $d_{eff} = 17\,\mathrm{pm/V}$ and designer phase-matching [14]), large transparency range, generally well-understood physical and optical properties, wide availability and low price. However, in the presence of visible light, lithium niobate is more sensitive to optical damage mechanisms such as photo-refraction [15–17] and green-induced infrared absorption (GRIIRA) [18–20] as described in section 2.4.2.1 as well as nonlinear absorption [18, 19], which at high pulse energies can all lead to a reduced conversion efficiency, a degraded beam quality, a higher oscillation threshold, temporal instabilities or even crystal damage. GRIIRA becomes a major problem when power-scaling OPOs, since the absorption of the NIR power grows quadratically with incident green power [18]. Furthermore, Hirohashi *et al.* report that both linear and nonlinear absorption (e.g. two-photon absorption), the latter especially in picosecond experiments, can occur in ferroelectric materials such as lithium niobate [19]. Impurities and defects can lead to linear absorption, whereas nonlinear absorption is possible because of the specific band gap of ferroelectrics. In any case the absorbed energy leads to thermal lensing and consequently resonator instability and degraded beam quality.

With improved material properties and advanced fabrication techniques, photo-refraction and GRIIRA can be reduced to a certain extent leading, in turn, to an increased damage threshold. To improve the performance of lithium niobate under the influence of high intensities in the visible, a stoichiometric rather than congruent composition [17], where the concentration of Li- and Nb-ions is balanced, can be used. Alternatively, MgO-doping of congruent material, where Mg-ions replace Nb anti-site defects [21], has similar benefits. MgO:PPLN has been successfully used in green-pumped CW OPOs [22, 23] as well as in CW second-harmonic generation (SHG) experiments with green average powers of up to 3 W for shorter periods of time [24] and 2.2 W ($> 200\,\mathrm{kW/cm^2}$) over more than 2000 h [25]. However, due to the onset of photo-refraction and GRIIRA and the high peak powers, there has been limited research activity with ultrashort-pulsed, green-pumped OPOs based on lithium niobate. Some work with PPLN in the ultrashort pulse regime was carried out previously [26] resulting in the demonstration of $\approx 2\,\mathrm{ps}$, 120 MHz pulses at a quasi-CW power of 140 mW with a total tuning range from 883 nm to 1285 nm using a mode-locked Nd:YLF laser and amplifier, whose output was frequency-doubled in LBO. However, to access higher peak powers in the kilowatt range from the amplifier, $10\,\mu\mathrm{s}$ / 2 kHz pulses were sliced from the seed picosecond pulse train and therefore the average power into the crystal was $50\times$ reduced. More recently, MgO:PPLN has been used in a picosecond, 80 MHz, green-pumped OPO producing 30 mW of signal and 30 mW of idler power over a tunability range of 880 nm to 1040 nm and 1090 nm to 1350 nm, respectively [27].

Investigations of the performance of an MgO:PPLN crystal in a green-pumped, picosecond SPOPO are presented in section 5.3. The limiting effects of photo-refraction, GRIIRA and nonlinear absorption and their associated thresholds are discussed and an optimal operation regime for MgO:PPLN under these conditions is investigated. A distinction is made here between optical damage, i.e. a reversible effect due to photo-refraction, and physical damage, i.e. an irreversible facet or bulk damage. The limitations are based both on intensity and average power and hence a quasi-CW mode-locked operation is favoured. A combined maximum output power of $\approx 270\,\mathrm{mW}$ for $\approx 1\,\mathrm{W}$ of pump power is generated (pump parameters: 530 nm, 20 ps, 230 MHz). Since damage threshold values of lithium niobate in conjunction with visible light, particularly in the ultrashort-pulse, high-intensity regime vary considerably in the literature (see for example [28]) and no safe operation regime can be clearly designated, the work carried out is also intended to add information to this incomplete picture.

The MOPA pump system (fibre-amplified, gain-switched laser diode) presented in this chapter was originally developed by Kang Kang Chen and modified and operated by Dr. Dejiao Lin. The frequency-doubling stage was setup by Dr. Dejiao Lin and the author. The transmission grating compressor was designed and initially set-up by Dr.

Jonathan Price. The SPOPOs were set-up and all experiments were carried out by the author.

5.2 Pump source experimental setup

The MOPA pump source for the SPOPO was similar to the source described in detail in chapter 3, but with an additional pre-amplifier and also the frequency-doubling stage to generate green light. Figure 5.1 shows the layout of this modified pump source.

5.2.1 Fibre-based NIR master-oscillator power-amplifier

This section discusses only the differences of the MOPA system compared to the one described in chapter 3 and the reader is referred to that chapter for a full and detailed description of the entire system.

The output pulses of the $1060\,\mathrm{nm}$ laser diode (LD) were chirp-compensated to a pulse duration of $\approx 20\,\mathrm{ps}$ for the experiments here. The amplification was performed in four polarisation-maintaining Ytterbium-doped fibre (YDF) amplifier stages. All other components in the setup were also PM, i.e. the fiberised OIs and the WDMs. The two pre-amplifiers used $3\,\mathrm{m}$-long, single-mode, Yb-doped, $5\,\mu\mathrm{m}$ core (NA 0.13), $130\,\mu\mathrm{m}$ cladding (NA 0.46), core-pumped fibres, pumped by $160\,\mathrm{mW}$, $975\,\mathrm{nm}$ LDs in a forward and a bi-directional scheme, respectively. The following third stage used the same fibre type, but a $9\,\mathrm{m}$-long piece, which was backward cladding-pumped with up to $10\,\mathrm{W}$ at $975\,\mathrm{nm}$. The final amplifier employed a $3.5\,\mathrm{m}$-long, cladding-pumped, LMA YDF with a $25\,\mu\mathrm{m}$ core (NA 0.06) and a $250\,\mu\mathrm{m}$ cladding (NA 0.46), which was backward-pumped by a $170\,\mathrm{W}$, $975\,\mathrm{nm}$ LD stack. To suppress the excitation of higher-order modes of the multi-modal YDF (V-number of $V > 4$, see equation (2.4)) a tapered splice between the preceding fiberised OI and the YDF [29] was applied and the fibre was coiled with a diameter of around $7.5\,\mathrm{cm}$ to increase the bend loss for higher-order modes.

A polarisation extinction ratio of $13\,\mathrm{dB}$ at the maximum power of $\approx 78\,\mathrm{W}$ was measured at the MOPA output. The signal beam polarisation was controlled with a combination of a half-waveplate and a PBS, which also served as a variable amplitude attenuator. The beam quality, also measured after the OI, HWP and PBS, was $M^2 \approx 1.25$ at an average power of $35\,\mathrm{W}$. The repetition rate was set to $230\,\mathrm{MHz}$, at which a maximum output power of $\approx 90\,\mathrm{W}$ before the OI, HWP and PBS was obtained for a launched pump power of $\approx 160\,\mathrm{W}$. This corresponded to an average power of $\approx 78\,\mathrm{W}$ (see figure 5.2) and a pulse energy of $340\,\mathrm{nJ}$ at the MOPA output. The spectra measured at

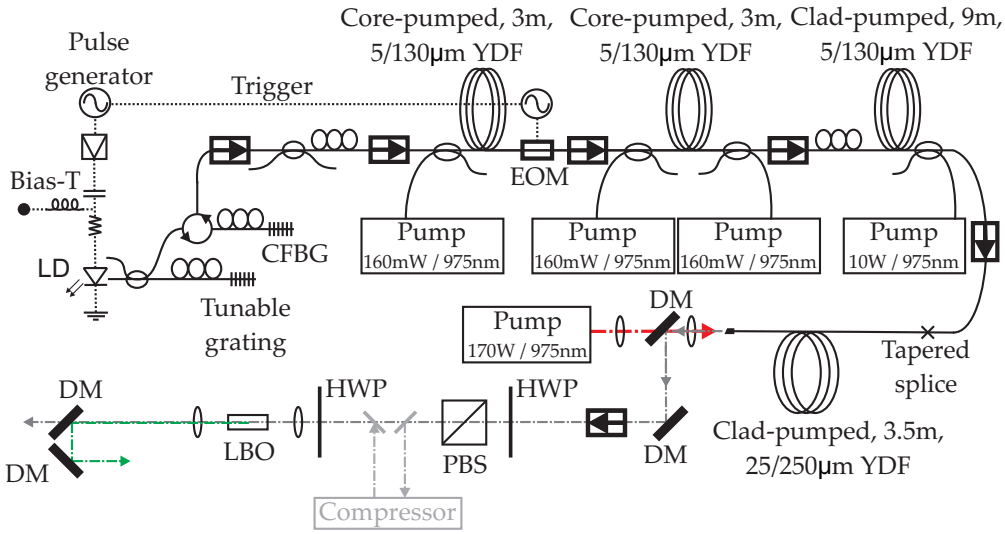

FIGURE 5.1: Schematic diagram of the fibre MOPA system including the LBO frequency-doubling arrangement. LD: Laser diode, CFBG: Chirped fibre Bragg grating, EOM: Electro-optic modulator, YDF: Ytterbium-doped fibre, DM: Dichroic mirror, HWP: $\lambda/2$-plate, PBS: Polarising beam splitter. All fibres, wavelength-division multiplexers and optical isolators were polarisation-maintaining. Dash-dot lines: red: free-space pump beam to final amplifier, grey: free-space signal beam, green: frequency-doubled signal beam.

different output power levels did not exhibit significant ASE background with an optical signal-to-noise ratio of $> 35\,\mathrm{dB}$ (see figure 5.3). However, SPM led to a gradual increase of the bandwidth with increasing power. At low power, the FWHM bandwidth was $0.155\,\mathrm{nm}$ and at the highest output power, the FWHM rose to $0.253\,\mathrm{nm}$, corresponding to a bandwidth-limited pulse duration of $\approx 6.5\,\mathrm{ps}$ (assuming a Gaussian pulse profile) and therefore the measured $\approx 20\,\mathrm{ps}$ pulses were approximately $3\times$ longer than the bandwidth limit.

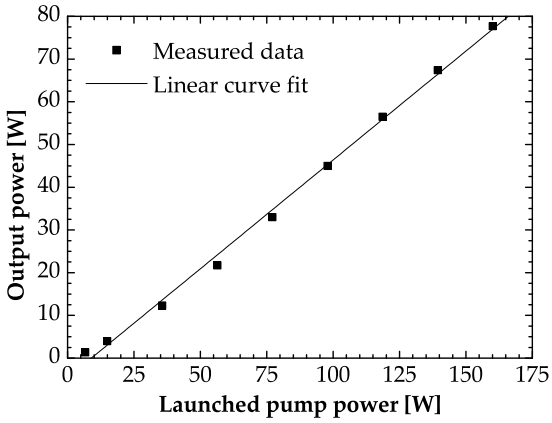

FIGURE 5.2: NIR output power versus launched pump power of the final MOPA amplifier. The slope efficiency was 51% and the maximum output power was 77.7 W.

In the experiments reported in section 5.4, the MOPA output pulses were compressed in a grating compressor and its position in the setup is indicated in figure 5.1. The compressor is described in detail in section 5.4.1.

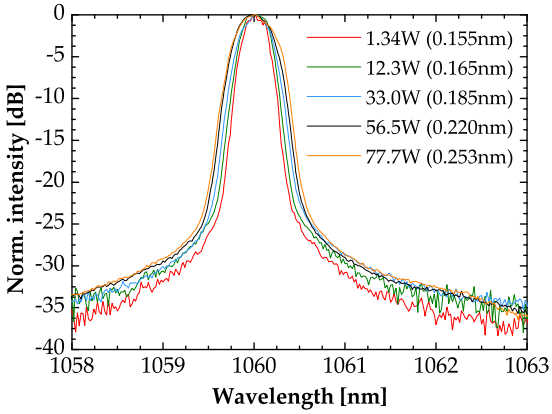

FIGURE 5.3: Spectra at different power levels of the final MOPA amplifier output. The spectra suffer from SPM broadening with increasing power, which is indicated with the FWHM bandwidths in parantheses.

5.2.2 Frequency-doubling stage

The NIR MOPA output was then frequency-doubled in a $15 \times 3 \times 3\,\mathrm{mm}^3$ LBO crystal cut along the x-axis with $\theta = 90°$ and $\phi = 0°$ for type I non-critical phase-matching (NCPM), as described in section 2.4.1.2. The crystal was AR-coated for $1060\,\mathrm{nm}$ and $530\,\mathrm{nm}$ on both end facets and held in an oven at an optimal phase-matching temperature of $154.5°\mathrm{C}$. The polarisation of the fundamental input wave was adjusted to the z-axis of the crystal with a HWP. Two $f = 150\,\mathrm{mm}$ lenses were used to focus the fundamental beam into the centre of the LBO (waist diameter $\approx 70\,\mu\mathrm{m}$) and to collimate the generated second-harmonic beam, respectively. Two dichroic mirrors filtered the unconverted fundamental light from the second-harmonic light. The experimental arrangement is depicted in figure 5.1.

For a maximum of $78\,\mathrm{W}$ of fundamental input power, $33\,\mathrm{W}$ of second-harmonic power was obtained corresponding to a conversion efficiency of 42% (repetition rate $230\,\mathrm{MHz}$). The somewhat low efficiency was attributed to crystal damage (bulk and / or coatings), which was visible under a microscope. The damage was possibly caused during extensive use of this LBO crystal in previous, high-power, frequency-doubling experiments [30]. Figure 5.4 shows the second-harmonic output power as a function of the fundamental input power. At higher power levels, non-negligible depletion of the fundamental on the one hand [31, 32] and a possible drop in conversion efficiency due to crystal damage on the other hand resulted in a levelling-off. The measured beam quality M^2-values were 1.65 and 1.79 in the z- and y-axis of the crystal, respectively.

Spectra of the second-harmonic output at different power levels and with the FWHM bandwidths denoted in parantheses are plotted in figure 5.5. The increase in bandwidth of the second-harmonic followed a similar trend as the bandwidth of the fundamental NIR light from the MOPA (figure 5.3) and can hence be traced back to SPM in

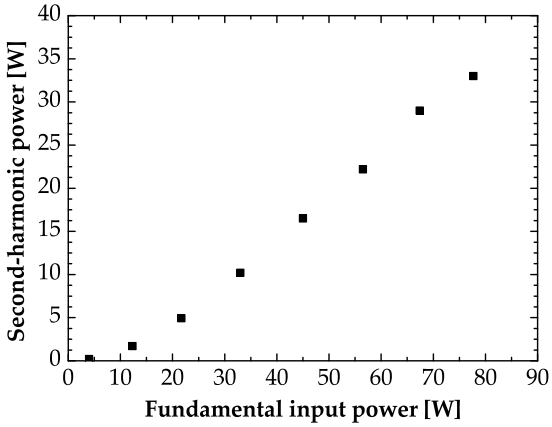

FIGURE 5.4: Second-harmonic power as a function of fundamental input power of the LBO crystal. A maximum power of 33 W at 530 nm was obtained. The levelling-off at higher power was attributed to non-negligible depletion of the fundamental wave.

the MOPA and was not a broadening effect in the LBO. At the highest power of 33 W, the FWHM was 0.117 nm leading to a theoretical bandwidth-limited pulse duration of ≈ 3.5 ps. The pulse duration of the second-harmonic pulses could not be directly measured due to the lack of appropriate pulse diagnostics for the green spectral region. In this work, it was assumed that their pulse duration was similar to the 20 ps-long input fundamental pulses, since three effects act on the pulses that approximately cancel each other out mutually: (1) Due to the quadratic power dependence, the pulse centre is converted with a higher efficiency than the wings resulting in a pulse shortening, (2) the group delay dispersion of the crystal leads to a pulse broadening, and (3) the GVM of fundamental and second-harmonic leads to a temporal walk-off [13, 31].

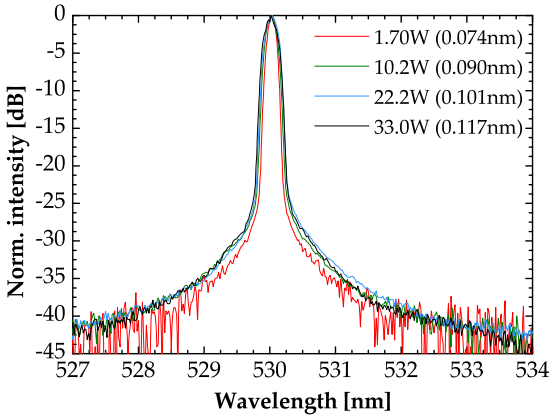

FIGURE 5.5: Spectra at different power levels of the frequency-doubled LBO output. The FWHM bandwidths are indicated in parantheses. The broadening of the spectra at higher powers can be traced back to the SPM broadening of the NIR MOPA output as shown in figure 5.3.

To avoid potential problems with power-dependent beam sizes and focus shifts, the MOPA and therefore the LBO output was kept at a constant power level throughout, and the amount of green power used for OPO pumping was controlled with a HWP and PBS variable attenuator.

5.3 MgO:PPLN-based, green-pumped, picosecond, high-repetition-rate optical parametric oscillator

5.3.1 Experimental setup of the MgO:PPLN optical parametric oscillator

The SPOPO was set-up in a bow-tie ring cavity configuration as shown in figure 5.6. The congruent MgO:PPLN crystal (provided by Covesion Ltd., United Kingdom) with a 5% MgO-doping concentration had dimensions of $20 \times 10 \times 0.5\,\mathrm{mm}^3$ and five poled gratings with periods of $\Lambda = 6.7, 6.8, 6.9, 7.0, 7.1\,\mu\mathrm{m}$. The crystal was AR-coated ($R < 0.5\%$) on both end facets for a pump wavelength of $523\,\mathrm{nm}$, a signal wavelength of $800\,\mathrm{nm}$ and the corresponding idler wavelength of $1510\,\mathrm{nm}$. The crystal was mounted in a gold-coated copper holder, which in turn was held in an oven at a temperature of $200^{\circ}\mathrm{C}$. The high temperature was a measure against photo-refraction (additional to the MgO-doping) and to tune the signal to a wavelength that provides minimum round-trip losses.

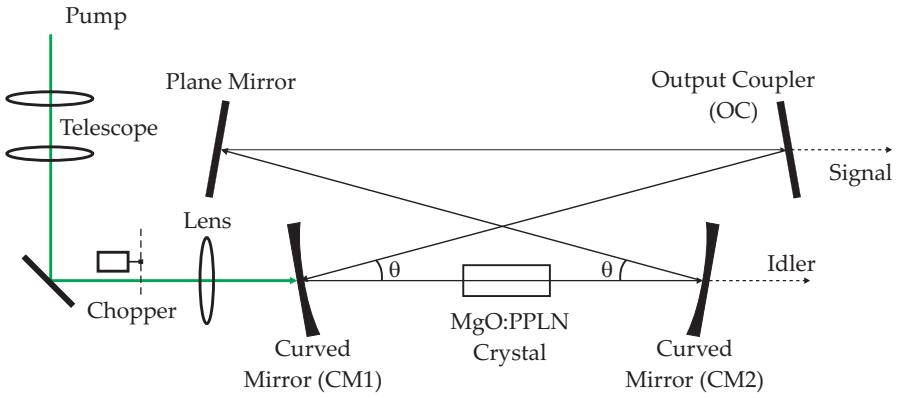

FIGURE 5.6: Layout of the singly resonant, bow-tie, green-pumped SPOPO ring resonator. The pump beam was focused with a $175\,\mathrm{mm}$ lens into the centre of the MgO:PPLN after reducing its size with a telescope. The radius of curvature of CM 1 and CM 2 was $-250\,\mathrm{mm}$. Two output coupler mirrors with signal transmission of 10% and 3% were available. The mechanical chopper allowed for reduction of the input average power without reduction of the pulse peak power.

The method of holding and heating the crystal was the same as described in the previous chapters, but shall be described in more detail here, since the experiments were concerned with photo-refraction and damage of the MgO:PPLN under the influence of visible radiation. An electrically conductive indium-tin-oxide-coated spacer window on one $10 \times 20\,\mathrm{mm}^2$ side and the gold-coated copper holder on the opposite side prevented the build-up of electrical charges on the crystal surface when it was heated up. Such electrical charges are induced by the pyroelectric and piezoelectric effect causing electrostatic fields across the domain boundaries, which can lead to crystal fracture.

The four-mirror, bow-tie ring resonator consisted of two curved mirrors CM 1 and CM 2 with a radius of curvature of $-250\,\mathrm{mm}$, one plane mirror and one plane OC mirror. For

practical reasons involving the bow-tie angle θ and mechanical restrictions with mirror mounts, the length of the cavity could not be set to a length that corresponds to the pump pulse repetition rate of $230\,\mathrm{MHz}$, but was set to $2.61\,\mathrm{m}$ instead corresponding to an effective round-trip repetition rate of $115\,\mathrm{MHz}$. Consequently, it was accepted that two pulses circulate at the same time in the ring cavity, which does not pose problems regarding OPO threshold or efficiency as was reported before [33, 34]. CM 1, CM 2 and the plane mirror were highly reflective over the signal tuning range ($R > 99.5\%$ from $650\,\mathrm{nm}$ to $1090\,\mathrm{nm}$) and highly transmissive for the pump ($T > 99\%$ at $530\,\mathrm{nm}$) and over the idler tuning range ($T > 90\%$ from $1.2\,\mu\mathrm{m}$ to $3\,\mu\mathrm{m}$) resulting in a singly resonant behaviour for the signal pulses. The two available OC mirrors were also highly transmissive for the pump and idler, but with transmissions of 3% and 10% over the signal wavelength range.

With the $-250\,\mathrm{mm}$ radius of curvature of CM 1 and CM 2, the $20\,\mathrm{mm}$-long MgO:PPLN and the resonator length of $2.61\,\mathrm{m}$ as input to a numerical ABCD matrix resonator model [35], the signal waist radius was calculated to be $42\,\mu\mathrm{m}$ and $43\,\mu\mathrm{m}$ parallel and perpendicular to the resonator plane, respectively. The slight beam ellipticity was due to the astigmatism of the curved mirrors related to the bow-tie angle θ of $4.2°$ [36]. This waist radius corresponded to a confocal parameter of $b_s \approx 31.6\,\mathrm{mm}$ and a focusing parameter of $\xi_s = 0.63$ (with $\lambda_s = 800\,\mathrm{nm}$ and $n_e = 2.23$ at $200°\mathrm{C}$ [37]), which was a good trade-off between a waist as large as possible (avoiding intensity-caused damage) and a confocal focusing situation with $\xi_s = 1$ (optimum conversion efficiency). To match the pump to the signal waist size in the centre of the MgO:PPLN, the pump beam size was reduced with a two-lens telescope and subsequently focused with a lens of focal length $175\,\mathrm{mm}$. A pump waist with a radius of $44\,\mu\mathrm{m}$ and $42\,\mu\mathrm{m}$ parallel and perpendicular to the resonator plane, respectively, was obtained corresponding to a confocal parameter of $b_p \approx 50\,\mathrm{mm}$ and a focusing parameter of $\xi_p = 0.4$.

Using the temperature-dependent Sellmeier equation of Gayer *et al.* for MgO:PPLN [37], the group velocities $v_g = c/n_g\,(\lambda, T)$ of characteristic OPO wavelengths (pump at $530\,\mathrm{nm}$, signal at $800\,\mathrm{nm}$ and idler at $1.57\,\mu\mathrm{m}$) were calculated. The group velocity mismatches were then calculated to be $\mathrm{GVM}_{s,p} = 0.67\,\mathrm{ps/mm}$, $\mathrm{GVM}_{s,i} = 0.28\,\mathrm{ps/mm}$ and $\mathrm{GVM}_{i,p} = 0.96\,\mathrm{ps/mm}$, which meant that the walk-off of the three waves in the $20\,\mathrm{mm}$ MgO:PPLN crystal were $13.4\,\mathrm{ps}$, $5.6\,\mathrm{ps}$ and $19.2\,\mathrm{ps}$, respectively. Therefore, the walk-offs were of similar magnitude to the $20\,\mathrm{ps}$ pulse duration of the pump and the expected pulse durations of the signal and idler. The FWHM signal gain bandwidth (equation (2.64)) was $9.8 \cdot 10^{11}\,\mathrm{rad/s}$ corresponding to a maximum signal bandwidth of $0.33\,\mathrm{nm}$ using the general relation $\Delta\lambda = \Delta\omega\lambda^2/2\pi c$·. The FWHM pump acceptance bandwidth (equation (2.65)) was $2.9 \cdot 10^{11}\,\mathrm{rad/s}$ resulting in a maximum pump bandwidth of $0.04\,\mathrm{nm}$. These calculations showed that the pump bandwidths as given in figure 5.5 exceed the acceptance bandwidth, which could result in reduced conversion

efficiencies. In order to increase the signal gain bandwidth and the pump acceptance bandwidth, a shorter crystal could be used instead.

A mechanical chopper placed in the pump beam allowed for a $10\times$ reduction of the input average power without reduction of the pulse peak power. The chopper wheel had a duty cycle of 1:9 (6 equally spaced slits, 54 metal sections), i.e. 10% transmitted light and 90% blocked light. The frequency was $150\,\mathrm{Hz}$, which meant that the "transmit" period was $0.67\,\mathrm{ms}$ and the "block" period $6\,\mathrm{ms}$ long (note that the frequency of $150\,\mathrm{Hz}$ was the inverse of the period between two "transmit" cycles and not the rotation frequency of the chopper wheel, which was $6\times$ lower).

5.3.2 Output power, pump depletion and stability

The signal and idler output power as well as the pump depletion as a function of pump power for two different OPO experiments are presented in this section. Observations of photo-refraction, GRIIRA and / or physical damage of the MgO:PPLN crystal during these experiments are discussed in the following section, but briefly mentioned here in order to clarify the chronology of the experiments.

5.3.2.1 Full average pump power as input to OPO (no mechanical chopping)

In order to clarify the structure of this section, "full average power" means that the input pump beam was not yet mechanically chopped as opposed to the experiments in the following section ("reduced average power").

Initial oscillation of the OPO was achieved by using the $7.1\,\mu\mathrm{m}$ poled grating of the MgO:PPLN and the OC with $T = 3\%$. In combination with the temperature of $200^{\circ}\mathrm{C}$, a signal wavelength of $808\,\mathrm{nm}$ was expected using the temperature-dependent Sellmeier equation for MgO:PPLN [37]. The average pump power at $530\,\mathrm{nm}$ was $2\,\mathrm{W}$ with an expected threshold of a few hundred milliwatts based on the same analysis as described below. The threshold, however, could not be experimentally confirmed due to the temporally unstable signal and idler output and physical damage in the centre of the poled grating after only $\approx 30\,\mathrm{min}$ of operation.

In the next step, the adjacent $7.0\,\mu\mathrm{m}$ grating and considerably less average pump power of only $500\,\mathrm{mW}$ was used, since the oscillation threshold was expected to be relatively low. An analysis of the threshold based on [38] for low-gain (i.e. no output coupling), CW OPOs with arbitrary focusing parameter and on its extension to synchronous pumping [39] yielded an estimated threshold value of $\approx 100\,\mathrm{mW}$ with the assumption of 5% signal power round-trip loss (3% output coupling, 1% crystal AR-coating reflections, 1% diffraction / scattering losses). Figure 5.7 shows the signal and

idler output power versus the input pump power as well as the pump depletion. The measured threshold pump power was $181\,\mathrm{mW}$ and the slope efficiencies extracted from the linear curve fits were $\approx 20\%$ for both idler and signal. The pump depletion was not yet saturated at $500\,\mathrm{mW}$ of pump power but reached a value between 50% and 60%.

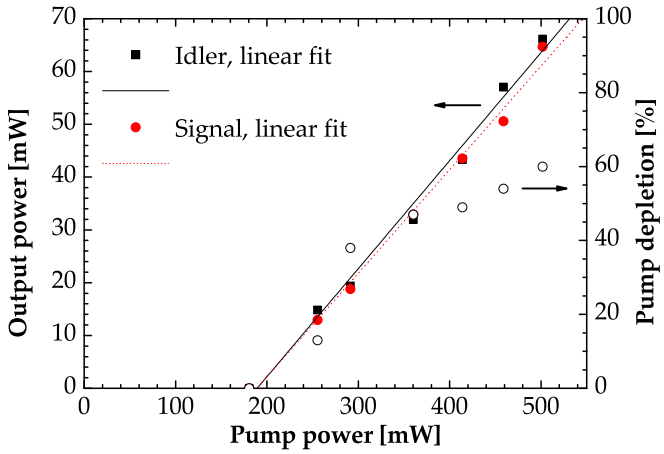

FIGURE 5.7: Output power and pump depletion versus pump power for the $7.0\,\mu\mathrm{m}$ poled grating of the MgO:PPLN and a 3% OC.

The calculated signal and idler wavelengths for $530\,\mathrm{nm}$ pump wavelength, $7.0\,\mu\mathrm{m}$ crystal grating, $200^{\circ}\mathrm{C}$ crystal temperature are $825\,\mathrm{nm}$ and $1483\,\mathrm{nm}$. M^2-values of 1.41 / 1.34 for the idler and 1.38 / 1.44 for the signal in the planes parallel / perpendicular to the OPO resonator were measured, respectively. The OPO output was still temporally unstable and a more careful optimisation of the alignment was not feasible. After a few hours of operation, a dark spot in the centre of the green pump spot at the location of the OC mirror was observed. This spot moved up and down relative to the stationary green pump spot when the crystal was moved up and down. This was a clear indication that it was necessary to further reduce the power that the MgO:PPLN was subjected to.

5.3.2.2 Reduced average pump power as input to OPO (with mechanical chopping)

To investigate whether the damage effects observed in the previous section were due to average power (thermally induced) or peak power, a mechanical chopper with a 1:9 duty cycle was inserted in the pump beam, as shown in figure 5.6, to reduce the input pump average power without reducing the pulse peak power. Note that a reduction of the pump source repetition rate to tens of megahertz would have the same effect, but this would be more difficult to implement, since a much longer OPO cavity, for example with a fibre for signal feedback [40, 41], and hence a complete re-alignment of the OPO would be required. During the $0.67\,\mathrm{ms}$-long "transmit" cycle of the chopper, the peak intensity of the focused picosecond pulses remained unaltered and hence the

OPO threshold unaffected. The power values in the graphs shown in figure 5.8 and figure 5.10 are the average powers within the "transmit" cycle, i.e. the measured powers multiplied by a factor of 10. The MgO:PPLN was translated to access the grating with a period of $6.9\,\mu\mathrm{m}$ yielding a signal and an idler wavelength of $845\,\mathrm{nm}$ and $1421\,\mathrm{nm}$, respectively. Due to the strongly reduced average power, no optical damage was observed in this experiment using the 3% OC (figure 5.8). The threshold was $120\,\mathrm{mW}$, the pump depletion $\approx 60\%$ and the slope efficiencies 18% (idler) and 14% (signal).

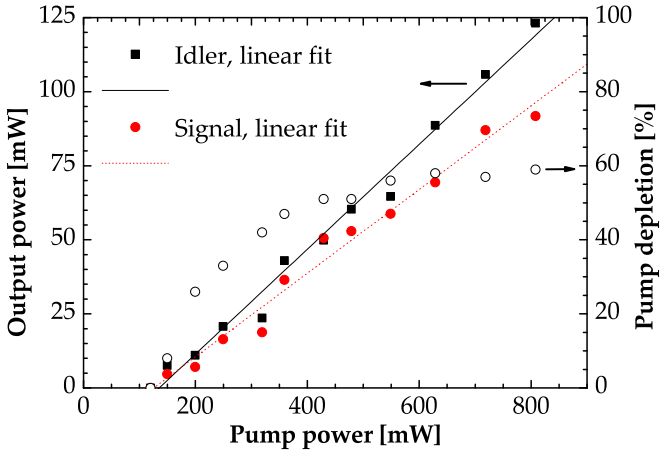

FIGURE 5.8: Output power and pump depletion versus pump power for the $6.9\,\mu\mathrm{m}$ poled grating of the MgO:PPLN and a 3% OC using a 1:9 duty cycle mechanical chopper to reduce the average input power by a factor of 10. All power values plotted represent the average power within the "transmit" cycle of the chopper.

In order to quantify the power stability of the OPO and also the pump source, the output power from the MOPA ($1060\,\mathrm{nm}$), the frequency-doubling stage ($530\,\mathrm{nm}$) and the OPO (signal at $845\,\mathrm{nm}$) were recorded over a period of $10\,\mathrm{min}$ and the fractional deviations from the mean values were plotted (figure 5.9). Polarisation drifts of the MOPA, air drifts and temperature fluctuations influence the transmission through the OI and PBS and the LBO conversion efficiency, which was expressed in a fractional deviation of the green power of approximately $\pm 2\%$ compared to $\pm 1\%$ from the MOPA. However, the fractional deviation of the OPO signal output of approximately $\pm 10\%$ could not be solely attributed to the input pump. The OPO was enclosed in a box to reduce air drifts and temperature fluctuations to a minimum. It was suspected that photo-refraction was the main source of the OPO power instability.

The 3% OC was then replaced by the 10% OC to extract more signal power from the resonator. The mechanical chopper was still placed in the pump beam. As shown in figure 5.10, the oscillation threshold was $369\,\mathrm{mW}$, the pump depletion saturated at $\approx 30\%$ and the slope efficiencies were 16% (idler) and 23% (signal). Signal and idler output powers of $165\,\mathrm{mW}$ and $107\,\mathrm{mW}$, respectively, were obtained at a pump power

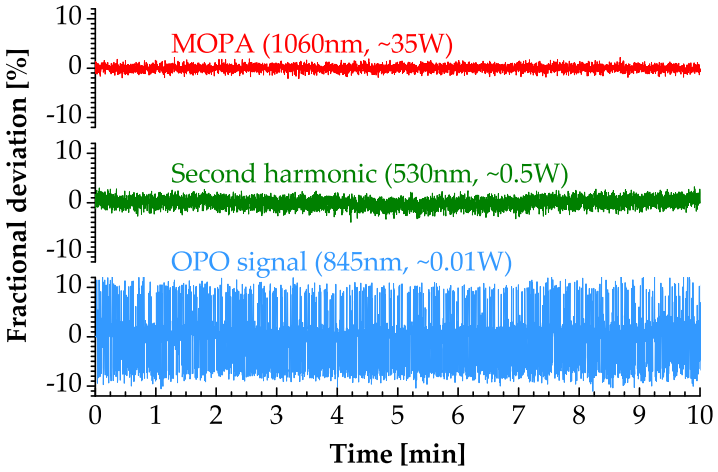

FIGURE 5.9: Temporal stability measurement of pump source and OPO outputs over a period of 10 min. The MOPA output at 1060 nm, the frequency-doubled output at 530 nm and the SPOPO signal output at 845 nm is plotted. The measured average powers are indicated in the figure.

of 1.05 W. The expected signal output power can be calculated with [11]

$$P_s = P_p \cdot D \cdot \frac{\lambda_p}{\lambda s} \cdot \frac{T_{OC}}{T_{OC} + \epsilon_s}\,, \tag{5.1}$$

where P_p is the input pump power, D the pump depletion (as a decimal number), λ_p and λ_s the pump and signal wavelengths, respectively, T_{OC} the output coupler transmission and ϵ_s the signal power round-trip loss (excluding the OC transmission here). At the highest pump power of 1.05 W, where the pump depletion was $D = 0.33$, with the signal wavelength of 845 nm and for an estimated loss of $\epsilon_s = 0.05$ (4% crystal coating reflections, 1% diffraction / scattering losses), P_s was calculated to be 145 mW, which was in good agreement with the measured value of 165 mW. Once again, no optical damage occurred in these experiments with the 10% OC.

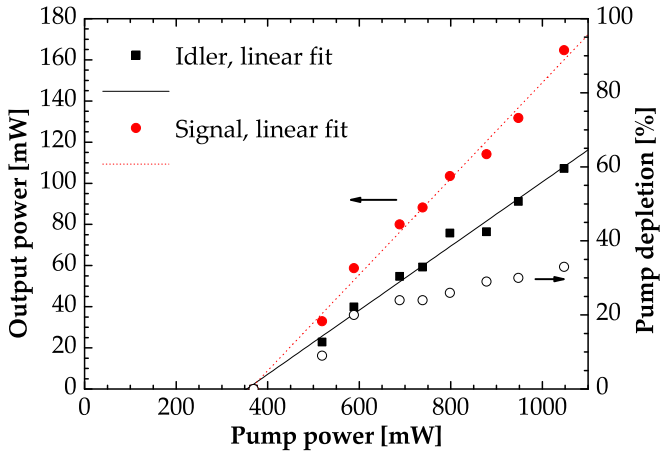

FIGURE 5.10: Same as figure 5.8, but with a 10% OC. All power levels plotted represent the average power within the "transmit" cycle of the chopper.

Due to the output power instability of the OPO, accurate recordings of spectra with an

OSA were not possible, since the scanning time of the device was considerably longer than the fluctuations of the OPO output and hence the spectra reflected the intensity fluctuations as well.

5.3.3 Nonlinear crystal performance and damage issues

In this section, the different damage effects that occurred during the experiments of section 5.3.2 are described and analysed.

The peak intensities discussed in this section were calculated with

$$I = \frac{P_{av}}{\tau f_{rep} \left(\frac{\pi}{2} w^2\right)} , \tag{5.2}$$

where P_{av} denotes the average power, τ the FWHM pulse duration, f_{rep} the repetition rate and w the $1/e^2$-waist radius, assuming a Gaussian spatial beam profile. An overview of the experimental parameters and the observed damage described in the following is given in table 5.1.

5.3.3.1 Crystal performance under the influence of the full pump power

With $2\,\mathrm{W}$ of average pump power corresponding to a peak intensity of $\approx 15\,\mathrm{MW/cm^2}$, incident for approximately $30\,\mathrm{min}$ to the $7.1\,\mu\mathrm{m}$ grating of the MgO:PPLN crystal, permanent physical damage was visible with the unaided eye. The $7.1\,\mu\mathrm{m}$ grating and the $200°\mathrm{C}$ temperature were chosen to tune the signal wavelength to $808\,\mathrm{nm}$, where the reflectivity of the crystal coatings has a minimum, in order to keep the signal round-trip loss low. Parametric oscillation was achieved in this case, but it was not possible to characterise the OPO output due to the damage onset. Figure 5.11 shows a schematic diagram and microscope images of the MgO:PPLN sample indicating the location, where the physical damage occurred. The microscope image in figure 5.12 clearly shows individual, closely spaced damage tracks within the cigar-shaped volume. This has been reported before and photo-refraction or self-focusing was suspected to cause the damage [42]. The damage is clearly associated with the high intensity pumping region, with the pump waist being located at the centre of the crystal. With the equation for the critical power of self-focusing given in [43], a critical power of $\approx 22\,\mathrm{kW}$ is calculated using the nonlinear refractive index $8.3 \cdot 10^{-19}\,\mathrm{m^2/W}$ at $532\,\mathrm{nm}$ [28], the linear refractive index 2.3 at $530\,\mathrm{nm}$ and assuming a Gaussian beam profile. The peak power of the $20\,\mathrm{ps}$-long pump pulses was only $435\,\mathrm{W}$ and, thus, self-focusing can be safely ruled out as the cause for the physical damage.

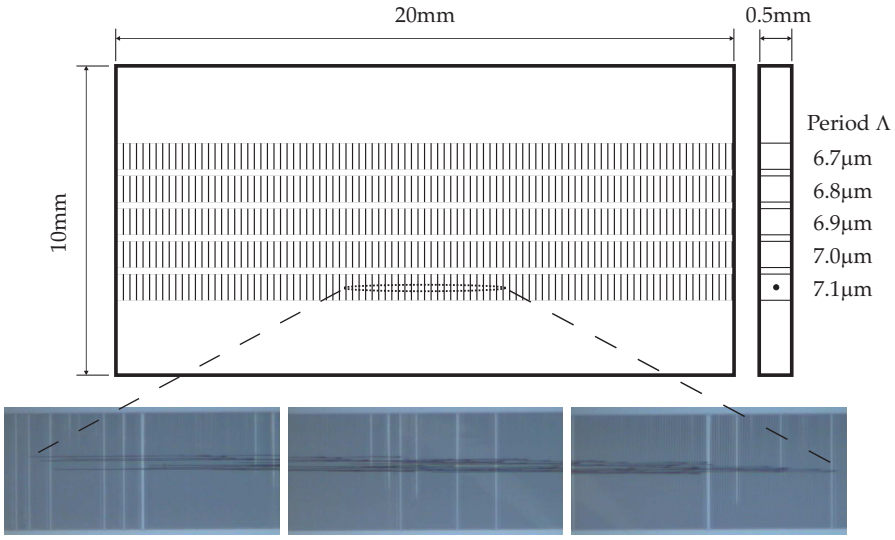

FIGURE 5.11: Schematic diagram and microscope images of the damaged MgO:PPLN sample used in the experiments depicting the location of the physical damage of the $7.1\,\mu\mathrm{m}$ poled grating that occurred when pumping the OPO with $2\,\mathrm{W}$ of average power.

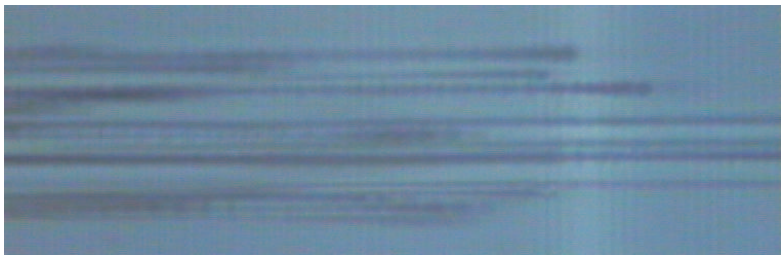

FIGURE 5.12: Zoomed microscope image of the crystal damage within the $7.1\,\mu\mathrm{m}$ poled grating, where the individual tracks are clearly visible. The microscope was focused to the damage tracks within the sample and not on the sample surface explaining why the domain boundaries are not in focus.

Additionally, the transmitted green pump beam was distorted and had a dark centre (region of physical damage) as observed in the green spot on the OC mirror. This beam distortion was previously described as a consequence of photo-refraction [14, 16]. The dark spot within the green spot could be a preceding, more sensitive sign of the physical track formation before it can be seen with a microscope and was possibly not only due to photo-refraction as reported before, but also due to GRIIRA. Since signal and idler waves in the infrared were generated, GRIIRA could have led to a thermal loading of the crystal and the associated physical damage. The inherent infrared absorption of lithium niobate can increase by up to a factor of five with green light present [18] and is quadratically dependent on the green power, but should recover to its initial value after $\approx 20\,\mathrm{s}$ [20] before physical damage occurs. According to the findings in [18], a higher MgO-doping concentration of $> 5\%$ could help to avoid GRIIRA because of a threshold-like behavior in terms of optical damage. For a higher concentration, all of the intrinsic Nb^{5+} anti-site defects (Nb^{5+}-ions at the lattice location of Li^{+}-ions) of congruent lithium niobate are replaced by Mg^{2+}-ions. In general, Nb^{5+} anti-site defects act as electron traps and locally change the absorption properties, referred to as

polaron absorption, which is inhibited when Mg^{2+}-ions occupy these anti-site defects. However, MgO:PPLN crystals with doping concentrations $> 5\%$ suffer from growth defects and can not be grown at high quality, which also impairs the subsequent poling process. Hence, an optimum concentration of 5% is typically used by commercial suppliers. Alternatively, a stoichiometric crystal composition with balanced Nb and Li concentrations could decrease GRIIRA due to the absence of anti-site defects.

To confirm whether or not GRIIRA caused the physical damage, an unpoled region of the MgO:PPLN sample was pumped for $30\,\mathrm{min}$ under the same conditions as above, i.e. $2\,\mathrm{W}$ of average power and $\approx 15\,\mathrm{MW/cm^2}$ of peak intensity. Since no parametric oscillation can occur in an unpoled region, no signal or idler in the IR can be generated and hence green-induced IR absorption can not occur. However, physical damage of the unpoled region was observed again, which is evidence that processes other than only GRIIRA contribute to the physical damage. Similar to Nb^{5+} anti-site defects, lattice impurities such as Fe^{2+}-ions can facilitate both linear and nonlinear (e.g. two-photon) polaron absorption [18, 19], which can potentially be a damage contributor [44]. Although the MgO:PPLN sample was of high quality, impurities on the order of parts-per-million naturally occur [17, 44, 45].

The $7.0\,\mu\mathrm{m}$ grating that was pumped with a $4\times$ lower average power of $0.5\,\mathrm{W}$ (after damage of the $7.1\,\mu\mathrm{m}$ grating at $2\,\mathrm{W}$) did not show any signs of visible physical damage after a few hours of OPO operation. However, the beam distortion and the dark spot within the green spot on the OC as described above were again existent. The lower average power and the lower peak intensity of $3.75\,\mathrm{MW/cm^2}$ did not trigger GRIIRA at a level that could have caused the catastrophic thermal loading and physical damage seen before (quadratic scaling law). Photo-refraction appears to be the dominating damage effect here. A comparison with reported photo-refractive damage threshold intensities of $2\,\mathrm{MW/cm^2}$ for a congruent 5% MgO:PPLN sample [21] and $> 8\,\mathrm{MW/cm^2}$ for a congruent 6% MgO:PPLN sample [18] (CW, green light, focused beams, no OPO operation) shows that the intensity of this experiment was on the same order of magnitude. On the other hand, damage thresholds vary largely in the literature based on the pump source parameters. Also, definitions of damage vary considerably in the published literature with some papers referring to damage as the onset of measurable changes in the refractive index, whilst others refer to damage as irreversible physical damage. Depending on the level of exposure, the effects of photo-refraction can be reversed by annealing the crystal for a few hours. However, the dark spot was still existent after $2\,\mathrm{h}$ of annealing at $220^{\circ}\mathrm{C}$ and a recovery period of many days (without using the crystal in the OPO). Thus in this case, the damage appears to be irreversible suggesting not only optical, but also physical damage.

5.3.3.2 Crystal performance under the influence of reduced pump power

The experiments with a mechanically chopped pump beam were carried out using the $6.9\,\mu\mathrm{m}$ grating of the MgO:PPLN. The importance of this experiment was to isolate the effect of high peak power from the effect of high average power on the damage and to investigate their impacts. A maximum of $\approx 1\,\mathrm{W}$ of average pump power before the chopper was $10\times$ reduced to $\approx 0.1\,\mathrm{W}$ (1:9 duty cycle) and then focused into the crystal. The peak intensity before and after the chopper was $7.5\,\mathrm{MW/cm^2}$, since the pulses within the $0.67\,\mathrm{ms}$-long, 10% "transmit" cycle were not affected by the chopping. Under these circumstances, i.e. with a true input average pump power of $0.1\,\mathrm{W}$, the OPO was operating without any permanent damage or dark spots observed. The $6\,\mathrm{ms}$-long chopper "block" cycle was too short for a recovery of the GRIIRA effect, which has a time constant of $\approx 20\,\mathrm{s}$ [20], but the significantly reduced average power avoided the physical damage. The strong signal and idler output power fluctuations as shown in figure 5.9 indicated that some low-level photo-refraction was still present. Again, the $6\,\mathrm{ms}$ "block" cycle was not long enough to allow for a natural recovery of the photo-refractive effect, i.e. a complete diffusion of the free charge carriers, since the time constants for this process, even at elevated temperatures, are orders of magnitude larger. With the intensity of $7.5\,\mathrm{MW/cm^2}$ being $2\times$ higher than in the previous experiment, the damage process appears to require high average power and not just high intensity.

5.3.4 Optimum operational regime

For a more exact determination of the damage threshold, a systematic investigation was carried out starting from the situation as given in column 5 of table 5.1 with $0.1\,\mathrm{W}$ of average power as input to the crystal, where no damage was observed. The average power was kept constant and the peak intensity was successively increased. This independent control was achieved by using a HWP and PBS to increase the average power and hence the peak intensity followed by a mechanical chopper with wheels of decreasing duty cycle to only reduce the average power but not the peak intensity of the pulses within the "transmit" cycle. After $1\,\mathrm{h}$ of operation (signal and idler present) using the previously unused $6.8\,\mu\mathrm{m}$ grating and a pump pulse intensity of $\approx 11\,\mathrm{MW/cm^2}$, the beam distortion and dark spot effect were observed, but no physical damage was generated. At an even higher intensity of $\approx 17\,\mathrm{MW/cm^2}$, physical damage occurred after only a few minutes in that same grating. Therefore, the peak intensity damage threshold can be pin-pointed to a range of around $7.5\,\mathrm{MW/cm^2}$ to $11\,\mathrm{MW/cm^2}$.

In order to further confirm the assumption that both average power and peak intensity lead to crystal damage, the influence of pulse peak power / intensity on the described damage was completely eliminated by using a frequency-doubled ($532\,\mathrm{nm}$),

diode-pumped, solid-state, CW laser with up to 2 W of average power focused to a spot with a $1/e^2$-radius of $35\,\mu\mathrm{m} \times 38\,\mu\mathrm{m}$ inside the MgO:PPLN. This corresponded to an intensity at the waist of $\approx 100\,\mathrm{kW/cm^2}$. If it was exclusively the average power of 2 W causing the physical damage, then using a 2 W green CW laser should also lead to this type of damage. Without operating the nonlinear crystal in an OPO but with simple transmission of the focused green beam through the $6.7\,\mu\mathrm{m}$ grating for a period of 1 h, this grating did not exhibit the previously observed physical damage (closely spaced tracks) or dark spots. Therefore, the damage threshold regarding the average power only (no pulses) exceeds 2 W. This observation is supported by OPO and SHG publications in the CW regime reporting several Watts of green light [22–25].

Table 5.1 gives a summary of the different OPO pump regimes used in the experiments and the parameters involved. In this context, optical damage means the dark spots within and the beam distortion of the transmitted green pump beam (typically reversible), whereas physical damage means a physical degradation of the crystal structure visible under a microscope (irreversible).

TABLE 5.1: Summary of the different MgO:PPLN OPO pump regimes and observed damage effects (optical = dark spots / beam distortion during operation, physical = degradation of the crystal visible with a microscope).

Pump source	**CW laser*** 532nm	**Frequency-doubled MOPA** (20 ps, 230 MHz, 530 nm)				
Average pump power [W]	2	2	0.5	$1 \rightarrow 0.1^{\ddagger}$		
$1/e^2$**-waist radius** [$\mu\mathrm{m}^2$]	35×38	44×42	44×42	44×42	49×51	49×51
Peak intensity [$\mathrm{MW/cm^2}$]	$\approx 0.1^{\dagger}$	≈ 15	≈ 3.75	≈ 7.5	≈ 11	≈ 17
Crystal grating used [$\mu\mathrm{m}$]	6.7	7.1	7.0	6.9	6.8	6.8
Permanent damage?	No	Yes (optical + physical)	Yes (optical)	No	Yes (optical)	Yes (optical + physical)

* no OPO operation

† intensity at the beam waist, no pulses

‡ mechanically chopped at 1:9 duty cycle to 0.1 W

After all the experiments were carried out, the crystal coatings were examined with a microscope and no anomalies were seen. Thus, all the effects described in this section were not caused by problems with the coatings.

5.3.5 Discussion

The damage observed can be classified into two categories: optical damage (dark spots and beam distortion) and physical damage (degradation of the crystal structure) depending on the average power and peak intensity conditions. However, it can not be ruled out that the optical damage was only a preceding, more sensitive sign of the physical damage before it can be seen with a microscope. Furthermore, instabilities due to photo-refraction were always present and could be quantified with an output power fluctuation of $\pm 10\%$ of the OPO signal beam.

It was found that high pulse peak intensities were required to damage the crystal, since an experiment with a green CW pump laser did not cause damage up to an average power of $2\,\mathrm{W}$ (the intensity at the focus was $0.1\,\mathrm{MW/cm^2}$). However, a reduction of the average power seemed to be beneficial in that for an average power of $0.1\,\mathrm{W}$, peak intensities of $11\,\mathrm{MW/cm^2}$ were required to cause damage, whereas only $3.75\,\mathrm{MW/cm^2}$ led to damage, when the average power was $0.5\,\mathrm{W}$.

It was also found that the green pump light alone led to optical and physical damage, which was demonstrated by subjecting an unpoled region of the MgO:PPLN sample to $2\,\mathrm{W}$ and $15\,\mathrm{MW/cm^2}$ of pump light for around $30\,\mathrm{min}$, after which the crystal was damaged. It was argued that if no parametric oscillation is possible and hence no signal and idler in the infrared are present, no green-induced IR absorption should be possible. From this observation, it is concluded that while GRIIRA may have contributed to the damage during OPO operation, it was not the sole damage process.

Given that the damage process appears to only require intense green light and not the presence of infrared light, it is speculated that the process is initially due to nonlinear absorption. The dependence of the damage process on average power as well as intensity suggests that linear absorption, perhaps as a result of defects formed by the high intensity visible light, also plays a role. It has previously been shown that lattice impurities, primarily Fe-ions on the parts-per-million scale, can facilitate linear and nonlinear absorption [17–19, 44, 45].

5.3.6 Section summary

In this section 5.3, a picosecond, $230\,\mathrm{MHz}$ SPOPO based on MgO:PPLN was demonstrated that produced $\approx 165\,\mathrm{mW}$ (signal, $845\,\mathrm{nm}$) and $\approx 107\,\mathrm{mW}$ (idler, $1421\,\mathrm{nm}$) of

average power for $\approx 1\,\mathrm{W}$ of $530\,\mathrm{nm}$ green pump power without crystal damage. However, crystal damage occurred under certain operating conditions with a complex interplay of high intensities and average powers. In order to avoid the damage, a viable option for an ultrashort, green-pumped SPOPO using MgO:PPLN as the nonlinear medium could be a low pump repetition rate and a long OPO resonator, where the average power is low but the peak intensity is high. To maintain a compact resonator, an intracavity single-mode fibre for signal feedback could be utilised [40, 41].

5.4 LBO-based, green-pumped, picosecond, high-repetition-rate optical parametric oscillator

Because of the problems and power limitations of MgO:PPLN in a green-pumped, ultrashort-pulse SPOPO as reported in the previous section 5.3, it was decided to use an LBO crystal instead to enable OPO operation at higher pump powers and hence higher average output powers. LBO is suitable for this kind of application due to its high damage threshold, its transparency range in the visible and NIR and its convenient non-critical BPM arrangement. However, the gain is lower compared to lithium niobate with an effective nonlinear coefficient of only $d_{eff} = 1.17\,\mathrm{pm/V}$.

5.4.1 Pulse compression of MOPA output

In order to have sufficient OPO gain using an LBO crystal with the lower d_{eff}, the $20\,\mathrm{ps}$ pulses from the MOPA at $1060\,\mathrm{nm}$ were compressed in a grating compressor before the frequency-doubling. The shorter pulse duration and hence higher peak power can partially compensate for the reduced effective nonlinear coefficient. Furthermore, it is also more attractive for CARS applications, where, for example, durations of a few picoseconds are considered optimal (best signal-to-noise and spectral resolution characteristics) [4, 12]. As described in section 5.2.1, the spectrum of the $20\,\mathrm{ps}$ pulses was nonlinearly broadened due to SPM during amplification in the YDFs and hence the additional bandwidth allowed for subsequent pulse compression. Equally, when using the instantaneous frequency picture in the time domain, SPM led to frequency chirping with a red shift at the leading edge and a blue shift at the trailing edge, without affecting the actual pulse duration [46]. The negative dispersion of the compressor (blue components faster than red components) could compensate for this chirp.

The $1060\,\mathrm{nm}$ MOPA output beam was redirected into the pulse compressor before focusing it into the frequency-doubling crystal as indicated in figure 5.1. The compressor used a fused silica transmission grating (Ibsen Photonics A/S, Denmark) in a four-pass

Littrow configuration as illustrated in figure 5.13. The fused silica grating with dimensions of $20\,\mathrm{mm} \times 10\,\mathrm{mm}$, an AR-coating for $1064\,\mathrm{nm}$ and a diffraction efficiency of $> 90\%$ had a groove period of $1250\,\mathrm{mm}^{-1}$. The angle of incidence of $41.5°$ was calculated with the Littrow ($\theta_{in} = \theta_d$) grating equation $m\lambda = 2d \sin\theta_{in}$. Two AR-coated right-angle prisms were used to direct the beam sideways (horizontal prism) and upwards (vertical prism), which permitted an accurate alignment. The dispersion of the prism glass material can be neglected, because of the low bandwidth of the picosecond pulses and because it can readily be compensated for by changing the separation between the horizontal prism and the transmission grating. A pick-off mirror directed the output beam (in red), which was elevated with respect to the input beam (in blue), towards the SHG stage.

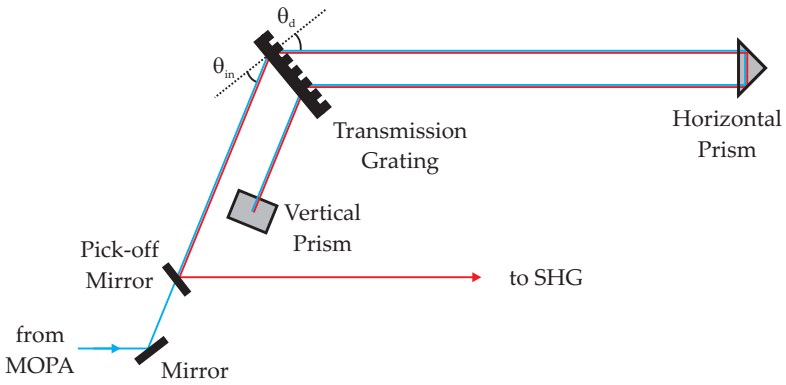

FIGURE 5.13: Schematic layout of the transmission grating compressor. The grating was operated in a four-pass Littrow configuration with $\theta_{in} = \theta_d = 41.5°$ for maximum diffraction efficiency. Right-angle prisms were used to direct the beams sideways (horizontal prism) and upwards (vertical prism). A pick-off mirror directed the elevated output beam (red line) to the SHG stage.

The throughput efficiency of the compressor was typically around 70%. The shortest pulse duration was experimentally found by changing the distance between the transmission grating and the horizontal prism and thus the GDD. An autocorrelation trace of the output pulses is shown in figure 5.14 with a FWHM width of $6.2\,\mathrm{ps}$, which corresponds to a pulse duration of $4.4\,\mathrm{ps}$ assuming a Gaussian temporal pulse profile. The distance corresponding to this optimal duration was $76\,\mathrm{cm}$. This shorter pulse duration produced a $4.5\times$ increased peak power compared to the uncompressed $20\,\mathrm{ps}$ pulses, but with the average power loss due to the 70% compressor efficiency taken into account, this number decreased to $3.2\times$.

The damaged $15\,\mathrm{mm}$-long LBO crystal in the SHG stage described in section 5.2.2 was replaced with a $20\,\mathrm{mm}$ crystal (all other specifications were the same) and the fundamental NIR beam was focused to a smaller waist diameter of $\approx 55\,\mu\mathrm{m}$. Both measures led to a higher SHG conversion efficiency. Under these improved conditions, a maximum of $25\,\mathrm{W}$ of second-harmonic green light was generated for $42\,\mathrm{W}$ of fundamental NIR light, corresponding to a conversion efficiency of 60%.

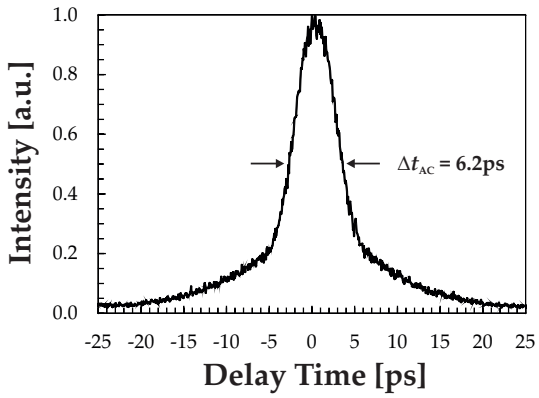

FIGURE 5.14: Autocorrelation trace of the transmission grating compressor output pulses. The FWHM autocorrelation width was $6.2\,\mathrm{ps}$ corresponding to a pulse duration of $4.4\,\mathrm{ps}$ assuming a Gaussian temporal pulse profile.

5.4.2 Experimental setup of the LBO optical parametric oscillator

The OPO ring resonator for the experiments with the LBO had the same layout and mirrors as the one in figure 5.6, but the resonator optical path length was now $1.3\,\mathrm{m}$ to achieve synchronism with the $230\,\mathrm{MHz}$ pump pulse train. Since the oven for the LBO had different dimensions, it was necessary to increase the bow-tie angle θ to around $15°$ with the advantage of realising a shorter, more compact resonator. Because of the relatively short resonator length of $1.3\,\mathrm{m}$, the beam ellipticity that is introduced by the curved mirror astigmatism and the bow-tie angle does not become significant.

The LBO crystal (Eksma Optics, Lithuania) had dimensions of $50 \times 5 \times 5\,\mathrm{mm}^3$ and was AR-coated on the input and output facet for the pump ($R < 0.1\%$ at $530\,\mathrm{nm}$) and the signal range ($R < 2\%$ from $650\,\mathrm{nm}$ to $1060\,\mathrm{nm}$). The crystal was cut for an NCPM type I interaction ($e \rightarrow o + o$) along the x-axis with $\theta = 90°$ and $\phi = 0°$. The extraordinary polarisation along the y-axis for the pump beam was adjusted with a HWP. The LBO crystal was held in an oven for temperature BPM, where the phase-matching condition

$$\frac{n_y\left(\lambda_p, T\right)}{\lambda_p} - \frac{n_z\left(\lambda_s, T\right)}{\lambda_s} - \frac{n_z\left(\lambda_i, T\right)}{\lambda_i} = 0 \tag{5.3}$$

must be fulfilled (with energy conservation $1/\lambda_p = 1/\lambda_s + 1/\lambda_i$). For example, for a temperature of $T = 129°\mathrm{C}$ and the pump wavelength of $530\,\mathrm{nm}$, a signal at $850\,\mathrm{nm}$ and the corresponding idler at $1.4\,\mu\mathrm{m}$ are generated. The temperature-dependent Sellmeier equation as reported by Kato [47] was used to calculate the phase-matching temperatures.

A similar analysis of the group velocity mismatches, the signal gain bandwidth and the pump acceptance bandwidth as discussed in section 5.3.1 showed that the use of LBO was much less critical compared to MgO:PPLN. With the Sellmeier equation [47] and the temperature and wavelengths as above, the group velocity mismatches

were $\mathrm{GVM}_{s,p} = 0.032\,\mathrm{ps/mm}$, $\mathrm{GVM}_{s,i} = 0.012\,\mathrm{ps/mm}$ and $\mathrm{GVM}_{i,p} = 0.044\,\mathrm{ps/mm}$, which resulted in walk-offs of $1.6\,\mathrm{ps}$, $0.6\,\mathrm{ps}$ and $2.2\,\mathrm{ps}$ in the $50\,\mathrm{mm}$-long LBO crystal, respectively. This was still acceptable even for the compressed pump pulses. The signal gain bandwidth and the pump acceptance bandwidth were $9.54 \cdot 10^{12}\,\mathrm{rad/s}$ and $2.52 \cdot 10^{12}\,\mathrm{rad/s}$, respectively, allowing for maximum signal and pump FWHM bandwidths of up to $3.66\,\mathrm{nm}$ and $0.38\,\mathrm{nm}$ at these particular wavelengths.

With the $-250\,\mathrm{mm}$ curved mirrors and the $1.3\,\mathrm{m}$ OPO cavity, $\lambda_s = 850\,\mathrm{nm}$ at $T = 129°\mathrm{C}$ and the corresponding refractive index $n_z\,(\lambda_s, T) = 1.61$ of LBO, the signal waist radius was calculated with the ABCD matrix resonator model to be $73\,\mu\mathrm{m}$ (negligible ellipticity, as mentioned above). The confocal parameter was $64\,\mathrm{mm}$ giving a focusing parameter of $\xi_s = 0.78$. A slightly elliptical pump waist radius of $72\,\mu\mathrm{m} \times 61\,\mu\mathrm{m}$, parallel and perpendicular to the resonator plane, respectively, was obtained with a two-lens telescope and an $f = 250\,\mathrm{mm}$ focusing lens, yielding a good match of pump and signal waists.

5.4.3 Experiments and results

For initial alignment of the SPOPO, a phase-matching temperature of $140°\mathrm{C}$ was chosen, as it was in the centre region of the theoretical wavelength tuning curve. For pump wavelengths lower than $\approx 600\,\mathrm{nm}$, LBO OPOs show a characteristic retracing behaviour of the temperature tuning curve with two signal and correspondingly two idler branches [10, 48]. That is two different signal (and two different idler) wavelengths can be phase-matched and can oscillate at the same temperature. Because of the different group delays of different signal wavelengths during one round-trip (mainly due to dispersion in the nonlinear medium) and the required pulse synchronism of pump and signal, the OPO operates first on one and then on the other signal as the cavity length is scanned [10, 49]. Additional to the group delay condition, the phase-matching condition must be fulfilled at the same time from one of the two pairs. The two pairs of signal and idler wavelengths at $140°\mathrm{C}$ were $679\,\mathrm{nm}$ / $2.42\,\mu\mathrm{m}$ and $877\,\mathrm{nm}$ / $1.34\,\mu\mathrm{m}$, respectively, and the ring cavity length was tuned by around $260\,\mu\mathrm{m}$ to access these two pairs of wavelengths.

Figure 5.15(a) shows the signal and idler power as well as the pump depletion as a function of the pump power with the SPOPO oscillating on the $679\,\mathrm{nm}$ mode and with an $R = 90\%$ output coupler. A maximum signal output power of $2.4\,\mathrm{W}$ for $18\,\mathrm{W}$ of pump power was produced and the slope efficiency was $\approx 17\%$. Oscillation started at a threshold of $\approx 4\,\mathrm{W}$ and the pump depletion reached values of more than 40% at higher pump power levels. The idler output at $2.42\,\mu\mathrm{m}$ could not be measured due to the lack of appropriate idler optics after curved mirror CM 2, which would ideally be

highly transmissive at this wavelength (for example with calcium fluoride substrates). These optics after CM 2 were in particular a collimation lens for the idler and a filter to separate the residual pump from the idler. The idler power generated within the crystal for $18\,\mathrm{W}$ of pump power was expected to be approximately $1.6\,\mathrm{W}$ based on the estimation in equation (5.1). For this estimation, the idler OC transmission and round-trip loss were neglected, because the idler was not resonant. In figure 5.15(b), the output power and pump depletion as a function of pump power for the other signal wavelength of $877\,\mathrm{nm}$ at $140°\mathrm{C}$ is shown. The highest combined output power was produced under these conditions with $2.5\,\mathrm{W}$ of signal and $1.7\,\mathrm{W}$ of idler power at a pump power of $17\,\mathrm{W}$. Since the idler wavelength was $1.34\,\mu\mathrm{m}$ now, the light was transmitted through all optics and could be measured. The signal and idler slope efficiencies were $\approx 17\%$ and $\approx 11\%$, respectively, the oscillation threshold was $1.3\,\mathrm{W}$ and the pump depletion reached 45%. Using this pump depletion, the pump and signal powers as given above, the quantum ratio $\lambda_p/\lambda s$ and the output coupling transmission of 10%, a signal round-trip loss of $\epsilon_s = 8.5\%$ was calculated [11], which was attributed to the LBO coating losses ($\approx 1.7\%$ per surface), some transmission loss of the imperfect mirror coatings ($T \approx 0.1\%$ per mirror at $877\,\mathrm{nm}$) and other scattering losses. Considering merely the signal power, more than $3.5\,\mathrm{W}$ could be generated at a phase-matching temperature of $110°\mathrm{C}$ corresponding to a signal wavelength of $740\,\mathrm{nm}$ as can be seen in figure 5.17 below, but with more pronounced power fluctuations.

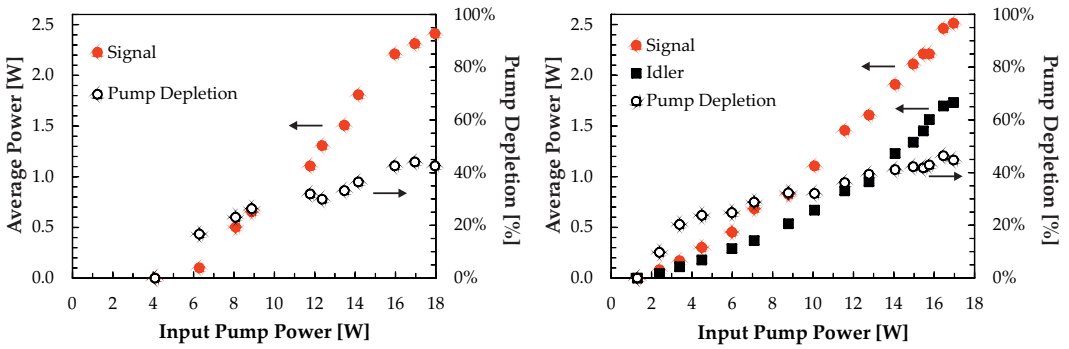

FIGURE 5.15: Output power and pump depletion as a function of input pump power of the picosecond, green-pumped LBO SPOPO operating at a signal wavelength of (a) $679\,\mathrm{nm}$ and (b) $877\,\mathrm{nm}$ and using an $R = 90\%$ signal output coupler. In (a), the idler output power could not be measured because of the lack of transmissive optics (collimation and filtering) at the idler wavelength of $2.42\,\mu\mathrm{m}$.

Previously, the highest output power from a picosecond LBO SPOPO of $1.6\,\mathrm{W}$ (signal only, no idler) tunable from $740\,\mathrm{nm}$ to $930\,\mathrm{nm}$ was reported by Tukker *et al.* using $5.6\,\mathrm{W}$ of pump power from a frequency-doubled, $50\,\mathrm{ps}$ Nd:YLF laser [11]. To the best of the author's knowledge, the total output power of $2.5\,\mathrm{W}$ and $1.7\,\mathrm{W}$ for signal and idler, respectively, in the picosecond regime was the highest produced in general and also the highest using a MOPA pump system based on YDF amplifiers in particular. The

benchmark for output power of SPOPOs using YDF MOPA pump sources was the demonstration of 270 mW (signal) and 300 mW (idler) with a signal tunability from 780 nm to 935 nm from Cleff *et al.*, but in the femtosecond regime [13].

The tuning behaviour of the SPOPO was investigated by changing the LBO temperature from 110°C to 200°C and additionally by changing the cavity length to access the other branch of the tuning curve as can be seen in figure 5.16. The signal could be tuned from 651 nm to 1040 nm and the idler from 1081 nm to 2851 nm. The solid red and black curves represent the theoretical tuning curve derived from the temperature-dependent Sellmeier equation of LBO as reported in [47]. The deviation between experiment and theory at the turning points, also reported in other publications [8, 11], may be explained by an inaccurate Sellmeier equation or possibly an insufficiently accurate temperature measurement inside the LBO oven. A uniform shift of the theory curve by 7°C yielded a good overlap between experiment and theory (requirement of uniform shift also reported by Kato [47]) around the turning points and at the degeneracy point. The dashed red and black curves represent the shifted tuning curves. However, the deviation between the theory curve and the long-wavelength idler arm becomes more apparent, which can be attributed to the Sellmeier coefficients that may not be accurate enough for this spectral range.

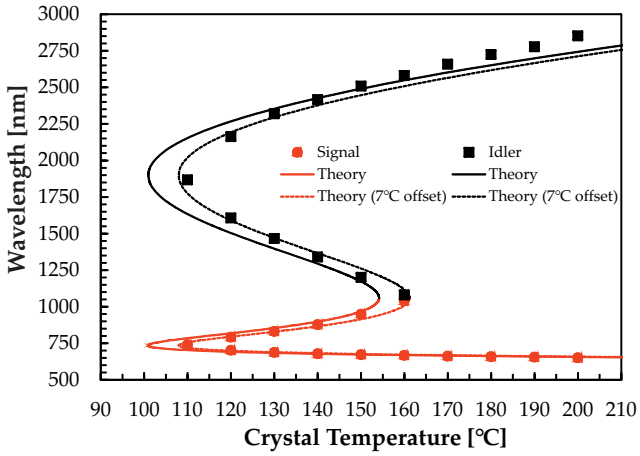

FIGURE 5.16: Temperature tuning curve of the picosecond, green-pumped LBO SPOPO (theory curve based on [47]). The transition between the two signal (or idler) wavelengths at one specific temperature was achieved by cavity length tuning. Deviations of experiment and theory may be explained by an inaccurate Sellmeier equation or an insufficiently accurate temperature measurement inside the oven. A good overlap between experiment and theory was obtained with a uniform shift of the theory curve by 7°C (dashed curves).

Figure 5.17 shows the output power versus the wavelength for the signal and idler, where the pump power was set to 17 W at any data point. It can be seen that the highest signal power of 3.7 W was produced at 740 nm (110°C) and the highest idler power of 1.8 W at 1.34 μm (140°C). The measured idler power dropped to zero at wavelengths $> 2\,\mu$m due to the inherent disadvantageous quantum ratio λ_p/λ_i and the absorption in the idler collimation lens and the pump / idler separation filter. The rapid drop of the

signal power on the short wavelength side was caused by the mirror coating characteristics (highly transmissive for the pump at $530\,\mathrm{nm}$), which hindered continuation of the signal resonance. The SPOPO operated unstably and with reduced output powers near the point of degeneracy at $1060\,\mathrm{nm}$, which was due to the mirror coating characteristics, their transition region from high reflection to high transmission at $\approx 1100\,\mathrm{nm}$ and the resulting doubly resonant operation with the additional constraint of simultaneous cavity resonances for both signal and idler as described before.

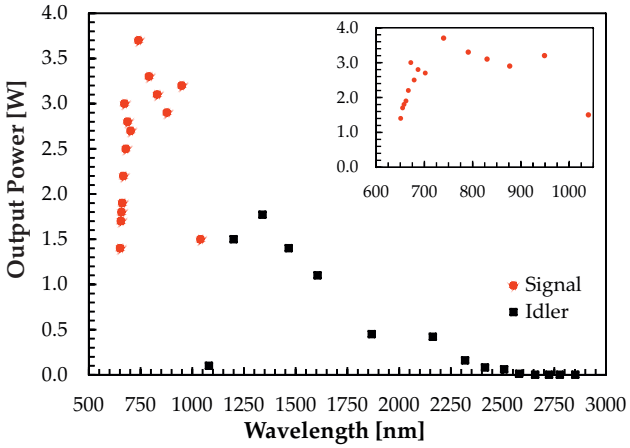

FIGURE 5.17: Output powers as a function of tuning wavelengths of the picosecond, green-pumped LBO SPOPO at 17 W of pump power. For clarity, the inset shows the signal only. The power drop near degeneracy at $1060\,\mathrm{nm}$ was due to the typical instabilities in this regime and the mirror coating characteristics.

The FWHM autocorrelation width of $4.5\,\mathrm{ps}$ of the signal at $740\,\mathrm{nm}$ was measured with an intensity autocorrelator and corresponds to a pulse duration of $3.2\,\mathrm{ps}$, if a Gaussian pulse profile is assumed. The pulse duration of the green pump pulses at $530\,\mathrm{nm}$ could not be measured for comparison, but the pulse duration of the $1060\,\mathrm{nm}$ pulses after compression was $4.4\,\mathrm{ps}$ (section 5.4.1). Thus, the signal pulse duration was somewhat shorter than the original NIR pump, which is under certain conditions typical for nonlinear frequency conversion processes and was observed in other experiments in this thesis as well.

Reliable values for the M^2-beam quality could not be recorded because of spatial instabilities of the SPOPO output beams and a beam profiler with a sensitive area that was too small. This was attributed to the performance of the pump source and not the SPOPO, because the input pump beam was spatially unstable already and this was transferred to the signal and idler output. The path length from the MOPA output to the SPOPO input was around $10.5\,\mathrm{m}$, which was mainly due to the long compressor and the SHG stage, but also due to other necessary optics. The maximum angular beam drift from the reference beam direction was measured to be approximately $0.5\,\mathrm{mrad}$. Therefore, even small changes to the final amplifier fibre in the MOPA had profound effects on the SPOPO input pump beam. The suboptimal launch efficiency of the pump

light into the inner cladding of this fibre led to thermal and thus mechanical problems with the fibre mount. This could be mitigated by active heat-sinking of the fibre and by ultra-stable fibre mounts. Also, since the final amplifier did not operate purely on the fundamental mode but with some higher-order modes ($V > 2.405$), beam pointing instabilities caused by modal interference [50] of the many modes were existent (see also chapter 7 regarding modal interference). Further improvement of the tapered splice quality could increase the mode purity, so that higher-order modes are not excited at all.

5.4.4 Section summary

In this section 5.4, a picosecond, $230\,\mathrm{MHz}$ SPOPO based on LBO was reported that generated the highest average output powers to date. For a pump power of $17\,\mathrm{W}$, a signal power of $3.7\,\mathrm{W}$ at $740\,\mathrm{nm}$ and a maximum combined output power of $2.5\,\mathrm{W}$ (signal at $877\,\mathrm{nm}$) and $1.7\,\mathrm{W}$ (idler at $1.34\,\mu\mathrm{m}$) was measured. The pump source was a fibre-amplified, gain-switched laser diode MOPA system, whose output pulses were compressed and frequency-doubled. The results demonstrated the effectiveness of such fibre-based amplifier systems as OPO pump sources for power scaling. However, further work is required to improve the spatial stability of the pump source.

5.5 Conclusions

In this chapter, two different types of high-power, picosecond OPOs synchronously pumped in the green were demonstrated. The pump source for both consisted of a frequency-doubled (to $530\,\mathrm{nm}$), fibre-amplified, gain-switched laser diode MOPA system operating at a repetition rate of $230\,\mathrm{MHz}$. The pulse duration of the fundamental wave at $1060\,\mathrm{nm}$ before SHG was either $20\,\mathrm{ps}$ or $4.4\,\mathrm{ps}$ (with pulse compression). Such OPOs can theoretically generate signal wavelengths between $650\,\mathrm{nm}$ and $1060\,\mathrm{nm}$ (plus the idler output from $1.06\,\mu\mathrm{m}$ to $2.87\,\mu\mathrm{m}$) and are thus an attractive alternative to Ti:Sapphire laser, currently the preferred choice for tunable ultrashort pulses in the near-infrared. Furthermore, such systems are practical and versatile tools in CARS spectroscopy / microscopy [1–5], stimulated Raman scattering microscopy [6], SHG microscopy [51–53] and STED microscopy [7]. The high repetition rate of $230\,\mathrm{MHz}$ of this system (up to $920\,\mathrm{MHz}$ possible) could also be attractive for these applications in terms of avoiding damage of biological samples. It has been shown that damage can be nonlinearly induced by high peak powers and thus an increase of the repetition rate to reduce the peak power below the damage threshold, but simultaneously retaining a high average power for good signal-to-noise ratio, is preferred in some circumstances

[51, 54, 55]. An advantageous side effect of the high repetition rate is the shorter pixel dwelling time and thus a faster acquisition time per frame in imaging applications.

The first OPO type that was demonstrated was a synchronously pumped OPO based on MgO:PPLN producing $\approx 165\,\mathrm{mW}$ (signal, $845\,\mathrm{nm}$) and $\approx 107\,\mathrm{mW}$ (idler, $1421\,\mathrm{nm}$) of average power for $\approx 1\,\mathrm{W}$ of green pump power at $530\,\mathrm{nm}$. The oscillation threshold was $369\,\mathrm{mW}$ and the pump depletion saturated at $\approx 30\%$. However, operation, especially at higher pump power, was complicated and even prevented due to well-known effects occurring in lithium niobate such as photo-refraction and GRIIRA. It was found that a combination of both high average power and high peak intensity led to crystal damage. An investigation of crystal damage mechanisms, when MgO:PPLN is subjected to light pulses in the visible (as opposed to CW operation with several Watts of power, where no such effects are observed), was carried out with the result that the observed damage required high peak intensities of around $10\,\mathrm{MW/cm^2}$. But at the same time, an influence of the average power to the damage was evident and a reduction of the average power appeared to be beneficial for the same peak intensity. Photo-refraction, GRIIRA and nonlinear absorption were identified as possible damage mechanisms with nonlinear absorption being the most likely process for physical damage of the crystal structure. The already wide-spread insight was confirmed that lithium niobate used in ultrashort-pulse nonlinear devices with visible light suffers from detrimental effects, which limit the device efficiency and beam quality, but additional important information as to where the limits and damage thresholds lie could be found. This information can be added to the "map" of safe operation regimes in terms of pulse duration, repetition rates, power levels, peak intensities and wavelengths. A viable option for a pulsed, green-pumped OPO based on MgO:PPLN could be a low pump repetition rate of a few megahertz and a long but still compact fibre-feedback OPO resonator [40, 41], where the average power is low but the peak intensity is relatively high. While the MgO:PPLN would still be susceptible to damage effects, it was shown here that under such conditions, the crystal could be operated in an OPO without suffering from catastrophic damage.

The second type of OPO was based on LBO, where the highest signal (idler) power of $3.7\,\mathrm{W}$ ($1.8\,\mathrm{W}$) and the highest combined output power of $2.5\,\mathrm{W}$ (signal) and $1.7\,\mathrm{W}$ (idler) was generated with a pump power of $17\,\mathrm{W}$. The pump depletion reached 45%, the oscillation threshold was $1.3\,\mathrm{W}$ and the signal and idler slope efficiencies were $\approx 17\%$ and $\approx 11\%$, respectively. To the best of the author's knowledge, this constituted the highest output power from a green-pumped, picosecond SPOPO to date. The pulse duration of the signal pulses was $3.2\,\mathrm{ps}$. Wavelength tuning from $651\,\mathrm{nm}$ to $1040\,\mathrm{nm}$ for the signal and from $1081\,\mathrm{nm}$ to $2851\,\mathrm{nm}$ for the idler was carried out by changing the LBO temperature from $110^\circ\mathrm{C}$ to $200^\circ\mathrm{C}$ and by changing the cavity length. The OPO operation suffered from problems with spatial instabilities, which were mainly due to the

inherently long path length of more than $10\,\mathrm{m}$ between MOPA output and OPO input. Thus, even small perturbations to the final amplifier fibre (thermal loading, mechanical instability, modal interference) had significant consequences for the OPO stability.

References

[1] R. F. Begley, A. B. Harvey, and R. L. Byer, "Coherent anti-Stokes Raman spectroscopy," Applied Physics Letters **25**(7), 387–390 (1974).

[2] A. M. Zheltikov, "Coherent anti-Stokes Raman scattering: from proof-of-the-principle experiments to femtosecond CARS and higher order wave-mixing generalizations," Journal of Raman Spectroscopy **31**(8-9), 653–667 (2000).

[3] C. L. Evans, E. O. Potma, M. Puoris'haag, D. Côté, C. P. Lin, and X. S. Xie, "Chemical imaging of tissue in vivo with video-rate coherent anti-Stokes Raman scattering microscopy," Proceedings of the National Academy of Sciences of the United States of America **102**(46), 16,807–16,812 (2005).

[4] C. L. Evans and X. S. Xie, "Coherent Anti-Stokes Raman Scattering Microscopy: Chemical Imaging for Biology and Medicine," Annual Review of Analytical Chemistry **1**(1), 883–909 (2008).

[5] F. Ganikhanov, S. Carrasco, X. Sunney Xie, M. Katz, W. Seitz, and D. Kopf, "Broadly tunable dual-wavelength light source for coherent anti-Stokes Raman scattering microscopy," Opt. Lett. **31**(9), 1292–1294 (2006).

[6] C. W. Freudiger, W. Min, B. G. Saar, S. Lu, G. R. Holtom, C. He, J. C. Tsai, J. X. Kang, and X. S. Xie, "Label-Free Biomedical Imaging with High Sensitivity by Stimulated Raman Scattering Microscopy," Science **322**(5909), 1857–1861 (2008).

[7] S. W. Hell and J. Wichmann, "Breaking the diffraction resolution limit by stimulated emission: stimulated-emission-depletion fluorescence microscopy," Opt. Lett. **19**(11), 780–782 (1994).

[8] S. D. Butterworth, S. Girard, and D. C. Hanna, "High-power, broadly tunable all-solid-state synchronously pumped lithium triborate optical parametric oscillator," J. Opt. Soc. Am. B **12**(11), 2158–2167 (1995).

[9] M. Jurna, J. P. Korterik, H. L. Offerhaus, and C. Otto, "Noncritical phase-matched lithium triborate optical parametric oscillator for high resolution coherent anti-Stokes Raman scattering spectroscopy and microscopy," Applied Physics Letters **89**(25), 251,116–3 (2006).

[10] J. D. Kafka, M. L. Watts, and J. W. Pieterse, "Synchronously pumped optical parametric oscillators with LiB_3O_5," J. Opt. Soc. Am. B **12**(11), 2147–2157 (1995).

[11] T. W. Tukker, C. Otto, and J. Greve, "Design, optimization, and characterization of a narrow-bandwidth optical parametric oscillator," J. Opt. Soc. Am. B **16**(1), 90–95 (1999).

[12] K. Kieu, B. G. Saar, G. R. Holtom, X. S. Xie, and F. W. Wise, "High-power picosecond fiber source for coherent Raman microscopy," Opt. Lett. **34**(13), 2051–2053 (2009).

[13] C. Cleff, J. Epping, P. Gross, and C. Fallnich, "Femtosecond OPO based on LBO pumped by a frequency-doubled Yb-fiber laser-amplifier system for CARS spectroscopy," Applied Physics B: Lasers and Optics **103**(4), 795–800 (2011).

[14] L. E. Myers, R. C. Eckardt, M. M. Fejer, R. L. Byer, W. R. Bosenberg, and J. W. Pierce, "Quasi-phase-matched optical parametric oscillators in bulk periodically poled $LiNbO_3$," J. Opt. Soc. Am. B **12**(11), 2102–2116 (1995).

[15] R. W. Boyd, *Nonlinear Optics*, 2nd ed. (Academic Press, San Diego, 2002).

[16] A. Ashkin, G. D. Boyd, J. M. Dziedzic, R. G. Smith, A. A. Ballman, J. J. Levinstein, and K. Nassau, "Optically-induced refractive index inhomogeneities in $LiNbO_3$ and $LiTaO_3$," Applied Physics Letters **9**(1), 72–74 (1966).

[17] F. Jermann, M. Simon, and E. Krätzig, "Photorefractive properties of congruent and stoichiometric lithium niobate at high light intensities," J. Opt. Soc. Am. B **12**(11), 2066–2070 (1995).

[18] Y. Furukawa, K. Kitamura, A. Alexandrovski, R. K. Route, M. M. Fejer, and G. Foulon, "Green-induced infrared absorption in MgO doped $LiNbO_3$," Applied Physics Letters **78**(14), 1970–1972 (2001).

[19] J. Hirohashi, V. Pasiskevicius, S. Wang, and F. Laurell, "Picosecond blue-light-induced infrared absorption in single-domain and periodically poled ferroelectrics," Journal of Applied Physics **101**(3), 033,105 (2007).

[20] R. G. Batchko, D. R. Weise, T. Plettner, G. D. Miller, M. M. Fejer, and R. L. Byer, "Continuous-wave 532-nm-pumped singly resonant optical parametric oscillator based on periodically poled lithium niobate," Opt. Lett. **23**(3), 168–170 (1998).

[21] M. Nakamura, S. Higuchi, S. Takekawa, K. Terabe, Y. Furukawa, and K. Kitamura, "Optical damage resistance and refractive indices in near-stoichiometric MgO-doped $LiNbO_3$," Japanese Journal of Applied Physics Part 2-Letters **41**(1AB), L49–L51 (2002).

[22] D.-H. Lee, S. K. Kim, S.-N. Park, H. Su Park, J. Y. Lee, and S.-K. Choi, "Continuous-wave 532nm pumped MgO:PPLN optical parametric oscillator with external power regulation and spatial mode filtering," Appl. Opt. **48**(1), 37–42 (2009).

[23] S. Zaske, D. H. Lee, and C. Becher, "Green-pumped cw singly resonant optical parametric oscillator based on MgO:PPLN with frequency stabilization to an atomic resonance," Applied Physics B: Lasers and Optics **98**(4), 729–735 (2010).

[24] H. Furuya, A. Morikawa, K. Mizuuchi, and K. Yamamoto, "High-beam-quality continuous wave 3 W green-light generation in bulk periodically poled MgO:$LiNbO_3$," Japanese Journal of Applied Physics Part 1-Regular Papers Brief Communications & Review Papers **45**(8B), 6704–6707 (2006).

[25] C. B. E. Gawith, Covesion Ltd., Romsey, SO51 9DG, UK, personal communication (2011).

[26] V. Pruneri, S. D. Butterworth, and D. C. Hanna, "Low-threshold picosecond optical parametric oscillation in quasi-phase-matched lithium niobate," Applied Physics Letters **69**(8), 1029–1031 (1996).

[27] P. F. Chimento, M. Jurna, H. S. P. Bouwmans, E. T. Garbacik, L. Hartsuiker, C. Otto, J. L. Herek, and H. L. Offerhaus, "High-resolution narrowband CARS spectroscopy in the spectral fingerprint region," Journal of Raman Spectroscopy **40**(9), 1229–1233 (2009).

[28] D. N. Nikogosyan, *Nonlinear optical crystals: a complete survey*, 1st ed. (Springer, Berlin / Heidelberg, 2005).

[29] K. K. Chen, J. H. V. Price, S.-U. Alam, J. R. Hayes, D. J. Lin, A. Malinowski, and D. J. Richardson, "Polarisation maintaining 100W Yb-fiber MOPA producing μJ pulses tunable in duration from 1 to 21 ps," Opt. Express **18**(14), 14,385–14,394 (2010).

[30] K. K. Chen, S.-U. Alam, J. R. Hayes, H. J. Baker, D. Hall, R. Mc Bride, J. H. V. Price, D. J. Lin, A. Malinowski, and D. J. Richardson, "56-W Frequency-Doubled Source at 530 nm Pumped by a Single-Mode, Single-Polarization, Picosecond, Yb^{3+}-Doped Fiber MOPA," IEEE Photonics Technology Letters **22**(12), 893–895 (2010).

[31] J. C. Diels and W. Rudolph, *Ultrashort Laser Pulse Phenomena*, 1st ed. (Academic Press, San Diego, 1996).

[32] B. E. A. Saleh and M. C. Teich, *Fundamentals of photonics*, 1st ed. (John Wiley & Sons, New York, 1991).

[33] S. Lecomte, R. Paschotta, M. Golling, D. Ebling, and U. Keller, "Synchronously pumped optical parametric oscillators in the 1.5-μm spectral region with a repetition rate of 10 GHz," J. Opt. Soc. Am. B **21**(4), 844–850 (2004).

[34] X. P. Zhang, J. Hebling, A. Bartels, D. Nau, J. Kuhl, W. W. Rühle, and H. Giessen, "1-GHz-repetition-rate femtosecond optical parametric oscillator," Applied Physics Letters **80**(11), 1873–1875 (2002).

[35] A. E. Siegman, *Lasers*, 1st ed. (University Science Books, Sausalito, California, 1986).

[36] D. C. Hanna, "Astigmatic Gaussian Beams Produced by Axially Asymmetric Laser Cavities," IEEE Journal of Quantum Electronics **5**(10), 483–488 (1969).

[37] O. Gayer, Z. Sacks, E. Galun, and A. Arie, "Temperature and wavelength dependent refractive index equations for MgO-doped congruent and stoichiometric $LiNbO_3$," Applied Physics B: Lasers and Optics **91**(2), 343–348 (2008).

[38] S. Guha, "Focusing dependence of the efficiency of a singly resonant optical parametric oscillator," Applied Physics B: Lasers and Optics **66**(6), 663–675 (1998).

[39] M. J. McCarthy and D. C. Hanna, "All-solid-state synchronously pumped optical parametric oscillator," J. Opt. Soc. Am. B **10**(11), 2180 (1993).

[40] T. Südmeyer, E. Innerhofer, F. Brunner, R. Paschotta, T. Usami, H. Ito, S. Kurimura, K. Kitamura, D. C. Hanna, and U. Keller, "High-power femtosecond fiber-feedback optical parametric oscillator based on periodically poled stoichiometric $LiTaO_3$," Opt. Lett. **29**(10), 1111–1113 (2004).

[41] F. Kienle, P. Siong Teh, S.-U. Alam, C. B. E. Gawith, D. C. Hanna, D. J. Richardson, and D. P. Shepherd, "Compact, high-pulse-energy, picosecond optical parametric oscillator," Opt. Lett. **35**(21), 3580–3582 (2010).

[42] D. H. Titterton, J. A. C. Terry, D. H. Thorne, I. R. Jones, and D. Legge, "Observation of damage in PPLN," in *Growth, Fabrication, Devices, and Applications of Laser and Nonlinear Materials*, vol. 4268, pp. 5–13 (San Jose, CA, USA, 2001).

[43] G. Fibich and A. L. Gaeta, "Critical power for self-focusing in bulk media and in hollow waveguides," Opt. Lett. **25**(5), 335–337 (2000).

[44] J. R. Schwesyg, A. Markosyan, M. C. C. Kajiyama, M. Falk, D. H. Jundt, K. Buse, and M. M. Fejer, "Optical loss mechanisms in magnesium-doped lithium niobate crystals in the 300 to 2950 nm wavelength range," in *Advances in Optical Materials (AIOM)*, vol. AIThE3 (Istanbul, Turkey, 2011).

[45] D. A. Bryan, R. Gerson, and H. E. Tomaschke, "Increased optical damage resistance in lithium niobate," Applied Physics Letters **44**(9), 847–849 (1984).

[46] G. P. Agrawal, *Nonlinear Fiber Optics*, Optics and Photonics, 3rd ed. (Academic Press, San Diego, 2001).

[47] K. Kato, "Temperature-Tuned 90° Phase-Matching Properties of LiB_3O_5," IEEE Journal of Quantum Electronics **30**(12), 2950–2952 (1994).

[48] S. Lin, B. Wu, F. Xie, and C. Chen, "Phase-matching retracing behavior: New features in LiB_3O_5," Applied Physics Letters **59**(13), 1541–1543 (1991).

[49] D. T. Reid, G. T. Kennedy, A. Miller, W. Sibbett, and M. Ebrahim-Zadeh, "Widely tunable, near- to mid-infrared femtosecond and picosecond optical parametric oscillators using periodically poled $LiNbO_3$ and $RbTiOAsO_4$," IEEE Journal of Selected Topics in Quantum Electronics **4**(2), 238–248 (1998).

[50] J. W. Nicholson, A. D. Yablon, S. Ramachandran, and S. Ghalmi, "Spatially and spectrally resolved imaging of modal content in large-mode-area fibers," Opt. Express **16**(10), 7233–7243 (2008).

[51] S.-W. Chu, T.-M. Liu, C.-K. Sun, C.-Y. Lin, and H.-J. Tsai, "Real-time second-harmonic-generation microscopy based on a 2-GHz repetition rate Ti:sapphire laser," Opt. Express **11**(8), 933–938 (2003).

[52] P. J. Campagnola and L. M. Loew, "Second-harmonic imaging microscopy for visualizing biomolecular arrays in cells, tissues and organisms," Nature Biotechnology **21**(11), 1356–1360 (2003).

[53] W. R. Zipfel, R. M. Williams, R. Christie, A. Y. Nikitin, B. T. Hyman, and W. W. Webb, "Live tissue intrinsic emission microscopy using multiphoton-excited native fluorescence and second harmonic generation," Proceedings of the National Academy of Sciences **100**(12), 7075–7080 (2003).

[54] K. König, T. W. Becker, P. Fischer, I. Riemann, and K. J. Halbhuber, "Pulse-length dependence of cellular response to intense near-infrared laser pulses in multiphoton microscopes," Opt. Lett. **24**(2), 113–115 (1999).

[55] A. Vogel, J. Noack, G. Hüttman, and G. Paltauf, "Mechanisms of femtosecond laser nanosurgery of cells and tissues," Applied Physics B: Lasers and Optics **81**(8), 1015–1047 (2005).

Chapter 6

Energy-scalable femtosecond pulse shaping in a fibre-based CPA system

6.1 Introduction

High-energy ultrashort pulses are demanded in many scientific as well as industrial applications. Furthermore, clean, high-quality pump pulses are needed to produce high-energy pulses from an OPO. Fibre amplifier systems are attractive sources for such ultrashort pulses. Pulse energies in the mJ-range generated from fibre-based CPA systems using Yb-doped double-clad LMA PCF have been demonstrated [1, 2]. A two-stage fibre amplifier with PCF core diameters of $40\,\mu\mathrm{m}$ and $80\,\mu\mathrm{m}$, respectively, is embedded in the stretcher and compressor setup in reference [2] to produce $71\,\mathrm{W}$ of average output power in $800\,\mathrm{fs}$ pulses at a repetition rate of $50\,\mathrm{kHz}$, which results in a pulse energy of $1.45\,\mathrm{mJ}$. However, nonlinear effects occurring in fibres, mainly SPM, can significantly degrade the pulse profile and hence reduce the peak power. The energy contained in a high-quality pulse is therefore limited.

Adaptive pulse shaping is an additional route to obtain high-energy, pedestal-free ultrashort pulses apart from scaling the fibre mode area. Schimpf *et al.* chose amplitude-only spectral shaping [3], but at low pulse energies of $20\,\mathrm{nJ}$. The spectrum was shaped with an LC SLM and an optical spectrum analyser (OSA) in the feedback loop to create a parabolic profile. The linear chirp associated with a parabolic spectrum can be efficiently removed in a dispersive pulse compressor to obtain transform-limited pulses. SPM could be compensated up to a B-integral of $\approx 5\pi\,\mathrm{rad}$. $410\,\mathrm{fs}$ pulses with an average power of $1.5\,\mathrm{W}$ at a high repetition rate of $75\,\mathrm{MHz}$ were reported. He *et al.* applied an LC SLM as well, but for phase-only shaping [4]. The peak of the output autocorrelation served as feedback parameter. The CPA system with an EOM and an AOM for repetition rate reduction produced $800\,\mathrm{fs}$ pulses at a minimum repetition rate of

$16.67\,\mathrm{kHz}$. The pulse energy reached $65\,\mu\mathrm{J}$ with an estimated B-integral of $2.5\pi\,\mathrm{rad}$. In another publication of phase-only pulse shaping in a fibre-based CPA system [5], the spectrum at the output was measured and used to derive a phase profile that generates the minimum pulse duration. This method is based on the assumption that when the stretcher and compressor dispersions are perfectly matched in the linear regime (low power), then the phase generated through SPM in the nonlinear regime, which is expressed in the spectrum, can be flattened by applying the inverse phase profile (the nonlinear phase is the product of B-integral and normalised spectrum). Compressed pulses with a duration of $780\,\mathrm{fs}$ and an energy of $840\,\mu\mathrm{J}$ up to a B-integral of $2.5\pi\,\mathrm{rad}$ were produced with this method by using a 640 pixel LC SLM. This is a non-adaptive approach to pulse shaping and is hence very fast and only requires the measurement of one output spectrum at the desired power level. However, some flexibility is lost and an accurate alignment of stretcher and compressor is needed to eliminate dispersive broadening. Prawiharjo *et al.* reported adaptive phase and amplitude shaping in a fibre CPA system with pulse energies of $\approx 250\,\mathrm{nJ}$ [6]. The average output power was $12.6\,\mathrm{W}$ and the $170\,\mathrm{fs}$ pulses had a repetition rate of $50\,\mathrm{MHz}$. A dual mask LC SLM, a TPA feedback signal and a differential evolution algorithm were used to implement the adaptive shaping loop.

In this chapter, a method to produce energy-scalable femtosecond pulses using adaptive phase and amplitude shaping with a dual mask LC SLM in a fibre-based CPA system is demonstrated. This system is potentially a very interesting and versatile pump source for synchronously pumped OPOs. After a description of the CPA system in section 6.2, pulse shaping results with a single, $1\,\mathrm{km}$-long fibre stretcher and at the full repetition rate are presented (section 6.3). Experiments at reduced repetition rates follow in section 6.4. This includes pulse shaping at $10\times$ and $100\times$ lower repetition rates still with a $1\,\mathrm{km}$ stretcher (section 6.4.1) as well as experiments with different setups using distributed fibre stretchers and pulse shaper locations (section 6.4.2). The distributed stretcher approach was intended to generate specific amounts of SPM per amplifier stage to broaden the pulse spectrum, which potentially yields shorter pulses. The problem of satellite pulse generation due to the generated SPM and the pixellated nature of the LC SLM is discussed as well. To be able to quickly rearrange the setup and for reasons of simplicity and costs, an SMF was solely used for pulse stretching rather than a grating compressor, knowing that the TODs of fibre stretcher and grating compressor add up and thus need to be compensated for by the pulse shaper.

The work was carried out with the author's co-supervisor at the time, Dr. Jerry Prawiharjo, who wrote the pulse shaping algorithms. The author was involved in the different rearrangments of the system, the pulse shaping experiments, the pulse characterisation and the data analysis.

6.2 Experimental setup

Figure 6.1 shows a schematic of the fibre CPA and pulse shaping experimental setup as used for the experiments with 1 km of fibre stretcher described in this chapter.

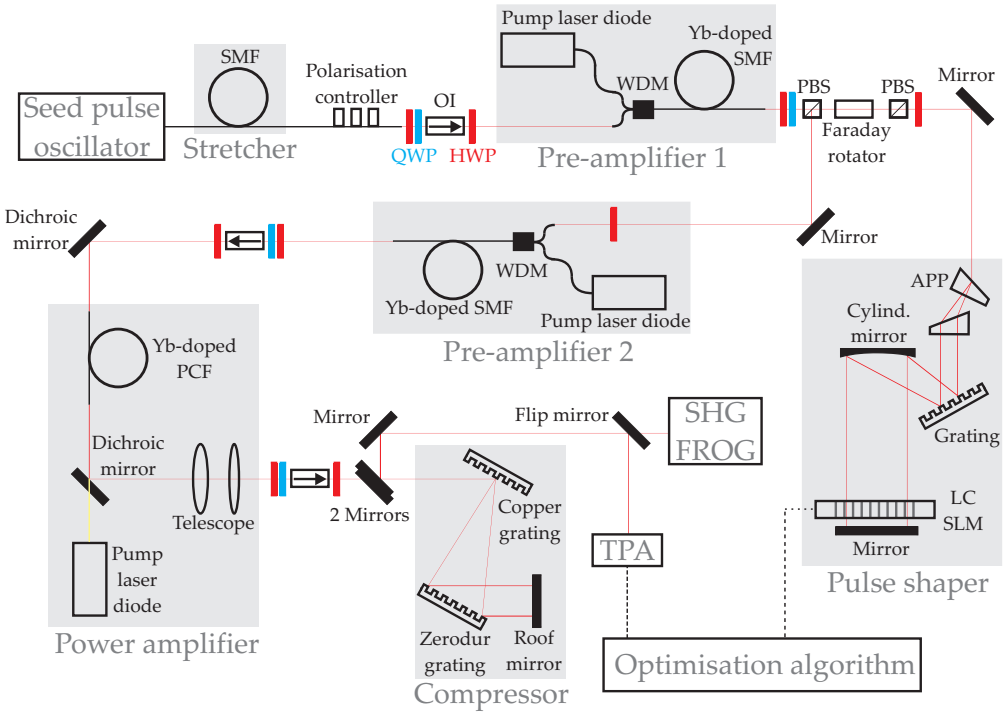

FIGURE 6.1: Schematic of the femtosecond fibre CPA and pulse shaping system. SMF: Single-mode fibre, QWP: $\lambda/4$-plate, HWP: $\lambda/2$-plate, OI: Optical isolator, WDM: Wavelength division multiplexer, PBS: Polarising beam splitter, APP: Anamorphic prism pair, LC SLM: Liquid-crystal spatial light modulator, PCF: Photonic crystal fibre, TPA: Two-photon absorption, SHG FROG: Second-harmonic generation frequency-resolved optical gating.

The seed pulse oscillator was a passively mode-locked Yb-doped fibre laser based on nonlinear polarisation rotation [7]. It used a Fabry-Perot cavity, was pumped with a 400 mW, 974 nm grating-stabilised LD and operated in the self-similar regime [8]. It also incorporated a saturable absorber mirror to ensure self-starting [9] and a grating pair for dispersion control. Control of the nonlinear switch was realised with a polarising beam splitter (PBS) and a quarter- and half-waveplate. Output coupling was performed by another PBS and a single half-waveplate. This oscillator, as described in detail in [10, 11], delivered chirped 2 ps pulses with 48.7 MHz repetition rate. The centre wavelength was 1040 nm with a FWHM of 16 nm (−20 dB-level: 23 nm). The average power was 30 mW, which yields a pulse energy of 0.6 nJ.

The pulses were coupled into 1 km of standard SMF (HI 1060, Corning Inc., USA) to temporally stretch the pulses. The dispersion of the HI 1060 fibre is $\beta_2 = 0.023\,\mathrm{ps}^2/\mathrm{m}$ and $\beta_3 = 3.9 \cdot 10^{-5}\,\mathrm{ps}^3/\mathrm{m}$ at 1030 nm [12]. The estimated duration after stretching was 240 ps. The total losses (fibre attenuation, coupling loss) were 30%. The output polarisation was adjusted by means of a manual fibre polarisation controller (PC).

The first pre-amplifier consisted of a $1.7\,\mathrm{m}$-long, core-pumped, Yb-doped SMF. The light of the $976\,\mathrm{nm}$, $450\,\mathrm{mW}$ fibre-coupled pump LD was combined with the seed pulses and coupled into the Yb-doped fibre by means of a WDM. The average output power of this amplifier was typically around $80\,\mathrm{mW}$.

The pulse shaping unit consisted of a 4-f-setup in reflective mode (see chapter 2.3.1). It was located between between pre-amplifier 1 and 2, because of the damage threshold of the SLM device, which limits it to lower powers. An anamorphic prism pair expanded the collimated input beam by a factor of three to achieve a larger time window and complexity. A diffraction grating (gold-coated, plane-ruled, period $1200\,\mathrm{mm}^{-1}$) dispersed the beam. A cylindrical mirror with $25.8\,\mathrm{cm}$ focal length focused the spectrum onto the SLM located in the Fourier plane. The SLM had two LC-array masks sandwiched between polarisers for phase and amplitude shaping. The device (SLM-128-D-NM, CRi Inc., USA) had 128 pixels per LC-mask, a pixel pitch of $100\,\mu\mathrm{m}$ giving a total array aperture of $12.8\,\mathrm{mm}$, a pixel height of $5\,\mathrm{mm}$, an inter-pixel gap of $2\,\mu\mathrm{m}$, a spectral range of $900\ldots1620\,\mathrm{nm}$ and a refresh rate of $4\,\mathrm{Hz}$. A maximum analogue drive voltage of $10\,\mathrm{V}$ could be applied per pixel. This was digitised at 12-bit resolution and hence equivalent to 4096 phase values in theory. However, only values between 600 and 4095 were usable due to the nonlinear mapping of voltage and phase from liquid crystals. The calibration curve of the SLM is shown in figure 6.2. The algorithm controlled only N_c pixels per LC-mask. They were then interpolated onto all 128 pixels. One controlled SLM pixel corresponded to one component x_j of an individual in the DE algorithm ($j = 1, 2, \ldots, 2N_c$). Since two masks were used, the number of components amounted to $2N_c$. Their values were $x_j \in [600, 4095]$. The maximum possible phase modulation was $6\pi\,\mathrm{rad}$ with the SLM in reflection mode. The $-20\,\mathrm{dB}$ pulse bandwidth of $23\,\mathrm{nm}$ was dispersed onto 97 pixels, which yielded a spatial dispersion of $0.24\,\mathrm{nm}$ per pixel. The time window of the setup (without SLM) was $23.9\,\mathrm{ps}$ and the complexity was 346. The pulse shaper had a throughput efficiency of 36%, therefore the power into the second pre-amplifier was around $29\,\mathrm{mW}$.

The second pre-amplifier was equivalent to pre-amplifier 1, but with a fibre length of only $1.5\,\mathrm{m}$. The amplification yielded an average power of $150\,\mathrm{mW}$.

The power amplifier comprised a $1.7\,\mathrm{m}$, double-clad, polarisation-maintaining, LMA, Yb-doped PCF as well as a $30\,\mathrm{W}$, $976\,\mathrm{nm}$, multi-mode, fibre-coupled pump LD. The PCF (DC-200/40-PZ-Yb-01, Crystal Fibre A/S, Denmark, cross section in figure 2.3(a)) had a core diameter of $40\,\mu\mathrm{m}$ with a numerical aperture of 0.03, the mode-field area was $650\,\mu\mathrm{m}^2$. The inner cladding had a diameter of $200\,\mu\mathrm{m}$ with a high numerical aperture of 0.55. The multi-mode pump was coupled into the inner cladding through a dichroic mirror (DM) in a counter-propagating configuration. The pump absorption

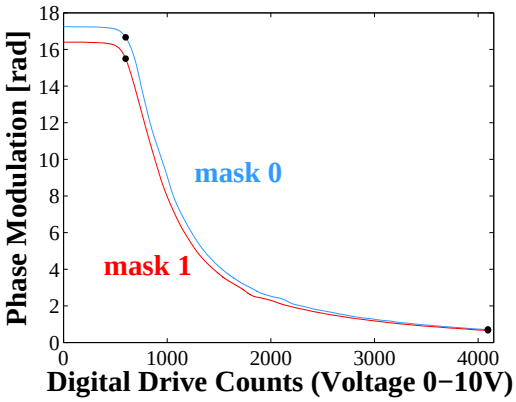

FIGURE 6.2: Calibration curve of the liquid crystal spatial light modulator. The phase modulation of each mask is a function of the applied voltage. The voltage is digitised with 12-bit resolution. The usable region stretches approximately from value 600 to 4095 (indicated with black dots).

was $10\,\mathrm{dB/m}$ at $976\,\mathrm{nm}$. Parasitic lasing of the PCF was suppressed with $5°$ angle-cleaved end facets. The fibre output beam was collimated with a lens telescope. The average output power of the power amplifier was $12\,\mathrm{W}$ corresponding to a pulse energy of $246\,\mathrm{nJ}$.

The pulse compressor consisted of a pair of diffraction gratings and a roof mirror in a double-pass arrangement. The plane, gold-coated, holographic, reflection gratings had a period of $1500\,\mathrm{mm}^{-1}$. The copper substrate of the first grating allows for efficient heat dissipation. The second grating was based on Zerodur®, which had a thermal expansion coefficient of almost zero. The roof mirror translated the outward beam vertically to a higher level on the gratings, so that its location on the gratings did not superimpose with the inward beam. This measure reduced effects from localised thermal loading of the gratings and simplified the alignment. The throughput efficiency of the compressor was 66%.

Each stage was protected from detrimental back-reflections and from amplified spontaneous emission (ASE) in the backward direction of the following stage by optical isolators (OI). A second-harmonic generation frequency-resolved optical gating (SHG FROG) setup was used to characterise the pulses [13]. To measure the pulse spectrum at different locations, an OSA with a resolution of $0.1\,\mathrm{nm}$ was applied.

6.3 Fibre CPA system at full repetition rate

In the following section, experiments of the fibre CPA system run at full repetition rate of $48.7\,\mathrm{MHz}$ are reported. The average power was relatively high and the pulse energies low compared to the contents of section 6.4. The experiments were performed

to investigate the capability of the pulse shaper in combination with the CPA system to generate short and clean femtosecond pulses.

6.3.1 Stretcher and compressor design

The fibre stretcher, chosen instead of a grating-based stretcher for reasons of practicality and costs, was placed directly after the oscillator and the grating-based compressor was located after the final amplifier as can be seen from figure 6.1. As described in section 2.2.5, the group delay dispersions of stretcher ($\mathrm{GDD_S}$), amplifier ($\mathrm{GDD_A}$) and compressor ($\mathrm{GDD_C}$) have to be balanced. The $\mathrm{GDD_A}$ was neglected in the design calculations for two reasons: Firstly, $\mathrm{GDD_A}$ is much smaller than $\mathrm{GDD_S}$ and $\mathrm{GDD_C}$, because amplifying fibres with lengths shorter than $2\,\mathrm{m}$ are used, and secondly, fine tuning to balance the total GDD can be carried out by careful alignment of the compressor grating separation after coarse values for fibre stretcher length and compressor grating separation have been found. Thus, equation (2.18) simplifies to $\mathrm{GDD_S} + \mathrm{GDD_C} = 0$. This can be fulfilled, because a grating compressor has negative GDD, whereas a standard fibre has positive GDD in the spectral region below approximately $1.3\,\mu\mathrm{m}$. The compressor gratings were set-up as close as possible to Littrow configuration (angle of incidence = angle of diffraction), however taking into account clipping of the beams at the edges. Another constraint was the limited width of the second grating in conjunction with the dispersed beam from the first grating [14, 15]. If the separation becomes too large, the spectrum on the second grating will exceed the width of $130\,\mathrm{mm}$ leading to a truncation of the spectrum. Trigonometric considerations of the physical setup for near-Littrow configuration lead to an angle of incidence to the first grating of $\theta_{in} = 53.5°$, a diffraction angle of $\theta_d = 49.2°$ and a perpendicular grating separation of $G = 804\,\mathrm{mm}$ (with centre wavelength $1040\,\mathrm{nm}$ and grating period $1500\,\mathrm{mm}^{-1}$). The grating slant distance $b = G/\cos\theta_d$ was $1230\,\mathrm{mm}$. With equation (2.15) for a double-pass setup, which effectively doubles the accumulated GDD per round-trip, the value of the compressor GDD becomes $-2.574 \cdot 10^{-23}\,\mathrm{s}^2$. An HI 1060 standard SMF acted as pulse stretcher. The GVD of this fibre type is $+2.568 \cdot 10^{-26}\,\mathrm{s}^2/\mathrm{m}$ at a wavelength of $1040\,\mathrm{nm}$. Therefore, with equation (2.16), a fibre with a length of $1002\,\mathrm{m}$ was required. A $1\,\mathrm{km}$-long piece of HI 1060 was inserted into the setup.

6.3.2 Pulse shaping results

The conventional DE algorithm with the trigonometric mutation operator (see section 2.3.4) was used in this experiment. The TPA signal of a gallium arsenide phosphide (GaAsP) detector taken at the output of the compressor is directly related to the pulse peak intensity and therefore to the pulse width. Thus, by using the peak TPA signal

as feedback parameter for f_{fit}, the DE optimisation algorithm searched for the minimum pulse width. The optimisation progress of the TPA signal during 400 iterations is shown in figure 6.3. The optimisation yielded a $9\times$ improved signal. The results of this adaptive optimisation experiment are shown in figures 6.4(b), 6.4(d) and 6.4(f) alongside the graphs for the unshaped pulses in figures 6.4(a), 6.4(c) and 6.4(e). The DE parameters were set to $F = 0.9$ and $CR = 0.9$ and phase and amplitude shaping was enabled. Every 8$^{\text{th}}$ pixel from pixel 12 to 116 (including) was actively controlled at each iteration, therefore $N_c = 14$. This was increased to every 4$^{\text{th}}$ pixel during the optimisation to get improved convergence. The phase profile was then interpolated over all pixels [16].

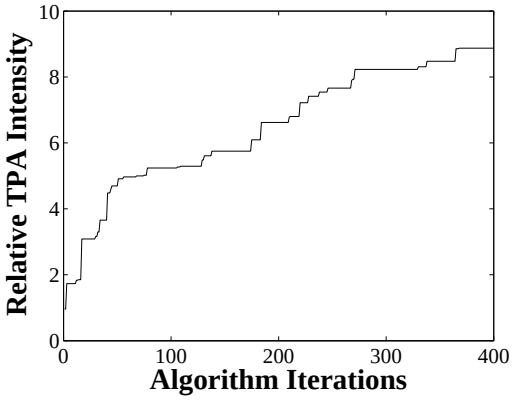

FIGURE 6.3: Optimisation progress of the TPA signal during 400 iterations of the DE algorithm.

A contour plot of the square root of the FROG trace is displayed in figures 6.4(a) and 6.4(b). The square root was applied to the raw FROG data to point out details at lower intensity. The contour levels indicate [0.05 0.1 0.2 0.3 0.4 0.5 0.6 0.7 0.8 0.9]. The temporal wing structure of the shaped pulses only extends out to approximately $\pm 2\,\mathrm{ps}$. Note the different scales for the delay in the two plots. The lowest contour line level is 0.0025 (without square root) corresponding to a peak-to-pedestal ratio of $26\,\mathrm{dB}$. Thus, there is no significant pulse pedestal indicating good higher-order dispersion compensation. After pulse retrieval from the FROG data, the temporal intensity profile and the instantaneous linear frequency $-1/2\pi \cdot d\varphi\,(t)\,/dt$ as well as the spectral intensity and the group delay $d\phi\,(\omega)\,/d\omega$ were calculated. Only a low-intensity pedestal and no side lobes are present in the temporal intensity profile in figure 6.4(f), which indicates a good compensation of TOD introduced in the individual stages of the setup. The flattened profile of the group delay curve in figure 6.4(d) compared to the unshaped case confirms this. The temporal oscillations and the quadratic group delay profile of the unshaped pulses are due to this uncompensated TOD (figures 6.4(c) and 6.4(e)) [13, 17]. The poor agreement of the retrieved and the measured spectra suggests an insufficient calibration of the SHG FROG setup leading to a systematic error, which could not be clarified. A comparison of the autoconvolution of the measured spectrum with

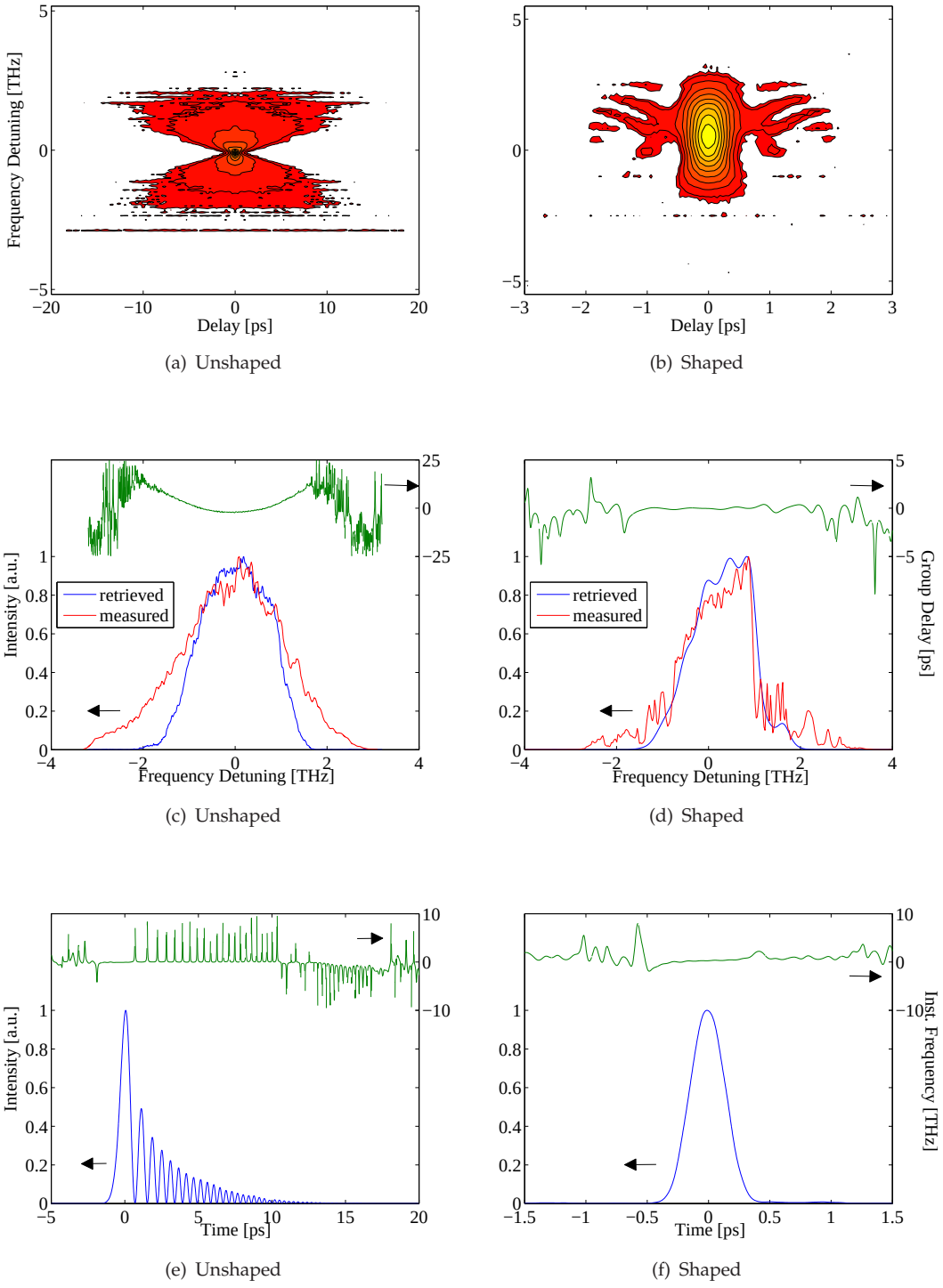

(a) Unshaped (b) Shaped

(c) Unshaped (d) Shaped

(e) Unshaped (f) Shaped

FIGURE 6.4: Initial pulse shaping results of experimental setup with 1 km fibre stretcher. The results for unshaped pulses are shown for comparison. (a), (b) Contour plot of the square root of the FROG trace (contour levels indicate [0.05 0.1 0.2 0.3 0.4 0.5 0.6 0.7 0.8 0.9], Fourier grid size 128×128). (c), (d) Spectral intensity and group delay vs. frequency, (e), (f) Temporal pulse profile and instantaneous frequency vs. time. See text for details.

the frequency marginal (integration of the FROG trace over the delay) could have been used to reveal an inconsistency of the FROG data and hence such a systematic error [13]. However, this was not carried out at the time of the experiments.

In this preliminary experiment, with an estimated $2\,\mathrm{W}$ of average power after the compressor and the repetition rate of $48.7\,\mathrm{MHz}$, the pulse energy was calculated to be $41\,\mathrm{nJ}$. The FWHM pulse width was $340\,\mathrm{fs}$ giving a pulse peak power of $113.4\,\mathrm{kW}$ (assuming a Gaussian temporal profile). Higher pulse energies could readily be obtained by increasing the pump power of the power amplifier.

6.3.3 Discussion

The measured spectrum after shaping had a FWHM bandwidth of $5.5\,\mathrm{nm}$. The theoretical FWHM pulse width for a transform-limited pulse that can be supported by this bandwidth is $289\,\mathrm{fs}$ assuming a Gaussian temporal profile with a time-bandwidth product of 0.441. The discrepancy between the measured $340\,\mathrm{fs}$ and the transform-limit $289\,\mathrm{fs}$ can be attributed to some remaining higher-order dispersion. For instance, the signs of the TOD term β_3 for stretcher and compressor are both positive, therefore the pulse shaper has to compensate for this large amount of TOD. The maximum TOD value that can be imposed on the pulse is $\pm 0.076\,\mathrm{ps}^3$ as calculated from equation (2.35) with $\lambda_0 = 1040\,\mathrm{nm}$, $N_{pix} = 97$, $c = 3 \cdot 10^8\,\mathrm{m/s}$, $\Delta\lambda_{pix} = 0.237\,\mathrm{nm}$ and taking the folded pulse shaper configuration (reflection mode) into account. This would be sufficient for a compensation of the TOD contribution of the $1\,\mathrm{km}$ of HI 1060 fibre alone, which is $0.039\,\mathrm{ps}^3$ [12]. But the TOD contribution from the grating compressor of $0.16\,\mathrm{ps}^3$ as calculated from equation (2.17) can not be fully compensated by the pulse shaper. A potential improvement would be the application of an SLM with more LC-pixels. The frequency span per pixel would then be reduced leading to a finer phase control over the entire spectrum and an increased compensation capability of the pulse shaper. Another possibility would be the use of a grating stretcher (with a 1-to-1 telescope) instead of the fibre. The TODs of grating stretcher and grating compressor have opposite signs and would cancel each other.

The presented results show that the configuration of stretcher and compressor as described above was capable of producing high-quality pulses in the femtosecond regime without significant pulse pedestal or side lobes.

6.4 Fibre CPA system at reduced repetition rate

The repetition rate of the seed pulse oscillator was reduced with an electro-optic modulator (EOM) and optionally with an acousto-optic modulator (AOM). They transmit single pulses of the pulse train and reject all intermediate pulses. Subsequent amplification produced high-energy pulses. Adaptive pulse shaping of the high-energy pulses was then carried out.

6.4.1 High-energy pulse shaping with 1km fibre stretcher

The approach chosen for these experiments was similar to reference [4], however with a $1\,\mathrm{km}$-long fibre stretcher, a phase and amplitude dual mask LC SLM and the implementation of a JADE algorithm rather than simulated annealing. The combined effect of phase and amplitude shaping gave another degree of freedom to find the optimum pulse shape. The TPA signal from a GaAsP photodiode at the output of the compressor was used in the feedback loop. Referring to figure 6.5, the fiberised, $3\,\mathrm{GHz}$, lithium niobate Mach-Zehnder interferometer EOM was inserted after the fibre stretcher. With a specific DC bias voltage applied, the EOM could be switched between zero and maximum light transmission with a modulation voltage that switches between zero and the half-wave voltage (corresponding to a phase retardation of 0 and π, respectively). The extinction ratio of the EOM was $> 40\,\mathrm{dB}$ and the insertion loss was $4.5\,\mathrm{dB}$, i.e. the transmission was 35%. The $110\,\mathrm{MHz}$ TeO_2 AOM with an extinction ratio of $33\,\mathrm{dB}$, a rise time of $160\,\mathrm{ns/mm}$ (dependent on beam diameter) and a first-order diffraction efficiency of 90% was inserted into the setup before the power amplifier. The first-order diffracted beam was coupled into the PCF of the power amplifier. An AOM was used at this position instead of another EOM, because of the higher damage threshold required after pulse amplification. The AOM supported the EOM extinction of rejected pulses and prevented ASE build-up of the fibre amplifiers in the forward direction. ASE becomes more problematic at lower repetition rates, where the time period between pulses increases and ASE can deplete the energy in the excited state of the ytterbium-doped fibre between two consecutive pulses.

The EOM and the AOM were both modulated with a pulse generator, which was externally triggered with the oscillator repetition rate. The pulse generator square wave output was set to a certain delay and triggered the modulators to transmit the specified pulses. The delay time controlled the final repetition rate. For $4.87\,\mathrm{MHz}$ repetition rate ($10\times$ reduction), the AOM was not operated, since the rise time is not sufficient for frequencies in the MHz-range and also ASE is not yet problematic. It was operated at $487\,\mathrm{kHz}$ repetition rate ($100\times$ reduction), however.

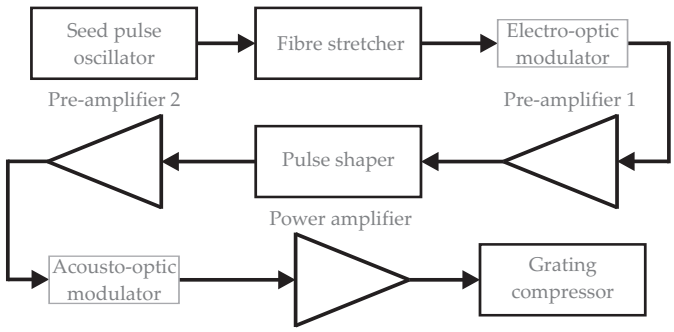

FIGURE 6.5: Block diagram of the 1 km stretcher setup indicating the position of the electro-optic and acousto-optic modulator in the CPA system.

Figures 6.6 and 6.7 show the FROG results of the unshaped / shaped pulses measured after the compressor for 4.87 MHz and 487 kHz repetition rate, respectively. The unshaped pulse profiles in figures 6.6(e) and 6.7(e) show prominent oscillations on the trailing edge, which is an indicator for a positive TOD contribution [13, 17]. For both repetition rates, the pulse quality improved after the adaptive pulse shaping as can be seen in 6.6(f) and 6.7(f). The experimental parameters are summarised in table 6.1.

TABLE 6.1: Experimental parameters of high-energy pulse shaping with 1 km fibre stretcher setup (*transform-limit in parenthesis; †relative improvement of peak power after shaping).

	10× Reduction	**100× Reduction**
Repetition rate	4.87 MHz	487 kHz
Average power	6.60 W	4.28 W
Pulse energy	1.35 μJ	8.79 μJ
B**-integral**	0.39π rad	2.08π rad
FWHM pulse width*	433 fs (280 fs)	515 fs (333 fs)
TPA signal improvement†	7.8×	11.0×

The pulse profile does not show the strong oscillations anymore at a repetition rate of 4.87 MHz. The originally quadratic group delay is flattened in the central part of the spectrum, but not over the full range. Using equation (2.33), it was found that the maximum group delay imposed by the pulse shaper was ± 7.5 ps. Group delays exceeding this could not be shaped and remained unchanged. The pulse energy was 1.35 μJ and the B-integral was relatively low at 0.39π rad. This indicates that the main contribution to the pulse degradation at the output was the accumulation of TOD from the fibre stretcher and grating compressor. As described and calculated in section 6.3, the maximum TOD that can be imposed on the pulse by the pulse shaper is $\pm 0.076\,\mathrm{ps}^3$, whereas the fibre stretcher already contributes a TOD of $0.039\,\mathrm{ps}^3$.

As the repetition rate was further reduced to 487 kHz, the pulse quality deteriorated and the group delay could not be fully flattened anywhere across the pulse spectrum. The pulse energy increased to 8.79 μJ and the B-integral to 2.08π rad implying a non-negligible contribution of accumulated nonlinear phase to the degradation of the pulse

quality. A strong modulation on the measured as well as the retrieved spectrum for the unshaped and shaped pulses (figures 6.7(c) and 6.7(d)) is observable, which is already existent on the oscillator spectrum and was amplified in the three amplifiers. Furthermore, the pixellation of the LC SLM enhanced the modulation [18]. In the time domain, this modulation is expressed as satellite pulses [19] as can clearly be seen in the FROG trace (6.6(b)) and the temporal intensity profile (6.6(f)) of the shaped pulses: Prominent satellite pulses occur at around $10\,\mathrm{ps}$, $20\,\mathrm{ps}$ and $30\,\mathrm{ps}$. The problem of spectral modulations leading to satellite pulses and pulse distortion will be discussed in more detail in section 6.4.2.

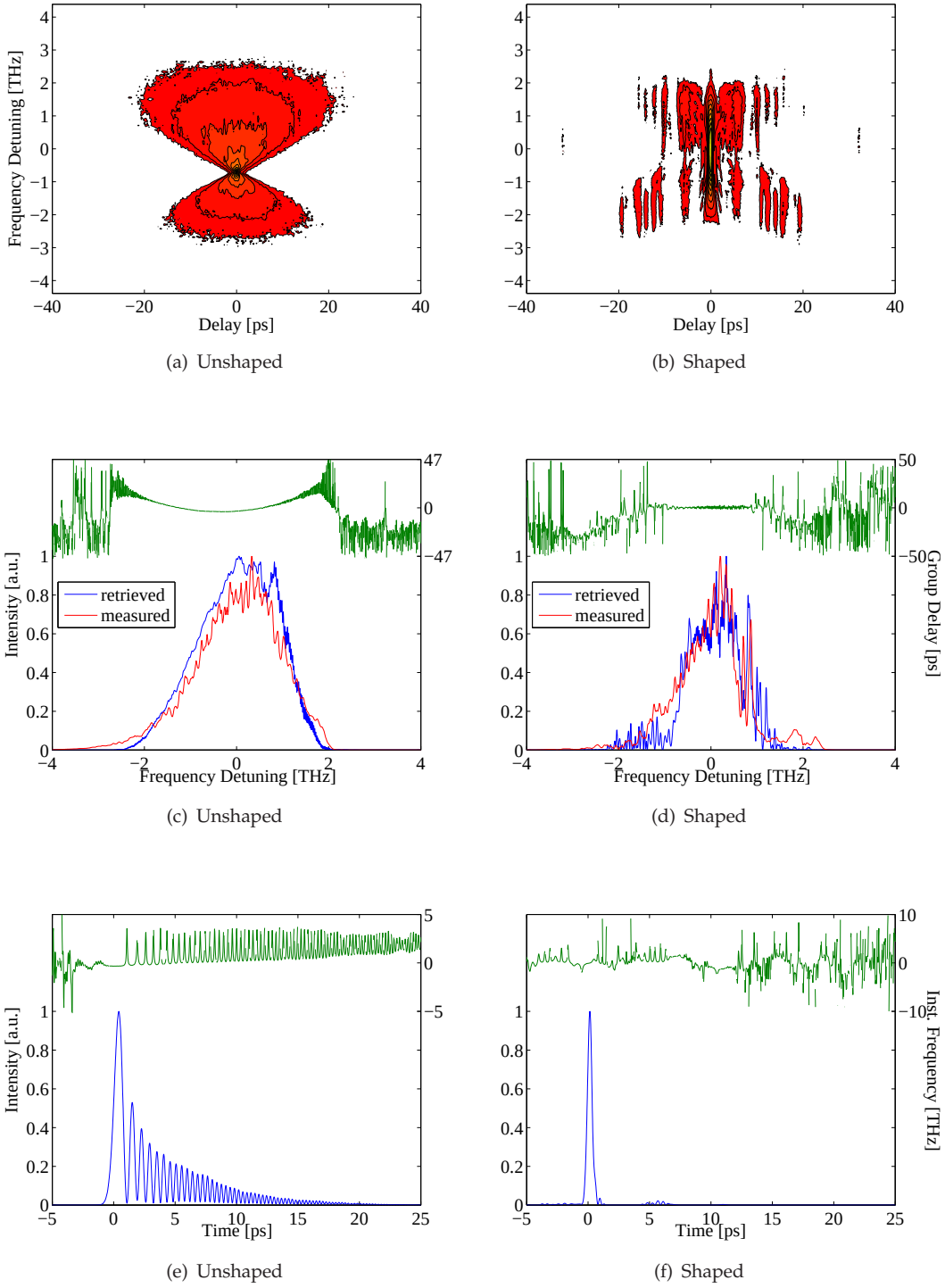

(a) Unshaped (b) Shaped

(c) Unshaped (d) Shaped

(e) Unshaped (f) Shaped

FIGURE 6.6: Pulse shaping results at 4.87 MHz repetition rate with the 1 km fibre stretcher setup. The results for unshaped pulses are shown for comparison. (a), (b) Contour plot of the square root of the FROG trace (contour levels indicate [0.05 0.1 0.2 0.3 0.4 0.5 0.6 0.7 0.8 0.9], Fourier grid size 1024×1024). (c), (d) Spectral intensity and group delay vs. frequency, (e), (f) Temporal pulse profile and instantaneous frequency vs. time. See text for details.

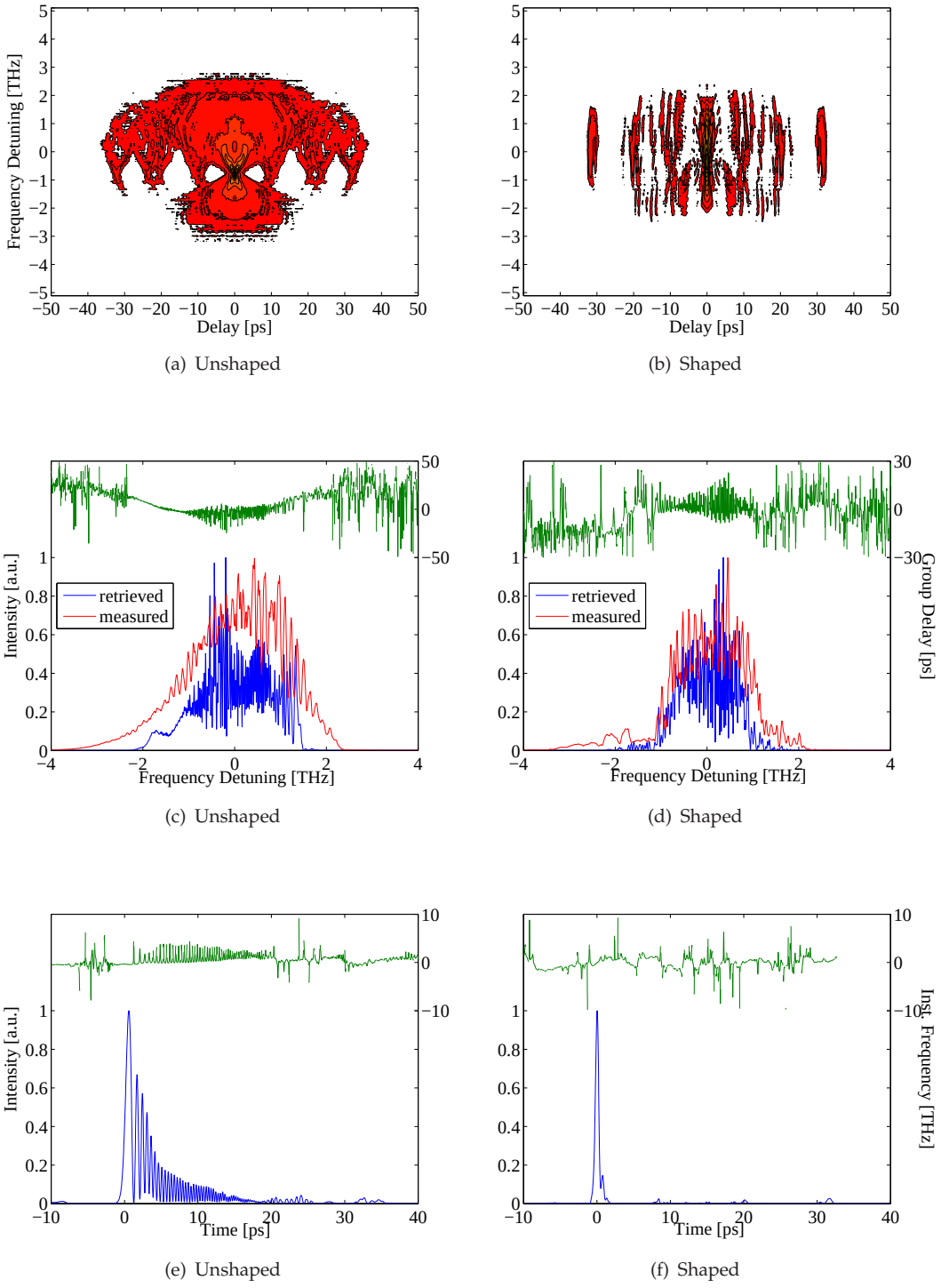

(a) Unshaped (b) Shaped

(c) Unshaped (d) Shaped

(e) Unshaped (f) Shaped

FIGURE 6.7: Pulse shaping results at 487 kHz repetition rate with the 1 km fibre stretcher setup. The results for unshaped pulses are shown for comparison. (a), (b) Contour plot of the square root of the FROG trace (contour levels indicate [0.05 0.1 0.2 0.3 0.4 0.5 0.6 0.7 0.8 0.9], Fourier grid size 1024×1024). (c), (d) Spectral intensity and group delay vs. frequency, (e), (f) Temporal pulse profile and instantaneous frequency vs. time. See text for details.

6.4.2 Limitations of high-energy pulse shaping

Pulse shaping of high-energy pulses in two different experimental configurations is presented in this section. Also, limitations of pulse shaping in a fibre CPA system with a pixellated SLM are shown. The differences with respect to the layout in figure 6.1 are pointed out. In the first setup, an EOM as well as a $12\,\mathrm{m}$ and a $302\,\mathrm{m}$ piece of HI 1060 fibre were used. In the second setup, only a $200\,\mathrm{m}$ piece of fibre was located before pre-amplifier 1 and the pulse shaper was located directly after the EOM. Furthermore, an AOM could be used additionally to the EOM as described in section 6.4.1. Figure 6.8 shows block diagrams of the two setups.

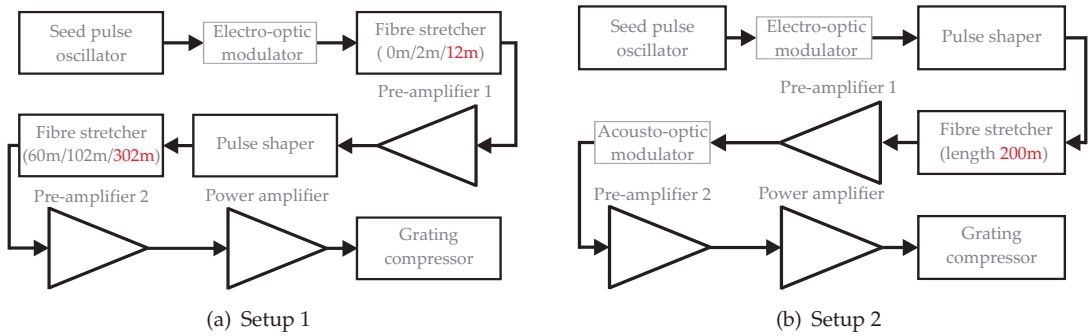

FIGURE 6.8: Block diagrams of two different experimental configurations for high-energy pulse shaping. The fibre stretcher length values in red denote the actual lengths used for the experiments, whereas the values in black are meant to clarify the system design steps described in this section.

The repetition rate had slightly changed to $47.75\,\mathrm{MHz}$ due to some minor rearrangements in the oscillator. For the design of the fibre stretcher(s) in the two setups, a $50\times$ repetition rate reduction was always taken as a reference. This repetition rate of $955\,\mathrm{kHz}$ is the minimum at which the system was operated and therefore produced the highest nonlinear effects. The anamorphic prism pair in the pulse shaper was not used anymore, since the increase in resolution on the LC SLM from the beam expansion and subsequent tighter focusing was only marginal. Furthermore, the prism pair introduced some spatial chirp and reflection losses of around 15%.

6.4.2.1 Experimental setup 1

A distributed stretcher configuration with moderate stretching factors was chosen here in order to intentionally generate a specific amount of SPM per amplifier stage. The SPM generates additional bandwidth and hence potentially shorter pulses. The system was thus operated in a highly nonlinear regime. The AOM was not used for these experiments, since ASE was not observed on the pulse spectrum.

The output spectra of pre-amplifier 1 for different lengths of fibre stretcher before this pre-amplifier are shown in figure 6.9(a) for a repetition rate of $955\,\mathrm{kHz}$. The spectrum without any stretcher and with full repetition rate is plotted for reference (blue graph). Due to an excessive amount of SPM, the spectrum was strongly distorted without a stretcher (green graph). Additionally, energy was lost as ASE, expressed by the broadening of the spectral wings, due to the long time span between two subsequent pulses. For a $2\,\mathrm{m}$-long stretcher, the distortion was reduced and additional bandwidth was generated (red graph). However, stimulated Raman scattering was observed at around $1091\,\mathrm{nm}$ corresponding well to the $13.2\,\mathrm{THz}$ Stokes shift in silica from the $1040\,\mathrm{nm}$ centre wavelength. The Raman peak was around $23\,\mathrm{dB}$ weaker than the peak of the main pulse spectrum. It was completely removed with a $12\,\mathrm{m}$ stretcher (black graph) because of the reduced peak power. The spectrum distortion was further reduced and the bandwidth was $2.9\,\mathrm{nm}$ lower compared to the $2\,\mathrm{m}$ stretcher. Thus, this length of stretcher gives a balance between spectral broadening and too much distortion.

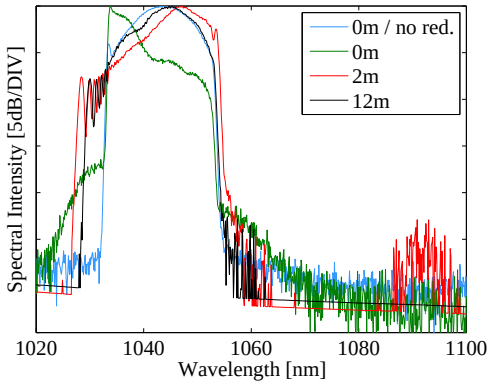

(a) Pre-amplifier 1

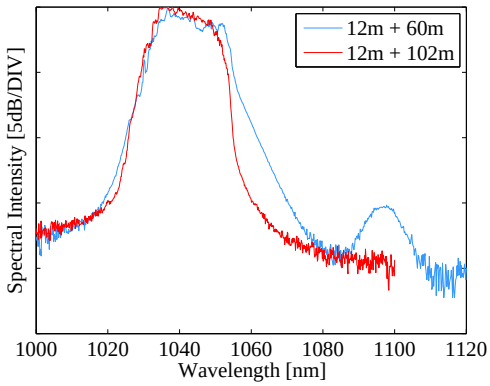

(b) Pre-amplifier 2

FIGURE 6.9: Comparison of spectra measured after (a) pre-amplifier 1 and (b) pre-amplifier 2 with different fibre stretcher lengths at $955\,\mathrm{kHz}$ repetition rate. The stretcher lengths are indicated in the legend. (a) Plot of the spectrum measured without stretcher and without repetition rate reduction (blue) as reference, where the $-20\,\mathrm{dB}$ bandwidth is $21.7\,\mathrm{nm}$. The bandwidth for the $2\,\mathrm{m}$ and $12\,\mathrm{m}$ stretcher is $28.4\,\mathrm{nm}$ and $25.5\,\mathrm{nm}$, respectively. (b) The bandwidth for the $60\,\mathrm{m}$ and $102\,\mathrm{m}$ stretcher is $36.5\,\mathrm{nm}$ and $29.2\,\mathrm{nm}$, respectively. See text for details.

In this setup, the second pre-amplifier was pumped with two LDs in a co- and counter-propagating scheme to obtain a higher average output power. The additional pump LD with a centre wavelength of $980\,\mathrm{nm}$ and an average power of $180\,\mathrm{mW}$ was used to backward-pump. The average output power at $47.75\,\mathrm{MHz}$ and $955\,\mathrm{kHz}$ repetition rate from this pre-amplifier configuration was $\approx 250\,\mathrm{mW}$ and $\approx 150\,\mathrm{mW}$, respectively. Using equation (2.14), the SRS threshold peak power is $3.22\,\mathrm{kW}$ with $A_{eff} = 30.2\,\mu\mathrm{m}^2$, $g_R = 10^{-13}\,\mathrm{m/W}$ [17] and $L_{eff} = 1.5\,\mathrm{m}$. For a repetition rate reduction to $955\,\mathrm{kHz}$ and $150\,\mathrm{mW}$ of average power, a minimum pulse width of $49\,\mathrm{ps}$ follows to avoid SRS. Therefore, the fibre stretcher length must be chosen such that the pulses are stretched to more than $49\,\mathrm{ps}$. The required length was extrapolated from previous autocorrelation measurements with different stretcher lengths assuming only a linear dispersion relation in the fibre as a first approximation. The fibre length was $\approx 77\,\mathrm{m}$ for the SRS threshold pulse width of $49\,\mathrm{ps}$. Figure 6.9(b) shows the spectra measured after pre-amplifier 2 for a $60\,\mathrm{m}$ and $102\,\mathrm{m}$ fibre stretcher at $955\,\mathrm{kHz}$. For $102\,\mathrm{m}$ of fibre, no SRS peak was existent anymore and the spectral bandwidth was $29.2\,\mathrm{nm}$. An autocorrelation of the pre-amplifier 2 output pulses yielded a width of $117\,\mathrm{ps}$ at $955\,\mathrm{kHz}$ corresponding to a pulse width of around $83\,\mathrm{ps}$ for a Gaussian profile.

Similar considerations to avoid SRS and to generate additional bandwidth led to a total fibre length of $302\,\mathrm{m}$ for both pre-amplifier 2 and the power amplifier as indicated in figure 6.8(a) (a single fibre stretcher was used before pre-amplifier 2, because fibre splicing to the power amplifier PCF was not possible). Figure 6.10(a) shows the spectrum after the power amplifier at an average output power of $8.5\,\mathrm{W}$. This corresponds to $8.9\,\mu\mathrm{J}$ at the repetition rate of $955\,\mathrm{kHz}$ with a bandwidth of $27.5\,\mathrm{nm}$ at the $-20\,\mathrm{dB}$-level. The decrease of the bandwidth from $29.2\,\mathrm{nm}$ before to $27.5\,\mathrm{nm}$ after the power amplifier can be attributed to gain narrowing in the power amplifier. For comparison, the spectrum with only $102\,\mathrm{m}$ of fibre is plotted as well, where a strong SRS peak was generated.

A comparison of the power amplifier output spectra at $100\times$ reduced repetition rate between the $1\,\mathrm{km}$ fibre stretcher configuration, as described in section 6.4.1, and the $12\,\mathrm{m} + 302\,\mathrm{m}$ distributed stretcher configuration shows a bandwidth increase of $6.8\,\mathrm{nm}$ from $20.8\,\mathrm{nm}$ to $27.6\,\mathrm{nm}$ (see figure 6.10(b)). Thus, the distributed fibre stretcher arrangement appears to have given the potential for shorter pulses by controlling the nonlinear broadening at each amplifier stage.

After finding the optimum distributed fibre stretcher configuration, the grating separation of the compressor was fine-tuned to balance the positive GDD of the stretchers and therefore to obtain a minimum pulse width.

Note: After only a few pulse shaping experiments with this experimental configuration, including the JADE algorithm and repetition rate reductions down to $50\times$, we were

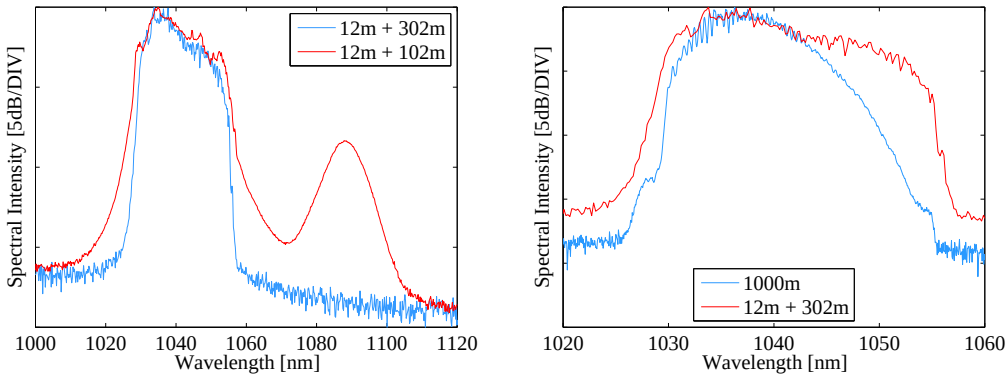

(a) 955 kHz repetition rate

(b) @ 100× repetition rate reduction

FIGURE 6.10: Power amplifier output spectra for different stretcher configurations. (a) The 12 m + 302 m configuration (12 m for pre-amplifier 1; 102 m and 200 m for pre-amplifier 2 and the power amplifier, respectively) produced a bandwidth of 27.5 nm at an average output power of 8.5 W and a repetition rate of 955 kHz. A strong SRS peak was generated, when the 302 m fibre piece was replaced by the 102 m piece. (b) Compared to the 1000 m fibre stretcher system configuration described in section 6.4.1, the bandwidth increased by 6.8 nm to 27.6 nm (note that this was at a repetition rate reduction of 100×).

unfortunately forced to rearrange the system due to the failure of the backward pump laser diode for the second pre-amplifier. Because of the lower average output power and hence pulse energy, the stretching factor from the 302 m fibre was no longer needed. We therefore decided to use only 200 m instead to maintain the increase of the spectral bandwidth from the distributed stretcher configuration.

Figure 6.11 shows the results from pulse shaping with this modified setup at full repetition rate (second column) and with 10× reduction (third column). The parameters for unshaped pulses at full repetition rate are shown for comparison (first column). A contour plot of the square-root of the FROG trace is shown in figures 6.11(a), 6.11(b) and 6.11(c). The contour levels indicate [0.05 0.1 0.2 0.3 0.4 0.5 0.6 0.7 0.8 0.9] with the square-root operator applied. Figures 6.11(d), 6.11(e) and 6.11(f) show the spectral intensity and group delay as a function of frequency and figures 6.11(g), 6.11(h) and 6.11(i) show the temporal pulse profile and instantaneous frequency as a function of time. The unshaped pulses had temporal oscillations, which is due to uncompensated TOD. The pulse shaping almost completely removed these oscillations and compressed the pulse as can be seen in figure 6.11(h). The FWHM pulse width is 290 fs with a flat group delay. The average output power from the compressor was 5.4 W giving a pulse energy of 113 nJ. For a reduced repetition rate of 4.775 MHz, the compensation of TOD and increased nonlinearities was not complete, which was expressed by remaining temporal oscillations and some pulse pedestal (figure 6.11(i)). The main pulse therefore suffered an unacceptable reduction in energy. However, efficient pulse compression was obtained indicated by a FWHM pulse width of 256 fs. With a measured average

output power of $5.1\,\mathrm{W}$, the total energy was $1.07\,\mu\mathrm{J}$ including the satellite pulses. Table 6.2 is an overview of the pulse parameters.

TABLE 6.2: Experimental parameters of high-energy pulse shaping with setup 1 (*transform-limit in parenthesis; †relative improvement of peak power after shaping).

	No Reduction	**10× Reduction**
Repetition rate	$47.75\,\mathrm{MHz}$	$4.775\,\mathrm{MHz}$
Average power	$5.4\,\mathrm{W}$	$5.1\,\mathrm{W}$
Pulse energy	$113\,\mathrm{nJ}$	$1.07\,\mu\mathrm{J}$
FWHM pulse width*	$290\,\mathrm{fs}$ ($211\,\mathrm{fs}$)	$256\,\mathrm{fs}$ ($209\,\mathrm{fs}$)
TPA signal improvement†	5.8×	3.0×

In contrast to the use of the single $1\,\mathrm{km}$ stretcher, it was possible to utilise nonlinear spectral broadening to obtain shorter rather than longer pulses at lower repetition rates. However, a variation of the JADE algorithm parameters with the system operated at $4.775\,\mathrm{MHz}$ did not show a considerable difference of the TPA signal improvement, the TOD and SPM compensation and the temporal FWHM. Possibly, the pulse shaper was not capable of compensating for the large amount of accumulated SPM in addition to the TOD from stretcher and compressor, which seems to set the ultimate limit of the pulse shaping in the highly nonlinear regime. The potential improvement in the temporal pulse width obtained by the larger spectral bandwidth was corrupted by this effect. Since it was intended to also perform pulse shaping at even lower repetition rates, where the SPM is higher, this configuration was abandoned and another configuration was investigated, where the pulse shaper input pulses were not amplified (setup 2 in figure 6.8(b)).

6.4.2.2 Experimental setup 2

In the configuration shown in figure 6.8(b), the overall SPM was not as high due to the stretching in $200\,\mathrm{m}$ of fibre before the three amplification stages. Furthermore, the pulse shaper was placed before the amplifiers. The AOM was only used for the experiments with $50\times$ reduced repetition rate to suppress ASE build-up.

Figures 6.12 and 6.13 show the pulse shaping results with the system operated at $47.75\,\mathrm{MHz}$ and $4.775\,\mathrm{MHz}$ repetition rate, respectively. A summary of the experimental parameters after shaping is presented in table 6.3. The poor agreement of measured and retrieved spectrum in some of the experiments was again attributed to a possible systematic error of the SHG FROG due to insufficient calibration, whose origin could not be identified. As with setup 1, the pulse shaping largely removed the TOD-induced temporal oscillations. The spectral modulation increased with reduced repetition rate and hence increased pulse energy, both for unshaped (figures 6.12(c) and 6.13(c)) and

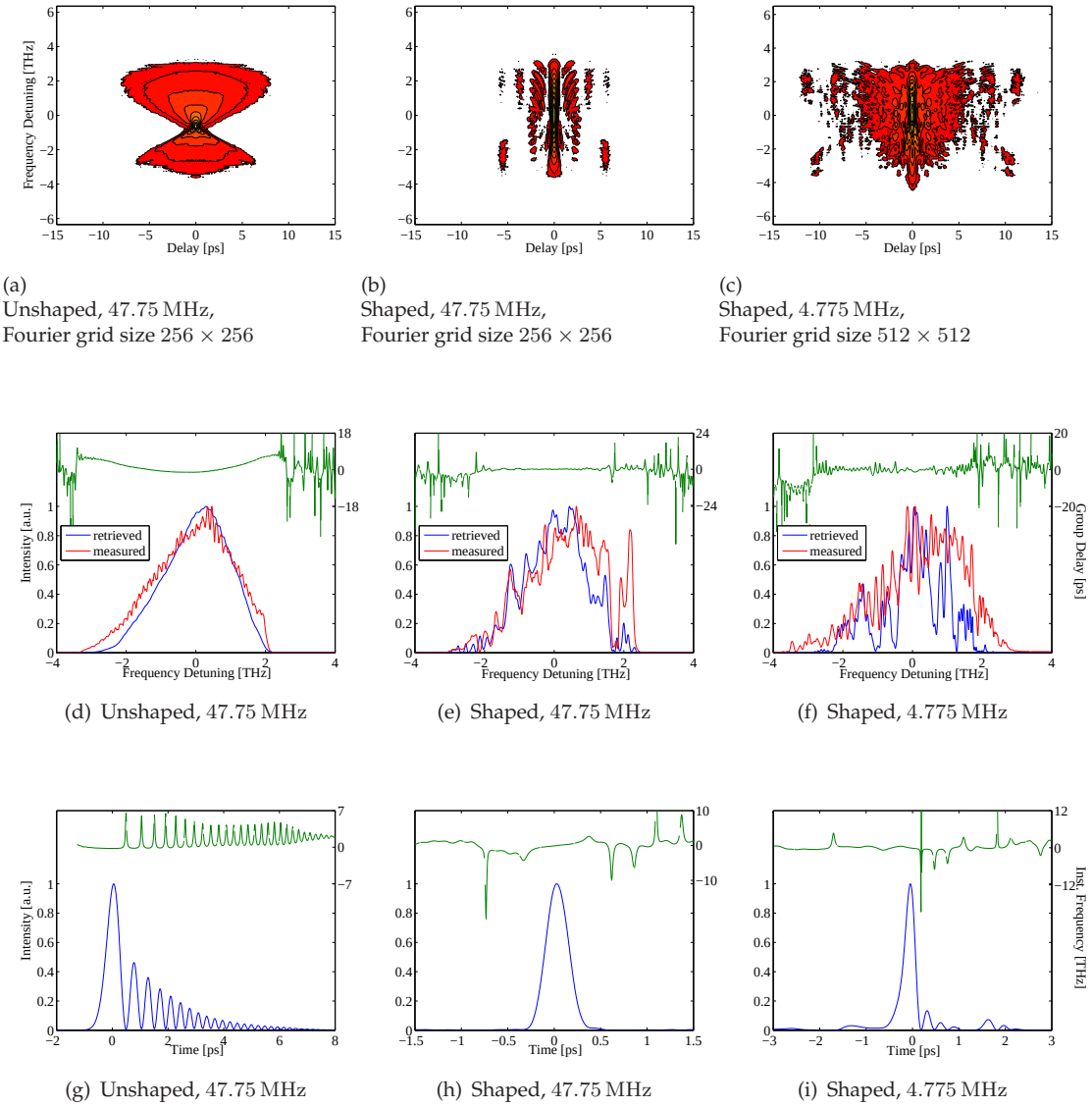

(a) Unshaped, 47.75 MHz, Fourier grid size 256 × 256

(b) Shaped, 47.75 MHz, Fourier grid size 256 × 256

(c) Shaped, 4.775 MHz, Fourier grid size 512 × 512

(d) Unshaped, 47.75 MHz

(e) Shaped, 47.75 MHz

(f) Shaped, 4.775 MHz

(g) Unshaped, 47.75 MHz

(h) Shaped, 47.75 MHz

(i) Shaped, 4.775 MHz

FIGURE 6.11: Pulse shaping results of setup 1 at 47.75 MHz and 4.775 MHz repetition rate. The results for unshaped pulses are shown as well for comparison. (a), (b), (c) Contour plot of the square root of the FROG trace, where the contour levels indicate [0.05 0.1 0.2 0.3 0.4 0.5 0.6 0.7 0.8 0.9], (d), (e), (f) Spectral intensity and group delay vs. frequency, (g), (h), (i) Temporal pulse profile and instantaneous frequency vs. time. See text for details.

shaped pulses (figures 6.12(d) and 6.13(d)), and also after each amplifier. This modulation corresponds to satellite pulses in the time domain, whose intensity also increased as can clearly be seen in the FROG trace contour plots of figure 6.12(b) and 6.13(b). The oscillator spectrum already exhibited a sinusoidal modulation, whose origin was not entirely clear but was assumed to stem from weak satellite pulses [19]. The sinusoidal modulations of the spectrum are mapped to the temporal pulse envelope via the linear chirp from the long, dispersive fibre stretcher [20]. When there is amplification now, the spectrum suffers SPM leading to an increased spectral modulation, which is superimposed onto the linear chirp curve and hence mapped to the temporal envelope as

well. The modulation depth is dependent on the B-integral. Thus, the temporal phase is affected by the initial oscillator spectral modulations and by the SPM modulations. This leads to pulse splitting and energy transfer from the main pulse to the satellite pulses, which can be described using Bessel functions. The strength of this process only depends on the B-integral and the initial pulse contrast [19]. Figure 6.14 shows autocorrelations of unshaped pulses at different repetition rates. As the repetition rate decreases, the pulse energy and nonlinearities increase, which leads to a growth of the satellite pulse intensities. The orange graph is the autocorrelation of a shaped pulse at $955\,\mathrm{kHz}$ repetition rate and shows that additional satellite pulses emerged at $\pm 62\,\mathrm{ps}$, when the JADE algorithm optimised the pulses for maximum peak power. The accumulated SPM expressed by a B-integral of $3.2\pi\,\mathrm{rad}$ is much higher ultimately leading to a stronger energy transfer.

TABLE 6.3: Experimental parameters of high-energy pulse shaping with setup 2 (*transform-limit in parenthesis; †relative improvement of peak power after shaping).

	No Reduction	**10× Reduction**
Repetition rate	47.75 MHz	4.775 MHz
Average power	8.04 W	8.18 W
Pulse energy	168 nJ	1.71 μJ
FWHM pulse width*	344 fs (252 fs)	318 fs (253 fs)
TPA signal improvement†	3.2×	2.8×

The pixellation of the LC SLM enhances the modulation additionally as can be seen in figure 6.15(a), where two spectra of unshaped pulses at a repetition rate of $1.91\,\mathrm{MHz}$ (25× reduction) are plotted. Unshaped pulses were chosen to show the effect of only the LC SLM pixellation and not the effect of the amplitude shaping on the spectrum. Furthermore, autocorrelations of unshaped pulses at $1.19\,\mathrm{MHz}$ (40× reduction) are shown in figure 6.15(b). The inset is a zoom of the satellite pulse region. The blue and green graph show autocorrelations with and without the LC SLM in the setup, respectively. Additional satellite pulses emerged at $\pm 31\,\mathrm{ps}$, when the LC SLM was inserted. The red graph in figure 6.15(b) shows the autocorrelation of shaped pulses, where the satellite pulses at $\pm 62\,\mathrm{ps}$ are visible again.

The discrete sampling of the spectrum by the pixellated LC SLM generates a higher spectral modulation depth, which leads to an increased energy transfer from the main pulse to the satellite pulses. This discrete sampling can also be described mathematically with a Fourier series, whose period is the inverse of the frequency span per pixel $\delta\nu^{-1}$ and where each component describes the phase and amplitude modulation of one pixel across the LC SLM. The temporal waveform is therefore infinitely repeated at times $t = \pm n\delta\nu^{-1}$ $(n = 1, 2, 3, \ldots)$ assuming negligibly small inter-pixel gaps and focused spot sizes (per frequency component) that are much smaller than an individual

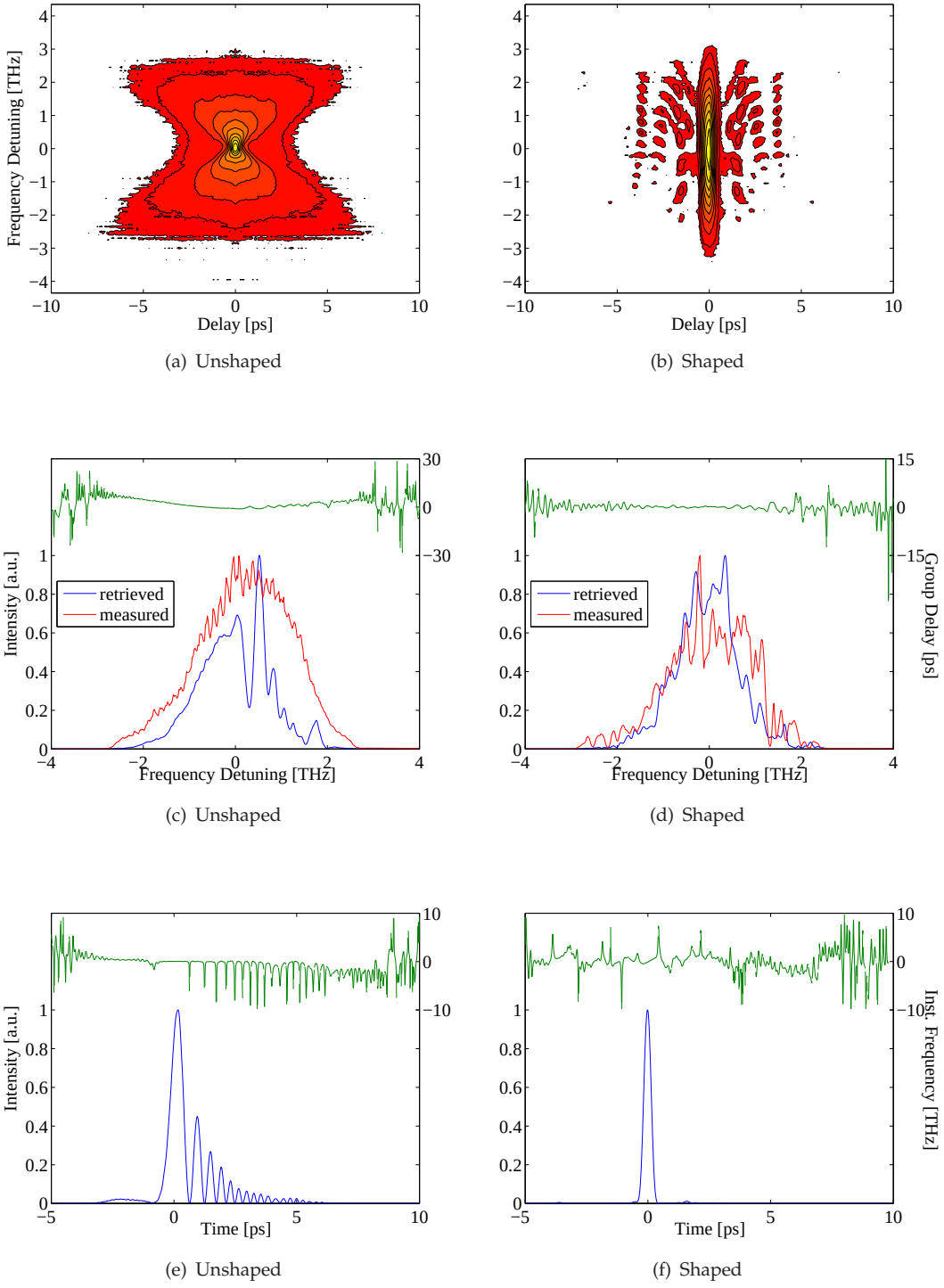

(a) Unshaped (b) Shaped

(c) Unshaped (d) Shaped

(e) Unshaped (f) Shaped

FIGURE 6.12: Pulse shaping results of setup 2 at 47.75 MHz repetition rate. The results for unshaped pulses are shown for comparison. (a), (b) Contour plot of the square root of the FROG trace (contour levels indicate [0.05 0.1 0.2 0.3 0.4 0.5 0.6 0.7 0.8 0.9], Fourier grid size 256×256). (c), (d) Spectral intensity and group delay vs. frequency, (e), (f) Temporal pulse profile and instantaneous frequency vs. time. See text for details.

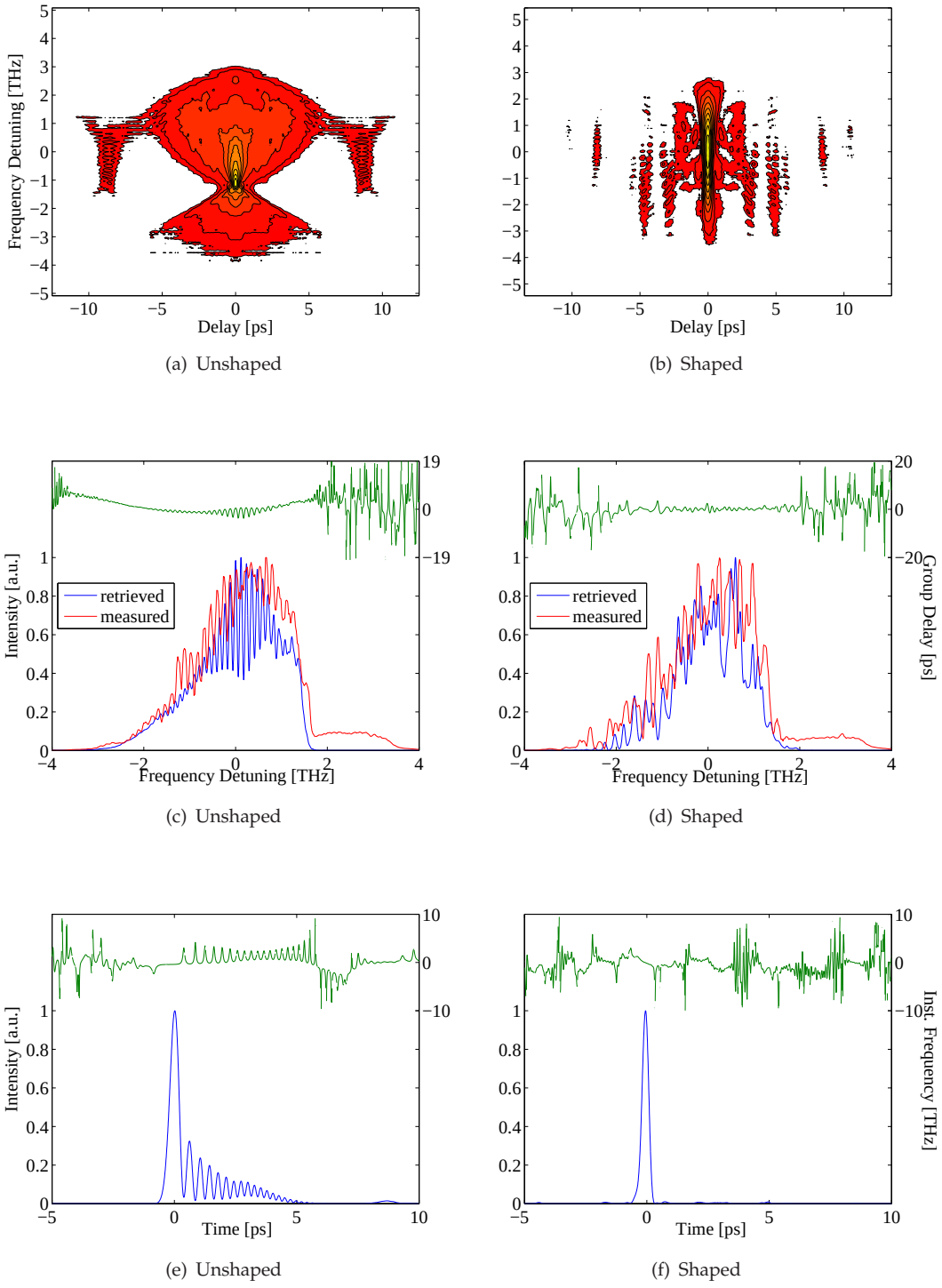

(a) Unshaped (b) Shaped

(c) Unshaped (d) Shaped

(e) Unshaped (f) Shaped

FIGURE 6.13: Pulse shaping results of setup 2 at 4.775 MHz repetition rate. The results for unshaped pulses are shown for comparison. (a), (b) Contour plot of the square root of the FROG trace (contour levels indicate [0.05 0.1 0.2 0.3 0.4 0.5 0.6 0.7 0.8 0.9], Fourier grid size 256×256). (c), (d) Spectral intensity and group delay vs. frequency, (e), (f) Temporal pulse profile and instantaneous frequency vs. time. See text for details.

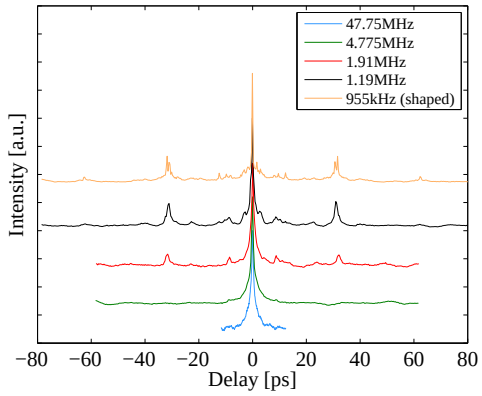

FIGURE 6.14: Comparison of autocorrelations of unshaped pulses at different repetition rates. The energy of the satellite pulses increases with decreasing repetition rate. The accumulated SPM becomes stronger, which enables the energy transfer to the satellite pulses [19]. The orange graph is the autocorrelation of a shaped pulse at $955\,\mathrm{kHz}$ repetition rate and shows that additional satellite pulses emerge at $\pm 12\,\mathrm{ps}$ and $\pm 62\,\mathrm{ps}$, when the peak power is optimised by the algorithm.

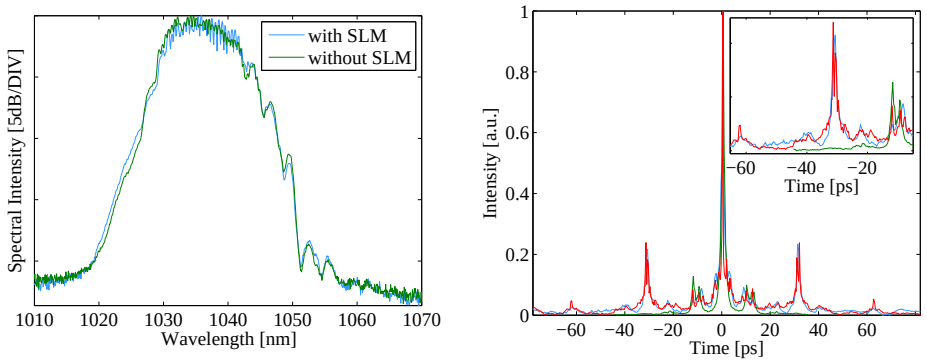

(a) Spectral modulation (b) Autocorrelations

FIGURE 6.15: Problem of spectral modulation enhanced by the LC SLM leading to satellite pulses. (a) With the LC SLM inserted into the pulse shaper, the spectral modulation is enhanced. The spectra are taken at a repetition rate of $1.91\,\mathrm{MHz}$ and with unshaped pulses. (b) Comparison of pulse autocorrelations with and without LC SLM in the pulse shaper at a repetition rate of $1.19\,\mathrm{MHz}$. The blue graph shows the autocorrelation of unshaped pulses with the LC SLM in the setup, whereas the green graph is without LC SLM. The red graph shows the autocorrelation of shaped pulses, where additional satellite pulses exist. The inset is a zoom of the satellite pulse region.

pixel [21]. However, a time window consisting of a Gaussian function (equation (2.30)), from the impulse response $h(t)$), with a width defined by the combined resolution of grating and lens, and of a sinc-function with a width defined by $\delta\nu$ suppresses satellites pulses further away from time $t = 0$ [18]. In other words, the relative intensities of satellite pulses are determined by the Gauss-sinc time window. Another effect in pixellated SLMs with the same result are phase distortions from $\mathrm{mod}(2\pi)$ phase wrapping. This could be avoided, if the maximum phase modulation of any pixel is $< 2\pi$, so that a phase wrap is not needed.

With a wavelength span per pixel of $\delta\lambda = 0.24\,\mathrm{nm}$ in this pulse shaper, which corresponds to a frequency span of $\delta\nu = 0.067\,\mathrm{THz}$, the theoretical positions of the satellite

pulses are $\pm 15\,\mathrm{ps}$, $\pm 30\,\mathrm{ps}$, $\pm 45\,\mathrm{ps}$, etc. This corresponds well with the experimental results in figure 6.14 and 6.15(b). The small satellite pulses around $\pm 10\,\mathrm{ps}$ stem from the modulation that exists on the oscillator spectrum already and are not related to the LC SLM.

6.4.3 Discussion

A comparison of setup 1 and setup 2 shows that the distributed stretcher configuration of setup 1 gave more spectral bandwidth and consequently shorter pulses. The pulse widths were $290\,\mathrm{fs}$ and $256\,\mathrm{fs}$ at $47.75\,\mathrm{MHz}$ and $4.755\,\mathrm{MHz}$, respectively. The transform-limited pulse width is $211\,\mathrm{fs}$ and $209\,\mathrm{fs}$, which gives ratios of real pulse width to transform-limited pulse width of 1.37 and 1.22, respectively. Setup 2 produced less bandwidth and hence the pulse widths were somewhat longer ($344\,\mathrm{fs}$ and $318\,\mathrm{fs}$), which obviously also applies to the transform-limited pulse width ($252\,\mathrm{fs}$ and $253\,\mathrm{fs}$). However, the ratios are 1.37 and 1.26 and are thus very similar to those of setup 1. This means that the pulse shaping potential reaches a limit in that transform-limited pulses are not feasible due to the problem of the spectral modulation.

The configuration of setup 2 ensured that the pulse spectrum entering the pulse shaper was not affected by SPM, since the pulses were not yet amplified. Since adaptive pulse shaping with a feedback loop was performed, where the feedback parameter was taken at the output of the system, the overall accumulated nonlinearities determined the pulse shaping limits and not just the nonlinearities directly experienced by the pulse shaper.

The detrimental effect of the spectral modulation was less pronounced in the configuration with the $1\,\mathrm{km}$ stretcher (section 6.4.1), because the B-integral was much lower due to the large stretching factor, e.g. only $2.08\pi\,\mathrm{rad}$ for a repetition rate as low as $487\,\mathrm{kHz}$ as opposed to $3.2\pi\,\mathrm{rad}$ for $955\,\mathrm{kHz}$ in the $200\,\mathrm{m}$ stretcher configuration of setup 2.

6.5 Conclusions

An investigation of pulse shaping in different fibre-based CPA configurations, mainly varying in the fibre stretcher length and the position of the pulse shaper, showed that energy-scalable, high-quality pulses can be obtained by simply reducing the repetition rate. A differential evolution algorithm was used to adaptively shape the phase and amplitude of the pulses. The pulse shaper compensated for the large amount of TOD from the stretcher and compressor. However, under certain circumstances, fibre nonlinearities can cause an energy transfer from the main pulse to satellite pulses. The

higher the pulse energy and peak power and therefore the B-integral in the system, the stronger are the satellite pulses. The pixellated nature of the LC SLM applied in the experiments contributed to this detrimental effect.

In a highly nonlinear system configuration with distributed fibre stretchers, the additional bandwidth generated through SPM allowed short pulse durations around $300\,\mathrm{fs}$ with pulse energies ranging from $\approx 100\,\mathrm{nJ}$ to $\approx 2\,\mu\mathrm{J}$, but the SPM also caused strong and unacceptable satellite pulses. The optimum system configuration used a $1\,\mathrm{km}$-long fibre stretcher to avoid an excessive build-up of SPM in the amplifier chain. At repetition rates of $4.87\,\mathrm{MHz}$ and $487\,\mathrm{kHz}$, pulse energies of $1.35\,\mu\mathrm{J}$ and $8.79\,\mu\mathrm{J}$ with pulse durations of $433\,\mathrm{fs}$ and $515\,\mathrm{fs}$ were achieved. The relative improvement of the TPA feedback signal is an indicator that the optimisation algorithm worked more efficiently in this configuration compared to the highly nonlinear configuration.

Such an energy-scalable femtosecond source at $1\,\mu\mathrm{m}$ can be used to synchronously pump an OPO. The flexibility of the source in terms of pulse energy, repetition rate, pulse duration and average power allows for the study of different OPO regimes.

References

[1] F. Röser, D. Schimpf, O. Schmidt, B. Ortaç, K. Rademaker, J. Limpert, and A. Tünnermann, "90 W average power 100μJ energy femtosecond fiber chirped-pulse amplification system," Opt. Lett. **32**(15), 2230–2232 (2007).

[2] F. Röser, T. Eidam, J. Rothhardt, O. Schmidt, D. N. Schimpf, J. Limpert, and A. Tünnermann, "Millijoule pulse energy high repetition rate femtosecond fiber chirped-pulse amplification system," Opt. Lett. **32**(24), 3495–3497 (2007).

[3] D. N. Schimpf, J. Limpert, and A. Tünnermann, "Controlling the influence of SPM in fiber-based chirped-pulse amplification systems by using an actively shaped parabolic spectrum," Opt. Express **15**(25), 16,945–16,953 (2007).

[4] F. He, H. S. S. Hung, J. H. V. Price, N. K. Daga, N. A. Naz, J. Prawiharjo, D. C. Hanna, D. P. Shepherd, D. J. Richardson, J. W. Dawson, C. W. Siders, and C. P. Barty, "High energy femtosecond fiber chirped pulse amplification system with adaptive phase control," Opt. Express **16**(8), 5813–5821 (2008).

[5] D. N. Schimpf, E. Seise, T. Eidam, J. Limpert, and A. Tünnermann, "Control of the optical Kerr effect in chirped-pulse-amplification systems using model-based phase shaping," Opt. Lett. **34**(24), 3788–3790 (2009).

[6] J. Prawiharjo, N. K. Daga, R. Geng, J. H. Price, D. C. Hanna, D. J. Richardson, and D. P. Shepherd, "High fidelity femtosecond pulses from an ultrafast fiber laser system via adaptive amplitude and phase pre-shaping," Opt. Express **16**(19), 15,074–15,089 (2008).

[7] M. E. Fermann, M. J. Andrejco, Y. Silberberg, and M. L. Stock, "Passive mode locking by using nonlinear polarization evolution in a polarization-maintaining erbium-doped fiber," Opt. Lett. **18**(11), 894 (1993).

[8] J. M. Dudley, C. Finot, D. J. Richardson, and G. Millot, "Self-similarity in ultrafast nonlinear optics," Nature Physics **3**(9), 597–603 (2007).

[9] M. H. Ober, M. Hofer, U. Keller, and T. H. Chiu, "Self-starting diode-pumped femtosecond Nd fiber laser," Opt. Lett. **18**(18), 1532 (1993).

[10] L. Lefort, J. H. V. Price, D. J. Richardson, G. J. Spüler, R. Paschotta, U. Keller, A. R. Fry, and J. Weston, "Practical low-noise stretched-pulse Yb^{3+}-doped fiber laser," Opt. Lett. **27**(5), 291–293 (2002).

[11] J. H. V. Price, "The Development of High Power, Pulsed Fiber Laser Systems and their Applications," Ph.D. thesis, Optoelectronics Research Centre, University of Southampton, Southampton (2003).

[12] C. K. Nielsen, "Mode-Locked Fiber Lasers: Theoretical and Experimental Developments," Ph.D. thesis, Department of Physics and Astronomy, University of Aarhus, Aarhus (2006).

[13] R. Trebino, *Frequency-Resolved Optical Gating: The Measurement of Ultrashort Laser Pulses*, 1st ed. (Kluwer Academic Publishers, Boston, 2002).

[14] M. Trentelman, I. N. Ross, and C. N. Danson, "Finite size compression gratings in a large aperture chirped pulse amplification laser system," Appl. Opt. **36**(33), 8567–8573 (1997).

[15] B. C. Li, W. Theobald, E. Welsch, and R. Sauerbrey, "Optimization of grating size in chirped-pulse-amplification laser system," Applied Physics B: Lasers and Optics **B71**(6), 819–26 (2000).

[16] R. Mizoguchi, K. Onda, S. S. Kano, and A. Wada, "Thinning-out in optimized pulse shaping method using genetic algorithm," Review of Scientific Instruments **74**(5), 2670–2674 (2003).

[17] G. P. Agrawal, *Nonlinear Fiber Optics*, Optics and Photonics, 3rd ed. (Academic Press, San Diego, 2001).

[18] J. Vaughan, T. Feurer, K. Stone, and K. Nelson, "Analysis of replica pulses in femtosecond pulse shaping with pixelated devices," Opt. Express **14**(3), 1314–1328 (2006).

[19] D. N. Schimpf, E. Seise, J. Limpert, and A. Tünnermann, "The impact of spectral modulations on the contrast of pulses of nonlinear chirped-pulse amplification systems," Opt. Express **16**(14), 10,664–10,674 (2008).

[20] A. Braun, S. Kane, and T. Norris, "Compensation of self-phase modulation in chirped-pulse amplification laser systems," Opt. Lett. **22**(9), 615–617 (1997).

[21] A. M. Weiner, "Femtosecond pulse shaping using spatial light modulators," Review of Scientific Instruments **71**(5), 1929–1960 (2000).

Chapter 7

Femtosecond, pulse-shaped, fibre-CPA-pumped optical parametric oscillator

7.1 Introduction

Tunable, femtosecond, high-power OPO systems can be applied as pump sources in the NIR around $1.5\,\mu\mathrm{m}$ for MIR lasers or MIR OPOs (using CdSe or ZGP, for example) [1]. They can also be used for nonlinear microscopy and imaging in the spectral region from $2\,\mu\mathrm{m}$ to $4\,\mu\mathrm{m}$, where the transmission loss of optical systems is typically very high and where many important absorption bands of chemical and biological molecules lie, e.g. –OH, –CH and –NH stretching modes [2]. The combination of high average power, femtosecond pulse duration with high repetition rate has proved to be difficult to achieve in the past, but it is required to make such microscopy and imaging tools practical and efficient.

There have been reports of picosecond, megahertz SPOPOs with MIR powers exceeding $1\,\mathrm{W}$ based on Nd:YAG pump sources and PPLN crystals [3], Nd:YVO pump sources and $KTiOAsO_4$ crystals [4] and YDF pump sources and MgO:PPLN crystals [5, 6], but few reports of femtosecond systems. Adler *et al.* demonstrated a YDF-pumped ($100\,\mathrm{fs}$, $136\,\mathrm{MHz}$, $10\,\mathrm{W}$, $1.07\,\mu\mathrm{m}$), PPLN-based SPOPO producing a maximum idler power of $1.5\,\mathrm{W}$ with idler and signal tunability from $2.8\,\mu\mathrm{m}$ to $4.8\,\mu\mathrm{m}$ and $1.37\,\mu\mathrm{m}$ to $1.76\,\mu\mathrm{m}$, respectively, which was used for frequency-comb applications [7]. Südmeyer *et al.* demonstrated an Yb:YAG thin-disk-pumped ($780\,\mathrm{fs}$, $56\,\mathrm{MHz}$, $58\,\mathrm{W}$, $1.03\,\mu\mathrm{m}$), PPsLT-based SPOPO, which generated $19\,\mathrm{W}$ ($7.8\,\mathrm{W}$) of signal (idler) power at $1.45\,\mu\mathrm{m}$ ($3.57\,\mu\mathrm{m}$) with a typical signal pulse duration of $840\,\mathrm{fs}$ [8].

The work presented in this chapter aims to demonstrate a femtosecond, high-power SPOPO that is tunable in the NIR and MIR region. The SPOPO is pumped by the $50\,\mathrm{MHz}$, fibre-based CPA system including the pulse shaping as described in chapter 6. A PPLN crystal is used as the nonlinear crystal to exploit the advantages of this material including the high effective nonlinear coefficient, the large transparency range and the possibility of QPM. To the best of the author's knowledge, the combination of a fibre-based CPA pump source (with pulse shaping capabilities) and a PPLN-based SPOPO constitutes a novel setup with many attractive features for the generation of widely tunable, femtosecond, high-power, high-repetition-rate pulses.

The seed source of the fibre-based CPA system was developed by Dr. Jerry Prawiharjo. The other stages of the pulse-shaped, fibre-based CPA system as well as the OPO were developed, set-up and operated by the author.

7.2 Fibre-based, high-power CPA pump source design

The fibre-based, high-power CPA system used to pump the femtosecond SPOPO was a modification of the system as described in chapter 6 (see figure 6.1) that produced moderate average output powers in the few-Watts range. Figure 7.1 shows a block diagram of the modified fibre CPA setup. The order of pulse shaper and pre-amplifier changed and the second pre-amplifier was removed. The main modification, however, was the addition of a second power amplifier to generate much higher average powers to pump the SPOPO.

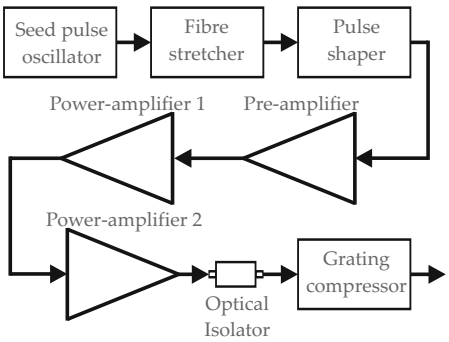

FIGURE 7.1: Block diagram of the high-power, femtosecond fibre CPA setup. The basic building blocks were the same as described in chapter 6 (see figure 6.1), except for the reverse order of pulse shaper and pre-amplifier, the omission of the second pre-amplifier and the addition of a power amplifier.

The chirp on the seed pulse oscillator was increased generating pulses with an autocorrelation FWHM duration of $10.5\,\mathrm{ps}$ as shown in the intensity autocorrelation in figure 7.2. This reduced the peak intensity sufficiently to avoid any nonlinearities in the $920\,\mathrm{m}$-long SMF-based pulse stretcher. The repetition rate of the oscillator was $47.75\,\mathrm{MHz}$, the centre wavelength was $1045\,\mathrm{nm}$, the FWHM bandwidth was $15.4\,\mathrm{nm}$ and the average

power was $20\,\mathrm{mW}$ (table 7.1 shows typical power levels after each CPA system stage). The throughput efficiency of the SMF was around 50% due to launch losses, splice losses and fibre loss of $1.5\,\mathrm{dB/km}$ (HI 1060 fibre). The estimated pulse duration of the stretched pulses was $> 500\,\mathrm{ps}$ using a simple first-order chromatic dispersion estimate and neglecting any other influence on the pulse as a first approximation.

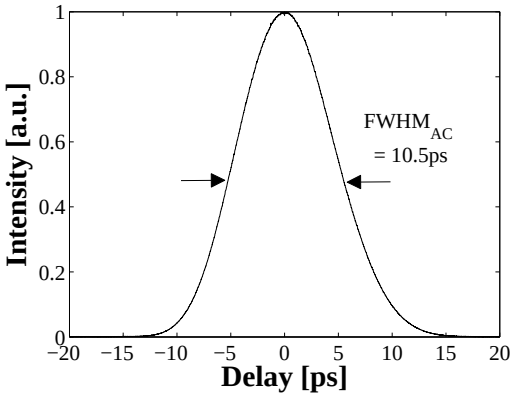

FIGURE 7.2: Intensity autocorrelation of the seed pulse oscillator showing chirped pulses with a FWHM autocorrelation width of $10.5\,\mathrm{ps}$.

A description of the pulse shaper, pre-amplifier and first power-amplifier was given in section 6.2 and will not be repeated at this point for brevity.

The second power amplifier consisted of a $1.7\,\mathrm{m}$-long piece of the PCF, which was also used in the first power amplifier (DC-200/40-PZ-Yb-01, Crystal Fibre A/S, Denmark) and a high-power, fibre-coupled pump diode module (Laserline GmbH, Germany) in a free-space, backward-pump configuration. Aspherical lenses were used to launch the signal into the fibre and to collimate the output. A pair of dichroic mirrors at the PCF output separated the pump light and the signal light. Furthermore, an optical isolator protected the amplifier from harmful back-reflections. The water-cooled pump diode module had a nominal CW output power of up to $350\,\mathrm{W}$ at a centre wavelength of $975\,\mathrm{nm}$. The light was delivered in a fibre with a core diameter of $400\,\mu\mathrm{m}$ and an NA of 0.2 and focused with a power delivery head to a $400\,\mu\mathrm{m}$ spot. An $f = -30\,\mathrm{mm}$ lens was inserted before this $400\,\mu\mathrm{m}$ focus to collimate this output beam and in combination with an $f = 18\,\mathrm{mm}$ aspherical lens on the PCF side, typical pump launch efficiencies of $> 80\%$ into the PCF were obtained. Figure 7.3 shows the output power as a function of the diode drive current of the pump diode module (power levels $> 300\,\mathrm{W}$ could not be measured due to the lack of an appropriate power meter). The temperature of the two laser diode stacks inside the pump diode module could be controlled to tune the emission wavelength for optimum absorption of the pump in the Yb-doped PCF. This tuning is shown in figure 7.4(a). It was furthermore observed that the emission wavelength drifted by approximately $5\,\mathrm{nm}$ as the output power was increased (figure 7.4(b)) due to the lack of a feedback mechanism of this particular module. This behaviour

poses problems inasmuch the absorption of the pump light and therefore the amplifier output power is reduced, when the centre wavelength shifts away from the peak absorption of Ytterbium, also leading to thermal problems. The pump diode module was typically operated at $30°\mathrm{C}$, which produced the highest amplifier signal output power. This signal output power was limited due to problems with thermal loading and fibre damage at this point to $57\,\mathrm{W}$ (after the OI with a transmission of 90%) at a pump power of $95\,\mathrm{W}$ and a signal seed power of $4.11\,\mathrm{W}$ (gain of $11.4\,\mathrm{dB}$), but the system can potentially deliver higher output powers. Figure 7.5 shows the signal output power versus launched pump power. A measurement of the M^2-values showed that the beam quality degraded somewhat in the second power amplifier. After the first power amplifier, operated at an output power of $4.3\,\mathrm{W}$, values of 1.33 (horizontal plane) and 1.07 (vertical plane) were measured, which degraded to 2.10 and 1.54 after the second power amplifier, operated at $\approx 33\,\mathrm{W}$. The beam radius as a function of the position from the focus point of this measurement is shown in figure 7.6. In general, the beam quality improved, when the second power amplifier was operated at high power, because the fundamental mode experiences higher gain under these circumstances and thus dominates over the higher-order modes.

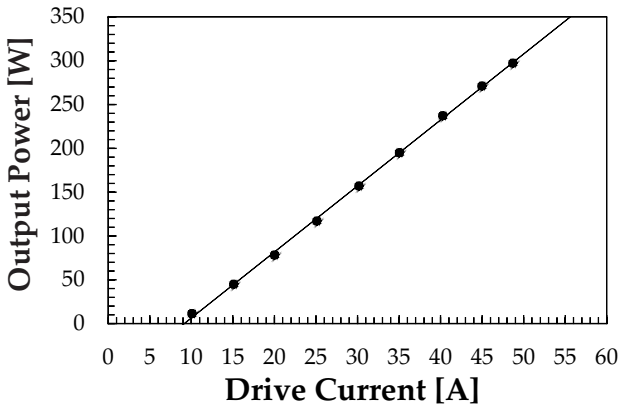

FIGURE 7.3: Laser output power as a function of drive current of the high-power pump diode stacks. The solid line represents a linear fit to the experimental data.

The compressor stage, as described in 6.2, had a typical throughput efficiency of only 55%, which was believed to be caused by grating damage, the required large beam size and possibly thermal problems. Due to the high average power that the compressor was subjected to, a large beam diameter of $1\,\mathrm{cm}$ was generated with an additional telescope in order to reduce the intensity on each grating and therefore avoid problems with localised heating. After calculation of the theoretical GDD of the compressor to match the GDD of the stretcher (see section 6.3.1) and coarse alignment of the gratings, the separation of the two gratings was fine-tuned and the pulses were autocorrelated at each point to find the optimum grating separation. The autocorrelation FWHM durations as a function of grating separation are shown in figure 7.7(a), where a minimum

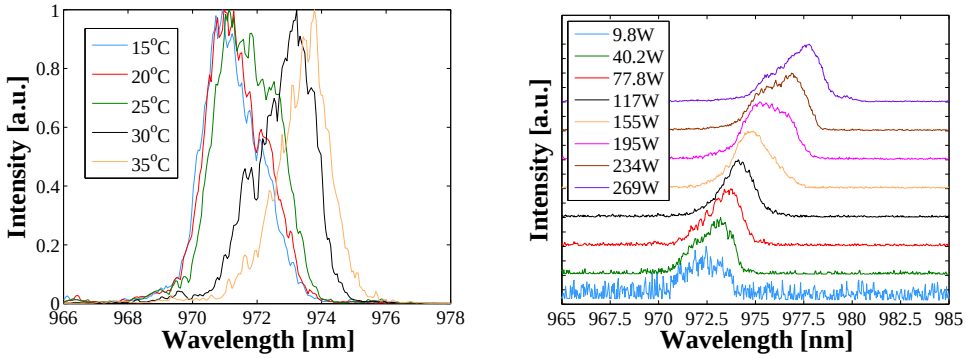

(a) Wavelength shift with temperature

(b) Wavelength shift with power

FIGURE 7.4: Spectral properties of the high-power pump diode stacks. (a) The centre wavelength can be tuned over more than 2 nm by changing the diode temperature to match the peak absorption of the Yb-doped fibre (output power set to 33 W throughout). (b) With increasing laser output power, the centre wavelength drifts by around 5 nm to higher values, which leads to a changing absorption of the pump in the Yb-doped fibre. The operating temperature was kept constant at 30°C. The curves are offset for clarity.

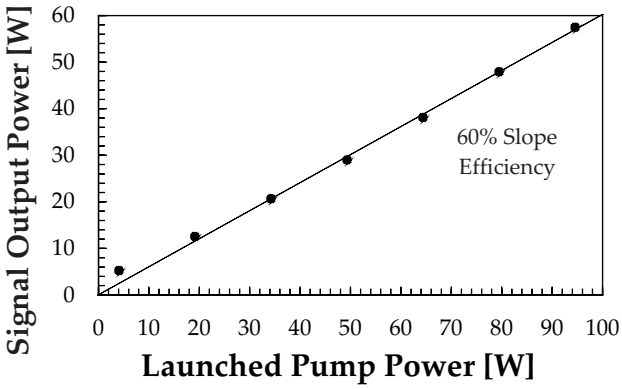

FIGURE 7.5: Signal output power of power amplifier 2 as a function of launched pump power. The solid line represents a linear curve fit and shows a slope efficiency of 60%. The signal power was measured after the OI, which had a transmission of 90%.

duration of $\approx 1.5\,\mathrm{ps}$ at a separation of $\approx 0.99\,\mathrm{m}$ can be identified. The solid line represents a quadratic fit to the experimental data. Figure 7.7(b) shows autocorrelation traces of the longest and shortest pulses in figure 7.7(a) for comparison. It was observed that the pulses did not have a Gaussian profile anymore, but a more complex profile and hence a simple conversion from autocorrelation width to pulse duration with a factor of $1/\sqrt{2}$ was no longer valid [9].

The output power levels and the spectra during normal operation conditions of the different CPA stages are presented in table 7.1 and figure 7.8, respectively. The second power amplifier was typically operated at a power of 30 W, which, including the compressor throughput efficiency, gave sufficient pump power for the SPOPO. The FWHM bandwidth was reduced from $15.4\,\mathrm{nm}$ to $7.1\,\mathrm{nm}$ due to gain narrowing effects. The pixellation of the LC SLM in the pulse shaper caused a spectral modulation amplified

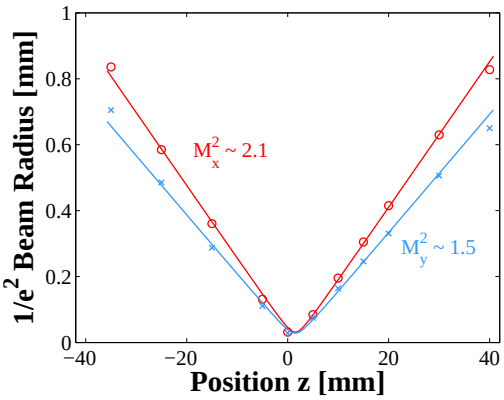

FIGURE 7.6: Beam quality measurement at the output of power amplifier 2 at a power of $\approx$ 33 W yielding M^2-values of 2.1 in the horizontal plane (x) and 1.5 in the vertical plane (y). Markers = experimental data, solid lines = Gaussian curve fit.

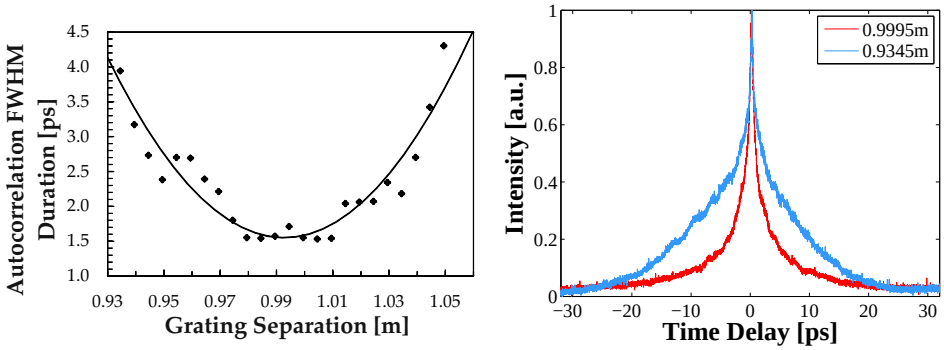

(a) (b)

FIGURE 7.7: Compressor fine tuning to obtain mimimum output pulse duration. (a) FWHM autocorrelation durations of the compressor output versus grating separation including a quadratic fit curve (solid line). The minimum pulse duration was expected at a separation of $\approx$ 0.99 m, which corresponds to a balance of stretcher and compressor GDD. (b) Comparison of the autocorrelation traces of the shortest and longest pulses.

in the subsequent stages as described in section 6.4.2. Furthermore, the centre wavelength shifted from 1045 nm to 1042 nm.

TABLE 7.1: Typical output power levels of the high-power, femtosecond fibre-based CPA system.

CPA stage	Average output power
Seed oscillator	20 mW
Fibre stretcher	10 mW
Pulse shaper	3 mW
Pre-amplifier	100 mW
Power amplifier 1	4 W
Power amplifier 2	30 W

A measurement of the temporal power stability of the compressor output was carried out and it was found that the power fluctuated over a period of 10 min by about $\pm 10\%$ compared to around $\pm 3\%$ of the amplifier output as shown in figure 7.9. The origins

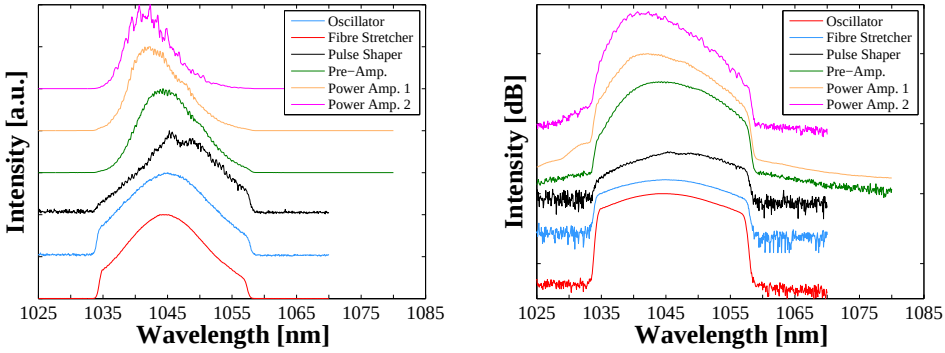

(a) Linear plot

(b) Logarithmic plot

FIGURE 7.8: Evolution of the pulse spectrum through the fibre CPA system. The LC SLM in the pulse shaper introduces spectral modulation, which was amplified in the subsequent amplifiers. No significant ASE build-up was observed. The original FWHM bandwidth of $15.4\,\mathrm{nm}$ of the oscillator reduced to $7.1\,\mathrm{nm}$ and the centre wavelength shifted from $1045\,\mathrm{nm}$ to $1042\,\mathrm{nm}$ due to gain narrowing / shifting effects. The curves are offset for clarity.

of this instability were twofold. Firstly, the periodicity visible in both measurements can be explained by the periodic injection of chilled water into the pump diode stacks, which led to a temperature change and thus a centre wavelength change. This changed the pump absorption in the PCF and finally the signal gain. The (clearly audible) switching of the water pumps had a period of roughly $33\,\mathrm{s}$ and corresponded to the period of the power fluctuations. A more precise temperature control of the pump diode module would be required to reduce the fluctuation. Secondly, spatial instabilities can contribute to an overall output power fluctuation. The path length from the output of the second power amplifier to the output of the compressor was around $8\,\mathrm{m}$ due to the large separation of the diffraction gratings and thus even the slightest mechanical or thermal instability of the PCF led to a noticeable spatial instability at the compressor output. Furthermore, an analysis of the spatial modes supported by the $40\,\mu\mathrm{m}$-core PCF showed that the V-number (equation (2.4)) was 3.62 with $a = 20\,\mu\mathrm{m}$, $\lambda = 1042\,\mathrm{nm}$ and NA $= 0.03$. Operation of only the fundamental mode is obtained for values $V < 2.405$ and thus higher-order modes were also excited. It was expected that five to six modes were existent by using the equation $4/\pi^2 \cdot V^2$ [10]. A well-known effect in LMA fibres is the modal interference caused by a slow drift of the mutual phases of different modes, which eventually leads to beam pointing instabilities of the output beam [11]. The existence of higher-order modes was supported by the measured M^2-values as shown in figure 7.6. In fact, the M^2 degraded even more to values of 2.6×1.7 after propagation of the beam through the compressor.

The CPA system worked reliably, yet with the described instabilities, at signal output powers up to $\approx 30\,\mathrm{W}$ and was used to pump the femtosecond SPOPO (see the following sections). When the pump power was increased to more than $150\,\mathrm{W}$ to generate much higher signal powers from the second power amplifier, the output end-facet of the PCF

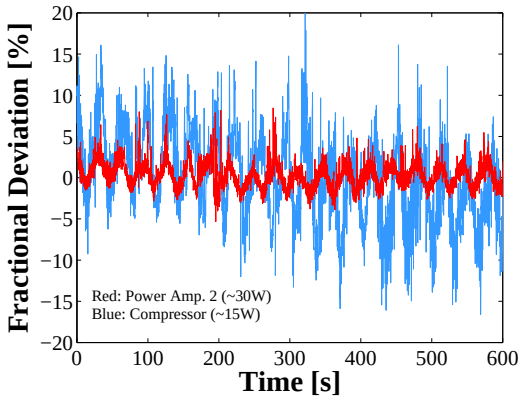

FIGURE 7.9: Temporal stability of the compressor output power. The periodicity of the output power can be traced back to the water cooling system of the pump diode stacks in that every time cool water was injected into the diode stacks the temperature and therefore centre wavelength changed. This occurred roughly every $33\,\mathrm{s}$ and correlated with the output power fluctuations. The overall fluctuations of $\pm 10\%$ of the compressor output (blue) were clearly more severe than the fluctuations of the power amplifier 2 output (red).

with the angle-cleaved end-cap exploded. Images of the crater-like damage are shown in figure 7.10(a). The most likely origin of this damage was a piece of dust or dirt on the end-facet that caught fire and triggered a sudden temperature increase, which melted the end-cap. Also, the pump power that was not launched into the inner cladding led to a heating-up of the PCF, which could have contributed to the catastrophic fibre failure. A first measure to avoid such damage in the future was a water-cooled heatsink holding the output end of the PCF in a V-groove. Thermal paste was applied and the water temperature was set to $15°\mathrm{C}$. This significantly reduced the thermal load on the PCF. Furthermore, the PCF output end was purged with nitrogen to generate a positive pressure around the end-cap, which should avoid dust to gather. Two steps were required to repair the PCF: (1) Putting an end-cap on the fibre and (2) angle-cleaving the end-cap. Splicing of a core-less end-cap to the PCF could not be achieved at high quality, since the splice point was very fragile and subsequent cleaving could not be carried out. Therefore, the PCF microstructure at the output end was collapsed over a length of $460\,\mu\mathrm{m}$ to imitate a real end-cap. This length allowed for a sufficient divergence of the signal beam to reduce the intensity at the silica–air interface and avoided clipping of the beam along the rim of the fibre. Careful mechanical polishing of the PCF was carried out to put a $5°$ angle on the fibre, since any type of cleaving (mechanical or laser-based) was not successful. Images of the repaired PCF are shown in figure 7.10(b). The fine lines on the left-hand side are the ring of air holes of the outer cladding. The entire microstructure was removed over the $460\,\mu\mathrm{m}$ length by the collapsing process.

The beam profile at the power amplifier 2 output as observed on a CCD camera is presented in figure 7.11 showing a Gaussian mode confined to the PCF core. The stress rods are the black ellipses on both sides of the fibre core.

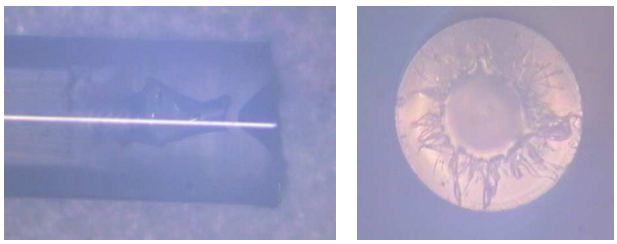

(a) Damaged PCF end-facet

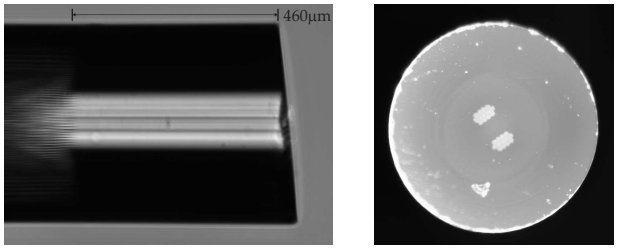

(b) Repaired PCF end-facet

FIGURE 7.10: Microscope images of the (a) damaged and (b) repaired output end-facet of the PCF. The explosion, which was most likely caused by dust on the end-facet, generated a crater-like damage to the end-cap. The PCF was repaired by collapsing it over a length of $460\,\mu\mathrm{m}$ to imitate a real end-cap and by mechanical polishing at an angle of 5°.

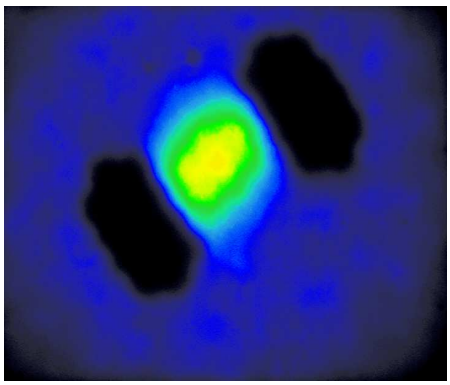

FIGURE 7.11: Beam profile of the signal emerging from the repaired PCF end-facet (see figure 7.10(b)) clearly showing the signal mode confinement to the core region and the polarisation-maintaining stress rods.

7.3 Femtosecond pulse shaping results

Adaptive pulse shaping was carried out after the fibre-based CPA system was fully operational. As in chapter 6, a GaAsP detector was placed at the compressor output and the beam was strongly focused onto its sensitive area. The generated TPA signal was used as feedback parameter for the optimisation algorithm. The JADE algorithm, as described in 2.3.4, was applied for these experiments with amplitude and phase shaping enabled. The number of controlled pixels (every 4^{th} of 128 pixels) did not dynamically change during the optimisation and it was interpolated over the uncontrolled pixels after each iteration. The population size was reduced three times during the optimisation and the initial control parameters were $F = 0.7$ and $CR = 0.5$.

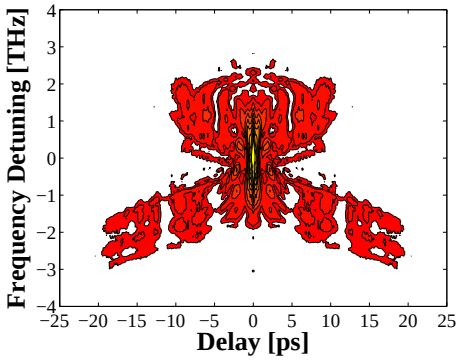

(a) FROG trace

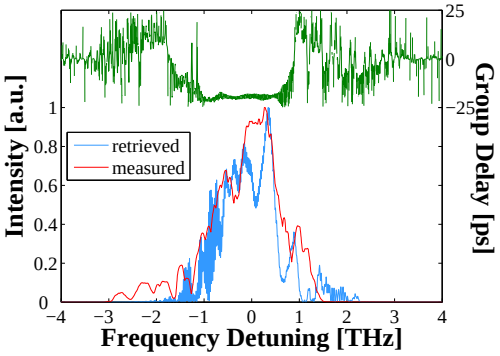

(b) Spectral characteristics

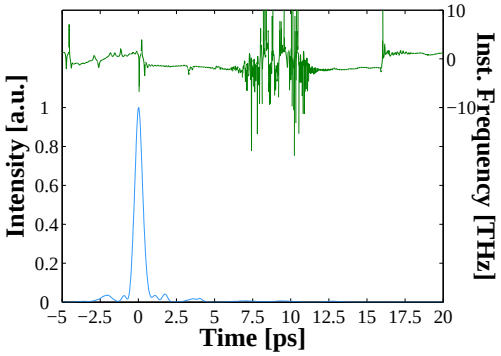

(c) Temporal characteristics

FIGURE 7.12: FROG results of the pulse-shaped, femtosecond pulses used to pump the optical parametric oscillator. Subfigure (a) shows the contour plot of the square-root of FROG trace after interpolation onto a 256×256 Fourier grid. The TPA signal improved $2.35\times$ during the optimisation, the output power after the compressor was $13.5\,\mathrm{W}$ and the FROG retrieval error was 0.01. The FWHM pulse duration improved from $1.07\,\mathrm{ps}$ before shaping to $615\,\mathrm{fs}$ after shaping.

The adaptive pulse shaping resulted in a $2.35\times$ improvement of the TPA signal at an average output power of the compressor of $13.5\,\mathrm{W}$. Figure 7.12 shows the FROG trace as well as the spectral and temporal properties of the shaped output pulses using an SHG FROG setup for characterisation. The FROG retrieval error was 0.01. It can be seen that a linear spectral phase was obtained across the pulse spectrum expressed in a flat group delay ($\tau_g = d\phi/d\omega$). Furthermore, the accumulated TOD from stretcher and compressor was largely removed by the pulse shaping as can be seen in the temporal intensity curve with no temporal oscillations present. A clean pulse with a FWHM duration of $615\,\mathrm{fs}$ was obtained. For comparison, the pulse duration of the unshaped pulse was $1.07\,\mathrm{ps}$ as determined by a FROG measurement.

7.4 Optical parametric oscillator setup

The layout of the ring cavity SPOPO is shown in figure 7.13. The pump source repetition rate of $47.75\,\mathrm{MHz}$ required a resonator length of $6.28\,\mathrm{m}$. Therefore, a setup with

folding mirrors was realised to accommodate the SPOPO on the optical table. A large beam waist radius of $\approx 100\,\mu\mathrm{m}$ was chosen to reduce the intensity in the nonlinear crystal centre, so that damage could be prevented. To generate such a large beam waist, a radius of curvature for the curved mirrors of $-1\,\mathrm{m}$ was required and such mirrors were not available at the time. Thus, plane mirrors in combination with lenses of focal length $0.5\,\mathrm{m}$ were applied to emulate the curved mirrors. All of the mirrors were coated for high transmission of the pump wavelength ($T = 92\%$) and the idler range (approximately $T = 88\%$) and for high reflectivity for the signal ($R > 99\%$), so that the SPOPO was singly resonant for the signal in the spectral range around $1.5\,\mu\mathrm{m}$. Five different signal output couplers with reflectivities from 95% to 25% were available. The two lenses in the resonator were AR-coated to reduce signal losses to a minimum.

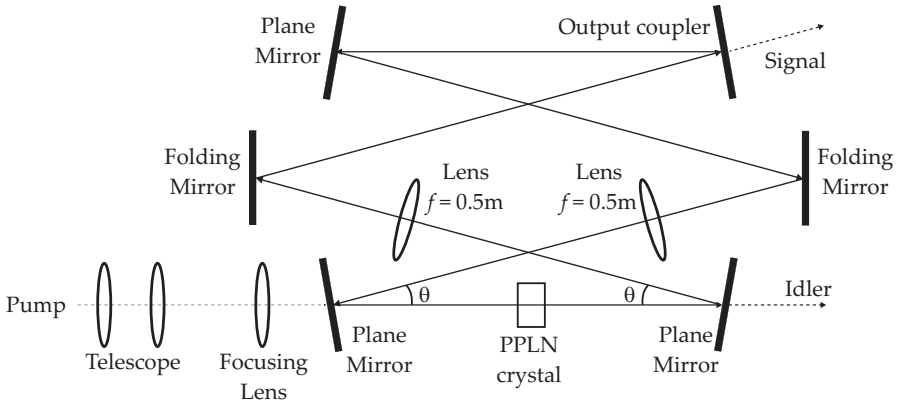

FIGURE 7.13: Experimental layout of the femtosecond PPLN SPOPO. The length of the SPOPO was $6.28\,\mathrm{m}$ to match the $47.75\,\mathrm{MHz}$ repetition rate of the fibre CPA, therefore a configuration with folding mirrors was realised. Instead of curved mirrors, lenses with a focal length of $0.5\,\mathrm{m}$ were chosen to obtain the required waist size inside the PPLN crystal.

A PPLN crystal with dimensions $L = 5\,\mathrm{mm}$, $W = 0.5\,\mathrm{mm}$, $H = 10\,\mathrm{mm}$ (see figure 3.3 for the crystal orientation) and 16 poled gratings was used inside the SPOPO (Covesion Ltd., United Kingdom). The grating periods ranged from $27\,\mu\mathrm{m}$ up to $30\,\mathrm{mm}$ in $0.2\,\mu\mathrm{m}$ steps. The crystal was AR-coated for the signal and idler wavelength range ($R < 2\%$) and for the pump ($R = 0.1\%$). It was operated in an oven at a temperature of $150^{\circ}\mathrm{C}$ to reduce the effect of photo-refraction.

The ABCD matrix model of the $6.28\,\mathrm{m}$ folded resonator with the $f = 0.5\,\mathrm{m}$ lenses and the $5\,\mathrm{mm}$-long PPLN crystal resulted in a signal waist radius of $101.8\,\mu\mathrm{m}$. Note that due to the use of lenses and perpendicular light incidence rather than curved mirrors aligned at an angle, astigmatism related to the bow-tie angle θ does not occur and the signal beam is not elliptical anymore. The confocal parameter was $b_s = 93\,\mathrm{mm}$, which gave a focusing parameter of $\xi_s = 0.054$ and hence the signal beam was nearly collimated along the length of the crystal. This was not ideal in terms of conversion efficiency, but the prevention of optical damage was given higher importance here. The pump beam was delivered through a lens telescope and a focusing lens to obtain a waist radius in the crystal centre that matches the signal waist. Initially, a waist of

$100\,\mu\mathrm{m} \times 130\,\mu\mathrm{m}$ was generated at a low power of $1.8\,\mathrm{W}$. The strong beam ellipticity was already observed at the compressor output and its origin could not be entirely clarified. Apart from the ellipticity, a dependence of the pump waist radius on the pump source output power was observed. The waist radius increased from $100\,\mu\mathrm{m} \times 130\,\mu\mathrm{m}$ to $125\,\mu\mathrm{m} \times 200\,\mu\mathrm{m}$ at $6.7\,\mathrm{W}$ and to $240\,\mu\mathrm{m} \times 325\,\mu\mathrm{m}$ at $13.5\,\mathrm{W}$. Thermal lensing of the crystal inside the optical isolator [12, 13] and / or of the compressor diffraction gratings was believed to cause this effect. Since such a change in the pump focusing condition was not acceptable, the pump source was constantly operated at the highest output power of $13.5\,\mathrm{W}$ and a focusing lens with $f = 250\,\mathrm{mm}$ was chosen to have a good match of pump and signal waist size resulting in a waist of $125\,\mu\mathrm{m} \times 85\,\mu\mathrm{m}$ (no telescope required under these conditions). The input power to the SPOPO was controlled with a combination of a HWP and a PBS as a variable attenuator.

7.5 Output power and pump depletion versus pump power

After initial oscillation of the SPOPO with a highly reflective OC was achieved, other OCs were successively used to find the condition, which produced the highest signal output power. The input pump power was $10\,\mathrm{W}$ and the signal centre wavelength was $1480\,\mathrm{nm}$ throughout. The different power levels and thresholds are summarised in table 7.2. The OC with $R = 45\%$ generated the highest output power and was thus chosen for the following experiments.

TABLE 7.2: SPOPO output parameters for different OC mirror reflectivities. The pump power was $10\,\mathrm{W}$.

Output coupler reflectivity [%]	**Threshold power** [W]	**Idler power** [W]	**Signal power** [W]	**Residual pump** [W]
95	1.7	0.65	0.22	4.1
85	1.1	0.58	0.33	4.0
65	3.3	0.76	0.95	3.8
45*	4.5	0.71	1.40	3.9
25†	6.3	0.50	1.00	4.8

* optimum output coupler; † unstable operation

The signal and idler output power as well as the pump depletion as a function of the input pump power is shown in figure 7.14. The threshold pump power was $4.1\,\mathrm{W}$, the pump depletion was approximately 33% and the slope efficiencies were $\approx 23\%$ (signal) and $\approx 15\%$ (idler). At the highest pump power of $12.4\,\mathrm{W}$, a signal and idler output power of $1.87\,\mathrm{W}$ and $1.23\,\mathrm{W}$ was obtained and this corresponded to a total conversion efficiency of 25%.

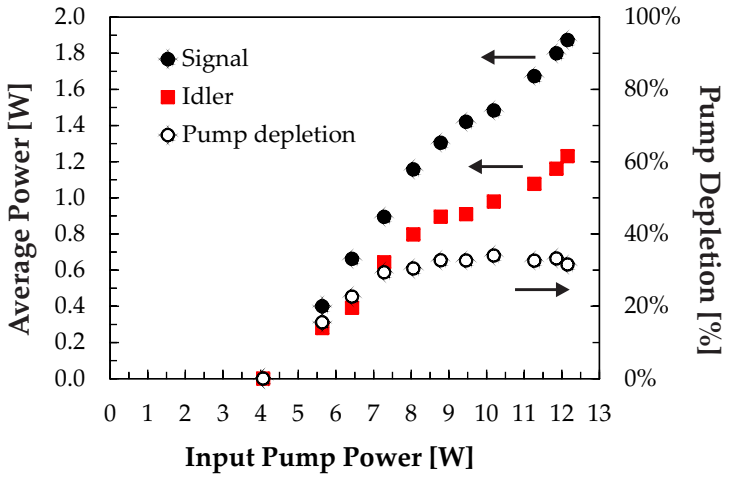

FIGURE 7.14: Output power and pump depletion as a function of input pump power of the femtosecond, PPLN SPOPO using an $R = 45\%$ signal output coupler.

The low pump depletion and efficiencies indicated significant cavity loss. A Findlay-Clay analysis using equation (2.68) gave an effective cavity loss of 23% (excluding the threshold value of the 95% OC that appears to be anomalously high). Idler absorption was not thought to be a major problem, since the wavelength was $3.6\,\mu\mathrm{m}$ and hence well within the transmission window (see figure 3.2, for instance).

Possibly, bad mode matching of the signal and the elliptical pump beam inside the PPLN crystal led to the low efficiency numbers. Additionally, the pump beam was spatially and temporally very unstable as explained in section 7.2 resulting in a measurement error of the values in table 7.2 and figure 7.14 of up to $\pm 10\%$. Thus, it is of paramount importance to improve the pump source in order to improve the performance of the SPOPO. If the final amplifier operated only with the fundamental mode and all higher-order modes were suppressed, the beam pointing instabilities due to the modal interference would be eliminated. A different LMA fibre with a smaller core diameter to reduce the V-number could achieve this, but the impact of nonlinearities on the pulses would be increased. Furthermore, thermal lensing problems of the OI and the diffraction gratings, which lead to a deteriorated beam quality, must be addressed by using components rated for these operating conditions. These include an OI that uses Brewster windows as polarising components rather than PBS cubes as well as bigger gratings to allow for a much bigger beam size and hence reduced intensities.

Because of the inherently more difficult alignment of a ring resonator and the associated instability, a standing-wave resonator could prove more advantageous to enable a careful alignment optimisation, so that the SPOPO operates more reliably and stably. The cavity length could be reduced to a half or a quarter of the length, which would, however, lead to increased signal round-trip loss. Furthermore, since a signal pulse was expected to have a pulse duration similar to the $615\,\mathrm{fs}$-long pump pulse right after

it was generated in the crystal, an estimate of the dispersive broadening during propagation through the two intracavity lenses is instructive. With the Sellmeier equation for the BK 7 lens substrate material and a signal wavelength of $\lambda = 1.5\,\mu\mathrm{m}$, a GVD of $-18.65\,\mathrm{fs}^2/\mathrm{mm}$ was calculated with [14]

$$\mathrm{GVD} = \frac{\lambda^3}{2\pi c^2} \cdot \frac{d^2 n}{d\lambda^2}\,, \tag{7.1}$$

where n is the refractive index and c the speed of light. The dispersive pulse broadening was calculated using [14]

$$\tau_{out}\,(L) = \tau_{in}\sqrt{1 + \left(4\ln 2 \cdot \frac{L \cdot \mathrm{GVD}}{\tau_{in}^2}\right)^2}\,, \tag{7.2}$$

where τ_{in} denotes the FWHM signal pulse duration (unchirped, Gaussian) and L the material thickness. With a $\tau_{in} = 615\,\mathrm{fs}$ pulse propagating through one lens of thickness $L = 2.5\,\mathrm{mm}$, an insignificantly broadened output pulse with a duration of $615.00004\,\mathrm{fs}$ was calculated. Thus, the lenses did not influence the signal pulse propagation in the resonator and the use of curved mirrors instead would not improve the SPOPO performance.

Some tens of milliwatts of parasitic, non-phase-matched green light (second harmonic of the pump) were generated for the high average pump power of $> 10\,\mathrm{W}$ and this led to more pronounced photo-refraction in the PPLN crystal, which can degrade the overall SPOPO performance. Replacing the PPLN crystal with another material (table 1.1), which is less sensitive to photo-refraction could be advantageous. However, some of the outstanding properties of lithium niobate, e.g. the high effective nonlinear coefficient, would be sacrificed. Nonlinear crystals from the KTP, KTA and RTA family have been used for MIR generation in OPOs. The effective nonlinear coefficients are high, the transparency reaches into the MIR and they can be phase-matched for such nonlinear interactions. KTP OPOs were demonstrated in type II and NCPM configurations, but with a limited MIR tuning of $< 4\,\mu\mathrm{m}$ [2, 15, 16]. RTA [17] and PPRTA [18, 19] have been used as well, but again with idler wavelengths not exceeding $4\,\mu\mathrm{m}$. Powers *et al.* used KTA to access MIR wavelengths between $4\,\mu\mathrm{m}$ and $5\,\mu\mathrm{m}$ [20]. Other materials that can be used in MIR OPO include ZGP (up to $12\,\mu\mathrm{m}$, but with a nanosecond pump laser at $2.93\,\mu\mathrm{m}$) [21] or OP-GaAs (up to $9\,\mu\mathrm{m}$ in a tandem-pumping arrangement with a nanosecond Nd:YAG laser and an NIR PPLN OPO) [22]. A widely used crystal for OPOs pumped with visible light is LBO (as reported in chapter 5.4), which has a high damage threshold suitable for high power operation and a moderate gain. However, it can not be applied in OPOs with pump sources in the $1\,\mu\mathrm{m}$ region due to the limited transparency range in the MIR for the idler output up to only $3.2\,\mu\mathrm{m}$.

Furthermore, temperature phase-matching in the convenient NCPM geometry would require temperatures of more than $1000^{\circ}\mathrm{C}$, which is impractical.

Further experiments with this SPOPO were not possible due to reoccuring damage of the PCF output end of the final amplifier as described in 7.2. Additionally, electrical failure of the $350\,\mathrm{W}$ pump diode module did not allow a continuation of this work.

7.6 Conclusions

The work presented in this chapter described a high-power, femtosecond, fibre-based CPA pump source including a pulse shaper, and a PPLN SPOPO for the generation of tunable, ultrashort, high-power pulses in the NIR and MIR.

The pulses from the YDF seed oscillator with an autocorrelation width of $10.5\,\mathrm{ps}$ were stretched to $> 500\,\mathrm{ps}$, then amplified in one core-pumped pre-amplifier and two cladding-pumped, PCF, LMA power amplifiers, and compressed to $1.07\,\mathrm{ps}$. The LC SLM pulse shaper and a JADE optimisation algorithm in an adaptive shaping arrangement compensated for accumulated TOD from the fibre stretcher and grating compressor to generate pulses with a FWHM duration of $615\,\mathrm{fs}$ at a repetition rate of $47.75\,\mathrm{MHz}$ and a centre wavelength of $1042\,\mathrm{nm}$. The maximum output power from the pump source was $\approx 30\,\mathrm{W}$ ($57\,\mathrm{W}$ before the compressor), which corresponds to a peak power of $1\,\mathrm{MW}$. The pump power for the SPOPO, however, was limited to around $15\,\mathrm{W}$ during the experiments due to problems with heating and beam instabilities.

The SPOPO ring cavity was realised in a folded, $6.28\,\mathrm{m}$-long, bow-tie configuration and had a $5\,\mathrm{mm}$-long PPLN crystal in its centre. Signal and idler output powers of $1.87\,\mathrm{W}$ at $1.48\,\mu\mathrm{m}$ and $1.23\,\mathrm{W}$ at $3.6\,\mu\mathrm{m}$, respectively, were obtained at an input pump power of $12.4\,\mathrm{W}$ (25% overall conversion efficiency) using an OC with a reflectivity for the signal light of 45%. The pulse duration of the signal and idler pulses was expected to be comparable to the pump pulse duration of $615\,\mathrm{fs}$.

The low pump depletion and efficiencies as well as the poor stability of the SPOPO had a number of reasons that have to be addressed in the future to improve the overall performance of the system. On the pump source side, modal interference leading to beam pointing instabilities, changing emission wavelength of the pump diodes leading to power fluctuations, thermal lensing in the OI crystal leading to a beam distortion as well as suboptimal pump launching into the PCF leading to thermal and thus mechanical problems with the fibre mount were identified as reasons for the poor performance. On the SPOPO side, mode matching of the pump and signal beams was impaired by the spatially unstable and low-quality pump beam. The folded ring cavity setup posed

inherent problems regarding the optimisation of the resonator alignment and influenced the oscillation performance. Furthermore, some tens of milliwatts of parasitic green light generated in the PPLN crystal led to photo-refraction, which contributed to the poor performance as well.

Such a fibre CPA / OPO system for the generation of high-power, femtosecond pulses tunable in the NIR and MIR was demonstrated for the first time in this chapter. Therefore, the obtained output powers can be regarded as the highest reported so far. However, many improvements must be made to be able to collect a full set of results in order to be able to make further judgements on its performance and practicality.

References

[1] M. A. Watson, M. V. O'Connor, D. P. Shepherd, and D. C. Hanna, "Synchronously pumped CdSe optical parametric oscillator in the 9-10μm region," Opt. Lett. **28**(20), 1957–1959 (2003).

[2] G. R. Holtom, R. A. Crowell, and X. S. Xie, "High-repetition-rate femtosecond optical parametric oscillator-amplifier system near 3μm," J. Opt. Soc. Am. B **12**(9), 1723–1731 (1995).

[3] C. W. Hoyt, M. Sheik-Bahae, and M. Ebrahim-Zadeh, "High-power picosecond optical parametric oscillator based on periodically poled lithium niobate," Opt. Lett. **27**(17), 1543–1545 (2002).

[4] B. Ruffing, A. Nebel, and R. Wallenstein, "All-solid-state cw mode-locked picosecond $KTiOAsO_4$ (KTA) optical parametric oscillator," Applied Physics B: Lasers and Optics **67**(5), 537–544 (1998).

[5] O. Kokabee, A. Esteban-Martin, and M. Ebrahim-Zadeh, "Efficient, high-power, ytterbium-fiber-laser-pumped picosecond optical parametric oscillator," Opt. Lett. **35**(19), 3210–3212 (2010).

[6] F. Kienle, K. K. Chen, S.-U. Alam, C. B. E. Gawith, J. I. Mackenzie, D. C. Hanna, D. J. Richardson, and D. P. Shepherd, "High-power, variable repetition rate, picosecond optical parametric oscillator pumped by an amplified gain-switched diode," Opt. Express **18**(8), 7602–7610 (2010).

[7] F. Adler, K. C. Cossel, M. J. Thorpe, I. Hartl, M. E. Fermann, and J. Ye, "Phase-stabilized, 1.5 W frequency comb at 2.8-4.8 μm," Opt. Lett. **34**(9), 1330–1332 (2009).

[8] T. Südmeyer, E. Innerhofer, F. Brunner, R. Paschotta, T. Usami, H. Ito, S. Kurimura, K. Kitamura, D. C. Hanna, and U. Keller, "High-power femtosecond fiber-feedback optical parametric oscillator based on periodically poled stoichiometric $LiTaO_3$," Opt. Lett. **29**(10), 1111–1113 (2004).

[9] R. Trebino, *Frequency-Resolved Optical Gating: The Measurement of Ultrashort Laser Pulses*, 1st ed. (Kluwer Academic Publishers, Boston, 2002).

[10] B. E. A. Saleh and M. C. Teich, *Fundamentals of photonics*, 1st ed. (John Wiley & Sons, New York, 1991).

[11] J. W. Nicholson, A. D. Yablon, S. Ramachandran, and S. Ghalmi, "Spatially and spectrally resolved imaging of modal content in large-mode-area fibers," Opt. Express **16**(10), 7233–7243 (2008).

[12] E. Khazanov, N. Andreev, O. Palashov, A. Poteomkin, A. Sergeev, O. Mehl, and D. H. Reitze, "Effect of terbium gallium garnet crystal orientation on the isolation ratio of a Faraday isolator at high average power," Appl. Opt. **41**(3), 483–492 (2002).

[13] E. Khazanov, N. F. Andreev, A. Mal'shakov, O. Palashov, A. K. Poteomkin, A. Sergeev, A. A. Shaykin, V. Zelenogorsky, I. A. Ivanov, R. Amin, G. Mueller, D. B. Tanner, and D. H. Reitze, "Compensation of Thermally Induced Modal Distortions in Faraday Isolators," IEEE Journal of Quantum Electronics **40**(10), 1500–1510 (2004).

[14] G. P. Agrawal, *Nonlinear Fiber Optics*, Optics and Photonics, 3rd ed. (Academic Press, San Diego, 2001).

[15] D. C. Edelstein, E. S. Wachman, and C. L. Tang, "Broadly tunable high repetition rate femtosecond optical parametric oscillator," Applied Physics Letters **54**(18), 1728–1730 (1989).

[16] E. S. Wachman, D. C. Edelstein, and C. L. Tang, "Continuous-wave mode-locked and dispersion-compensated femtosecond optical parametric oscillator," Opt. Lett. **15**(2), 136–138 (1990).

[17] P. E. Powers, C. L. Tang, and L. K. Cheng, "High-repetition-rate femtosecond optical parametric oscillator based on $RbTiOAsO_4$," Opt. Lett. **19**(18), 1439–1441 (1994).

[18] D. T. Reid, Z. Penman, M. Ebrahim-Zadeh, W. Sibbett, H. Karlsson, and F. Laurell, "Broadly tunable infrared femtosecond optical parametric oscillator based on periodically poled $RbTiOAsO_4$," Opt. Lett. **22**(18), 1397–1399 (1997).

[19] D. T. Reid, G. T. Kennedy, A. Miller, W. Sibbett, and M. Ebrahim-Zadeh, "Widely tunable, near- to mid-infrared femtosecond and picosecond optical parametric oscillators using periodically poled $LiNbO_3$ and $RbTiOAsO_4$," IEEE Journal of Selected Topics in Quantum Electronics **4**(2), 238–248 (1998).

[20] P. E. Powers, S. Ramakrishna, C. L. Tang, and L. K. Cheng, "Optical parametric oscillation with $KTiOAsO_4$," Opt. Lett. **18**(14), 1171–1173 (1993).

[21] K. L. Vodopyanov, F. Ganikhanov, J. P. Maffetone, I. Zwieback, and W. Ruderman, "$ZnGeP_2$ optical parametric oscillator with 3.8-12.4-μm tunability," Opt. Lett. **25**(11), 841–843 (2000).

[22] K. L. Vodopyanov, O. Levi, P. S. Kuo, T. J. Pinguet, J. S. Harris, M. M. Fejer, B. Gerard, L. Becouarn, and E. Lallier, "Optical parametric oscillation in quasi-phase-matched GaAs," Opt. Lett. **29**(16), 1912–1914 (2004).

Chapter 8

Conclusions

8.1 Summary of results

There is a growing demand for ultrashort, high-power, tunable light sources for applications as diverse as materials processing (e.g. ablation and deposition of polymers [1, 2]), telecommunications [3–5], nonlinear microscopy and spectroscopy (e.g. CARS [6–8], SHG [9–11] or STED [12, 13]), time-resolved pump-probe spectroscopy, photodynamic therapy, IR countermeasures or light detection and ranging. For this reason, ultrashort OPOs with a high degree of flexibility regarding tunability, output power, pulse energy, pulse duration and repetition rate were investigated in this thesis.

As for the pump sources used to synchronously pump the OPOs, the main focus was on Yb:fibre-based amplification systems due to the ease of power and energy scaling. Recently, such systems have also been used as a practical, robust and compact replacement of more traditional Ti:sapphire laser and amplifier systems. Two different ultrashort laser systems were implemented and characterised for the purpose of OPO pumping: (1) a picosecond master-oscillator power-amplifier (MOPA) system with a gain-switched laser diode as front-end seed source, as well as (2) a femtosecond chirped-pulse amplifier (CPA) with a YDF laser seed source. The femtosecond CPA system included a pulse shaper module based on a liquid crystal spatial light modulator, which was used to remove the accumulated third-order dispersion from the pulse stretcher and compressor to achieve high-quality, pedestal-free, femtosecond pulses.

The OPOs were mainly set-up as bow-tie ring cavities, since this offers the highest degree of freedom in terms of spatial and temporal alignment and since the resonating signal exhibits the lowest losses in a ring cavity. Periodically poled lithium niobate (PPLN) or lithium triborate (LBO) were used as nonlinear crystals. PPLN doped with magnesium oxide was mainly applied in the OPOs pumped at $1\,\mu\mathrm{m}$, since all of its excellent

properties such as designer phase-matching (periodic poling), high effective nonlinear coefficient and hence gain, wide availability and low costs, high damage threshold as well as wide transparency in the NIR and MIR could be fully exploited. For high-power, green-pumped OPOs, LBO with a high damage threshold was selected instead due to its proven reliability and performance under the influence of high intensities in the visible. Here, phase-matching could be achieved in the convenient non-critical phase-matching configuration.

The experiments with the picosecond MOPA pump source emitting at $\approx 1\,\mu\mathrm{m}$ were described in chapter 3 and 4. An OPO based on MgO:PPLN was demonstrated that generated a total output power of $10.4\,\mathrm{W}$ and $17\,\mathrm{ps}$-long pulses and that was tunable in the NIR and MIR ($1.4\,\mu\mathrm{m} \ldots 4.4\,\mu\mathrm{m}$) [14]. The repetition rate of this system was widely selectable up to nearly $1\,\mathrm{GHz}$. The picosecond pump source has in principle the potential for operation at much higher repetition rates. Previous reports of high repetition rate OPO pump sources include $82\,\mathrm{GHz}$ [5], $10\,\mathrm{GHz}$ [3] and $2.5\,\mathrm{GHz}$ [15]. However, unlike these publications, the pump source used here could still operate at high average output powers. The highest average power from a synchronously pumped OPO reported to date did not feature the attractive combination of a fibre-based pump source and a PPLN-based OPO, but instead used a fixed-repetition-rate, femtosecond Yb:YAG thin-disk laser pumping a PPsLT OPO that produced $\approx 27\,\mathrm{W}$ of total output power [16]. In the picosecond regime, Kokabee *et al.* demonstrated a YDF laser pumping an MgO:PPLN OPO that generated $\approx 17\,\mathrm{ps}$-long signal pulses with a combined signal and idler power of $\approx 12\,\mathrm{W}$ [17]. The repetition rate of this system was, however, also not variable. Further work in this thesis (chapter 4) included the demonstration of a high-pulse-energy, MgO:PPLN OPO with a similar tunability range as above, where a combined pulse energy of $680\,\mathrm{nJ}$ was obtained with pulse durations of $\approx 100\,\mathrm{ps}$ [18]. In this case, the repetition rate of the pump system was reduced to under $8\,\mathrm{MHz}$ and to achieve a compact resonator, a single-mode fibre for signal feedback was incorporated in the OPO resonator. Südmeyer *et al.* also demonstrated an OPO with an intracavity fibre, but with the focus on high average powers [16]. A combined pulse energy of $\approx 480\,\mathrm{nJ}$ was obtained from the fibre-feedback PPsLT OPO pumped with $840\,\mathrm{fs}$-long pulses at $56\,\mathrm{MHz}$ from a thin-disk laser. Another approach to scale to higher pulse energies chosen by Lamour *et al.* employed a relay-imaging cavity and cavity dumping [19, 20]. A signal pulse energy of $650\,\mathrm{nJ}$ was measured at the output of the MgO:PPLN OPO (no idler output), which was pumped with a YDF laser ($< 400\,\mathrm{fs}$, $15.3\,\mathrm{MHz}$). To ensure stable long-term operation, an active wavelength stabilisation scheme was required, which added significant complexity to the system. Both OPOs described in chapter 3 and 4 exhibited a power roll-off effect, whose origin could not be unambiguously determined. However, thermal instabilities and thermal lensing in crystals (OPO

crystal, optical isolator crystal [21, 22]) caused by parasitic absorption were thought to affect the beam quality and resonator stability.

Chapter 6 and 7 still dealt with OPO systems pumped at $\approx 1\,\mu\mathrm{m}$, but now in the femtosecond regime. Femtosecond output pulses at high output power were achieved via the CPA / pulse shaper pump system. Energy-scalable output pulses were demonstrated by reduction of the $50\,\mathrm{MHz}$ system repetition rate, careful control of the amplifier nonlinearities and adaptive pulse shaping [23]. The maximum pulse energy obtained was $8.8\,\mu\mathrm{J}$ in $\approx 500\,\mathrm{fs}$-long pulses at $500\,\mathrm{kHz}$. In another configuration, $1.7\,\mu\mathrm{J}$ clean, pedestal-free $\approx 300\,\mathrm{fs}$ pulses were obtained at a repetition rate of $5\,\mathrm{MHz}$. A power-scaled version of the pump system was also used for a PPLN OPO and $\approx 3\,\mathrm{W}$ of combined output power was produced at $50\,\mathrm{MHz}$. The typical pump pulse duration was $600\,\mathrm{fs}$ after the adaptive pulse shaping. Adler *et al.* reported on a YDF-laser-pumped, femtosecond PPLN OPO that was tunable from $1.4\,\mu\mathrm{m}$ to $4.8\,\mu\mathrm{m}$ with a maximum output power of $1.5\,\mathrm{W}$ [24]. The benchmark in terms of total output power in the femtosecond regime was again the publication of Südmeyer *et al.* with an output of $\approx 27\,\mathrm{W}$ in $840\,\mathrm{fs}$-long pulses [16]. However, this report did not incorporate a fibre-based pump source and the convenient PPLN material, but a thin-disk laser and PP-sLT. The difficulties to reliably operate the entire system in chapter 7 concerned beam pointing instabilities from modal interference in large mode area fibres [25], recurring fibre end-facet damage due to high pump powers, accumulated third-order dispersion requiring pulse shaping (added system complexity), mode mismatch of pump and signal beams in the OPO crystal, photo-refraction in lithium niobate due to parasitic green light [26, 27], and the free-space nature of the system in combination with the long optical path lengths.

Picosecond OPOs that were tunable in the visible and NIR by means of pumping with green light were discussed in chapter 5. The green pump light was obtained by frequency-doubling of the $1.06\,\mu\mathrm{m}$ output from the picosecond MOPA system, which was here operated at $230\,\mathrm{MHz}$. Firstly, an OPO using MgO:PPLN was investigated, whose pulse duration was $20\,\mathrm{ps}$ and whose output power was limited to a few hundred milliwatts only. A careful investigation of the limiting effects (photo-refraction, induced absorption, nonlinear absorption) was carried out to determine a safe operation regime of MgO:PPLN under the influence of visible light. PPLN was used before in ultrashort, green-pumped OPOs, where similar power levels were achieved and the same limiting effects were encountered. A quasi-CW power of $140\,\mathrm{mW}$ was reported from a setup consisting of a PPLN OPO and a mechanically chopped, frequency-doubled Nd:YLF pump source [28]. The pulse duration was $2\,\mathrm{ps}$, the repetition rate $120\,\mathrm{MHz}$ and the tuning range $880\,\mathrm{nm} \ldots 1.29\,\mu\mathrm{m}$. More recently, Chimento *et al.* used MgO:PPLN in a picosecond, green-pumped OPO to demonstrate a similar tuning range [29]. However, the combined output power was well below $100\,\mathrm{mW}$. Secondly, an LBO crystal

was applied in the OPO instead to avoid damage problems. High combined output powers of $> 4\,\mathrm{W}$ were obtained and the tunability extended from $0.65\,\mu\mathrm{m}$ to $2.85\,\mu\mathrm{m}$ with typical pulse durations around $4\,\mathrm{ps}$. To date, the highest output power of $1.6\,\mathrm{W}$ (signal only) from such an LBO OPO was measured by Tukker *et al.*, who used an Nd:YLF pump source [30]. The OPO was tunable from $740\,\mathrm{nm}$ to $1.83\,\mu\mathrm{m}$ and produced $< 30\,\mathrm{ps}$ signal pulses. YDF MOPA configurations were also used in the past, however, with average powers not exceeding $1\,\mathrm{W}$ (picosecond [31], femtosecond [32]). Generally, the green pump light raised additional problems in terms of suitable nonlinear crystals. Lithium niobate seemed to be suboptimal due to known damage effects. LBO was performing much better under comparable operating conditions. However, similar problems with the pump source as mentioned above were still existent. These included beam pointing instabilities in conjunction with long path lengths, fibre damage, polarisation drifts affecting the frequency-doubling efficiency and stability, and insufficient beam quality.

8.2 Discussion and outlook

The fibre amplifier sources for the OPOs suffered from problems when operated at high output power and they must be addressed to make the sources more stable and robust. These problems mainly concerned the large-mode-area, double-clad fibres of the final power amplifiers. In order to mitigate thermal problems at high-power operation, active heat-sinking, not only of the fibre output side, but along the entire length of the fibre, is needed and a practical setup is currently being designed. The mechanical stability of the fibre tip can be improved with the application of ultra-stable fibre-mounts that firmly hold the fibre up to the end-cap. A suppression of the beam pointing instabilities from modal interference of the many supported fibre modes can only be achieved, if the fibre can be operated such that solely the fundamental mode is guided. Possible approaches are the improvement of the tapered splice quality that can increase the mode purity, so that higher-order modes are not excited at all, as well as the use of fibres with a smaller core diameter. A smaller core diameter, however, leads to increased nonlinearities that, in turn, need to be dealt with. Regarding the fibre-based, femtosecond CPA system, adaptive pulse shaping is a powerful tool to remove the accumulated third-order dispersion and to obtain ultrashort, pedestal-free pulses. However, this adds considerable complexity to the system (free-space optical setup, time-consuming optimisation procedure, sophisticated computer algorithm, expensive equipment). As an alternative, a CPA system with a grating-based stretcher or a chirped fibre Bragg grating stretcher rather than a simple single-mode fibre would allow for a compensation of second- and third-order dispersion. Furthermore, the free-space nature of the amplifier chain lacks user-friendliness and thus turning it into an all-fibre system

is another useful step. It can be realised, if a chirped fibre Bragg grating is used for stretching, so that the pulse shaper is not required anymore, and if the photonic crystal fibres are replaced with other fibres, so that splicing is feasible.

Material properties of nonlinear crystals appear to be the limiting factors for high-power, ultrashort OPO operation. For OPOs reaching into the MIR using $1\,\mu\mathrm{m}$ pump sources, PPLN or MgO:PPLN are very attractive materials. In order to avoid damage of these crystals, waist size scaling of the beams inside the crystals is the most convenient method to reduce the intensities. For this, it is necessary to use thick crystals, which are now becoming more readily available from commercial suppliers thanks to improved poling processes. Since material damage is not only caused by high peak intensities, but can also be triggered by parasitic absorption of the average power via lattice impurities, high-purity crystals are of paramount importance. Alternatively, MgO-doped stoichiometric lithium tantalate can be used, which has better material properties for high-power operation, but it is more expensive and has a lower nonlinear coefficient. For green-pumped OPOs, lithium triborate appears to be more advantageous, since it has better material properties with respect to photo-refraction and induced / nonlinear absorption compared to lithium niobate. Importantly, the pump beam entering the OPO must be as stable (spatially and temporally) as possible, which requires short free-space path lengths between the individual system stages. Additionally, compact OPO resonators improve the stability of the output beams and this can be achieved, especially at low repetition rates, if a fibre for signal feedback is part of the resonator. Further modelling and experiments are required to get a better understanding of the roll-off effect observed in some of the OPO experiments in this thesis. The origin of this effect may be parasitic absorption in the nonlinear crystal and / or the optical isolator crystal leading to thermal lensing and hence reduced beam quality and resonator stability.

Nevertheless, the systems developed in this thesis have the potential for real-world applications as stated in the previous section. As one example, a three-year project at the Optoelectronics Research Centre aiming on further development, improvement and scaling of the high-pulse-energy, picosecond, MIR, fibre-feedback OPO (chapter 4) for application in resonant-IR pulsed laser deposition has just started. Resonant-IR pulsed laser deposition of thin-film polymers is a method, where picosecond pulses with microjoule energies in the MIR are used to break weak intermolecular bonds in the polymer to ablate it from the substrate material and deposit it on the target material. The bonds have vibrational resonances that are typically in the so-called fingerprint region in the MIR, e.g. the stretch modes of –OH at $2.9\,\mu\mathrm{m}$ or –CH at $3.4\,\mu\mathrm{m}$. The attractiveness and importance of this method lies in the fact that the polymer structure is not chemically modified during the process, whereas other methods alter the chemical structure and may require solvents. The growth of high-quality thin-film polymers is important

in numerous areas including photonics (e.g. flexible displays), electronics (e.g. thin-film transistors), micro-mechanical systems (e.g. anti-stiction coatings) and medicine (e.g. drug delivery). To date, large and expensive, low-repetition-rate, high-pulse-energy, picosecond free-electron lasers have mostly been used to access the MIR, but they are clearly not practical for commercial usage. Therefore, this project addresses the development of a compact and robust OPO source pumped with an Yb:fibre-amplified gain-switched laser diode, which operates at high repetition rates to enhance throughput and with microjoule pulse energies to ablate only a small amount of material at a time. Among others, the project objectives regarding the source are the production of average powers of $> 30\,\mathrm{W}$ and pulse energies of $> 1\,\mu\mathrm{J}$ in the MIR spectral region. Another example, where high pulse energies in the MIR are required, is ultrafast waveguide inscription by means of refractive index modification in materials such as silicon or germanium and OPO sources are being developed for this purpose [19, 20].

References

[1] D. M. Bubb and R. F. Haglund Jr., "Resonant Infrared Pulsed Laser Ablation and Deposition of Thin Polymer Films," in *Pulsed Laser Deposition of Thin Films*, R. W. Eason, ed., pp. 35–60 (John Wiley & Sons, Hoboken, New Jersey, 2006).

[2] V. Z. Kolev, M. W. Duering, B. Luther-Davies, and A. V. Rode, "Compact high-power optical source for resonant infrared pulsed laser ablation and deposition of polymer materials," Opt. Express **14**(25), 12,302–12,309 (2006).

[3] S. Lecomte, R. Paschotta, M. Golling, D. Ebling, and U. Keller, "Synchronously pumped optical parametric oscillators in the 1.5-μm spectral region with a repetition rate of 10 GHz," J. Opt. Soc. Am. B **21**(4), 844–850 (2004).

[4] S. Lecomte, R. Paschotta, S. Pawlik, B. Schmidt, K. Furusawa, A. Malinowski, D. J. Richardson, and U. Keller, "Optical parametric oscillator with a pulse repetition rate of 39 GHz and 2.1-W signal average output power in the spectral region near 1.5μm," Opt. Lett. **30**(3), 290–292 (2005).

[5] S. Lecomte, R. Paschotta, S. Pawlik, B. Schmidt, K. Furusawa, A. Malinowski, D. J. Richardson, and U. Keller, "Synchronously pumped optical parametric oscillator with a repetition rate of 81.8 GHz," IEEE Photonics Technology Letters **17**(2), 483–485 (2005).

[6] C. L. Evans, E. O. Potma, M. Puoris'haag, D. Côté, C. P. Lin, and X. S. Xie, "Chemical imaging of tissue in vivo with video-rate coherent anti-Stokes Raman scattering microscopy," Proceedings of the National Academy of Sciences of the United States of America **102**(46), 16,807–16,812 (2005).

[7] C. L. Evans and X. S. Xie, "Coherent Anti-Stokes Raman Scattering Microscopy: Chemical Imaging for Biology and Medicine," Annual Review of Analytical Chemistry **1**(1), 883–909 (2008).

[8] F. Ganikhanov, S. Carrasco, X. Sunney Xie, M. Katz, W. Seitz, and D. Kopf, "Broadly tunable dual-wavelength light source for coherent anti-Stokes Raman scattering microscopy," Opt. Lett. **31**(9), 1292–1294 (2006).

[9] P. J. Campagnola and L. M. Loew, "Second-harmonic imaging microscopy for visualizing biomolecular arrays in cells, tissues and organisms," Nature Biotechnology **21**(11), 1356–1360 (2003).

[10] W. R. Zipfel, R. M. Williams, R. Christie, A. Y. Nikitin, B. T. Hyman, and W. W. Webb, "Live tissue intrinsic emission microscopy using multiphoton-excited native fluorescence and second harmonic generation," Proceedings of the National Academy of Sciences **100**(12), 7075–7080 (2003).

[11] S.-W. Chu, T.-M. Liu, C.-K. Sun, C.-Y. Lin, and H.-J. Tsai, "Real-time second-harmonic-generation microscopy based on a 2-GHz repetition rate Ti:sapphire laser," Opt. Express **11**(8), 933–938 (2003).

[12] S. W. Hell and J. Wichmann, "Breaking the diffraction resolution limit by stimulated emission: stimulated-emission-depletion fluorescence microscopy," Opt. Lett. **19**(11), 780–782 (1994).

[13] S. W. Hell, "Nanoscopy with focused light," in *The Rank Prize Funds - Symposium on Ultrafast Biophotonics* (Grasmere, UK, 2010).

[14] F. Kienle, K. K. Chen, S.-U. Alam, C. B. E. Gawith, J. I. Mackenzie, D. C. Hanna, D. J. Richardson, and D. P. Shepherd, "High-power, variable repetition rate, picosecond optical parametric oscillator pumped by an amplified gain-switched diode," Opt. Express **18**(8), 7602–7610 (2010).

[15] A. Robertson, M. E. Klein, M. A. Tremont, K. J. Boller, and R. Wallenstein, "2.5-GHz repetition-rate singly resonant optical parametric oscillator synchronously pumped by a mode-locked diode oscillator amplifier system," Opt. Lett. **25**(9), 657–659 (2000).

[16] T. Südmeyer, E. Innerhofer, F. Brunner, R. Paschotta, T. Usami, H. Ito, S. Kurimura, K. Kitamura, D. C. Hanna, and U. Keller, "High-power femtosecond fiber-feedback optical parametric oscillator based on periodically poled stoichiometric $LiTaO_3$," Opt. Lett. **29**(10), 1111–1113 (2004).

[17] O. Kokabee, A. Esteban-Martin, and M. Ebrahim-Zadeh, "Efficient, high-power, ytterbium-fiber-laser-pumped picosecond optical parametric oscillator," Opt. Lett. **35**(19), 3210–3212 (2010).

[18] F. Kienle, P. Siong Teh, S.-U. Alam, C. B. E. Gawith, D. C. Hanna, D. J. Richardson, and D. P. Shepherd, "Compact, high-pulse-energy, picosecond optical parametric oscillator," Opt. Lett. **35**(21), 3580–3582 (2010).

[19] T. P. Lamour, L. Kornaszewski, J. H. Sun, and D. T. Reid, "Yb:fiber-laser-pumped high-energy picosecond optical parametric oscillator," Opt. Express **17**(16), 14,229–14,234 (2009).

[20] T. P. Lamour and D. T. Reid, "650-nJ pulses from a cavity-dumped Yb:fiber-pumped ultrafast optical parametric oscillator," Opt. Express **19**(18), 17,557–17,562 (2011).

[21] E. Khazanov, N. Andreev, O. Palashov, A. Poteomkin, A. Sergeev, O. Mehl, and D. H. Reitze, "Effect of terbium gallium garnet crystal orientation on the isolation ratio of a Faraday isolator at high average power," Appl. Opt. **41**(3), 483–492 (2002).

[22] E. Khazanov, N. F. Andreev, A. Mal'shakov, O. Palashov, A. K. Poteomkin, A. Sergeev, A. A. Shaykin, V. Zelenogorsky, I. A. Ivanov, R. Amin, G. Mueller, D. B. Tanner, and D. H. Reitze, "Compensation of Thermally Induced Modal Distortions in Faraday Isolators," IEEE Journal of Quantum Electronics **40**(10), 1500–1510 (2004).

[23] J. Prawiharjo, F. Kienle, N. K. Daga, D. C. Hanna, D. J. Richardson, and D. P. Shepherd, "High-Quality Energy-Scalable Femtosecond Pulses from a Fibre-Based Chirped Pulse Amplification System via Adaptive Pulse Shaping," in *Conference on Lasers and Electro-Optics (CLEO) Europe*, vol. CJ9.5 (Munich, Germany, 2009).

[24] F. Adler, K. C. Cossel, M. J. Thorpe, I. Hartl, M. E. Fermann, and J. Ye, "Phase-stabilized, 1.5 W frequency comb at 2.8-4.8 μm," Opt. Lett. **34**(9), 1330–1332 (2009).

[25] J. W. Nicholson, A. D. Yablon, S. Ramachandran, and S. Ghalmi, "Spatially and spectrally resolved imaging of modal content in large-mode-area fibers," Opt. Express **16**(10), 7233–7243 (2008).

[26] A. Ashkin, G. D. Boyd, J. M. Dziedzic, R. G. Smith, A. A. Ballman, J. J. Levinstein, and K. Nassau, "Optically-induced refractive index inhomogeneities in $LiNbO_3$ and $LiTaO_3$," Applied Physics Letters **9**(1), 72–74 (1966).

[27] F. Jermann, M. Simon, and E. Krätzig, "Photorefractive properties of congruent and stoichiometric lithium niobate at high light intensities," J. Opt. Soc. Am. B **12**(11), 2066–2070 (1995).

[28] V. Pruneri, S. D. Butterworth, and D. C. Hanna, "Low-threshold picosecond optical parametric oscillation in quasi-phase-matched lithium niobate," Applied Physics Letters **69**(8), 1029–1031 (1996).

[29] P. F. Chimento, M. Jurna, H. S. P. Bouwmans, E. T. Garbacik, L. Hartsuiker, C. Otto, J. L. Herek, and H. L. Offerhaus, "High-resolution narrowband CARS spectroscopy in the spectral fingerprint region," Journal of Raman Spectroscopy **40**(9), 1229–1233 (2009).

[30] T. W. Tukker, C. Otto, and J. Greve, "Design, optimization, and characterization of a narrow-bandwidth optical parametric oscillator," J. Opt. Soc. Am. B **16**(1), 90–95 (1999).

[31] K. Kieu, B. G. Saar, G. R. Holtom, X. S. Xie, and F. W. Wise, "High-power picosecond fiber source for coherent Raman microscopy," Opt. Lett. **34**(13), 2051–2053 (2009).

[32] C. Cleff, J. Epping, P. Gross, and C. Fallnich, "Femtosecond OPO based on LBO pumped by a frequency-doubled Yb-fiber laser-amplifier system for CARS spectroscopy," Applied Physics B: Lasers and Optics **103**(4), 795–800 (2011).

Appendices

Appendix A

List of publications

A.1 Journal publications

[1] **F. Kienle**, P. S. Teh, D. Lin, S.-U. Alam, J. H. V. Price, D. C. Hanna, D. J. Richardson, and D. P. Shepherd, "High-power, high-repetition-rate, green-pumped, picosecond LBO optical parametric oscillator," Opt. Express, Focus Issue on Next-Generation Modular Ultrafast Lasers [**Accepted**]

[2] **F. Kienle**, D. Lin, S.-U. Alam, H. S. S. Hung, C. B. E. Gawith, H. E. Major, D. J. Richardson, and D. P. Shepherd, "Green-pumped, picosecond MgO:PPLN optical parametric oscillator," J. Opt. Soc. Am. B **29**(1), 144–152 (2012).

[3] **F. Kienle**, P. S. Teh, S.-U. Alam, C. B. E. Gawith, D. C. Hanna, D. J. Richardson, and D. P. Shepherd, "Compact, high-pulse-energy, picosecond optical parametric oscillator," Opt. Lett. **35**(21), 3580–3582 (2010).

[4] **F. Kienle**, K. K. Chen, S.-U. Alam, C. B. E. Gawith, J. I. Mackenzie, D. C. Hanna, D. J. Richardson, and D. P. Shepherd, "High-power, variable repetition rate, picosecond optical parametric oscillator pumped by an amplified gain-switched diode," Opt. Express **18**(8), 7602–7610 (2010).

A.2 Conference publications

[1] **F. Kienle**, P. S. Teh, S.-U. Alam, C. B. E. Gawith, D. C. Hanna, D. J. Richardson, and D. P. Shepherd, "High pulse energy, picosecond MgO:PPLN optical parametric oscillator using a single-mode fiber for signal feedback," in *2011 Advanced Solid-State Photonics (ASSP)* , paper AMB03 (Istanbul, Turkey, 2011).

[2] D. J. Richardson, K. K. Chen, D. Lin, E. L. Lim, P. S. Teh, A. Malinowski, J. H. V. Price, **F. Kienle**, D. P. Shepherd, and S.-U. Alam, "Ultrafast fibre lasers for biophotonics," presented at the *Rank Prize Funds Symposium on Biophotonics* (Grasmere, England, 23-26 August 2010). [**Invited**]

[3] **F. Kienle**, K. K. Chen, S.-U. Alam, C. B. E. Gawith, J. I. Mackenzie, D. C. Hanna, D. J. Richardson, and D. P. Shepherd, "A high power, variable repetition rate, picosecond, optical parametric oscillator pumped by an amplified gain-switched diode," presented at the *Rank Prize Funds Symposium on Biophotonics* (Grasmere, England, 23-26 August 2010). [**Invited**]

[4] **F. Kienle**, K. K. Chen, S.-U. Alam, C. B. E. Gawith, J. I. Mackenzie, D. C. Hanna, D. J. Richardson, and D. P. Shepherd, "Variable Repetition Rate, High Power, Picosecond Optical Parametric Oscillator Synchronously Pumped by a Fibre-Amplified Gain-Switched Laser Diode," presented at the *International Summer School in Ultrafast Nonlinear Optics SUSSP 66* (Edinburgh, Scotland, 11-21 August 2010).

[5] **F. Kienle**, K. K. Chen, S.-U. Alam, C. B. E. Gawith, J. I. Mackenzie, D. C. Hanna, D. J. Richardson, and D. P. Shepherd, "A Picosecond Optical Parametric Oscillator Synchronously Pumped by an Amplified Gain-Switched Laser Diode," in *2010 Conference on Lasers and Electro-Optics (CLEO) US*, paper CThZ7 (San Jose, California, USA, 2010).

[6] J. Prawiharjo, **F. Kienle**, N. K. Daga, D. C. Hanna, D. J. Richardson, and D. P. Shepherd, "High-Quality Energy-Scalable Femtosecond Pulses from a Fibre-Based Chirped Pulse Amplification System via Adaptive Pulse Shaping," in *2009 Conference on Lasers and Electro-Optics (CLEO) Europe*, paper CJ9.5 (Munich, Germany, 2009). [**Invited**]

Appendix B

Calculation of the B-integral

As described in section 2.2.3, the B-integral is a measure for the accumulated nonlinear phase shift in a medium (here: optical fibres). Equation (2.10) defines the B-integral mathematically. In order to calculate a value for the B-integral from the experimental parameters of a laser or amplifier system, we start with the equation for homogeneous gain [1]

$$P_{0,out} = P_{0,in} \cdot e^{\gamma_g z} \,, \tag{B.1}$$

where $P_{0,out}$ denotes the output peak power, $P_{0,in}$ the input peak power, γ_g the small signal gain coefficient (see equation (2.3)) and z the propagation distance. Starting from equation (2.10), reproduced here for completeness [2]

$$\begin{aligned} B &= \frac{2\pi}{\lambda_0} \int n_2 I(z)\, dz \\ &= \frac{2\pi}{\lambda_0} \frac{n_2}{A_{eff}} \int P_0(z)\, dz \,, \end{aligned} \tag{B.2}$$

we insert equation (B.1) and integrate over the entire length L of the laser medium

$$\begin{aligned} B &= \frac{2\pi n_2}{\lambda_0 A_{eff}} \int_0^L P_{0,in} \cdot e^{\gamma_g z}\, dz \\ &= \frac{2\pi n_2}{\lambda_0 A_{eff}} \left[\frac{P_{0,in}}{\gamma_g} \cdot e^{\gamma_g z} \right]_0^L \\ &= \frac{2\pi n_2}{\lambda_0 A_{eff}} \left(\frac{P_{0,in}}{\gamma_g} e^{\gamma_g L} - \frac{P_{0,in}}{\gamma_g} e^{\gamma_g 0} \right) . \end{aligned} \tag{B.3}$$

Solving equation (B.1) for γ_g and substituting into (B.3), we arrive at

$$B = \frac{2\pi n_2}{\lambda_0 A_{eff}} \left(\frac{P_{0,out} - P_{0,in}}{\ln \frac{P_{0,out}}{P_{0,in}}} \right) L \,, \tag{B.4}$$

which can be calculated by using the experimental parameters: The peak powers at the input and output of the fibre amplifier can be calculated with

$$P_0 = \frac{P_{av}}{f_{rep}\tau} \,, \tag{B.5}$$

where P_{av} is the average power, f_{rep} the repetition rate and τ the FWHM pulse duration (if a Gaussian beam profile is assumed, the value for P_0 is reduced by a factor of $\sqrt{4\ln 2/\pi}$); the centre wavelength λ_0 can be measured with an OSA; the nonlinear refractive index n_2 for silica fibres can be found in the literature [3]; the fibre mode-field area A_{eff} can be calculated from the core diameter and the length of the fibre L can easily be measured.

References

[1] A. E. Siegman, *Lasers*, 1st ed. (University Science Books, Sausalito, California, 1986).

[2] M. D. Perry, T. Ditmire, and B. C. Stuart, "Self-phase modulation in chirped-pulse amplification," Opt. Lett. **19**(24), 2149–2151 (1994).

[3] G. P. Agrawal, *Nonlinear Fiber Optics*, Optics and Photonics, 3rd ed. (Academic Press, San Diego, 2001).